EXPERIMENTAL AND VALIDATED MODELING STUDIES OF ELECTROLYTE FLOW AND ANODE SLIME BEHAVIOR AND TRANSPORT IN COPPER ELECTROREFINING

by

Weizhi Zeng

A dissertation submitted to the faculty of
The University of Utah
in partial fulfillment of the requirements for the degree of

Doctor of Philosophy

Department of Metallurgical Engineering

The University of Utah

December 2016

The University of Utah Graduate School

STATEMENT OF DISSERTATION APPROVAL

The dissertation of **Weizhi Zeng**

has been approved by the following supervisory committee members:

Michael L. Free	, Chair	**10/06/2016** Date Approved
Manoranjan Misra	, Member	**10/06/2016** Date Approved
Zhigang Zak Fang	, Member	**10/06/2016** Date Approved
Edward M. Trujillo	, Member	**10/06/2016** Date Approved
Shijie Wang	, Member	**10/06/2016** Date Approved

and by Manoranjan Misra , Chair/Dean of

the Department/College/School of **Metallurgical Engineering**

and by David B. Kieda, Dean of The Graduate School.

ABSTRACT

Electrorefining is widely utilized to refine nonferrous metals such as copper, zinc, and nickel as a final step to meet purity requirements. Thus, it is critical to control impurities and maintain high cathode purity in electrorefining. In copper electrorefining, slime particles are responsible for most cathode contamination. As a result, the adhesion, mobility, and transport of anode slime particles in flowing electrolyte are of significance and worth comprehensive studies.

A 3-factor 2-level designed set of experiments was performed to determine the effects of inlet flow rate, temperature, and current density on impurity particle behavior in electrolyte and the associated distribution on the cathode in copper electrorefining.

A model based in COMSOL Multiphysics® consisting of an electrorefining cell was utilized to simulate copper electrorefining. The model data for impurity particle distribution were compared with measured impurity particle contamination at the cathode surface, and the results show a very good correlation.

Four series of copper electrorefining tests were performed using four different types of anodes. Test results show that the high impurity anodes and the scrap cycle anodes have more inclusions associated with the Pb-Bi-S compounds that show evidence of sintering at 50 ℃, whereas the low impurity anodes and the strip cycle anodes have more inclusions related with the Pb-Bi-S-As compounds that demonstrate evidence of sintering above 65 ℃. Arsenic content in copper anode and cell temperature are major factors

affecting slime sintering and coalescence, which can improve anode slime adhesion and reduce the amount of suspended slimes.

Copper electrorefining tests were conducted in a pilot scale cell made of transparent cell walls. Fluid flow velocities in the gaps between adjacent electrodes were measured. Modeling and simulation of copper electrorefining in this cell were performed. The flow velocity field results from modeling agree reasonably well with the measured electrolyte velocities.

The effects of anode compositions, current density, cathode blank width, and flow rate on anode slime behavior and cathode copper purity were studied by performing copper electrorefining tests in the pilot scale cell under commercial tankhouse environment.

TABLE OF CONTENTS

LIST OF TABLES

Page

ACKNOWLEDGEMENTS

First of all, I gratefully acknowledge Rio Tinto Kennecott Utah Copper for sponsoring the project of "Improving slime adhesion and cathode purity," which gave me the opportunity to study phenomena in copper electrorefining. Furthermore, I sincerely thank my advisor, Dr. Michael Free, who offered me the chance to study abroad in an interesting field for my doctorate degree. He is very knowledgeable, experienced, and noted in the fields of hydrometallurgy and electrochemistry. He helped me develop my capabilities in these fields, as well as research abilities for scientific projects.

Besides, I appreciate the mentoring from other professors in the Department of Metallurgical Engineering. They are responsible, inspiring, and are very willing to pass on knowledge and experience to me. I also thank all of my colleagues and friends at the University of Utah, who helped me in various ways. Additionally, I would like to thank Dr. Shijie Wang, the Principal Advisor at Kennecott Copper Refinery and an expert in extractive metallurgy of copper, for his mentoring and help during the project.

Above all, my greatest and deepest appreciation goes to my parents, Hongyan Lin and Xiaolin Zeng, for their endless love, encouragement, and support. There are not enough words in the world to express my gratitude for them. I also thank my girlfriend, who has been accompanying and supporting me along the way for all these years. This dissertation is hereby dedicated to them.

CHAPTER 1

INTRODUCTION

1.1 Overview

Electrorefining is a widely utilized process whose purpose is to remove impurities from a metal anode by electrolysis, and it is an important process for nonferrous metals. During the process of electrorefining, the anode is cast from a metal melt, which contains a variety of impure elements. When the current is conducted through the electrodes and the electrolytic solution that contains the metal in its dissolved state, the anode is oxidized and dissolved into the electrolyte. However, most anode impurities are not dissolved. Thus, the dissolved metal ions are electrodeposited at the cathode with significantly less impurities. As a result, the electrorefining process can produce refined metal on the cathode.

Contact reduction, a natural electrochemical reaction, is the underlying principle for cementation, which is an old technique for metal recovery from metal bearing solution. Dissolved metal ions in the solution that are more noble take electrons from a metal that is less noble. Consequently, the less noble metal is dissolved and the more noble metal ions are reduced to the metallic state.[1] Nevertheless, sometimes we need to reverse the original electrochemical reaction in order to produce products that are desired.

Electrowinning and electrorefining are two processes that practice this by applying an external potential to drive electrochemical reactions in the desired direction.

Then the desired metal is electroplated on the cathode, even if it cannot be recovered in natural reactions such as contact reduction. It is noteworthy that the applied potential in electrorefining mainly overcomes the electrochemical and concentration overpotentials. The current density is a direct measure of the electrorefining rate, which is closely related to the applied potential but limited by diffusion.

Ores are the most common form for most metals in nature. Consequently, most metals must be recovered to their elemental forms to be further processed. The metal ore can be dissolved by processes such as leaching in aqueous solution or melted by processes such as smelting in molten form. The target metal in pregnant solution acquired from leaching is then separated by solvent extraction and finally recovered by electrowinning, while the molten form metal compounds obtained from smelting are converted, fire refined, and electroplated by electrorefining. In electrorefining and electrowinning, the metal desired is electrodeposited on cathodes that are usually metal sheets, with the metal dissolution and the oxygen evolution on the anode respectively. Some metals normally exist as metal sulfides in nature, which are difficult to dissolve in aqueous solution by leaching, and are therefore typically processed by pyrometallurgical methods through smelting, converting, and fire refining. Some other metals are normally present as metal oxides in nature, which can be easily dissolved in aqueous solution by hydrometallurgical methods and then separated and electrowon. It is noteworthy that electrowinning can perform in molten metal salt, allowing metal salts and sulfides that are conductive in their molten form to be electrolyzed directly and recovered on the cathode that may be liquid. For copper in the form of chalcopyrite ore, it is processed by pyrometallurgical methods and the resulting anode copper is sent for copper electrorefining.

Copper electrorefining is the most widely utilized process in the world to refine copper to very high purity, though about 20% of the high purity copper production is fulfilled by copper electrowinning. Copper electrorefining generally uses the copper of intermediate purity from 98 to 99% produced from smelters as the anode, from which less pure copper is electrolytically dissolved, along with soluble inclusions containing arsenic, bismuth, and antimony.[1] Insoluble inclusions are liberated from the anode in the form of anode slimes. Then the desired copper ions are transported to the cathode and electroplated on the cathode sheet, which is usually made of stainless steel. The cathode copper products are more pure compared to the original anode copper, with a purity typically higher than 99.99%. The electrolytic solution in copper electrorefining usually contains copper sulfate, sulfuric acid and other additives such as glue, thiourea, gelatin, and chloride, which play the role of reducing dentrite growth, facilitating copper nucleation, and thus producing cathodes with smoother and denser surfaces.[1]

The late nineteenth century witnessed the establishment of industrial scale copper electrorefining and this process has been improved considerably since then. Progress is made everywhere, including but not limited to impurity control, anode slime characterization and processing, electrolyte purification, online monitoring, and electrolyte additives. In recent decades, remarkable production increases have been reached in copper electrorefining as a result of all these improvements. Chapter 2 presents a literature review of these aspects, as well as backgrounds and theories in copper electrorefining.

1.2 Objectives

This research focuses on the improvement of purity level in copper cathode in electrorefining by studying the effects of process parameters, the fluid flow field in

electrorefining cells, and the coalescence, adhesion, and transport of anode slimes. Figure 1.1 shows the slime particle origination, behavior, and transport in copper electrorefining. Since most contamination in copper cathode is caused by slime particles, it is significant to study their characteristics, adhesiveness, and transport throughout the process, which are presented through Chapters 3-7. Chapter 3 evaluates the effects of different process parameters including flow rate, temperature, and current density, on the transport of impurity particles by a factorial design of experiments in a lab-scale electrorefining cell. Chapter 4 presents the modeling, simulation, and validation of the fluid flow field and the impurity particle movement in the lab-scale electrorefining cell. Chapter 5 studies anode slime sintering and coalescence after they are released from anodes, by performing a series of lab-scale experiments and characterizing anodes, cathodes, and anode slimes. Chapter 6 shows experimental measurement and simulation of the electrolyte flow field in a pilot scale cell in the commercial tankhouse of Kennecott Copper Refinery. The slime particle movement in the cell was also simulated and validated in this chapter. Chapter 7 studies the effects of anode composition and process parameters on anode slime coalescence, adhesion, and transport in the pilot scale cell.

1.3 References

1. M. L. Free: *Hydrometallurgy: Fundamentals and Applications*, John Wiley & Sons, Inc., Hoboken, NJ, 2013.

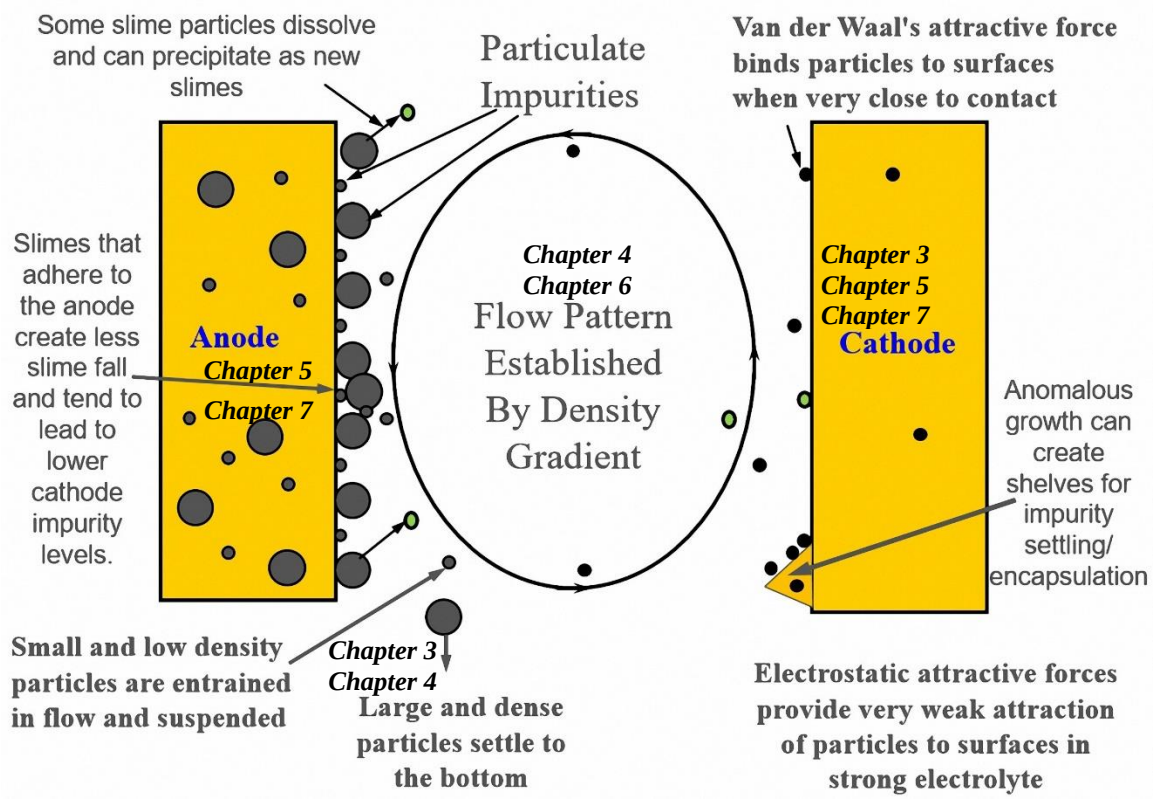

Figure 1.1 Slime particle transport and potential deposition at a cathode

CHAPTER 2

BACKGROUND AND LITERATURE REVIEW

The theoretical fundamentals in copper electrorefining are discussed, including transport laws, thermodynamics, and kinetics. Previous studies on behavior of impurities, electrolyte purification, impurity precipitation, electrolyte additives, cathode surface quality control, anode mineralogy and microstructures, and anode slime phases, microstructures, and adhesiveness are reviewed. A considerable amount of research has been done in these areas in the past and significant findings, studies, and conclusions are summarized.

2.1 The Fundamentals of Copper Electrorefining

2.1.1 Transport Laws for Copper Electrorefining

Copper electrorefining takes place in an electrochemical cell, so it follows certain transport laws established in electrochemical systems. Dissolution and deposition phenomena are observed in the process, in which mass transfer is involved and plays a significant role. There is a set of fundamental equations for mass transfer in electrolyte. These equations describe current density, the movement of ionic species, electroneutrality, material balances, and fluid mechanics. Here the medium described is dilute solution, comprising ionized species, uncharged minor components, and a nonionized solvent. Although concentrated solutions are the cases for most times in reality, these equations can

describe most of them in an approximate approach.

First of all, it is the motion of various charged species that constitute the current in electrolyte. Therefore, the current density in an electrolytic solution is given by:

$$\boldsymbol{i} = F\sum_i z_i \boldsymbol{N_i} \tag{2.1}$$

where $\boldsymbol{i}$ is the current density, F is Faraday's constant, z_i is the charge of species i, and $\boldsymbol{N_i}$ is the flux density of species i. We can express the flux density quantitatively by:[1]

$$\boldsymbol{N_i} = -z_i u_i F c_i \nabla\Phi - D_i \nabla c_i + c_i \boldsymbol{v} \tag{2.2}$$

where D_i, z_i, u_i are the diffusivity, charge, and mobility of species i, F is Faraday's constant, $-\nabla\Phi$ is an electric field, ∇c_i is a concentration gradient, and $\boldsymbol{v}$ is the velocity field.

Substituting the equation for flux density $\boldsymbol{N_i}$, the current density in an electrolytic solution can be further expressed by:[1]

$$\boldsymbol{i} = -F^2\nabla\Phi\sum_i z_i^2 u_i c_i - F\sum_i z_i D_i \nabla c_i + F\boldsymbol{v}\sum_i z_i c_i \tag{2.3}$$

Except in certain boundaries, the electrolyte is electrically neutral:

$$\sum_i z_i c_i = 0 \tag{2.4}$$

Therefore the current density becomes:

$$\boldsymbol{i} = -F^2\nabla\Phi\sum_i z_i^2 u_i c_i - F\sum_i z_i D_i \nabla c_i \tag{2.5}$$

Lastly, the material balance needs to be considered, which can be given by equation:[1]

$$\frac{\partial c_i}{\partial t} = -\nabla\cdot\boldsymbol{N_i} + R_i \tag{2.6}$$

where R_i is the homogeneous chemical reaction (production) rate per unit volume for

species *i*. It is noteworthy to point out that these reactions typically take place in the bulk solution, and do not include electrode reactions at the electrode boundary. Since reactions in electrolytic solutions only take place on the surface of electrodes for most situations, the homogeneous chemical reaction rate term would most often be zero.

Due to the low flow rate in most electrorefining processes, the fluid flow in the electrolytic solution is assumed to be laminar. The fluid flow is governed by the continuity and the momentum equation:[1]

$$\frac{\partial \rho}{\partial t} + \nabla \cdot (\rho \boldsymbol{v}) = 0 \tag{2.7}$$

$$\rho \frac{\partial \boldsymbol{v}}{\partial t} + \rho \boldsymbol{v} \cdot \nabla \boldsymbol{v} = -\nabla p + \nabla \cdot \left(\mu (\nabla \boldsymbol{v} + (\nabla \boldsymbol{v})^{\mathrm{T}}) - \frac{2}{3} \mu (\nabla \cdot \boldsymbol{v}) \boldsymbol{I} \right) + \boldsymbol{F} \tag{2.8}$$

where $\boldsymbol{v}$ is the fluid velocity field, p is the pressure, μ is the dynamic viscosity, and $\boldsymbol{F}$ is the body force (per unit volume) acting on the fluid. The fluid flow in copper electrorefining is important not only for species transfer, but also for slime transport that mostly affects cathode purity.

2.1.2 Copper Electrorefining Thermodynamics

In electrolytic processes, half-cell reactions take place on electrodes and the free energy for the half-cell reaction can be determined by the equation:

$$\Delta G_r = \Delta G_r^o + RTlnQ \tag{2.9}$$

where ΔG_r^o is the standard free energy for the reaction, Q is the ratio of activities of products to reactants or the mass action coefficient.[2]

If the reaction takes place under nonstandard temperatures and without phase transformations, the following equation needs to be used to calculate the free energy of the reaction:[2]

$$\Delta G_T^o = \Delta H_{298}^o + \int_{298}^{T} \Delta c_p dT - T\Delta S_{298}^o - T\int_{298}^{T} \frac{\Delta c_p}{T} dT \tag{2.10}$$

where ΔH_{298}^o is the standard enthalpy of the reaction at 298 K, ΔS_{298}^o is the standard entropy of the reaction at 298K, and Δc_p is the heat capacity change of the reaction.

If the reaction happens under nonstandard pressures, the free energy of the reaction can be determined by:

$$\Delta G_p^o - \Delta G_{1atm}^o = \int_{1atm}^{p} \Delta V_m dp \tag{2.11}$$

where ΔG_{1atm}^o is the standard free energy under 1 atm, and ΔV_m is the molar volume changes in the reaction. The free energy of a reaction usually varies by 0.1 J/mole/bar.[2]

Potential is the commonly used parameter rather than the free energy when dealing with electrolysis problems, so there is a need to convert free energy of a half-cell reaction to its electrochemical potential:

$$\frac{-\Delta G_r}{nF} = \frac{-\Delta G_r^o}{nF} - \frac{RT}{nF} lnQ \tag{2.12}$$

which leads to,

$$E = E^o - \frac{\mathrm{RT}}{nF} lnQ \tag{2.13}$$

which is widely known as the Nernst Equation. E^o is the standard potential, E is the equilibrium potential affected by the activities of dissolved species, n is the number of electrons transferred per mole of the reaction, and F is Faraday constant.[2]

The applied voltage in an electrochemical cell needs to overcome the potential difference between the two half-cell reactions, as well as overpotentials and resistance voltage drop. The applied voltage needed for an electrolytic process is given by the equation:

$$V_{applied} = E_{anodic} - E_{cathodic} + \eta_{anodic} + \eta_{cathodic} + IR \qquad (2.14)$$

where E is the half-cell reaction potential, η is the overpotential, I is the overall current, and R is the resistance.[2]

The anodic reaction in copper electrorefining is:

$$Cu = Cu^{2+} + 2e^{-} \qquad E^{o} = 0.34\ V \qquad (2.15)$$

for which the standard free energy is 65,520 J/mole.

And the cathodic reaction is:

$$Cu^{2+} + 2e^{-} = Cu \qquad E^{o} = 0.34\ V \qquad (2.16)$$

for which the standard free energy is -65,520 J/mole.

Apparently, the free energy changes of the two half-cell reactions are equivalent in magnitude and opposite in signs, so the free energy change of the complete reaction is zero. The difference in two half-cell reaction potentials is zero and is overcome without consumption of energy. Nevertheless, applied voltage is required for electrochemical overvoltage, concentration overvoltage, and other overvoltage caused by other resistance. In copper electrorefining, the overvoltage for copper deposition and dissolution are much smaller in comparison with water hydrolysis.

Additionally, the impurity metal ions in the electrolytic solution would severely affect the purity of the desired metal at the cathode, if their concentrations are not controlled properly. In copper electrorefining, impurity metals that have standard reduction potentials similar to that of copper are more troublesome, such as arsenic, antimony, bismuth, with their half-cell reactions and standard potentials shown below.[3]

$$BiO^{+} + 2H^{+} + 3e^{-} = Bi + H_2O \qquad E^{o} = 0.32\ V \qquad (2.17)$$

$$HAsO_2 + 3H^{+} + 3e^{-} = As + 2H_2O \qquad E^{o} = 0.25\ V \qquad (2.18)$$

$$SbO^{+} + 2H^{+} + 3e^{-} = Sb + H_2O \qquad E^{o}= 0.21\ V \qquad (2.19)$$

The concentrations of the common species in copper electrorefining are generally within the following ranges:[2]

Cu = 40-50 g/l; H_2SO_4= 170-200 g/l; As < 10 g/l; Bi < 0.2 g/l; Sb < 0.5 g/l; Fe < 2 g/l; Ni < 20 g/l; Cl < 0.03 g/l.

In copper electrorefining, the concentrations of impurity elements and the applied voltage need to be controlled properly to improve the purity of the cathode, which is achieved by changing thermodynamic properties of impurity species and thus avoiding their co-deposition on the cathode.

2.1.3 Copper Electrorefining Kinetics

Not only is the rate of electrorefining determined by common chemical reaction kinetic parameters such as concentration and the order of the reaction, it also heavily depends on the applied voltage and the associated electrochemical reaction kinetic parameters. The current density, which is commonly in logarithmic scale, is often used to represent electrorefining reaction rate.

For a half-cell reaction shown below,

$$cM^{a+} + ne^{-} = dM^{b+} \qquad (2.20)$$

its current density can be determined by the Butler-Volmer equation:

$$i = k_b C_{Mb+}^{d} nF \exp\left(\frac{\alpha_a zFE}{RT}\right) - k_f C_{Ma+}^{c} nF \exp\left(\frac{-\alpha_c zFE}{RT}\right) \qquad (2.21)$$

where k_b is the backward reaction rate constant, k_f is the forward reaction rate constant, C is the specified surface concentration for $M^{b+}$and M^{a+}, d is the reaction order with respect to M^{b+}, c is the order the reaction with respect to M^{a+}, n is the number of

electrons transferred per mole of reaction, F is the Faraday constant, α_a is the anodic symmetry factor (typically 1.5 for copper half-cell reaction), α_c is the cathodic symmetry factor (typically 0.5), z is the number of electrons transferred in the rate limiting step (typically 1), and E is the electrochemical potential.[2]

By using the equilibrium exchange current density i_o, the Butler-Volmer equation becomes:

$$i = i_o[\exp\left(\frac{\alpha_a F\eta}{RT}\right) - \exp\left(\frac{-\alpha_c F\eta}{RT}\right)] \tag{2.22}$$

$$i_o = k_f C^c_{Ma+} nF \exp\left(\frac{-\alpha_c F E_{equi}}{RT}\right) = k_b C^d_{Mb+} nF \exp\left(\frac{\alpha_a F E_{equi}}{RT}\right) \tag{2.23}$$

where η is the electrochemical overpotential.

The Butler-Volmer equation describes the electrochemical kinetics for one half-cell reaction, which can be combined with other half-cell reactions to form a complete reaction. When coupled, each half-cell reaction still follows its own electrochemical kinetics, but the sum of anodic current flow must counterbalance the sum of cathodic current flow and the rate limiting half-cell reaction controls the combined reaction rate:

$$\sum I_{anodic} = -\sum I_{cathodic} \tag{2.24}$$

From the Butler-Volmer equation, it is apparent that the current density is determined by the applied potential: as the applied potential increases, the magnitude of current density becomes larger (shown in Figure 2.1).[2] Nevertheless, electrorefining involves both electrochemical reaction and mass transport and it is mixed controlled kinetically. As a result, equations valid only for extreme cases of electrochemical reaction control or mass transfer control cannot be utilized. Rather, combined equations considering

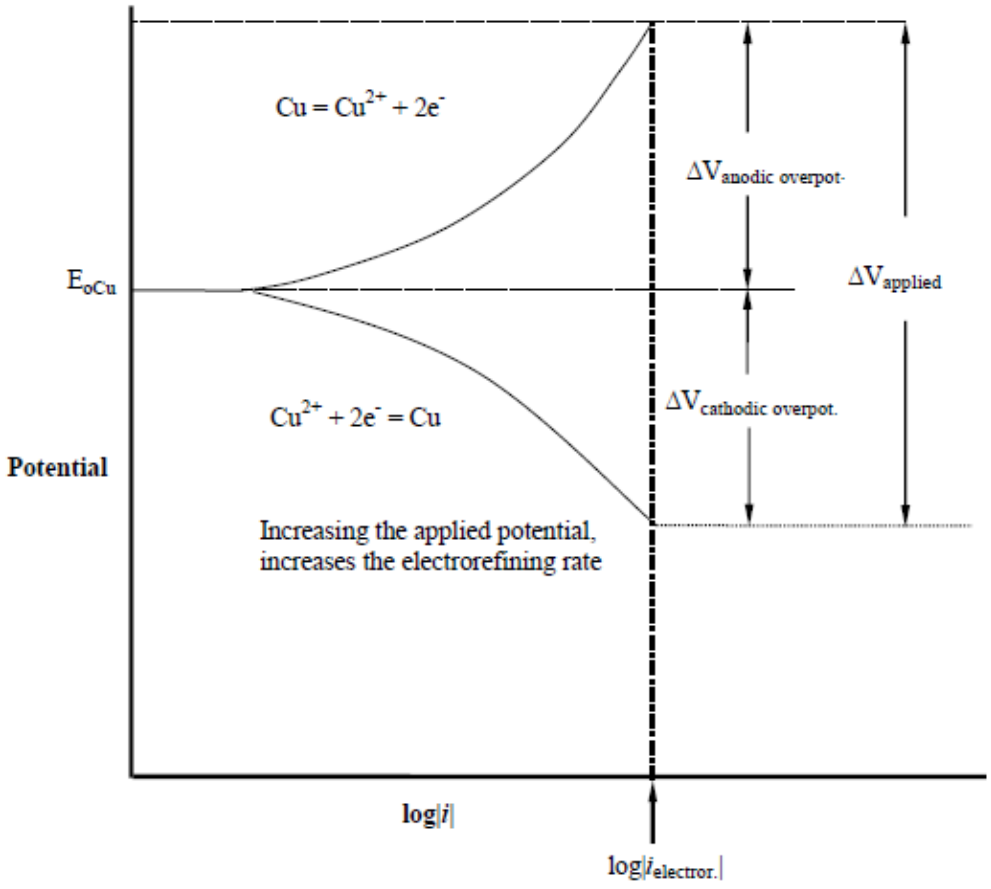

Figure 2.1 The relationship between applied potentials and the logarithm of the absolute value of the current density in copper electrorefining.[2]

both mass transport and electrochemical reaction should be used for mixed-control kinetics processes such as electrorefining and electrowinning.

As mentioned above, the concentration terms in the Butler-Volmer equation are not bulk concentrations, but surface concentrations. However, if the equilibrium exchange current density is used in the equation, it is assumed that the bulk concentration equals the surface concentration at the electrode surface and the bulk concentration is implicit in i_o.[2] In other words, i_o is a function of the bulk concentration rather than the surface concentration. Nevertheless, if the electrochemical process is limited by mass transfer, we cannot make the above assumption any more. In this case, the surface concentration of specified species is no longer equivalent to the bulk concentration and the surface concentration term needs to be substituted for the inherent bulk concentration term in the equilibrium exchange current density i_o, which should thus be multiplied by the term $\frac{C_{surface}}{C_{bulk}}$:

$$i = i_o[\frac{C_{surface,m^{b+}}}{C_{bulk,m^{b+}}}\exp\left(\frac{\alpha_a F\eta}{RT}\right) - \frac{C_{surface,m^{a+}}}{C_{bulk,m^{a+}}}\exp\left(\frac{-\alpha_c F\eta}{RT}\right)] \qquad (2.25)$$

where m^{a+} is the reactant of the cathodic reaction and m^{b+} is the reactant of the anodic reaction. $C_{surface}$ is surface concentration and C_{bulk} is bulk concentration. First order reaction is assumed.[4]

In mass transport limiting process, reactant concentration is typically low and fluid flow becomes significant. It is the mass transport process that moves reactant species from bulk solution to the electrochemical reaction interface. The migration term in the mass transport equation is generally small under most cases and is therefore neglected. The convection term is combined with diffusion in the equation of Fick's first law through the

diffusion layer thickness.[2] The molar rate of diffusion is converted to current density, with Fick's first law equation multiplied by the term *nF*:

$$i = \frac{nFD(c_{bulk} - c_{surface})}{\delta} \tag{2.26}$$

where *D* is the diffusion coefficient, δ is the diffusion boundary layer thickness.

The low surface concentration of reactants results in a limiting current density, which can be acquired through the extreme case of zero surface concentration:

$$i_{limiting} = \frac{nFDc_{bulk}}{\delta} \tag{2.27}$$

Further substitution of this equation into the expression for *i* results in:

$$i = i_{limiting}\left(1 - \frac{C_{surface}}{C_{bulk}}\right) \tag{2.28}$$

or,

$$\frac{C_{surface}}{C_{bulk}} = 1 - \frac{i}{i_{limiting}} \tag{2.29}$$

Substituting the expression for $\frac{C_{surface}}{C_{bulk}}$ into the Butler-Volmer equation modelling mixed-control kinetics leads to:[2]

$$i = \frac{i_o[\exp\left(\frac{\alpha_a F\eta}{RT}\right) - \exp\left(\frac{-\alpha_c F\eta}{RT}\right)]}{1 + i_0\left[\left(\frac{1}{i_{limiting,a}}\right)exp\left(\frac{\alpha_a F\eta}{RT}\right) - \left(\frac{1}{i_{limiting,c}}\right)exp\left(\frac{-\alpha_c F\eta}{RT}\right)\right]} \tag{2.30}$$

This form of Butler-Volmer equation considers both the electrochemical kinetics and the mass transport (migration is assumed negligible) and therefore can model combined kinetic control of electrochemical processes including the copper electrorefining process.

The difference between surface concentration and bulk concentration leads to concentration overpotential, which is the driving force to overcome mass transfer limitation

and can be derived as follows:

$$\eta_{concentration} = E_{surface} - E_{equi}$$

$$= \left(E^o - \frac{RT}{nF} ln \frac{C_{surface,m^{b+}}}{C_{surface,m^{a+}}}\right) - \left(E^o - \frac{RT}{nF} ln \frac{C_{bulk,m^{b+}}}{C_{bulk,m^{a+}}}\right)$$

$$= \frac{RT}{nF} ln \frac{C_{surface,m^{a+}} * C_{bulk,m^{b+}}}{C_{bulk,m^{a+}} * C_{surface,m^{b+}}} = \frac{RT}{nF} ln \frac{\frac{C_{surface,m^{a+}}}{C_{bulk,m^{a+}}}}{\frac{C_{surface,m^{b+}}}{C_{bulk,m^{b+}}}}$$

$$= \frac{RT}{nF} \ln \frac{1 - \frac{i}{i_{limiting,m^{a+}}}}{1 - \frac{i}{i_{limiting,m^{b+}}}}$$

$$= \frac{2.303RT}{nF} \log \frac{1 - \frac{i}{i_{limiting,m^{a+}}}}{1 - \frac{i}{i_{limiting,m^{b+}}}} \quad (2.31)$$

where $i_{limiting,m^{a+}}$ is the limiting current density of the cathodic reaction and $i_{limiting,m^{b+}}$ is the limiting current density of the anodic reaction.

The electrochemical overpotential, another form of overpotential, is required in order to have a reasonable anodic or cathodic reaction rate. The electrochemical overvoltage ($\eta_{electrochemcial}$) can be derived from the Butler-Volmer equation when the equation is controlled by one of the two exponential terms. When $\eta_{electrochemcial}$ has a positive value larger than 0.15 V,[5] the anodic exponential term dominates the equation, while the cathodic exponential term turns out to be negligible. As a result,

$$i = i_o \left[\exp\left(\frac{\alpha_a F \eta}{RT}\right)\right] \quad (2.32)$$

Solving for η results in:

$$\eta_a = \beta_a \log\left(\frac{i}{i_o}\right) \tag{2.33}$$

$$\beta_a = \frac{2.303RT}{\alpha_a F} \tag{2.34}$$

where η_a is the anodic electrochemical overpotential and β_a represents the slope of the corresponding line. This set of equations is known as Tafel equations which indicate that the electrochemical overpotential is directly proportional to the logarithm of the current density.

Similarly, when $\eta_{electrochemcial}$ has a negative value less than -0.15 V, the cathodic exponential term dominates the equation, resulting in:

$$\eta_c = \beta_c \log\left(\frac{|i|}{i_o}\right) \tag{2.35}$$

$$\beta_c = \frac{2.303RT}{-(1-\alpha_c)F} \tag{2.36}$$

where η_c is the cathodic electrochemical overpotential and β_c represents the slope of the corresponding line.

The concentration overpotential, together with the electrochemical overpotential and the overpotential due to other resistance, constitute the total overpotential given as:[5]

$$\eta_{total} = \eta_{electrochemcial} + \eta_{concentration} + \eta_{other\ resistance} \tag{2.37}$$

All overpotentials normally result in about 0.2 to 0.3 V applied potential in copper electrorefining. As a result, the energy consumed in electrorefining is much less and the current efficiency is higher (above 98%) than electrowinning. Additives like glue and thiourea are added to the electrolyte, for they enhance nucleation at the surface of cathode and therefore lead to lower overpotentials and increase the copper electrorefining rate.[2]

2.1.4 Copper Electrorefining Energy Consumption

According to Faraday's Law and assuming 100% current efficiency,

$$M = \frac{ItM_w}{nF} = \frac{iAtM_w}{nF} \tag{2.38}$$

where M is the mass of metal deposited, I is the current, i is the current density, A is the depositing area on the cathode, t is the time, M_w is the molecular weight of the specific metal, n is the number of electrons transferred per mole of reaction, and F is the Faraday constant.

Nevertheless, other accompanying reactions take a certain fraction of the total electrons, leading to less than 100% current efficiency, which means that copper deposition doesn't take all available electrons. As a result, the current efficiency should be included in the above equation:

$$M = \beta \frac{ItM_w}{nF} = \beta \frac{iAtM_w}{nF} \tag{2.39}$$

Consequently, the electrodeposition rate in terms of mass deposited, can be derived by dividing the above equation by time t:[2]

$$R_{electrodeposition} = \beta \frac{IM_w}{nF} = \beta \frac{iAM_w}{nF} \tag{2.40}$$

Thus, it is apparent that the electrodeposition rate is determined by current density. Nevertheless, the applied current density in electrorefining should not exceed half of the limiting current density. Otherwise, the metal deposits on the cathode would be rough due to the formation of nodules that can contact nearby anodes and cause short circuiting in copper electrorefining.

The energy consumed in copper electrorefining can be derived as:

$$W = Pt = EIt \tag{2.41}$$

where W is the energy consumed, P is the power, t is the time, E and I are the applied voltage and current.

The energy consumed per unit mass can be therefore derived by dividing the above equation by the mass of metal deposited:

$$\frac{W}{M} = \frac{EIt}{\frac{\beta I t M_w}{nF}} = \frac{EnF}{\beta M_w} \tag{2.42}$$

Under 0.2 to 0.35 V applied voltages and 98% current efficiency, about 172 to 301 kWhr of energy is consumed for every tonne of copper in most copper electrorefining tankhouses.[2]

2.2 Industrial Overview of Copper Electrorefining

Along with iron and aluminum alloy, copper is among the major metals in industry. One of the facts that demonstrates its significance is that about 15 million tonnes of copper are consumed every year worldwide as reported.[6] To produce copper with purity higher than 99.99%, copper electrorefining and copper electrowinning are the most commonly and widely used electrochemical processes.[7-9] In both electrolytic processes, copper ions dissolved in electrolytic solution are electrodeposited on cathodes. Nevertheless, copper electrorefining uses copper anodes with a purity of about 99% produced from copper smelters through pyrometallurgical processing. Then less pure copper in the anode is electrolytically dissolved as cupric ions, which are selectively electrodeposited on the cathode sheets that are generally made of stainless steel.[2] As a result, cathode copper deposit has higher purity than the original copper anode.[10] Usually, pyrometallurgically produced copper anode with purity of 98-99% can be further electrorefined to copper cathode with >99.99% purity, which is referred to as grade A copper.[11] On the other hand,

copper electrowinning recovers cupric ions in the loaded aqueous solution produced from hydrometallurgical processes including leaching and solvent extraction. The recovered copper is in the form of cathode deposit, with the lead alloy sheet commonly used as the anode. Overall, most of the high purity copper in the world is produced from copper electrorefining rather than electrowinning.[12] In 2004, approximately 11 million tonnes of copper were produced worldwide from copper sulfate electrolyte through electrorefining.[6]

Copper electrorefining is operated in large tankhouses in industry, which can contain, for example, an average of 40,000 cathodes in 4 groups of 200 cells connected in series that are powered by 12 pulse transformer-rectifiers rated.[10] The applied potential is typically between 0.2 and 0.4 V, the common cathode current density is 240 A/m^2, and the average energy consumption is approximately 315 kWh/Ton.[13]

There are typically two cycles in copper electrorefining: the strip cycle and the scrap cycle. In the strip cycle, new anodes and cathode blanks are used; in the scrap cycle, only the cathode blanks with deposited copper are harvested and replaced by new blanks and the remaining anodes are kept in cells for further dissolution. The cathode strip cycle can be 9 to 13 days and the scrap cycle length is normally the same as the strip cycle. As we know, continuous observation of the process of copper electrorefining is necessary to operate refinery tankhouse with high efficiency. Recently, Outotec has developed a Cell Sense System, which can provide powerful online cell operation monitoring to enhance operational efficiency and Kennecott Utah Copper Corporation owns the largest Cell Sense System to continuously monitor 1412 cells in their tankhouse online.[14]

It was indicated that the bottom section of copper cathodes is more contaminated, the scrap cycle copper has higher impurity concentrations than the strip cycle copper, and

the arsenic, lead, and antimony concentrations in the copper cathode correlate with the amount of slimes.[15]

2.3 Floating Slimes in Copper Electrorefining

Silver, lead, arsenic, bismuth, antimony, selenium, and nickel are common impurities existing in copper anodes. Some impurities dissolved from the anodes can precipitate, if their concentrations in the electrolytic solution are above saturation levels. Some of these precipitates can settle down but some are floating slimes and can be a source of cathode contamination by their incorporation into the cathode.[16]

These floating slimes are amorphous and typically have compositions of Sb-As-O and Bi-As-O, precipitated in the electrolyte, rather than on the surface of anodes.[17] Like the small anode slime particles that are liberated from the anode slimes layer, these floating slimes are generally small and, therefore, are suspended in the solution. They can be transported to the cathode by the fluid flow in an electrorefining cell and get entrapped on the cathode. Some studies on its formation and deposition mechanism and associated prevention have been carried out. Antimony is widely considered as a major source of floating slimes. F. Noguchi, H. Itoh and T. Nakamura studied the dissolution mechanism of antimony from the anode and its effect on floating slimes. They intentionally added antimony oxides such as Sb_2O_3 and Sb_2O_5 to the solution and found that these quasi-floating slimes could cause the contamination of the cathodic copper.[18] Lead, arsenic, bismuth, and antimony are the most hazardous impurities, in terms of their impact on the cathode copper purity.[19] It was proposed by J. Brent Hiskey that reducing the tendency for antimony oxidation could prevent the formation of floating slimes and help maintain cathode copper purity.[16]

2.4 Control of Impurity Dissolution and Purification of Electrorefining Electrolyte

Electrochemically active impurities contained in solid solution in the copper matrix are typically dissolved in electrolyte as copper dissolves. These solubilized impurities, however, may also jeopardize the quality of cathodes.[2] Group 15 elements (As, Sb, Bi, etc.) are impurities that are potentially detrimental in many metallurgical processes and to the environment.[16] Therefore, the plating characteristics of Group 15 elements are significant in copper electrorefining. The most troublesome elements are arsenic, antimony, and bismuth, as their reduction potentials are very close to that of copper. Thus, they can be co-deposited on the cathode when copper is reduced at the cathode, thereby causing cathode contamination.

Some impurities such as bismuth and antimony are partially dissolved into the electrolytic solution as copper dissolves, while some impurities like arsenic are mostly dissolved.[20] If no electrolyte is bled from the copper electrorefining circuit, the concentrations of various impurities in the circuit would increase due to accumulation.[3] When the concentrations of these impurities accumulated in the electrolyte exceed certain levels, they will co-deposit with copper and cause various problems such as the deterioration of cathode quality. Besides, as mentioned in section 2.3, some dissolved impurities can form floating slimes, which also lead to cathode contamination. Therefore, the concentrations of dissolved impurities in electrorefining electrolyte, especially As, Sb, and Bi, must be controlled.

Japanese Scientists proposed the method of using dissolved oxygen to control impurities in copper electrolyte. They found that the dissolution of antimony can be

controlled by the dissolved oxygen but it has only a small effect on bismuth and no effect on arsenic.[21] This discovery threw light on how to control dissolution of minor elements from the anode. Before, it was widely considered that antimony is oxidized in the layer of slimes formed on the surface of the anode and its dissolution is influenced by lead and arsenic in the anode. Now it is possible to take advantage of the dissolved oxygen to suppress the dissolution of minor elements in the anode.

Some studies place focus on the effect of the lead content of copper anodes on the dissolution of other impurities in anodes during copper electrorefining. For anodes with low lead, the lead in the Cu-Pb-As-Sb-Bi phases along copper grain boundaries becomes $PbSO_4$, and the remaining As, Bi, and Sb are dissolved into electrolyte with some of them reprecipitated afterwards; for anodes with high lead, the Cu-Pb-As-Sb-Bi phases in grain boundaries are harder to dissolve but rapidly transform to other phases including a low solubility Pb-Sb-As-Bi-S phase and $PbSO_4$ phase, without the reprecipitation of dissolved As, Bi, and Sb.[22]

A variety of processes have also been proposed for the purification of electrorefining electrolyte. Nowadays, the conventional method of electrowinning to remove As, Bi, and Sb impurities from electrolyte is still widely adopted.[23] Another traditional process is called as multistage electrolytic deposition.[24] Nevertheless, the conventional methods are all passive to remove these impurities from copper electrolytic solution and it remains difficult to extensively adopt these techniques in copper refineries. A variety of technologies for the purification of copper electrolytic solution were recently proposed.[25-32] Molecular recognition technology was reportedly used for removing bismuth in copper electrolyte,[33] which is a very hazardous impurity and often leads to failures in

copper rod and wire production. Molecular recognition technology is an absorption method with high efficiency, high loading capacity, and high bismuth selectivity, and it can be used to produce commercial grade bismuth bisulfate by utilizing the recovered bismuth from the molecular recognition technology ion exchange resin.[33]

2.5 Removal of Impurities from Electrolyte by Precipitation

A new technology, self-purification of electrorefining electrolyte, has been proposed.[34, 35] Some of the impurities dissolved from the copper anode including As, Sb and Bi can co-precipitate to the anode slimes from the copper electrolyte in electrorefining as reported.[36] The homogeneous co-precipitation of arsenic, antimony and bismuth in the copper electrolytic solution is the basic principal behind the technology of self-purification to reduce the impurity level in the electrolyte. More specifically, bismuth and antimony can precipitate onto the anode slimes with arsenic spontaneously if the concentration of arsenic in electrolyte is at an appropriate level.[36] The rate of homogeneous precipitation of impurities in the electrolyte varies depending on process conditions.[37]

This has been studied by many researchers. Firstly, Hoffmann reported in 2004 that when the concentration of pentavalent arsenic was controlled in the range of 15-20 g/L, the levels of antimony and bismuth could be reduced to less than 100 ppm in the copper solution.[38] Secondly, X.W. Wang, et al. have contributed a great deal to this field. They made a conclusion in 2006 that pentavalent arsenic and pentavalent antimony can react and lead to different types of arsenato-antimonic acids that have the tendency to continue to react with trivalent bismuth, antimony, and arsenic, forming insoluble arsenato-antimonates that are stable even in strong acidic solutions.[39] Further in 2011, they proposed that when the mole ratio of As/Sb/Bi in copper anode was appropriately controlled and the

concentration of arsenic in solution is higher than 7 g/L, the impurities of arsenic, bismuth, and antimony dissolved in the electrolytic solution can be mostly precipitated as arsenato-antimonates onto the anode slimes,[36] avoiding floating slime formation in copper electrolyte. Wang, et al. also indicated that the oxidation of trivalent antimony and the arsenato-antimonate formation are the two control-steps in the reaction of homogeneous precipitation.[36] Thirdly, arsenic and antimony play significant roles in the self-purification of copper electrolytic solution. Antimony is indispensable for homogeneous precipitation, because it is a reactant of the arsenato-antimonate formation. Arsenic is even more significant, for the pentavalent arsenic is necessary for arsenato-antimonate formation as well as trivalent antimony oxidation and the trivalent arsenic can accelerate the formation rate of arsenato-antimonates and impede the formation of floating slimes.[40] Additionally, Y. Peng, et al. found in their experiments that impurities (arsenic, bismuth, and antimony) homogeneous precipitation in copper solution depends on the concentration of trivalent arsenic and is closely related with the oxidation of trivalent arsenic that can be fit to a pseudo-first order kinetic model.[41] Fourthly, F. Xiao, et al. also made significant contributions to this field. It was concluded in their articles that trivalent arsenic could react with trivalent and pentavalent antimony to form antimony arsantimonate, leading to decreased concentrations of antimony and arsenic in the solution.[42] They found that when copper arsenite is added into electrolyte, impurities bismuth and antimony mostly precipitate with arsenic and are removed from the electrolytic solution.[35, 37]

It is apparent that the pentavalent antimony ion is indispensable for the formation of either arsenato-antimonates or antimony arsantimonate. Nevertheless, similar to arsenic, most antimony in the copper solution is trivalent rather than pentavalent after dissolution

from anodes during copper electrorefining.[43] F. Xiao, et al. designed experiments to study the function of trivalent antimony ions in precipitating the impurities of arsenic, bismuth, and antimony, as well as the corresponding precipitation mechanism. They found that the trivalent antimony ion can remove arsenic, bismuth, and antimony from the electrolytic solution by forming a precipitate mixture including microcrystalline $(Sb, As)_2O_3$ and $SbAsO_4$, and amorphous phases.[44]

There are some other methods for removing impurities in copper electrolyte by precipitation. G. Cifuentes, et al. found that bismuth and antimony can precipitate out from copper solution with the addition of PbO_2 and this newly developed process is a practicable alternative for antimony and bismuth control in electrorefining solution.[19] This process requires simple operation even for industrial scale and is more economical than other processes, leading to high efficiency of impurities removal.[19] In addition, precipitation of electrolyte impurities can happen naturally in circulation systems of refinery tankhouses, which however obstructs fluid flow of copper electrolyte. At the Kennecott Copper Refinery, electrolyte impurities precipitate and form hard layers inside the pipes and the main elements in the pipe hard scale are arsenic, bismuth, and antimony with the main phase to be antimony arsenate.[45]

2.6 Electrolyte Additives in Copper Electrorefining

Electrolyte additives such as thiourea, glue, gelatin, and chloride are extensively used in copper refineries to produce copper cathode with better surfaces. Thiourea increases the copper nucleation rate on cathode surface and thus lowers the applied potential and enables higher current density use. Thiourea can have polarizing or depolarizing influences on copper electrorefining based on its concentration (less or more

than 0.1 mmol/L, respectively) and nodules will be formed when the thiourea concentration is in the polarizing range.[46] Thiourea can also reduce the copper grain size.[46] For glue, it was indicated that dendrites growing out from the copper surface would have more glue in the electrolyte attached to them, which can impede further growth of the dendrites and thus lead to smooth and dense copper deposit.[47] Glue can also improve the copper nucleation rate on the cathode surface and thereby enhance smoothness.[48, 49] Gelatin has effects on the type of copper grain produced, the copper crystal structure, the surface morphology, and the polarization curve.[50] It was reported that the TU-G-Cl^- system can better reduce dendrites, nodules, and porosities than the TU-Cl^- and G-Cl^- systems.[50, 51] The TU-G-Cl^- system can largely enhance edge and surface quality and reduce anomalous copper growth structures, with the best quality copper harvested at the G/TU ratio of 0.8 to 1.7.[50]

Electrorefining additives have effects on anode passivation behavior. Chloride can extend the time to passivation.[52] For glue and thiourea, the best concentration is approximately 1 ppm, at which an increase in the passivation time can be observed, but if the concentration of thiourea or glue is further increased beyond this optimal value, the passivation time will decrease.[52]

2.7 The Mineralogy and Microstructures of Copper Anodes

In this field, T. T. Chen and J. E. Dutrizac performed a large amount of research and made essential contributions to it. They found a variety of information about the phases existing in anodes.[53-60] First of all, Kupferglimmer ($Cu_3Ni_{2-x}SbO_{6-x}$ where x= 0.1–0.2), an important structure in the anode, formed when the concentration of antimony or tin, which are important for the formation of Kupferglimmer structure, was higher than 200 ppm and the concentration of nickel was larger than 0.30%. Secondly, cuprous oxide, some

of which existed with Cu_2(Se, Te) and formed selenide spheroids or tubular phases, was found to be the most abundant secondary phase. Cu_2(Se, Te) seemed to be the only Se bearing inclusion, and Ag_2Se and AgCuSe were not found even in high silver bearing anodes. Cu_2(Se, Te) inclusions were discovered to be constantly associated with cuprous oxide and other compound constituents that were frequently found to be with Cu_2O-Cu_2(Se, Te) and Kupferglimmer structures at copper grain boundaries. This kind of complex inclusion at grain boundaries was often detected and it seemed to originate during solidification. Thirdly, around 90% of silver in the anode existed in the form of solid solution and the rest was found in oxides and selenides. Similarly, solid solution was also the most common form for arsenic up to 60% and the remainder existed in oxides that were connected with complicated lead compound structures. Nickel could exist in solid solution up to 3000 ppm and nickel oxide or Kupferglimmer structure would be found if Ni exceeded 3000 ppm. The air side of the anode generally contained more NiO because oxygen concentration was higher close to the atmosphere exposure. Fourthly, although some lead existed in solid solutions, most of it was contained in Group VB elements-enriched compounds. Lastly, silicates were found in different compositions. Between 3-8% of tellurium was found in copper tellurides. However, if its concentration was low, it existed in solid solution within the selenide phases.

Furthermore, Dutrizac's and Chen's work was continued and expanded by other scientists. Firstly, O. Forsen and K. Lilius determined a more accurate nickel concentration above which nickel oxide and Kupferglimmer structure form. T. T. Chen and J. E. Dutrizac found this value to be 3000 ppm as indicated above, while O. Forsen and K. Lilius disagreed with it and reported the value should be 2500 ppm. They found the

Kupferglimmer abundance and nickel oxide morphology to be correlated with cooling rate and they developed an equation based on nickel and oxygen concentrations within copper matrix to compute the abundance of Kupferglimmer.[61] M. Mitan found that there were more Kupferglimmer structures in anodes with larger grain sizes. Also, he indicated that time to passivation for an anode was correlated to the maximum average grain size of it.[62] Since anode passivation is associated with slime layer formation, there may be a correlation between anode slime adhesion and the maximum average grain size of the anode.

2.8 The Phases and Structures of Anode Slimes

When the anode is exposed to the electrolytic solution during the process of copper electrorefining, fewer noble impurity elements in solid solution in the copper matrix are dissolved into the electrolyte, but most inclusion phases at the copper grain boundaries are insoluble and become exposed to the solution, forming an anode slimes layer between the anode and the electrolyte.

T. T. Chen and J. E. Dutrizac investigated the phases existing in the anode slimes. Some of the significant findings are summarized below.[53, 56-58, 63] Firstly, cuprous oxide, which is the most abundant inclusion phase in almost all anodes, becomes comparatively rare in anode slimes, because the acid in the electrolyte along with dissolved oxygen can react with and dissolve Cu_2O as cupric ions and water. However, if the slimes layer is dense and thick with smaller pore sizes, Cu_2O can be present in the layer. Secondly, NiO, Ni-Fe oxides and Kupferglimmer are insoluble when exposed to the electrolyte. Thirdly, the selenide inclusions maintain their morphologies. Fourthly, lead in solid solution or oxides could react with sulfuric acid and form lead sulfate, which is insoluble. Fifthly, although in the original anode only a small portion of silver is present in solid solution in Cu_2(Se, Te)

inclusions and does not exist in the form of Ag_2Se/AgCuSe and Selenium is present only in Cu_2(Se, Te) at grain boundaries, silver ions will react with Cu_2(Se, Te) to form Ag_2Se, according to J. D. Scott, T. T. Chen and J. E. Dutrizac.[64, 65] These selenide species can co-exist in the anode slimes layer and each individual selenide particle typically contains at least two kinds of selenide species. Xuan Cheng and J. Brent Hiskey found that silver's reaction with Cu_2(Se, Te) would cause the volume of the selenide phases to increase 20%.[66] To summarize, the major phases and structures existing in anode slimes layers include Kupferglimmer, euhedral NiO crystals, Ni-Fe oxides, lead sulfate, $(Cu,Ag)_2Se$ structures, and silicates.

2.9 The Adhesion of Anode Slimes

Since the mineralogy and microstructure of the anode slimes layer have been discussed, the adhesion of slimes, a key issue in maintaining cathodic quality in the process, should also be discussed. Many researchers contributed greatly to this area by studying anode passivation, and the factors affecting the amount of slimes and the adhesiveness of slimes, although their objective was to reduce passivation and anode slime formation in copper electrorefining. According to the information in the literature,[67-71] increasing the sulfuric acid or copper concentration, or decreasing the temperature, can intensify anode passivation. The impurities in the anode such as lead, bismuth, arsenic, antimony, nickel, and silver also place significant effects on the anode passivation behavior.[62, 72-75]

F. Noguchi, N. Iida, and T. Nakamura found that internal factors such as the type, form, and concentration of impurities had great effects on the amount of slimes.[76] In contrast, external factors such as concentration of impurities and dissolved oxygen in solution, and the electrolytic conditions such as current density also affected the amount of

slimes. They claimed that the amount of slimes increased with increasing content of impurities existing in inclusions such as sulfur, but it decreased a little as impurities in solid solution such as Sb, Ni or Sn increased. Also, they discovered that higher oxygen content in anodes increases the amount of slimes due to impurity oxides forming in the anodes during copper electrorefining. For external factors, they concluded that in general the amount of slimes increased as the current density, dissolved oxygen, concentration of impurities, and H_2SO_4 in electrolyte increased. Secondly, they reached the conclusion that the slime adherence was affected by several factors. Higher current density and impurity content in anodes increased the amount of adhered slimes. The slime adhesion was reduced with a large total electric charge, a smoother slime surface, and large inclusion particle size.

There have been other investigations into the effect of specific impurities on the adhesiveness of anode slimes. J. P. Demaerel studied the behavior of arsenic in copper electrorefining, since arsenic in both the anode and the electrolyte can directly exert an effect on cathode purity, together with other impurity elements such as lead, bismuth, and antimony. He found that arsenic has a depassivating effect on the anode, and it influences the anode slime adhesion.[77] Danuta Hanus did research on the effect of the composition and passivation on anode slimes. Several findings from his research are summarized as follows: arsenic, lead, selenium and nickel existing in the anode improved anode adhesion, but antimony, silver and tin had no consistent results; almost all lead, tin and selenium from the anode could be transferred into the slime; bismuth and antimony could only be partially transferred because of the formation of moving slimes; arsenic, nickel and cobalt tended to be dissolved and remained in the solution.[78]

2.10 Anode Slime Processing

Small anode slimes are usually filtered from the electrolyte and large anode slimes are collected from the cell bottom. Then they are processed to recover the desirable metals, as appreciable amounts of platinum, gold, and silver exist in anode slimes. In the meantime, the undesirable and environmentally harmful elements need to be treated. Common anode slime processes include pyrometallurgical process, pyro-pretreatment and hydrometallurgical process, pyro-hydro-pretreatment and pyrometallurgical process, hydro-pyrometallurgical process, hydro-pyro-hydrometallurgical process, and hydrometallurgical process.[79] Hydrometallurgical processes such as Saganoseki process and INER are more economical, but the selection of a particular process should be determined by the chemical and mineralogical features of specific anode slimes.[79]

Due to the vital role of anode slimes played in the process of copper electrorefining, many investigations have been conducted on their characteristics. As for the mineralogical characteristics of anode slimes, it was reported in the literature that the important phases exist in untreated anode slimes include Cu_2O, Cu_2Se, CuSe, $CuSO_4 \cdot 5H_2O$, Ag_2Se, AgCuSe, Ag_2Te, NiO, $SbAsO_4$, Cu–Ni–Sb, $BaSO_4$, $PbSO_4$, $(Cu_{0.2}Ni_{0.8})O$, etc.[79, 80] If anode slimes are leached by sulfuric acid, their residues do not contain phases such as $(Cu_{0.2}Ni_{0.8})O$ and have a large scale of porous structures, where the leaching reaction is very likely to be ash (product layer)-diffusion-controlled.[80]

2.11 References

1. J. Newman and K. E. Thomas-Alyea: *Electrochemical Systems*, third ed., John Wiley & Sons, Inc., Hoboken, NJ, 2004.

2. M. L. Free: *Hydrometallurgy: Fundamentals and Applications,* John Wiley & Sons, Inc., Hoboken, NJ, 2013.

3. W. G. Davenport, M. King, M. Schlesinger, and A. K. Biswas: *Extractive Metallurgy of Copper*, fourth ed., Pergamon Press, Elmsford, NY, 2002, pp. 276-350.

4. J. O. M. Bockris and A. K. N. Reddy: *Modern Electrochemistry*, Plenum Press, New York City, NY, 1970, pp. 1143.

5. D. A. Jones: *Principles and Prevention of Corrosion*, second ed., Prentice Hall, Inc., Upper Saddle River, NJ, 1996.

6. M. Stelter and H. Bombach: *Adv. Eng. Mater.*, 2004, vol. 6, pp. 558-62.

7. M. L. Free: *JOM*, 2007, vol. 59, pp. 28-33.

8. M. Moats and M. Free: *JOM*, 2007, vol. 59, pp. 34-36.

9. P. M. Tyroler, T. S. Sanmiya, D. W. Krueger, and S. Stupavsky: *The Electrorefining and Winning of Copper: Proceedings of the Symposium in TMS 116th Annual Meeting*, Denver, CO, 1987, pp. 421-35.

10. A. S. Morales, E. P. Wiechmann, P. Aqueveque, and E. Pino: *2010 IEEE Industry Applications Society Annual Meeting*, Houston, TX, 2010, pp. 1-5.

11. A. Watt: *Electro-Deposition A Practical Treatise*, Read Books, Worcestershire, UK, 2008.

12. P. E. Aqueveque, E. P. Wiechmann, and A. S. Morales: *IEEE Trans. Ind. Appl.*, 2010, vol. 46, pp. 1764-68.

13. T. Robinson, J. Quinn, W. Davenport, and G. Karcas*: Proceedings of the Copper 2003-Cobre 2003*, Santiago, Chile, 2003, vol. 5, pp. 3-66.

14. A. Rantala and D. Kim: *T.T. Chen Honorary Symposium on Hydrometallurgy, Electrometallurgy and Materials Characterization*, John Wiley & Sons, Inc., Hoboken, NJ, 2012, pp. 77-90.

15. M. Free, U. Marshall, J. McAllister, D. Kim, and S. Wang: *T.T. Chen Honorary Symposium on Hydrometallurgy, Electrometallurgy and Materials Characterization*, John Wiley & Sons, Inc., Hoboken, NJ, 2012, pp. 157-66.

16. J. B. Hiskey: *T.T. Chen Honorary Symposium on Hydrometallurgy, Electrometallurgy and Materials Characterization*, John Wiley & Sons, Inc., Hoboken, NJ, 2012, pp. 101-12.

17. T. B. Braun, J. R. Rawling, and K. J. Richards: *Extractive Metallurgy of Copper: An International Symposium on Copper Extraction & Refining*, Las Vegas, NV, 1976, pp. 511-24.

18. F. Noguchi, H. Itoh, and T. Nakamura: *Proceedings of the Copper 95-Cobre 95*, Santiago, Chile, 1995, vol. 3, pp. 337-48.

19. G. Cifuentes, J. Simpson, and C. Vargas: *T.T. Chen Honorary Symposium on Hydrometallurgy, Electrometallurgy and Materials Characterization*, John Wiley & Sons, Inc., Hoboken, NJ, 2012, pp. 125-30.

20. S. J. Wang: *JOM*, 2004, vol. 56, pp. 34-37.

21. K. Ando, N. Tsuchida, and M. Imamura: *J. MMIJ*, 2001, vol. 117, pp. 979-84.

22. T. T. Chen and J. E. Dutrizac: *Can. Metall. Q.*, 2003, vol. 42, pp. 421-32.

23. F. Xiao, J. Mao, D. Cao, X. Shen, and F. Ren: *Miner. Eng.*, 2012, vol. 35, pp. 9-15.

24. D. C. Cupertino, P. A. Tasker, M. G. King, and J. S. Jackson: *Hydrometallurgy'94*, Cambridge, England, 1994, pp. 591-600.

25. M. Tomita, H. Hiai, and T. Ishii: *Adding sodium hydrogen sulfide to precipitate metals including copper, arsenic, antimony, and bismuth as sulfides*, U.S. Patent No. 5,783,057, U.S. Patent and Trademark Office, Washington, D.C., 1998.

26. P. Navarro and F. J. Alguacil: *Can. Metall. Q.*, 1996, vol. 35, pp. 133-41.

27. P. Navarro, J. Simpson, and F. J. Alguacil: *Hydrometallurgy*, 1999, vol. 53, pp. 121-31.

28. P. Navarro and F. J. Alguacil: *Hydrometallurgy*, 2002, vol. 66, pp. 101-05.

29. S. R. Izatt, N. E. Izatt, J. B. Dale, and R. L. Bruening: *Proceedings of Copper 2010 Conference*, Hamburg, Germany, 2010.

30. P. A. Riveros: *Hydrometallurgy*, 2010, vol. 105, pp. 110-14.

31. L. Cifuentes, G. Crisóstomo, J. P. Ibáñez, J. M. Casas, F. Alvarez, G. Cifuentes: *J. Membr. Sci.*, 2002, vol. 207, pp. 1-16.

32. X. W. Wang, Q. Y. Chen, Z. L. Yin, P. M. Zhang, Z. P. Long, and Z. F. Su: *Hydrometallurgy*, 2003, vol. 69, pp. 39-44.

33. L. Navarro, W. Read, and T. Morris: *T.T. Chen Honorary Symposium on Hydrometallurgy, Electrometallurgy and Materials Characterization*, John Wiley & Sons, Inc., Hoboken, NJ, 2012, pp. 141-50.

34. X. W. Wang: Doctorate Thesis, Central South University, 2003.

35. F. X. Xiao, Y. J. Zheng, Y. Wang, W. Xu, C. H. Li, and H. S. Jian: *Trans. Nonferrous Met. Soc. China*, 2007, vol. 17, pp. 1069-74.

36. X. W. Wang, Q. Y. Chen, Z. L. Yin, M. Y. Wang, B. R. Xiao, and F. Zhang: *Hydrometallurgy*, 2011, vol. 105, pp. 355-58.

37. F. Xiao, J. Mao, D. Cao, X. Shen, and A. A. Volinsky: *Hydrometallurgy*, 2012, vol. 125-126, pp. 76-80.

38. J. E. Hoffmann: *JOM*, 2004, vol. 56, pp. 30-33.

39. X. W. Wang, Q. Y. Chen, Z. L. Yin, and L. S. Xiao: *Hydrometallurgy*, 2006, vol. 84, pp. 211-17.

40. X. W. Wang, Q. Y. Chen, Z. L. Yin, M. Y. Wang, and F. Tang: *Hydrometallurgy*, 2011, vol. 108, pp. 199-204.

41. Y. L. Peng, Y. J. Zheng, and W. M. Chen: *Hydrometallurgy*, 2012, vol. 129-130, pp. 156-60.

42. F. X. Xiao, Y. J. Zheng, Y. Wang, H. S. Jian, X. G. Huang, and Y. T. Ma: *Trans. Nonferrous Met. Soc. China*, 2008, vol. 18, pp. 1275-79.

43. Y. Wen, Y. Z. Sheng, and S. Zhang: *The Symposium of Production, Technology, Equipment, Materials and Market of National Copper Nickel and Cobalt*, Beijing, China, 2003, pp. 93.

44. F. X. Xiao, D. Cao, J. W. Mao, X. N. Shen, and F. Z. Ren: *Int. J. Miner., Metall. Mater.*, 2013, vol. 20, pp. 9-16.

45. J. McAllister, D. Kim, and S. Wang: *T.T. Chen Honorary Symposium on Hydrometallurgy, Electrometallurgy and Materials Characterization*, John Wiley & Sons, Inc., Hoboken, NJ, 2012, pp. 131-40.

46. H. Kuboyama, H. Nakano, S. Oue, H. Fukushima, and S. Kobayashi: *J. Min. Metall. Inst. Jpn.*, 2009, vol. 125, pp. 62-67.

47. A. K. Biswas and W. G. Davenport: *Extractive Metallurgy of Copper*, second ed., Pergamon Press, Elmsford, NY, 1980, pp. 312-13.

48. K. Knuutila, O. Forsen, and A. Pehkonen: *The Electrorefining and Winning of Copper: Proceedings of the Symposium in TMS 116th Annual Meeting*, Denver, CO, 1987, pp. 129-43.

49. M. L. Free, R. Bhide, A. Rodchanarowan, and N. Phadke: *ECS Trans.*, 2006, vol. 2, pp. 335-43.

50. B. Veilleux, A. M. Lafront, and E. Ghali: *Can. Metall. Q.*, 2002, vol. 41, pp. 47-62.

51. B. Veilleux, A. M. Lafront, and E. Ghali: *Can. Metall. Q.*, 2001, vol. 40, pp. 343-54.

52. M. Moats and J. B. Hiskey: *Can. Metall. Q.*, 2000, vol. 39, pp. 297-306.

53. T. T. Chen and J. E. Dutrizac: *JOM*, 1990, vol. 42, pp. 39-44.

54. T. T. Chen and J. E. Dutrizac: *Can. Metall. Q.*, 1990, vol. 29, pp. 27-37.

55. T. T. Chen and J. E. Dutrizac: *Can. Metall. Q.*, 1988, vol. 27, pp. 91-96.

56. T. T. Chen and J. E. Dutrizac: *Metall. Mater. Trans. B*, 2005, vol. 36, pp. 229-40.

57. T. T. Chen and J. E. Dutrizac: *Can. Metall. Q.*, 1991, vol. 30, pp. 95-106.

58. T. T. Chen and J. E. Dutrizac: *Can. Metall. Q.*, 1989, vol. 28, pp. 127-34.

59. T. T. Chen and J. E. Dutrizac: *Can. Metall. Q.*, 1996, vol. 35, pp. 337-51.

60. T. T. Chen and J. E. Dutrizac: *Can. Metall. Q.*, 1991, vol. 30, pp. 173-85.

61. O. Forsen and K. Lilius: *The Electrorefining and Winning of Copper: Proceedings of the Symposium in TMS 116th Annual Meeting*, Denver, CO, 1987, pp. 47-69.

62. M. Mitan: *Microstructure and Morphology of Impure Copper Anodes*, University of AZ, 1997.

63. T. T. Chen and J. E. Dutrizac: *Can. Metall. Q.*, 1988, vol. 27, pp. 97-105.

64. J. D. Scott: *Metall. Trans. B*, 1990, vol. 21, pp. 629-35.

65. T. T. Chen and J. E. Dutrizac: *Metall. Trans. B*, 1989, vol. 20, pp. 345-61.

66. X. Cheng and J. B. Hiskey: *Metall. Mater. Trans. B*, 1996, vol. 27, pp. 610-16.

67. S. Abe, B. W. Burrows, and V. A. Ettel: *Can. Metall. Q.*, 1980, vol. 19, pp. 289-96.

68. X. Ling, Z. H. Gu, and T. Z. Fahidy: *J. Appl. Electrochem.*, 1994, vol. 24, pp. 1109-15.

69. J. Sedzimir and W. Gumowska: *Hydrometallurgy*, 1990, vol. 24, pp. 203-17.

70. G. N. Srinivasan, P. Adaikkalam, P. Radhakrishnamurty, R. Srinivasan, P. Ramachandran, and K. Naganathan: *J. Electrochem. Soc. India*, 1982, vol. 31, pp. 60-63.

71. Z. H. Gu, J. Chen, and T. Z. Fahidy: *Hydrometallurgy*, 1995, vol. 37, pp. 149-67.

72. J. A. Sawicki, J. E. Dutrizac, J. Friedl, F. E. Wagner, and T. T. Chen: *Metall. Trans. B*, 1993, vol. 24B, pp. 457-62.

73. T. T. Chen and J. E. Dutrizac: *Can. Metall. Q.*, 1993, vol. 32, pp. 267-79.

74. T. T. Chen and J. E. Dutrizac: *Can. Metall. Q.*, 1990, vol. 29, pp. 293-305.

75. J. B. Hiskey, X. Cheng, M. S. Moats, and S. C. Campin: *4th International Symposium on Electrochemistry in Mineral and Metal Processing*, Los Angeles, CA, 1996, pp. 439-56.

76. F. Noguchi, N. Iida, T. Nakamura, and Y. Ueda: *Proceedings of the Copper 1991-Cobre 91*, Ottawa, Canada, 1991, vol. 3, pp. 391-404.

77. J. P. Demaerel: *The Electrorefining and Winning of Copper: Proceedings of the Symposium in TMS 116th Annual Meeting*, Denver, CO, 1987, pp. 195-209.

78. D. Hanus: *Pr. Inst. Met. Niezelaz.*, 1987, vol.16, pp. 35-39.

79. J. Hait, R. K. Jana, and S. K. Sanyal: *Miner. Process. Extr. Metall.*, 2009, vol. 118, pp. 240-52.

80. J. Hait, R. K. Jana, and S. K. Sanyal: *Ind. Eng. Chem. Res.*, 2004, vol. 43, pp. 2079-87.

CHAPTER 3

EXPERIMENTAL STUDIES OF IMPURITY PARTICLE BEHAVIOR IN ELECTROLYTE AND ITS DISTRIBUTION ON THE CATHODE

A 3-factor 2-level designed set of experiments was performed to determine the effects of inlet flow rate, temperature, and current density on impurity particle behavior in electrolyte and the associated distribution on the cathode in copper electrorefining. Laser-Induced Breakdown Spectroscopy (LIBS) was used to measure the concentration of impurities on the cathode. The results of the experiments were statistically analyzed using Minitab. The inlet flow rate was identified as the most significant factor. All three factors and their 2-factor interactions have a significant effect on impurity concentration on the cathode. The impurity concentrations in corner positions of cathodes had higher impurity levels than those in the center position of cathodes. The current density exerts more influence on impurity concentrations at corner positions than at the center position. A possible explanation for the phenomena observed is proposed.

3.1 Introduction

Anodes consisting of copper with its inherent silver, lead, nickel, bismuth, antimony, and arsenic impurities are common in copper electrorefining. Although arsenic and antimony can exert positive effects in producing copper cathodes of better quality and

thus might be added intentionally, impurities existing in anodes generally tend to jeopardize the quality of cathodes.[1] During the process of copper electrorefining, these impurities are typically transferred to the electrolytic solution as soluble species or impurity particles as the anode dissolves. Impurities in solid solutions and soluble inclusions are dissolved into electrolyte and some of them can co-precipitate if the concentrations of these impurities in the electrolyte reach saturation levels. Precipitates that are amorphous are referred to as floating slimes, which can affect cathode purity.[2] The elements such as Pb, As, Bi, Sb, and Se are the most significant impurities.[3]

Cast anode inclusions within the copper matrix result from the existence of impurities within the copper melt. When the copper anodes dissolve in electrorefining, many of these inclusions are liberated to form anode slimes. Chen and Dutrizac have carried out detailed investigation of the phases and structures existing in the anode slimes, such as kupferglimmer, euhedral NiO crystals, $(Cu,Ag)_2Se$ rings, $PbSO_4$, Ni-Fe oxides, silicates, and a variety of complex oxides.[4-8] The majority of anode slimes settle to the bottom of the cells. However, anode slimes that do not settle can be transported and trapped into cathodes.[1, 9, 10] Therefore, slime particles are responsible for a major part of cathode contamination.[11-14]

It is helpful to study anode slime behavior in the flowing electrolyte. Unfortunately, few flow studies involving slime particles can be found and the effect of main electrorefining parameters on slime transport in electrolyte is not fully understood.[15-17]

In this chapter, electrorefining testing was performed to understand the behavior of anode slimes in flowing electrolyte and their distribution on the cathode using tracer impurity nanoparticles.

3.2 Experimental Method

Laser-Induced Breakdown Spectroscopy (LIBS), which can analyze the localized concentration of impurities on the cathode, was utilized. The analysis using LIBS works by firing a high powered laser beam onto a metal sample. The focused thermal energy produced by the laser beam creates a plasma. This plasma ionizes the atoms which emit different colors of light that are unique to each atom's outer electrons in proportion to concentration.[18-20] If a spectrometer is used to measure the exact wavelengths of emitted light, these wavelengths are compared to standard wavelengths and signal intensity to calculate the chemical composition of the tested sample.

A series of copper electrorefining tests were performed using two different types of tracer nanoparticles: titanium dioxide nanoparticles (200 nm) and silver nanoparticles (100 nm). The particle size distribution analyses of the particle aggregates (added to and stirred in water, and injected into the size analyzer through a syringe pump) were performed before the experiments. The results of the analyses are shown in Figure 3.1 and Figure 3.2. The TiO_2 particle sizes are distributed mostly at 14.5 μm, and the Ag particle sizes are distributed mostly at 1.13 μm. The two kinds of particles are added to and stirred in water and pumped into the cell through a syringe pump. Each test was performed for 5 hours with 45 g/L Cu(II) as $CuSO_4$, 2 g/L Fe(II) as $FeSO_4$, 180 g/L H_2SO_4, 30 mg/L Cl^- as HCl, 100 mg/L Co(II) as $CoSO_4$. Eight tests were performed for the 3-factor 2-level experimental design (high and low inlet flow rate (pumping rate), high and low temperature, and high and low current density). Another 8 tests were performed using the same experimental design to verify the reproducibility of the tests. The total number of tests completed was 16, which includes 8 original tests and 8 repeated tests.

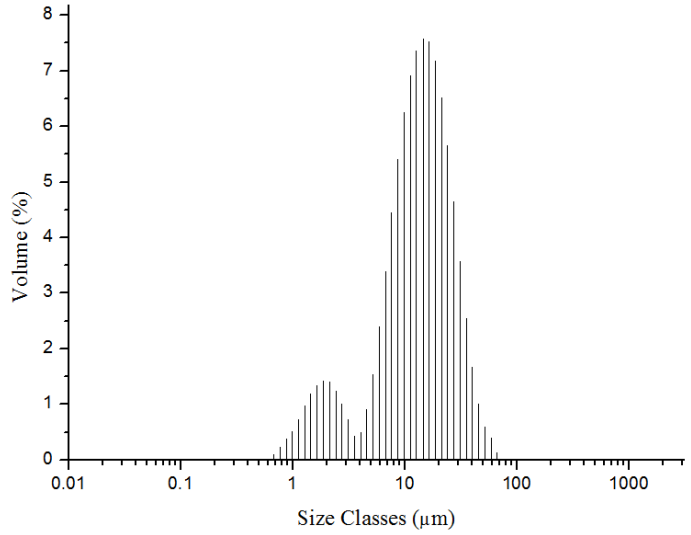

Figure 3.1 Particle size distribution analyses of TiO_2

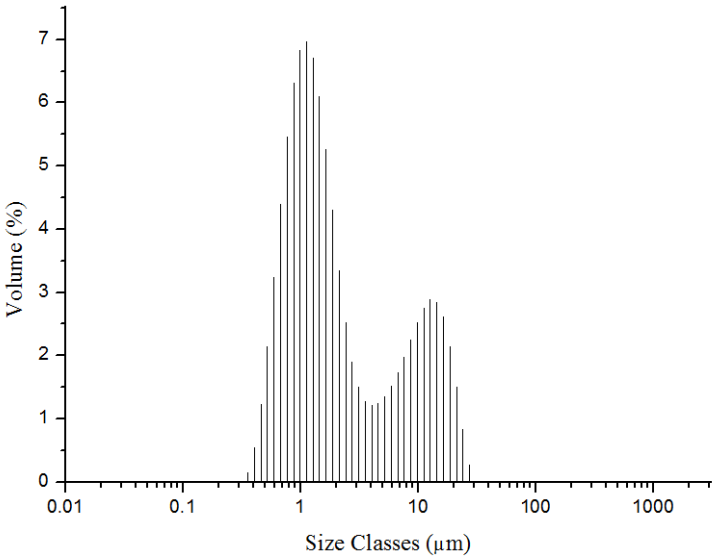

Figure 3.2 Particle size distribution analyses of Ag

The test cell consists of a 12.5×10×10 cm vessel that is continuously fed electrolyte and tracer particles at specified levels through an inlet and an outlet as shown in Figure 3.3 and Figure 3.4. The cathode is a stainless steel sheet that is approximately 8×9.5×0.1 cm with a corresponding Cu anode that is about 5 mm shorter than the cathode sheet. The current was supported by a power supply. An isothermal bath and heater were used to maintain the temperature. A peristaltic pump was used to move the electrolyte solution from the containment system to the cell. The electrolyte solutions were prepared in a 5-liter container and the amount of the solution is calculated on a 6-hour basis to supply the solution required for 5 hours of testing. A syringe pump was used to supply the two kinds of impurity particles at a rate equal to 500 mg/L TiO_2 nanoparticles and 200 mg/L Ag nanoparticles over each 5-hour period.

Plates were collected after 5 hours of testing. Pictures of each plate were taken: one example is shown in Figure 3.5. Samples were then stripped from the cathode plates and cut into 9 equivalent pieces as shown in Figure 3.6, but only the 4 corner pieces and the center piece (the shaded pieces in Figure 3.6) were analyzed later. Once cut, odd numbered pieces were analyzed by LIBS to determine the localized concentration of the added impurities. Ten points were analyzed randomly over each piece and the average intensities were calculated with reasonable standard variations among the 10 points. Examples of the resulting spectrum are presented in Figure 3.7. To determine the concentration of the impurities, calibration curves for each impurity were performed. After the impurity concentrations were measured on the five sections of each cathode deposit, concentration data were collected, compiled, and statistically analyzed using Minitab.

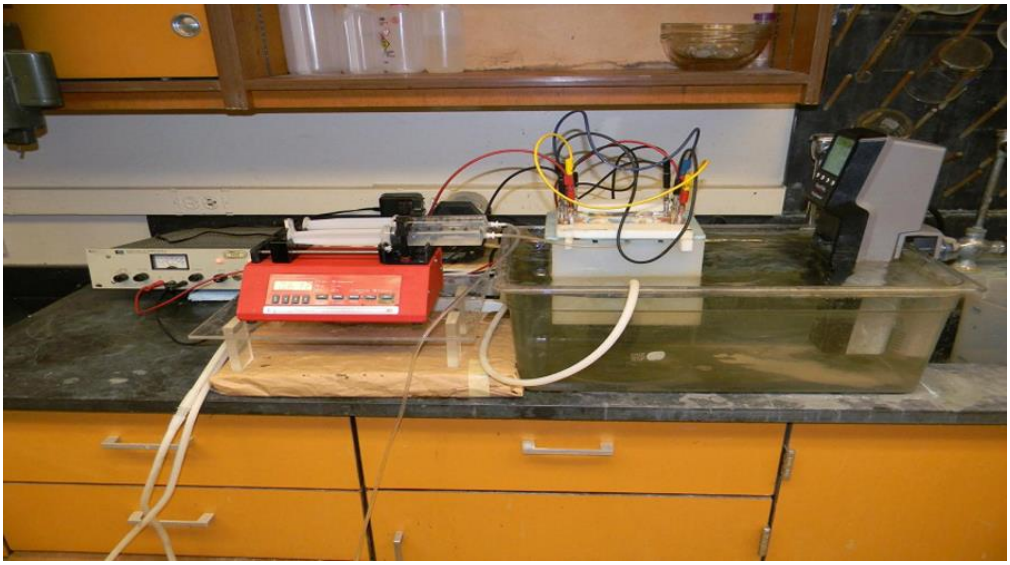

Figure 3.3 The electrorefining cell and associated equipment used in the experiments

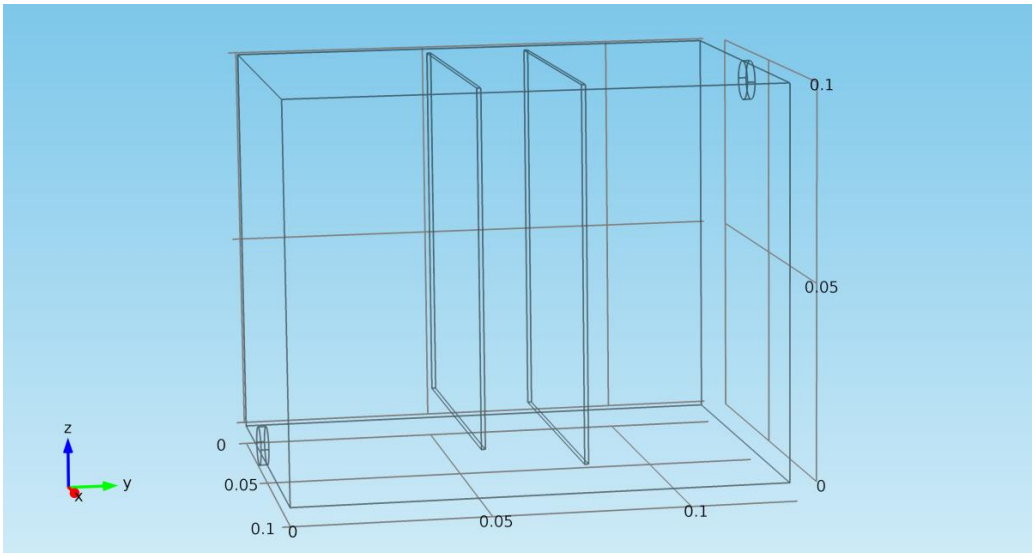

Figure 3.4 The geometry of the electrorefining cell with an inlet at a lower position and an outlet at a higher position

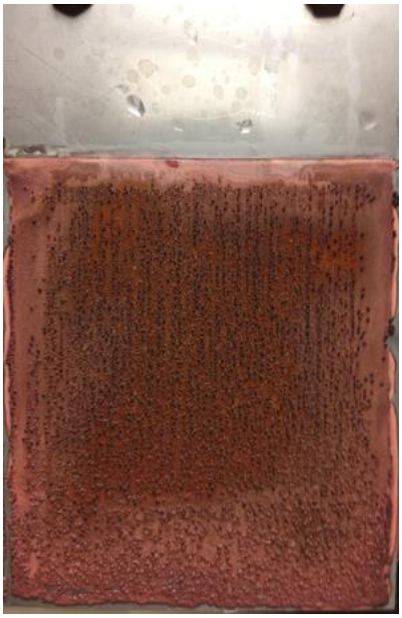

Figure 3.5 Sample of the copper plated cathode

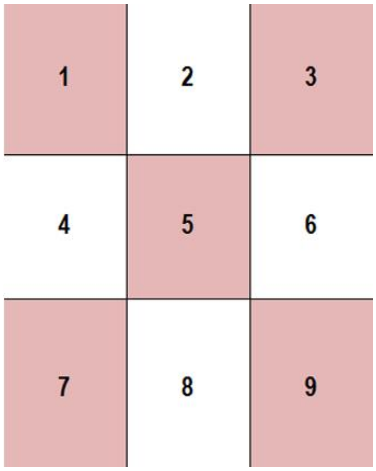

Figure 3.6 Diagram of tested areas of each plate sample

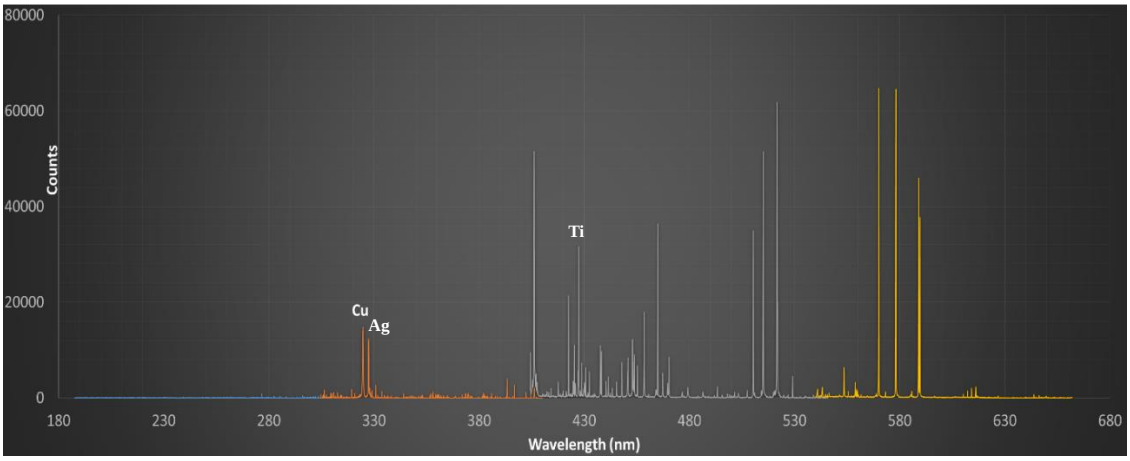

Figure 3.7 LIBS Spectrum for a sample (x axis represents wavelength (nm) and y axis represents intensity (counts))

3.3 Experimental Results

LIBS calibrations for titanium dioxide particles and silver particles were performed, based on the calibration methods described in published books.[21, 22] The results of the calibrations are shown below.

The linear relationship between TiO_2 normalized intensity and concentration can be described by:

$$\text{Normalized Intensity (\%)} = 8.601 * \text{Concentration of } TiO_2 \text{ (wt.\%)}$$

$$\text{R} - \text{Sq(adj)} = 99.9\% \quad (3.1)$$

Similarly, there is a conversion equation for Ag nanoparticles:

$$\text{Normalized Intensity (\%)} = 5.432 * \text{Concentration of Ag (wt.\%)}$$

$$\text{R} - \text{Sq(adj)} = 99.9\% \quad (3.2)$$

Based on the above two equations, the impurity concentrations were calculated for the five sections of each sample (Tables 3.1 and 3.2), after the normalized intensity data were measured using LIBS.

The concentration data were then statistically analyzed using Minitab. Through a 2-level factorial design (3 factors), the following statistical results were obtained. Please note the error was determined by reducing the model through the exclusion of the 3-factor interaction.

The significance of each factor on the concentration of TiO_2 particles in the center position of cathode is shown in Figure 3.8 and Figure 3.9. Figure 3.8 shows the factors and interactions in terms of their contribution to the standardized effect. The standard effect is the coefficient of each factor divided by the standard error of the coefficient. The red line shows the equivalent position for an Alpha level of 0.05 in terms of standard effect.

Table 3.1 Concentration of TiO_2 nanoparticles in each section

Conditions			Concentration (wt.%) at different positions				
Temp (^{o}C)	Current_D (A/m^2)	Flow Rate (mL/min)	Position 1	Position 3	Position 5	Position 7	Position 9
50	225	3.5	1.26	1.51	0.40	1.08	2.40
			1.32	1.47	0.38	1.01	2.35
70	225	3.5	0.48	0.69	0.22	0.67	0.55
			0.59	0.41	0.25	0.61	0.58
50	375	3.5	1.07	1.98	0.80	2.69	2.11
			1.33	1.74	1.02	2.66	2.42
70	375	3.5	0.79	1.35	0.54	1.90	1.09
			0.85	0.99	0.47	1.72	1.30
50	225	11	10.57	4.91	3.70	5.80	10.26
			10.36	5.04	3.76	5.56	10.39
70	225	11	9.42	3.34	1.59	3.09	9.94
			6.97	3.03	1.26	3.41	8.86
50	375	11	16.12	10.78	6.44	20.91	14.44
			15.31	11.09	5.87	19.95	16.10
70	375	11	11.80	8.35	3.50	5.84	11.98
			10.63	7.43	3.45	6.02	11.44

16 samples, 8 repeated

Table 3.2 Concentration of Ag nanoparticles in each section

Conditions			Concentration (wt.%) at different positions				
Temp (^{o}C)	Current_D (A/m^2)	Flow Rate (mL/min)	Position 1	Position 3	Position 5	Position 7	Position 9
50	225	3.5	1.95	2.17	1.84	3.41	3.89
			1.76	2.02	1.79	3.24	3.61
70	225	3.5	0.77	2.10	1.34	1.94	1.19
			0.72	1.51	1.07	1.73	1.24
50	375	3.5	4.59	4.79	2.72	7.76	9.37
			4.78	4.75	2.76	7.71	7.96
70	375	3.5	0.86	2.30	2.07	2.06	2.52
			1.51	2.18	1.54	2.42	2.83
50	225	11	14.50	10.43	8.89	15.59	12.26
			14.74	9.94	8.95	16.29	11.46
70	225	11	7.62	2.99	5.45	6.77	3.70
			5.58	3.42	5.08	5.56	3.93
50	375	11	11.67	10.10	9.30	17.32	9.35
			15.45	13.02	9.52	17.83	12.94
70	375	11	7.25	7.03	6.97	5.46	6.36
			8.45	7.86	6.55	6.60	6.53

16 samples, 8 repeated

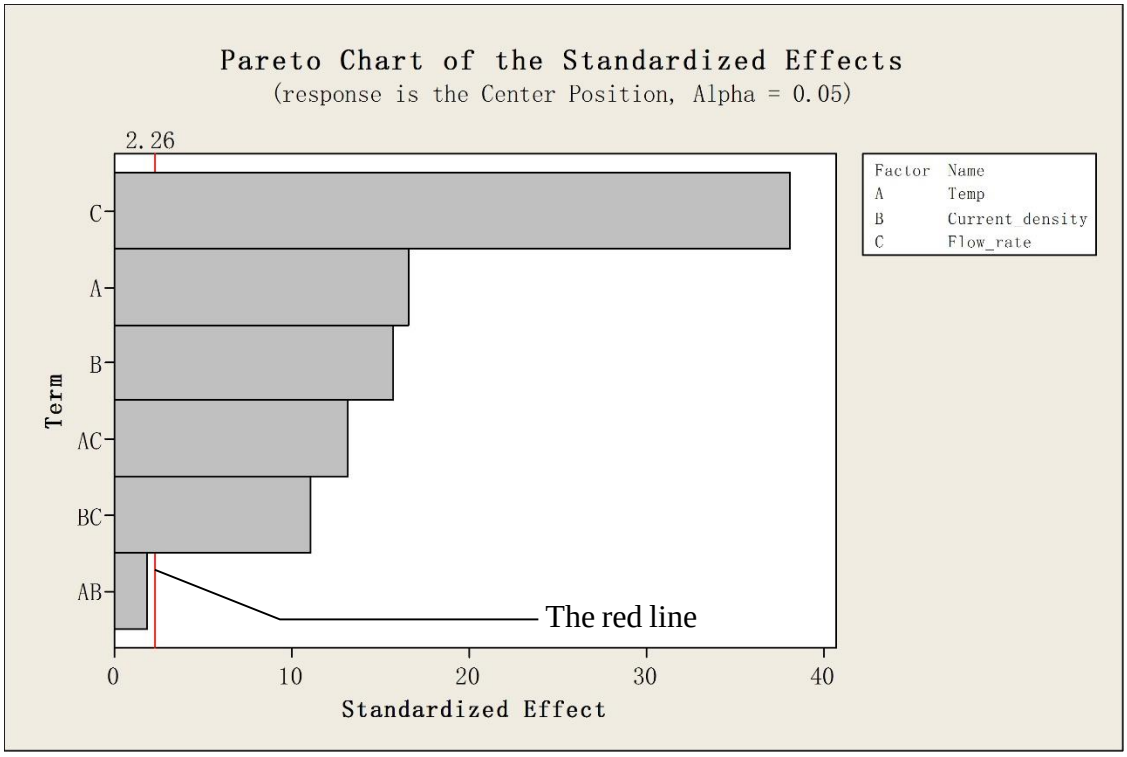

Figure 3.8 Pareto chart of the standardized effects for TiO_2 at the center position

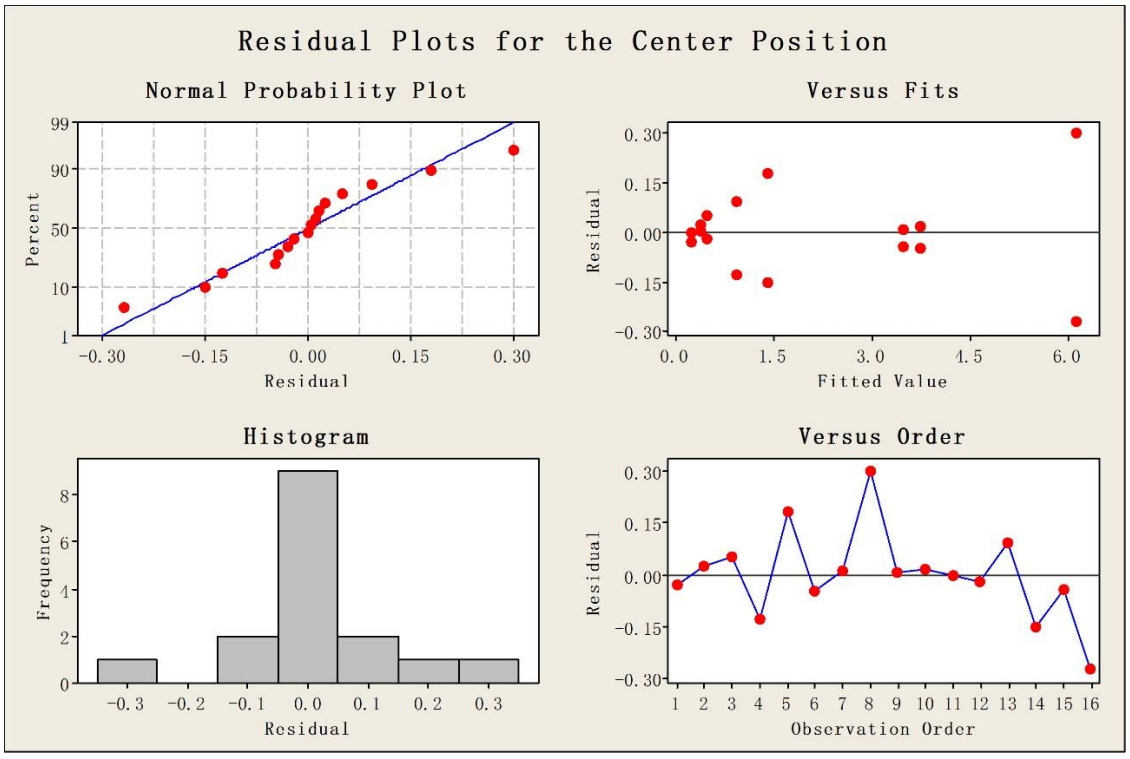

Figure 3.9 Residual plots for TiO_2 at the center position

Factors that are greater may be significant to the experiment. The Pareto chart shows all three main effects (temperature, current density, and flow rate) to be significant as well as two interactions of temperature-flow rate and current density-flow rate. The residual vs. order plot appears to be random with no issues, and this is also the case with the residual vs. fit plot (Figure 3.9).

Similar results are shown among the corner positions of cathode and the upper-right corner position is taken as an example shown in Figure 3.10 and Figure 3.11. Note that current density and the interaction of current density-flow rate become more significant to the experiment at the upper-right corner position than at the center position. It is most likely because of the larger current density and flow velocity effects on corner positions.

The concentration of TiO_2 at the center position can be calculated through the correlation equation (3.3).

$$\begin{aligned}\text{Concentration of } TiO_2\ (\text{wt.}\%) &= 2.1032 - 0.6927 * \text{Temp} + 0.6586 * \text{Current\_density} + 1.5932 \\ &* \text{Flow\_rate} - 0.0781 * \text{Temp} * \text{Current\_density} - 0.5527 * \text{Temp} \\ &* \text{Flow\_rate} + 0.4611 * \text{Current\_density} * \text{Flow\_rate} \\ \text{R} - \text{Sq(adj)} &= 99.34\% \end{aligned} \tag{3.3}$$

TiO_2 concentration at the upper-right position can be calculated by equation (3.4).

$$\begin{aligned}\text{Concentration of } TiO_2\ (\text{wt.}\%) &= 4.0070 - 0.8080 * \text{Temp} + 1.4571 * \text{Current\_density} + 2.7393 \\ &* \text{Flow\_rate} - 0.1255 * \text{Temp} * \text{Current\_density} - 0.4008 * \text{Temp} \\ &* \text{Flow\_rate} + 1.2092 * \text{Current\_density} * \text{Flow\_rate} \\ \text{R} - \text{Sq(adj)} &= 98.93\% \end{aligned} \tag{3.4}$$

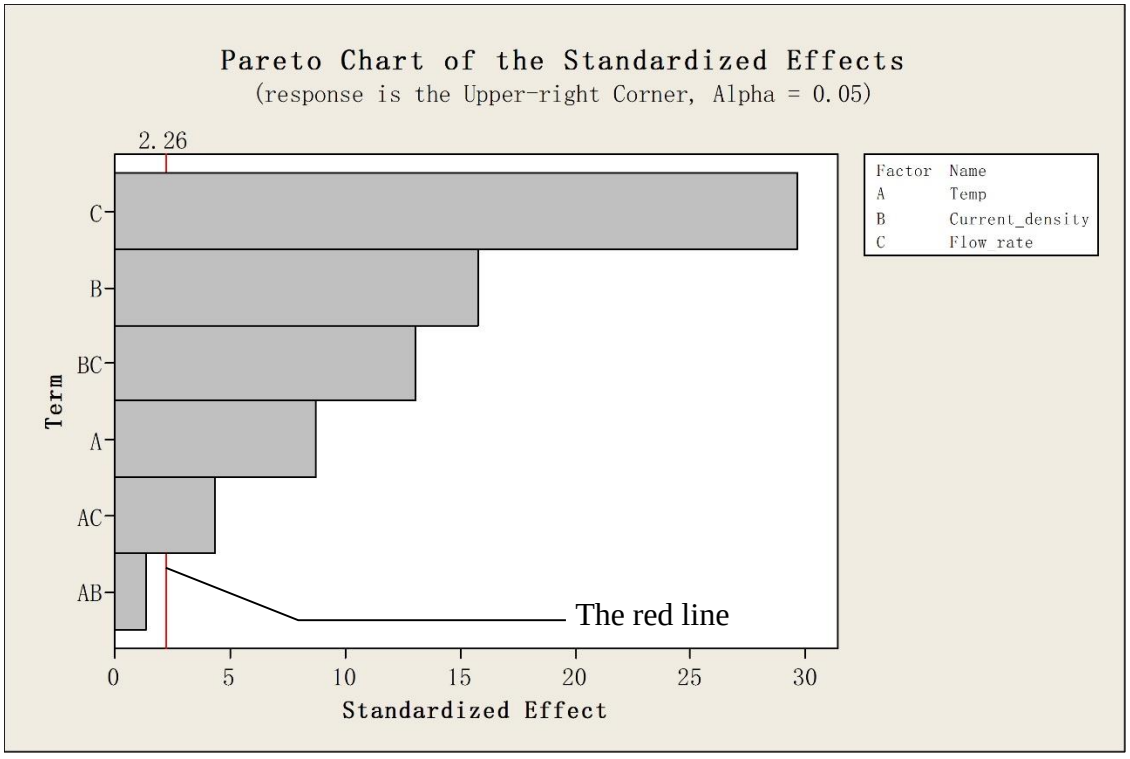

Figure 3.10 Pareto chart of the standardized effects for TiO_2 at the upper-right corner position

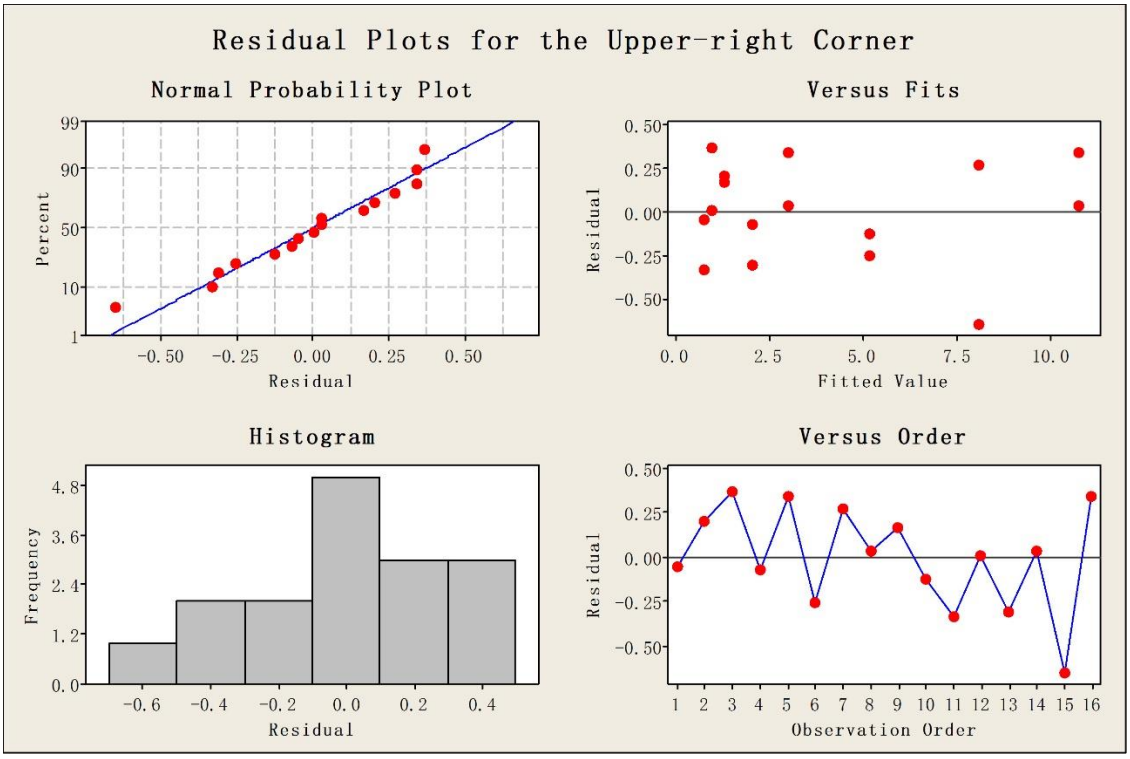

Figure 3.11 Residual plots for TiO_2 at the upper-right corner position

With the same methods, the significance of each factor on the concentration of Ag particles on the center position of cathode is shown in Figure 3.12 and Figure 3.13. The Pareto chart (Figure 3.12) of Ag at the center position is similar to that of TiO_2, except for a slight change of order of the factors. Notice that the interaction of current density and flow rate is not as significant as for TiO_2 and this is most likely because of the different charges of these two types of nanoparticle aggregates in electrolyte as well as their sizes. The review of the residual plots (Figure 3.13) is similar to that discussed for Figure 3.9.

Similar trends are shown among the results from the corner positions. The upper-right position is taken as an example shown in Figure 3.14 and Figure 3.15. It is obvious that current density becomes more significant to the experiment at the upper-right corner position than at the center position, due to larger current density effect on corner positions.

The concentration of Ag at the center position can be represented by eq. (3.5).

$$\begin{aligned}\text{Concentration of Ag (wt.\%)} &= 4.7407 - 0.9815 * \text{Temp} + 0.4389 * \text{Current\_density} + 2.8479 \\ &* \text{Flow\_rate} + 0.0851 * \text{Temp} * \text{Current\_density} - 0.5951 * \text{Temp} \\ &* \text{Flow\_rate} + 0.0570 * \text{Current\_density} * \text{Flow\_rate} \\ \text{R} - \text{Sq(adj)} &= 99.14\% \end{aligned} \quad (3.5)$$

Ag concentration at the upper-right position can be represented by equation (3.6).

$$\begin{aligned}\text{Concentration of Ag (wt.\%)} &= 5.413 - 1.740 * \text{Temp} + 1.091 * \text{Current\_density} + 2.686 \\ &* \text{Flow\_rate} + 0.078 * \text{Temp} * \text{Current\_density} - 1.034 * \text{Temp} \\ &* \text{Flow\_rate} + 0.313 * \text{Current\_density} * \text{Flow\_rate} \\ \text{R} - \text{Sq(adj)} &= 90.96\% \end{aligned} \quad (3.6)$$

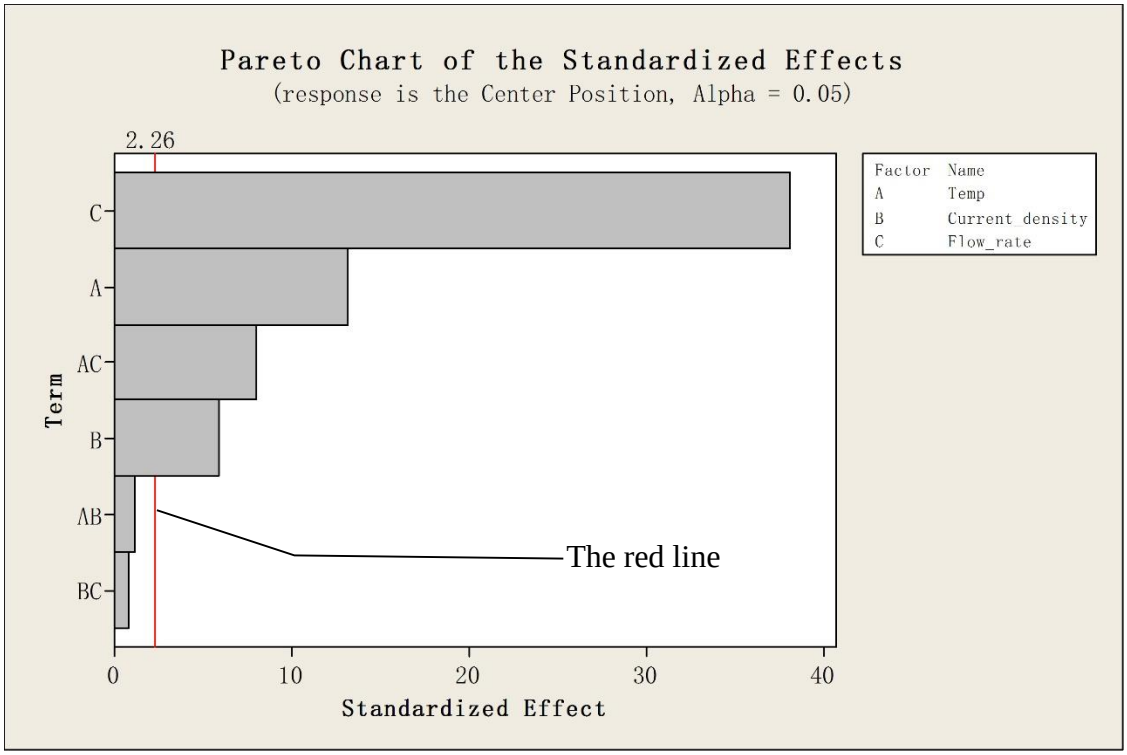

Figure 3.12 Pareto chart of the standardized effects for Ag at the center position

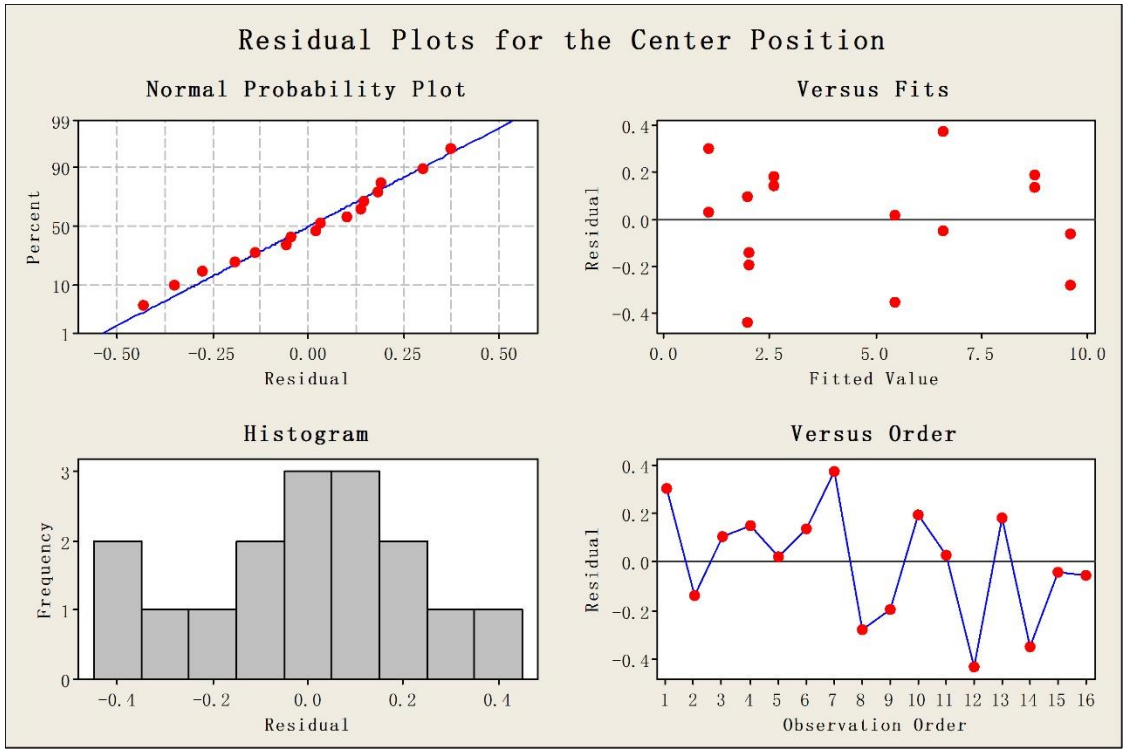

Figure 3.13 Residual plots for Ag at the center position

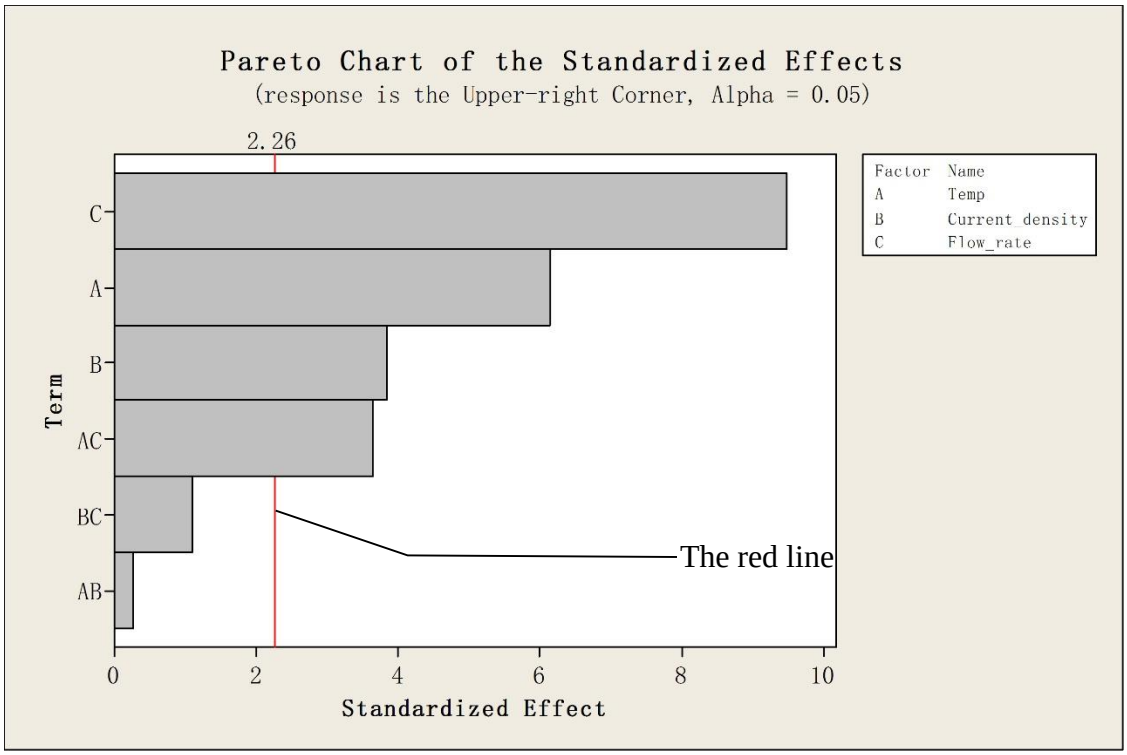

Figure 3.14 Pareto chart of the standardized effects for Ag at the upper-right corner position

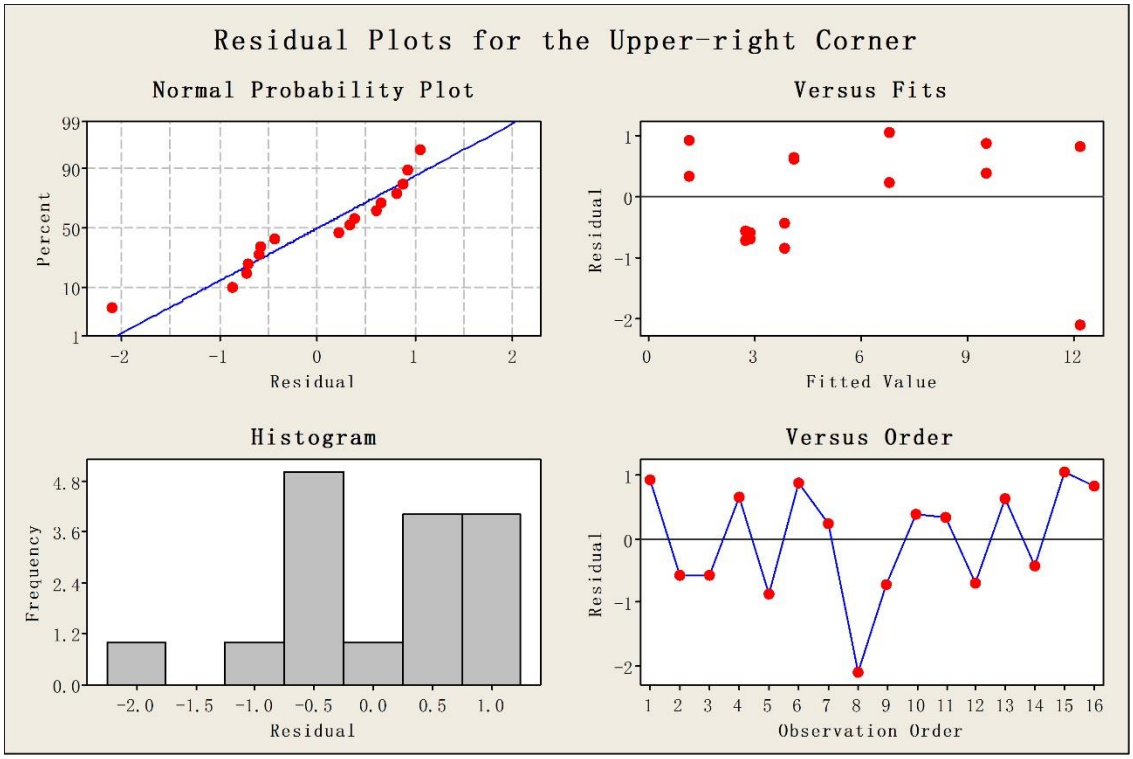

Figure 3.15 Residual plots for Ag at the upper-right corner position

From the statistical analysis of the experimental results, we can conclude that:

a. The three main effects are more significant than 2-factor interactions in this series of experiments (3-factor interaction neglected).
b. The inlet flow rate plays the most important role in the process and increases the concentration of impurity on the cathode.
c. There exists a positive correlation between the impurity concentration on the cathode and current density.
d. A negative effect of temperature on the concentration of impurity on the cathode can be observed in both cases.
e. The flow rate-temperature interaction plays a significant role in the process and can help explain the phenomena.
f. The interaction of current density and flow rate has different significance to the experiment for TiO_2 and Ag nanoparticle aggregates, which have different sizes and densities and are very likely to carry different charges in the electrolyte.
g. The current density exerts a greater effect on both impurities concentrations at corner positions than at the center position.

Also, from the tables of the experimental results, it is obvious that:

a. The concentrations of both silver and titanium dioxide on corner positions are higher than those on the center position.

3.4 Discussion

According to prior work on modelling and measurement of flow in electrorefining cells,[23-25] there exists a loop between the anode and the cathode, which is caused by the density gradient. The fluid near the anode is denser than that in front of the cathode, because

copper dissolves from the anode, while it is recovered on the cathode. As a result, some of the electrolyte solution is flowing between the electrodes in a loop, with a downward direction along the anode and an upward direction along the cathode. When the cell is continuously fed electrolyte from the inlet, a flow pattern with a direction from the lower inlet to the higher outlet will be generated. As a result, the upward electrolyte flow near the cathode will be intensified. This upward flow has a significant effect on impurity particle behavior.

The proposed theory is that most aggregates settle to the bottom of the cell, but some fine particles remain in suspension, providing them with more opportunities to be incorporated into the cathodic deposit by van der Waals force or electrostatic force if charged. Conversely, larger particles with a higher settling velocity will be removed from suspension more rapidly, and hence be less likely to be co-deposited. Thus, it is expected that small impurity nanoparticles will deposit on the cathode with copper. Co-deposition is related to the settling velocity. Since the concentration of each type of nanoparticle is extremely low compared to other species, we can assume that the motion of each nanoparticle is not influenced by other nanoparticles. Thus, for dilute suspensions, Stokes' law predicts the settling velocity of small spheres in fluid. Based on Stokes' law, the settling velocity is given by:

$$V = \frac{(\rho_p - \rho_f) g d^2}{18\mu} \tag{3.7}$$

where V is the settling velocity, ρ is density (the subscripts p and f indicate particle and fluid respectively), g is the acceleration due to gravity, d is the diameter of the particle and μ is the kinematic viscosity of the fluid.[26]

In eq. (3.7), the density of both particle and fluid, and the radius of the particle are

known parameters, according to the specification and results of particle aggregate size distribution analyses of these two types of nanoparticles. The dynamic viscosity of the fluid can be calculated from the empirical equation based on our laboratory measurements:

$$\mu(cP) = 1.928 - 0.01569 * T(\,^{o}C) \tag{3.8}$$

or

$$\mu(Pa \cdot S) = \frac{1}{1000}(1.928 - 0.01569 * T(\,^{o}C)) \tag{3.9}$$

Based on eq. (3.7) – eq. (3.9), settling velocity for both types of impurities can be calculated for both temperature conditions. Table 3.3 shows TiO_2 nanoparticle aggregates (14.5 μm) information as an example.

Therefore, cell temperature has a major effect on the settling velocities of impurity particles. In order to be suspended in the electrolyte, the settling velocity of an impurity particle cannot be larger than the local upward fluid velocity. Therefore,

$$V_{settling} = \frac{(\rho_p - \rho_f)gd^2}{18\mu(T)} \leq V_{upward_{fluid}} \tag{3.10}$$

The z component (upward flow) of the localized velocity of the fluid near the cathode will be computed by simulation and discussed in a later chapter. If the z component of localized velocity of the fluid is higher or equal to the settling velocity, the impurity particles at this position should suspend in the electrolyte and thus have larger probability to deposit on the cathode. Otherwise, the impurity particles should settle down. The larger the velocity difference between the local upward fluid velocity and settling velocity, the larger the probability that impurity particles suspend and get incorporated into cathodic deposit. Besides, a higher velocity pathway to this position will lead to more impurity particles in front of the cathode, and thus larger impurity particle concentration on the

Table 3.3 Effect of temperature on settling velocity of TiO_2

Temperature (ºC)	Settling velocity (m/s)
70	4.18E-04
50	3.03E-04

cathode.

Generally, a higher inlet flow rate will result in larger upward flow velocities in front of the cathode. Also, fluid velocities in front of cathode edges or corners would be higher than those in front of the center area of the cathode. Moreover, higher inlet flow rate is very likely to increase the agitation near the bottom of the cell and therefore increase the number of suspended particles there, which can then be picked up by the recirculation between the electrodes.

Hence, this approach may explain why the concentrations of impurities on the cathode become higher under high inlet flow rate and low temperature conditions and why the impurities concentrations in the center position are much lower than those on corner positions. This is also consistent with the statistical analysis, which showed that the flow rate-temperature interaction has a significant impact on the impurity concentration.

This phenomenon can also be partly explained by current density. If the current density is enhanced, the electrode reaction rate increases, which means that more copper dissolves from the anode and more copper ions deposit on the cathode. Consequently, the density gradient between the electrodes becomes larger and the velocity of the fluid in the loop cycle increases, which offers more opportunities for the nanoparticles to be suspended and co-deposited. Moreover, at corner positions, the current density becomes larger than at the center position, resulting in an even larger density gradient and higher local upward flow velocity. Thus the impurities concentrations are much higher at the corners than at the center. These reasons explain why the interaction of current density and flow rate is significant to the impurity concentration on the cathode, especially at corner positions, in the statistical analysis results.

Furthermore, the current density in an electrochemical cell can also be expressed as,

$$\boldsymbol{i} = -F^2\nabla\Phi\sum_i z_i^2 u_i c_i - F\sum_i z_i D_i \nabla c_i + F\boldsymbol{v}\sum_i z_i c_i \tag{3.11}$$

where D_i, z_i, u_i are the diffusivity, charge, and mobility of species i, respectively, F is Faraday's constant, $-\nabla\Phi$ is an electric field, and ∇c_i is a concentration gradient.[27]

Due to the electroneutrality of the electrolytic solution, the last term on the right is zero, which means $\sum z_i c_i = 0$. Therefore,

$$\boldsymbol{i} = -F^2\nabla\Phi\sum_i z_i^2 u_i c_i - F\sum_i z_i D_i \nabla c_i \tag{3.12}$$

If the current density increases, the migration rate and the diffusion rate of dissolved species need to be larger to match it.

Using the flux density to express the movement of each dissolved species,

$$\boldsymbol{N_i} = -z_i u_i F c_i \nabla\Phi - D_i\nabla c_i + c_i\boldsymbol{v} \tag{3.13}$$

where $\boldsymbol{N_i}$ is the flux density of species i.[27]

If the migration rate and the diffusion rate of species *i* increases, the vector $\boldsymbol{N_i}$ would be changed in both direction and magnitude. Because the directions of migration, diffusion, and convection are close to each other, the magnitude of vector $\boldsymbol{N_i}$ would become larger. That is to say, the velocity (magnitude) of species *i* is raised up. Eventually, the general velocity of the electrolyte would increase due to the effects of accelerated dissolved species. Then the z component of the fluid velocity along the cathode would increase accordingly. Therefore, the larger the current density (including the case of larger current densities at corner positions), the higher the fluid velocity, which makes nanoparticles more likely to stay in the solution and deposit on the cathode.

Lastly, the two types of nanoparticle aggregates may be charged in the electrolyte and thus may be affected by current density. As the current density increases, more charged nanoparticle aggregates would be transported to the cathode and get deposited.

3.5 Tracer Particle Analysis Conclusions

We can make a series of conclusions based on the experimental results and the proposed theory provides a reasonable explanation on the interesting phenomena observed.

1. The interaction between flow rate and temperature plays a significant role in the process, as the temperature determines the viscosity and thus the settling velocity and the inlet flow rate affects the z component of the localized fluid velocity near the cathode. Whether or not particles settle down to the bottom or become co-deposited on cathodes is dependent on the interaction between settling velocity and the z component of localized fluid velocities.

2. The inlet flow rate exerts the most significant effect on particle behavior in electrolyte and the associated distribution on the cathode. It has a positive effect on the concentration of impurity on the cathode.

3. There exists a positive correlation between the impurity concentration on the cathode and current density.

4. Temperature has a negative effect on the concentration of impurity on the cathode.

5. The concentrations of both titanium dioxide and silver on corner positions are higher than those on the center position.

6. The current density has more impact on both impurities concentrations at corner positions than at the center position.

7. Titanium dioxide and silver nanoparticle aggregates are very likely to carry different charges in the electrolyte.

3.6 References

1. M. L. Free: *Hydrometallurgy: Fundamentals and Applications*, John Wiley & Sons, Inc., Hoboken, NJ, 2013.

2. J. B. Hiskey: *T.T. Chen Honorary Symposium on Hydrometallurgy, Electrometallurgy and Materials Characterization*, John Wiley & Sons, Inc., Hoboken, NJ, 2012, pp. 101-12.

3. G. Cifuentes, J. Simpson, and C. Vargas: *T.T. Chen Honorary Symposium on Hydrometallurgy, Electrometallurgy and Materials Characterization*, John Wiley & Sons, Inc., Hoboken, NJ, 2012, pp. 125-30.

4. T. T. Chen and J. E. Dutrizac: *JOM*, 1990, vol. 42, pp. 39-44.

5. T. T. Chen and J. E. Dutrizac: *Can. Metall. Q.*, 1989, vol. 28, pp. 127-34.

6. T. T. Chen and J. E. Dutrizac: *Can. Metall. Q.*, 1991, vol. 30, pp. 95-106.

7. T. T. Chen and J. E. Dutrizac: *Metall. Mater. Trans. B*, 2005, vol. 36, pp. 229-40.

8. T. T. Chen and J. E. Dutrizac: *Can. Metall. Q.*, 1988, vol. 27, pp. 97-105.

9. W. G. Davenport, M. King, M. Schlesinger, and A. K. Biswas: *Extractive Metallurgy of Copper*, fourth ed., Pergamon Press, Elmsford, NY, 2002.

10. J. B. C. Kershaw: *Electro-Metallurgy*, Biblio Bazaar LLC, Charleston, SC, 2010.

11. S. Abe, B. W. Burrows, and V. A. Ettel: *Can. Metall. Q.*, 1980, vol. 19, pp. 289-96.

12. X. Ling, Z. H. Gu, and T. Z. Fahidy: *J. Appl. Electrochem.*, 1994, vol. 24, pp. 1109-15.

13. J. Sedzimir and W. Gumowska: *Hydrometallurgy*, 1990, vol. 24, pp. 203-17.

14. G. N. Srinivasan, P. Adaikkalam, P. Radhakrishnamurty, R. Srinivasan, P. Ramachandran, and K. Naganathan: *J. Electrochem. Soc. India*, 1982, vol. 31, pp. 60-63.

15. Z. H. Gu, J. Chen, and T. Z. Fahidy: *Hydrometallurgy*, 1995, vol. 37, pp. 149-67.

16. J. A. Sawicki, J. E. Dutrizac, J. Friedl, F. E. Wagner, and T. T. Chen: *Metall. Trans. B*,

1993, vol. 24B, pp. 457-62.

17. T. T. Chen and J. E. Dutrizac: *Can. Metall. Q.*, 1993, vol. 32, pp. 267-79.

18. N. Reinhard: *Laser-Induced Breakdown Spectroscopy: Fundamentals and Applications*, Springer, Berlin, Germany, 2012.

19. J. M. Vadillo and J. J. Laserna: *Spectrochim. Acta, Part B*, 2004, vol. 59, pp. 147-61.

20. W. B. Lee, J. Wu, Y. I. Lee, and J. Sneddon: *Appl. Spectrosc. Rev.*, 2004, vol. 39, pp. 27-97.

21. D. A. Cremers and L. J. Radziemski: *Handbook of Laser-Induced Breakdown Spectroscopy*, John Wiley & Sons Ltd., West Sussex, England, 2006.

22. A. W. Miziolek, V. Palleschi, and I. Schechter: *Laser-induced Breakdown Spectroscopy (LIBS): Fundamentals and Applications*, Cambridge University Press, Cambridge, UK, 2006.

23. D. Ziegler and J. Evans: *J. Electrochem. Soc.*, 1986, vol. 133, pp. 559-66.

24. M. J. Leahy and M. P. Schwarz: *16th Australasian Fluid Mechanics Conference*, Gold Coast, Australia, 2007.

25. M. J. Leahy and M. P. Schwarz: *Metall. Mater. Trans. B*, 2011, vol. 42, pp. 875-90.

26. M. Rhodes: *Introduction to Particle Technology*, second ed., John Wiley & Sons Ltd., West Sussex, England, 2008.

27. J. Newman and K. E. Thomas-Alyea: *Electrochemical Systems*, third ed., John Wiley & Sons, Inc., Hoboken, NJ, 2004.

CHAPTER 4

SIMULATION AND VALIDATION STUDIES OF IMPURITY PARTICLE BEHAVIOR IN COPPER ELECTROREFINING

A model based in COMSOL Multiphysics® consisting of an electrorefining cell was utilized to simulate copper electrorefining. Concentration and electrolyte density profiles were generated as electrochemical simulation results. Fluid velocity field, particle trajectories, and particle distribution maps were generated to study impurity particle behavior in electrolyte. A 3-factor designed set of boundary conditions was used to determine the effects of inlet flow rate, temperature, and current density on impurity particle behavior in electrolyte and the associated distribution in the cross-section (slice) 100 microns away from the front surface of the cathode during copper electrorefining. The number of impurity particles on the cross-section was counted for each set of boundary conditions. The model data for impurity particle distribution were compared with measured impurity particle contamination at the cathode surface, and the results show a very good correlation, which suggests the model is reasonable. The model results show the three factors have significant effects on the number of impurity particles in the cross-section. The impurity particle counts at the corner positions of the slice are much higher than those at the center position of the slice. Possible explanations for the simulation results are proposed.

4.1 Introduction

Cast anode has inclusions within the copper matrix, due to the existence of its inherent impurities such as lead, arsenic, bismuth, antimony, and silver impurities. During electrorefining, copper in the anode dissolves. As a result, many of these inclusions are liberated in the electrolytic solution as anode slimes, though some of them stick to the remaining anode by adhesion. Anode slimes that are larger and denser tend to settle to the bottom of the cells. Nevertheless, finer anode slimes do not settle, but remain in suspension in solution. They can be transported and incorporated into cathodes.[1-3] Consequently, anode slimes are a major potential source of impurities in the cathode.[4-7]

To improve cathode purity, anode slime transport in the flowing electrolyte has been studied. There are some studies on modeling and measurement of flow in electrorefining cells, which indicate the existence of recirculation between anodes and cathodes.[8-10] Many studies considering anode slime and its characteristics have been performed.[11-13] But flow studies involving slimes are rarely found in the literature, and the major electrorefining parameters' effects on slime behavior in electrolytic solution are not well known.

Modeling and simulations can be cost effective ways of predicting the behavior of impurity particles in the electrolytic solution. Models can compute the solution concentrations, electrolyte density distribution, fluid velocity, particle trajectories, and particle distributions.

There are several commercially available software packages on the market, including Elsyca, Cell Design, and COMSOL Multiphysics®.[14] These software packages make complex geometries modeling and complex simulations, such as particle tracing,

possible.[15]

In this chapter, modeling, simulation, and experimental validation of the copper electrorefining process were completed to understand the behavior of anode slimes in flowing electrolyte and their distribution on the cross-section 100 microns away from the front surface of the cathode. COMSOL Multiphysics® with its Electrodepostion, Computational Fluid Dynamics, and Particle Tracing modules, was utilized to simulate the process.

COMSOL Multiphysics is capable of combining electrodeposition, fluid flow, and particle tracing into one model. Furthermore, it has the ability to model in three dimensions and provide results in three-dimensional images and animations.[16] COMSOL Multiphysics uses the finite element method to compute model solutions.

4.2 Model Description

4.2.1 Governing Equation Description

To model the electrodeposition process, the Tertiary Nernst-Planck current distribution model was utilized to solve for the electrolyte potential (Φ_l), the current density distribution ($\boldsymbol{i_l}$), and the concentrations of various species (c_i).[15] A set of governing equations was used and solved.[17, 18]

In electrolyte, the governing equation for the mass transfer in the solution is the Nernst-Plank equation:

$$\boldsymbol{N_i} = -z_i u_i F c_i \nabla\Phi_l - D_i \nabla c_i + c_i \boldsymbol{v} \tag{4.1}$$

where $\boldsymbol{N_i}$, z_i, u_i, c_i, D_i are the flux density, charge, mobility, concentration, and diffusivity of species i, F is Faraday's constant, $-\nabla\Phi_l$ is an electric field, ∇c_i is a concentration gradient, and $\boldsymbol{v}$ is the velocity vector.

No homogeneous reaction in the electrolyte in the electrorefining cell was assumed, so the material balance is governed by the equation:

$$\frac{\partial c_i}{\partial t} + \nabla \cdot \boldsymbol{N_i} = 0 \tag{4.2}$$

In the electrolyte, the current density is governed by:

$$\boldsymbol{i_l} = -F^2 \nabla \Phi_l \sum_i z_i^2 u_i c_i - F \sum_i z_i D_i \nabla c_i + F\boldsymbol{v} \sum_i z_i c_i \tag{4.3}$$

where $\boldsymbol{i_l}$ is the current density in the electrolyte, and other variables are defined previously.

Due to the electroneutrality of the electrolytic solution, the last term on the right is zero ($\sum z_i c_i = 0$). Therefore,

$$\boldsymbol{i_l} = -F^2 \nabla \Phi_l \sum_i z_i^2 u_i c_i - F \sum_i z_i D_i \nabla c_i \tag{4.4}$$

On the electrodes, the current density is governed by Ohm's Law:

$$i_s = -\sigma_s \nabla \Phi_s \tag{4.5}$$

where i_s is the current density in the electrode, σ_s is the conductivity of the electrode and $\nabla \Phi_s$ is an electric field. It was assumed that the electrical potential on the anode and cathode was constant, due to their much lower electric resistance compared to the electrolyte. Note that only the front side face of each electrode had electrode reactions with all other faces insulated (see section 4.2.2 and associated figures). The electrical potential of the cathode (the front side face) was assumed to be 0 V and therefore all other potentials were measured with this reference.

With conservation of current in the electrolyte and electrodes, we have:

$$\nabla \cdot \boldsymbol{i_k} = Q_k \tag{4.6}$$

where *k* denotes an index that is *l* for the electrolyte and *s* for the electrode, and Q_k is a

general current source term and was zero in this model.[18] Therefore, eq. (4.6) becomes:

$$\nabla \cdot \boldsymbol{i_k} = 0 \tag{4.7}$$

At the electrode-electrolyte-interface, the overpotential η (the driving force for the electrochemical reactions at the interface) is defined as:

$$\eta = \Phi_S - \Phi_l - \Delta\Phi_{eq} \tag{4.8}$$

where Φ_S is the electrical potential of the electrode, Φ_l is the potential of the electrolyte adjacent to the electrode, and $\Delta\Phi_{eq}$ is the difference between the electrode and the electrolyte potentials at the interface measured at equilibrium using a common reference potential and was assumed to be zero in this model.[18] Since the electrical potential of the electrode was assumed to be constant, it was the electrolyte potential at the interface that would lead to variations in overpotential.

The local overpotential determines the local current density at the electrode-electrolyte-interface by the concentration dependent Butler-Volmer equation:

$$i_{loc} = i_0 \left[\frac{C_{R,S}}{C_{R,B}} \exp\left(\frac{\alpha_a z F}{RT} \eta \right) - \frac{C_{O,S}}{C_{O,B}} \exp\left(-\frac{\alpha_c z F}{RT} \eta \right) \right] \tag{4.9}$$

where i_{loc} is the local current density at the interface (also called as charge transfer current density), i_0 is equilibrium exchange current density, $C_{R,S}$ is the surface reductant concentration, $C_{R,B}$ is the bulk reductant concentration, $C_{O,S}$ is the surface oxidant concentration, $C_{O,B}$ is the bulk oxidant concentration, α_a is the anodic symmetry factor, α_c is the cathodic symmetry factor, z is the number of electrons transferred in the rate limiting step (typically 1), F is the Faraday constant, R is the gas constant, T is the absolute temperature, and η is the overpotential.[1, 18] The values of equilibrium exchange current density, anodic and cathodic symmetry factors, and the temperature are specified in Table

4.1 (the equilibrium exchange current density and anodic and cathodic symmetry factors were assumed to be the typical values in copper electrorefining).[19] The value of $\frac{C_{R,S}}{C_{R,B}}$ is 1 for both anodic and cathodic reactions, since the reduced species in both reactions is metallic copper. The expression for $\frac{C_{O,S}}{C_{O,B}}$ is $\frac{C_{Cu}}{C_{initial\_Cu}}$, where C_{Cu} is the localized time-dependent concentration of cupric ions at the interface and $C_{initial\_Cu}$ is the initial cupric ion concentration in the cell that is equal to the bulk cupric ion concentration.

Besides the conservation of current in the electrolyte and electrodes, the current must also be conserved at the electrode-electrolyte-interface. In this model, current is transferred between the electrolyte and electrode domains by an electrochemical reaction (Faradaic current). Thus the current density in the electrolyte adjacent to the electrode has the following relationship with the local current density term in the Butler-Volmer equation:[18]

$$\boldsymbol{i_l} \cdot \boldsymbol{n} = i_{loc} \quad \text{at the electrode} - \text{electrolyte} - \text{interface} \tag{4.10}$$

where $\boldsymbol{i_l}$ is the current density in the electrolyte at the interface, $\boldsymbol{n}$ is the unit normal vector to the electrode surface, and i_{loc} is the local current density.

This current density distribution model had the average current density on the anode, rather than the electrical potentials of the electrodes, as the boundary condition. Besides, the balance of current (an equal amount of current that left at the anode also enters at the cathode) needs to be satisfied. Therefore, the current densities in the electrolyte adjacent to the electrode are constrained by the following integral equations:

$$\int_{anode\ surf.} \boldsymbol{i_l} \cdot \boldsymbol{n}\, dS = \int_{cathode\ surf.} \boldsymbol{i_l} \cdot \boldsymbol{n}\, dS = i_{avz.} \int_{anode\ surf.} dS \tag{4.11}$$

Table 4.1 Main parameters set in the model

Description	Value	Description	Value
Exchange current density	0.2 [A/m^2]	Anode symmetry factor	1.5
Temperature	323.15/343.15 [K]	Cathode symmetry factor	0.5
Concentration of H_2SO_4	180 [g/l]	Initial concentration of cupric ion	45 [g/l]
(Average) Current density	225/375 [A/m^2]	Inlet flow rate	3.5/11 [ml/min]
Impurity particle diameter	14.5E-6 [m]	Impurity particle density	4200 [kg/m^3]

where $\boldsymbol{i_l}$ is the current density in the electrolyte adjacent to the electrode, $\boldsymbol{n}$ is the unit normal vector to the electrode surface, and $i_{avz.}$ is the average current density applied.[18]

In this model, the electrolyte current density $\boldsymbol{i_l}$, the electrolyte potential Φ_l are governed by eq. (4.4) and eq. (4.7) in the electrolyte and by eq. (4.8 – 4.11) at the interface, while the electrode potential Φ_s and current density i_s are governed by eq. (4.5) and eq. (4.7) on the electrodes and by eq. (4.8 – 4.9) at the interface. The Butler-Volmer equation connects the electrode and electrolyte variables at the interface through overpotential η and local current density i_{loc}. Note that the electrode potential and current density are peripheral to this model and the electrodes are just two geometric faces in the model as discussed previously. The species concentration c_i can be solved with the addition of eq. (4.2). The flow velocity term $\boldsymbol{v}$ in eq. (4.1) connects the current distribution with flow field. As a result, with the constraints of eq. (4.1) to eq. (4.11), the electrolyte potential, the current density distribution, and concentrations of various species can be solved, given the parameters (such as diffusivity D_i and mobility u_i) and boundary conditions (such as average current density $i_{avz.}$).

The Navier-Stokes equations were used to model the fluid flow in this study and they were coupled with the electrochemistry model. Turbulence was not considered here because of the small dimensions of both inlet pipe and the electrochemical cell, and the low flow rates exerted and internally generated. Thus the Reynolds numbers of the flow in the pipe (about 32.86 at the flow rate of 11 ml/min) and in the cell (about 141 in the interelectrode domain using the highest flow velocity of the flow between the electrodes) are relatively low. The flow field and current distribution can almost reach steady state after 5000 s in the time-dependent simulation, and the steady state solutions were also obtained.

Furthermore, it was assumed that the impact of impurity particles on the fluid velocity field is negligible. Lastly, the general particle trajectory caused by the general fluid field driven by the inlet inflow and the density gradients between the electrodes is the main issue studied in this chapter and the minor turbulence in the cell and the turbulent dispersion of particles are not considered in this study but could be considered for future work. Another set of governing equations was used and solved for fluid flow.[18, 20]

A variable density flow was assumed, dependent on temperature and concentrations of cupric ions and acid. It is governed by the following continuity and momentum equations:

$$\frac{\partial \rho}{\partial t} + \nabla \cdot (\rho \boldsymbol{v}) = 0 \tag{4.12}$$

$$\rho \frac{\partial \boldsymbol{v}}{\partial t} + \rho \boldsymbol{v} \cdot \nabla \boldsymbol{v} = -\nabla p + \nabla \cdot \left(\mu (\nabla \boldsymbol{v} + (\nabla \boldsymbol{v})^{\mathrm{T}}) - \frac{2}{3} \mu (\nabla \cdot \boldsymbol{v}) \boldsymbol{I} \right) + \boldsymbol{F} \tag{4.13}$$

where ρ is the density, $\boldsymbol{v}$ is the fluid velocity vector, p is the pressure, μ is the dynamic viscosity, $\boldsymbol{I}$ is the identity tensor, and $\boldsymbol{F}$ is the body force vector (per unit volume) acting on the fluid.

Simulations of the impurity particle motion in the electrolytic solution were time dependent and were based on fluid flow field solutions. Negligible impact of particles on the flow velocity field was assumed. The motion of a particle is governed by Newton's second law:

$$m \frac{d^2 \boldsymbol{x}}{dt^2} = \boldsymbol{F}(t, \boldsymbol{x}, \frac{d\boldsymbol{x}}{dt}) \tag{4.14}$$

where m is the particle mass, $\boldsymbol{x}$ is the position of the particle, and $\boldsymbol{F}$ is the sum of all forces acting on the particle, such as drag and gravity forces.[18]

4.2.2 Model Geometry

The geometry of the model is presented in Figures 4.1 – 4.2 with a three-dimensional coordinate system. The size of the cell is 0.125×0.10×0.10 m. The anode is 0.08×0.09×0.001 m in size, and the cathode is 0.08×0.095×0.001 m in size. The distance between the anode and the cathode is 0.025 m. The inflow pipe is 0.005 m in radius and 0.002 m in length. The axis of the inflow pipe is in the y direction, with its coordinates of x= 0.05 m and z=0.005 m. The outflow pipe is also 0.005 m in radius and 0.002 m in length. The axis of the outflow pipe is in the y direction, with its coordinates of x= 0.05 m and z=0.095 m.

Only the front side faces of the anode and the cathode have electrode reactions. The left end of the inflow pipe is the inlet, and the right end of the outflow pipe is the outlet.

4.2.3 Model Boundary Conditions

The anodic reaction and cathodic reactions were assumed to be:

$$\mathrm{Cu(s)} \rightarrow \mathrm{Cu^{2+}_{(aq)}} + 2\mathrm{e^-} \tag{4.15}$$

$$\mathrm{Cu^{2+}_{(aq)}} + 2\mathrm{e^-} \rightarrow \mathrm{Cu(s)} \tag{4.16}$$

Faces other than the two electrode faces have insulation boundary condition:

$$-\boldsymbol{n} \cdot \boldsymbol{i} = 0 \tag{4.17}$$

where $\boldsymbol{n}$ is the unit normal vector to the face, and $\boldsymbol{i}$ is the current density.

Faces other than the two electrode faces, the inlet face, and the outlet face, were set to have no flux boundary condition:

$$-\boldsymbol{n} \cdot \boldsymbol{N_i} = 0 \tag{4.18}$$

where $\boldsymbol{n}$ is the unit normal vector to the face, and $\boldsymbol{N_i}$ is the flux density of species *i*.

The conductivity of the solution is governed by the following equation:[17]

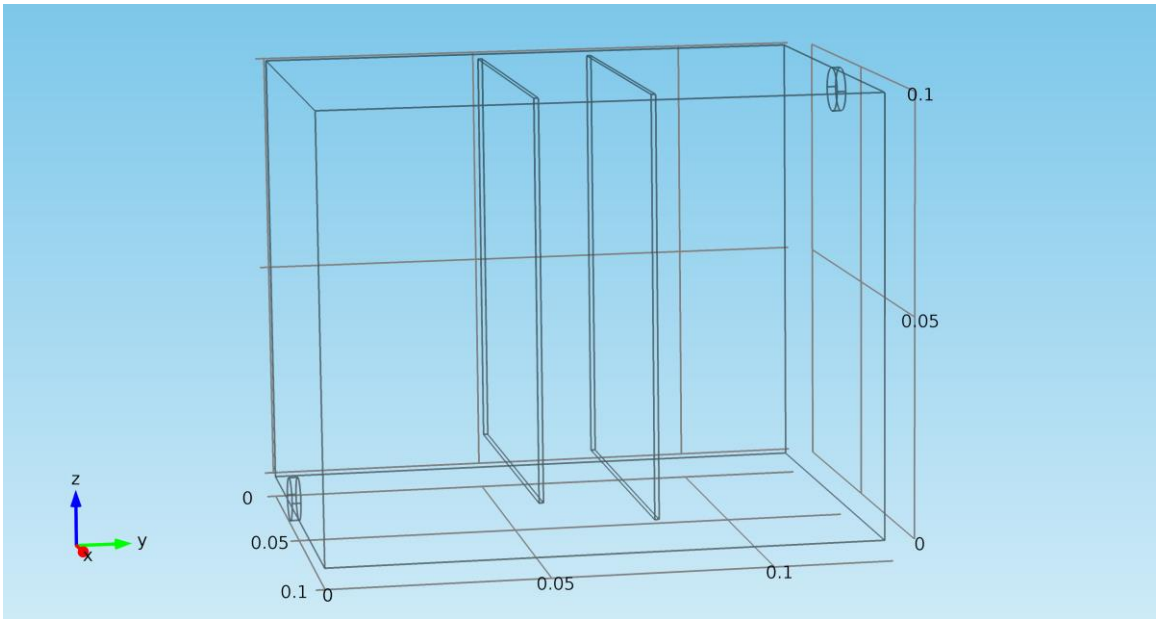

Figure 4.1 Front view of the geometry of the copper electrorefining cell in the COMSOL® model (all units in meters)

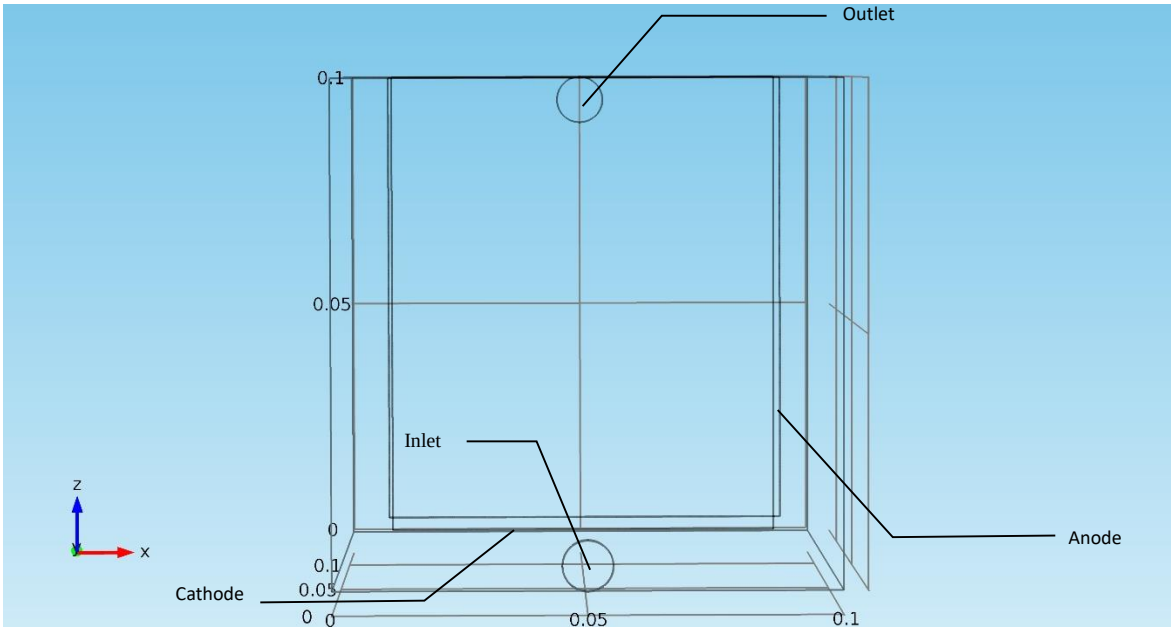

Figure 4.2 Side view of the geometry of the copper electrorefining cell in the COMSOL® model (all units in meters)

$$\sigma_l = F^2 \sum_i z_i^2 u_i c_i \tag{4.19}$$

where σ_l is the conductivity of the solution, and z_i, u_i, c_i are the charge, mobility, and concentration of species i. The diffusivity was estimated using the equation:

$$D = D_0 e^{-E_a/RT} \tag{4.20}$$

where D is the diffusivity, D_0 is the maximum diffusivity at infinite temperature, R is the gas constant, T is the absolute temperature, and E_a is the activation energy for diffusion.

Eq. (4.21) was derived from the experimental data from Moats, et al.:[21]

$$D\ [cm^2/s] = 10\text{^}(-0.676 - 0.481 * log_{10}\, C_{H2SO4} - 0.156 * log_{10}(0.06355 * [Cu]) + 0.9885 * \frac{-8340.61}{8.314 * T}) \tag{4.21}$$

where C_{H2SO4} is the initial H_2SO_4 concentration in Kg/m^3, $[Cu]$ is the localized cupric ion concentration in mol/m^3. The fitting plot for the diffusivity is shown in Figure 4.3.

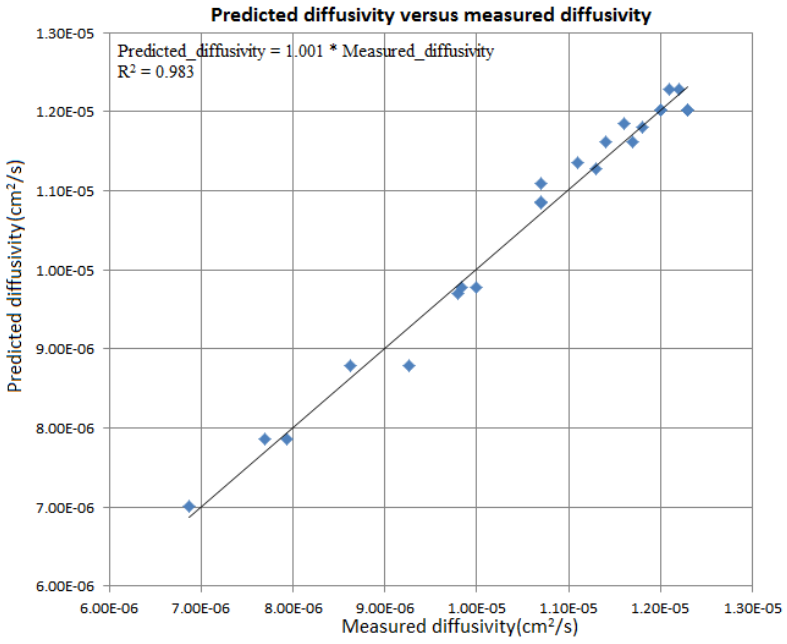

Figure 4.3 Fitting plot of predicted diffusivity versus measured diffusivity

The diffusivity in this study was treated as an overall diffusivity. For every set of cell conditions, cupric ions, sulphate ions, and hydrogen ions were assumed to have the same overall diffusivity. The mobility was calculated using the relationship:

$$u_i = \frac{D_i}{RT} \tag{4.22}$$

where u_i and D_i are the mobility and diffusivity of species *i*, *R* is the gas constant, and *T* is the absolute temperature. The electrolyte density in the cell was estimated by eq. (4.23), modified from the empirical equation from Price and Davenport:[22]

$$\rho\ [kg/m^3] = 1018.56 + 0.1512 * [Cu] + 0.54 * C_{H2SO4} - 0.59 * T \tag{4.23}$$

where ρ is the fluid density in kg/m^3, $[Cu]$ is the localized cupric ion concentration in mol/m^3, C_{H2SO4} is the initial H_2SO_4 concentration in Kg/m^3, and *T* is the temperature in ℃. The fitting plot for the electrolyte density is shown in Figure 4.4.

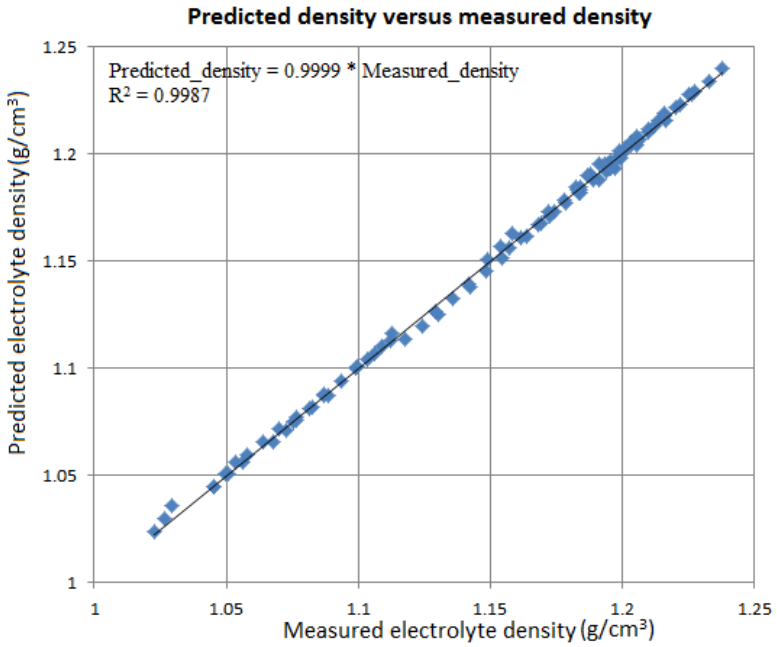

Figure 4.4 Fitting plot of predicted electrolyte density versus measured electrolyte density

The volume force for the fluid was determined by multiplying eq. (4.23) by the gravitational constant and applying it in the negative z direction.

$$F_z\,[N/m^3] = -g * (1018.56 + 0.1512 * [Cu] + 0.54C_{H2SO4} - 0.59T) \quad (4.24)$$

where F_z is the volume force in the z direction, ρ is the fluid density, and g is the gravitational constant. The dynamic viscosity of the fluid was estimated by the following empirical equation, which is based on the experimental data from Price and Davenport:[22]

$$\mu(Pa * s) = \frac{1}{1000}\left(-1989.46 + 0.010353 * (0.06355 * [Cu]) + 0.0014685 * C_{H2SO4} + 1983.72 * exp\left(\frac{1}{T}\right)\right) \quad (4.25)$$

where μ is the dynamic viscosity in Pa * s, $[Cu]$ is the localized cupric ion concentration in mol/m^3, C_{H2SO4} is the initial H_2SO_4 concentration in Kg/m^3, and T is in Kelvin. The fitting plot for the dynamic viscosity is shown in Figure 4.5.

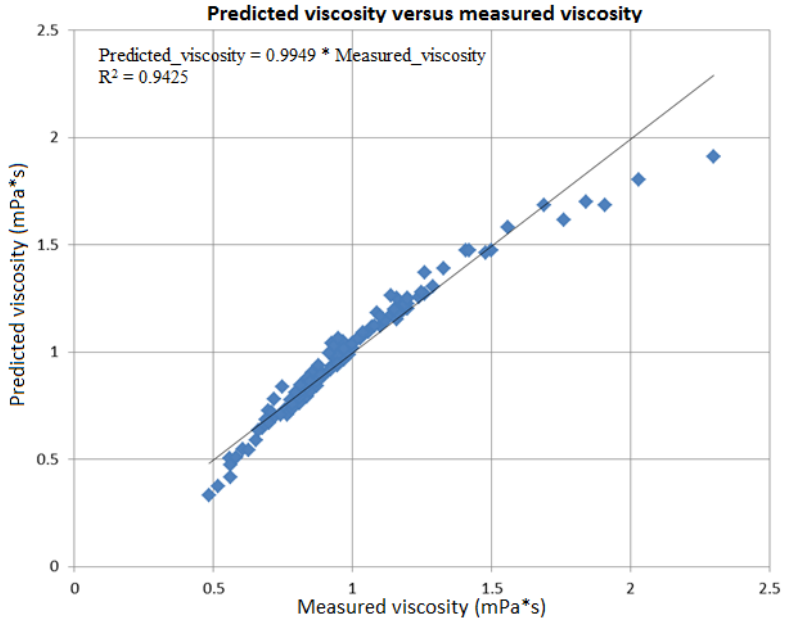

Figure 4.5 Fitting plot of predicted dynamic viscosity versus measured dynamic viscosity

The inner top face of the cell was set to have a wall slip boundary condition,[18] due to the absence of a wall on the cell top.

$$\boldsymbol{v} \cdot \boldsymbol{n} = 0 \tag{4.26}$$

$$\mu(\nabla \boldsymbol{v} + (\nabla \boldsymbol{v})^T)\boldsymbol{n} - (\,\mu(\nabla \boldsymbol{v} + (\nabla \boldsymbol{v})^{\mathrm{T}})\boldsymbol{n} \cdot \boldsymbol{n})\boldsymbol{n} = 0 \tag{4.27}$$

where $\boldsymbol{v}$ is the fluid velocity vector, $\boldsymbol{n}$ is the unit normal vector to the inner top face, and μ is the dynamic viscosity.

The inlet face was set to have the flow rate in the designed boundary conditions (Table 4.2), with the inflow electrolyte having the initial concentrations of cupric ion, sulfate ion, and hydrogen ion.

The outlet conditions were specified by prescribing a pressure on the outlet face without viscous stress:[18]

$$\left(\mu(\nabla \boldsymbol{v} + (\nabla \boldsymbol{v})^{\mathrm{T}}) - \frac{2}{3}\mu(\nabla \cdot \boldsymbol{v})\boldsymbol{I}\right)\boldsymbol{n} = 0 \tag{4.28}$$

$$p = p_{\mathrm{o}} \tag{4.29}$$

where μ is the dynamic viscosity, $\boldsymbol{v}$ is the fluid velocity vector, $\boldsymbol{I}$ is the identity tensor, $\boldsymbol{n}$ is the unit normal vector to the outlet face, and p_{o} is the pressure at the outlet.

All other faces were set to have a no slip wall boundary condition:[18]

$$\boldsymbol{v} = 0 \tag{4.30}$$

where $\boldsymbol{v}$ is the fluid velocity vector.

The drag force on an impurity particle was set to follow Stokes' law:

$$\boldsymbol{F} = \frac{18\mu m_p}{\rho_p d_p^2}\left(\boldsymbol{v}_f - \boldsymbol{v}_p\right) \tag{4.31}$$

where $\boldsymbol{F}$ is the drag force vector, m_p, ρ_p, d_p, $\boldsymbol{v}_p$ are the mass, density, diameter, velocity vector of the particle, $\boldsymbol{v}_f$ is the velocity vector of the fluid, μ is the dynamic viscosity.[18]

Table 4.2 Boundary conditions used in the simulation

Inlet Flow Rate (ml/min)	Temperature (ºC)	Current Density (A/m^2)
3.5	50	225
11	50	225
11	50	375
11	70	225

The gravity force and the buoyancy force on a particle is expressed as:

$$F_z = -(\rho_p - \rho_f) g V_p \tag{4.32}$$

where F_z is the sum of the two forces in the z direction, ρ_p and V_p are the density and volume of the particle, and ρ_f is the density of the fluid.

The inlet and outlet of particles are the same as the fluid flow. From the inlet plane, 10000 particles were uniformly released at each step from t=0 s to t=18000 s with a step interval of 500 s.

The electrorefining process was simulated under four different boundary condition combinations with varying inlet flow rate, temperature, and current density to understand the effects of inlet flow rate, temperature, and current density on impurity particle behavior in electrolyte. Table 4.2 shows the four different boundary conditions set in the simulations. Table 4.1 shows the main parameters used in the model.

4.2.4 Mesh Setting

The model in this study discretized the domains (including the electrorefining cell and pipes) into tetrahedral mesh elements as shown in Figure 4.6. The maximum element size in the model was 0.0053 m, and the minimum element size was 0.001 m, as shown in Figure 4.7.

There were finer structured layers of elements along all surface boundaries. These layers of finer elements were integrated into the existing tetrahedral mesh elements in the 3D model. There were two boundary layers over each boundary, with the first layer thickness set at 0.00129 m and the second layer thickness to be 0.00155 m. Along surface boundaries of the anode and cathode front side faces (shown in Figure 4.7), there were eight even finer layers of elements, with the first layer thickness to be 0.0001 m and a

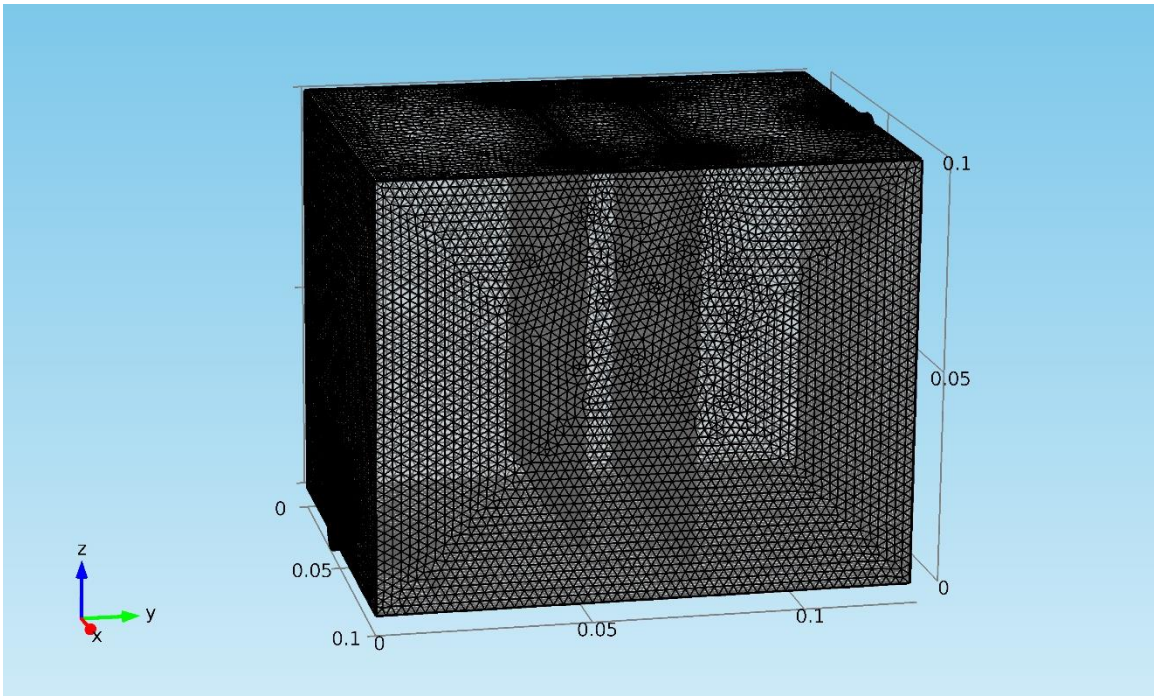

Figure 4.6 Model mesh for the copper electrorefining cell defined in section 4.2.2

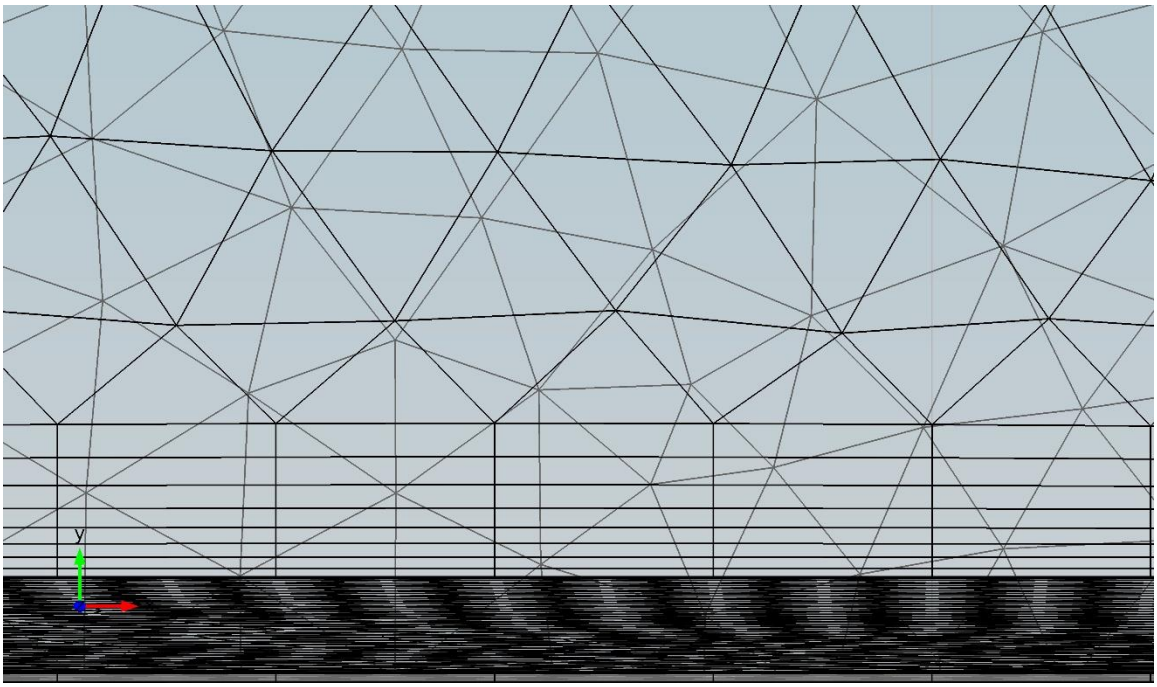

Figure 4.7 Boundary layer meshes at the anode surface boundary in the copper electrorefining cell defined in section 4.2.2

boundary layer stretching factor of 1.2 (the thickness increases by 20% from one layer to the next).

These geometry boundaries are discretized into triangular boundary elements. On all the boundaries in the model, these triangular boundary elements had a maximum element size of 0.0023 m, and a minimum element size of 0.00015 m. The edges and vertices in the geometry are discretized into edge elements and vertex elements respectively.

The current cell meshes are the result of several mesh refinement through the development of the model and the simulation results from the current meshes do not show appreciable difference from those from the last meshes of coarser quality.

4.3 Fluid Flow Simulation Results and Discussion

The electrodeposition, fluid flow, and impurity particle transportation processes were simulated in the model and the following results were obtained in the forms of line plots and three-dimensional plots. The time-dependent simulations of current distribution and fluid flow field from 0 s to 18000 s had results almost at steady state with tiny changes after t = 5000 s. The further stationary simulations of current distribution and fluid flow field gave the steady state solutions for different boundary conditions, which are presented below. The simulations of impurity particle motions in the flowing electrolyte were time dependent from 0 s to 18000 s and the results of particle distributions in front of the cathode at 18000 s for different boundary conditions are presented.

First of all, the copper concentration distribution in the cell and the associated copper concentration profile between the electrodes at steady state under boundary conditions of 11 ml/min, 50 ^{o}C, and 225 A/m^2 are shown in Figure 4.8 as an example, and selected concentration/concentration difference statistics among the four boundary

condition sets are shown in Figure 4.9.

As shown in the plots, the cupric ion concentration levels near anodes are much higher than that near cathodes, which results from the fact that copper is dissolved at the anode and recovered at the cathode. Among four sets of boundary conditions, there are some differences in the resulting copper concentrations. The general difference between the copper concentration near the anode and copper concentration near the cathode is highest under the condition of 11 ml/min, 50 ºC, and 375 A/m^2, followed by 3.5 ml/min, 50 ºC, and 225 A/m^2; 11 ml/min, 50 ºC, and 225 A/m^2; and 11 ml/min, 70 ºC, and 225 A/m^2.

During the electrorefining process, cupric ions are liberated from the anode and recovered along the cathode, but the diffusion rate is not high enough to transport cupric ions away from the anode diffusion layer and into the cathode diffusion layer. As a result, the cupric ions will be accumulated near the anode and depleted near the cathode, leading to the concentration differences between the electrodes. It is apparent that the higher the current density, the larger the concentration differences. When the inlet flow rate is raised from 3.5ml/min to 11ml/min, the convection between the electrodes is larger, resulting in smaller concentration differences. When the temperature is increased to 70 ºC, the diffusivity coefficient is larger according to eq. (4.21), resulting in a higher diffusion rate and smaller concentration differences between the electrodes.

The fluid density profile in the cell is directly determined by the cupric ion concentration distribution, and the density distribution on a slice 100 microns away from the front surface of the cathode is shown, which is important in this study. The density profiles in front of the cathode can significantly influence the fluid flow near the cathode front surface, which then affects the motion of impurity particles. Figure 4.10 shows

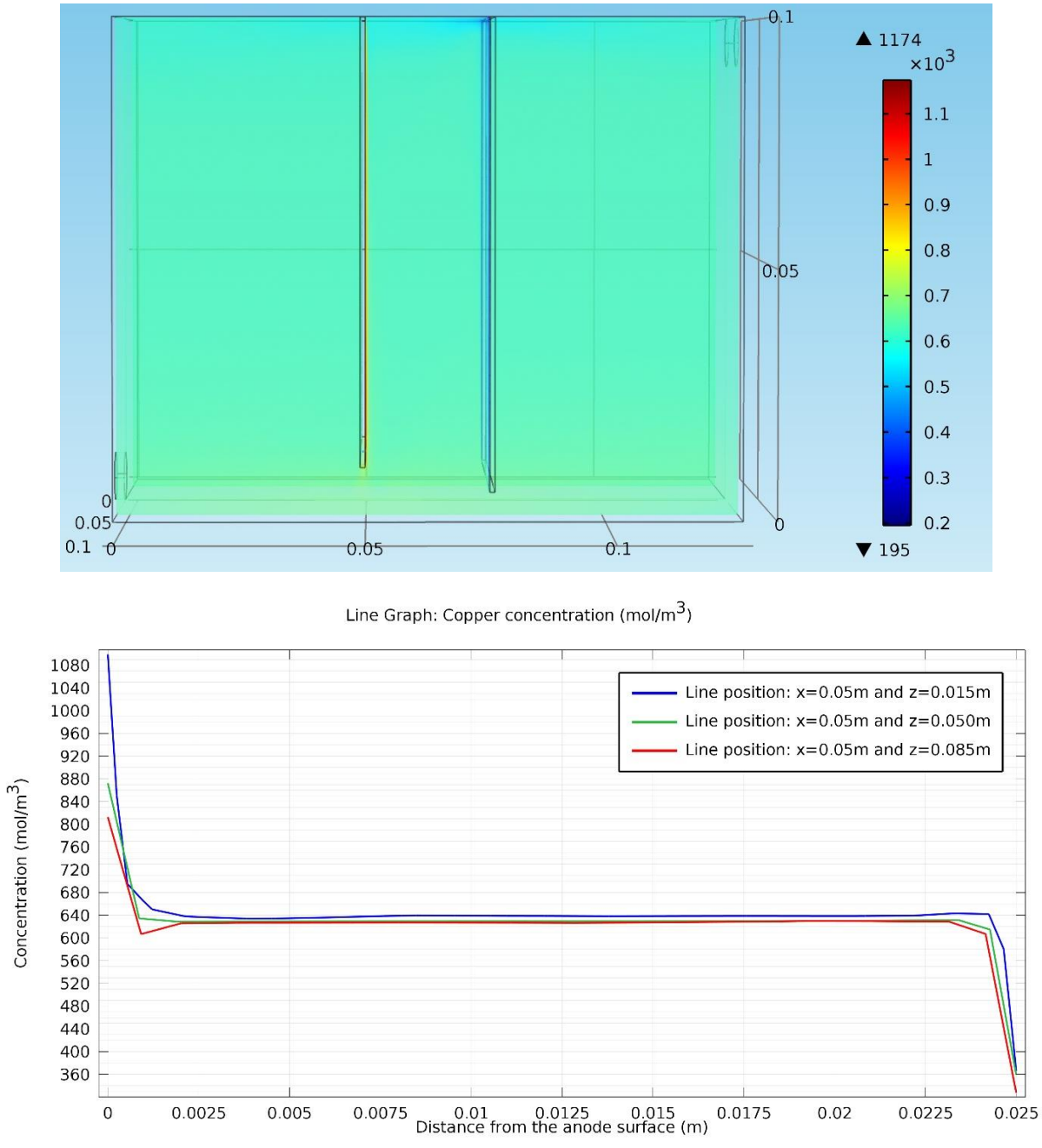

Figure 4.8 Cu^{2+} concentration profile at steady state under conditions of 11 ml/min, 50 ºC, and 225 A/m^2, in the copper electrorefining cell defined in section 4.2.2 (the color expresses the magnitude of localized Cu^{2+} concentration) and the associated copper concentration profile between the anode (the left side) and the cathode (the right side)

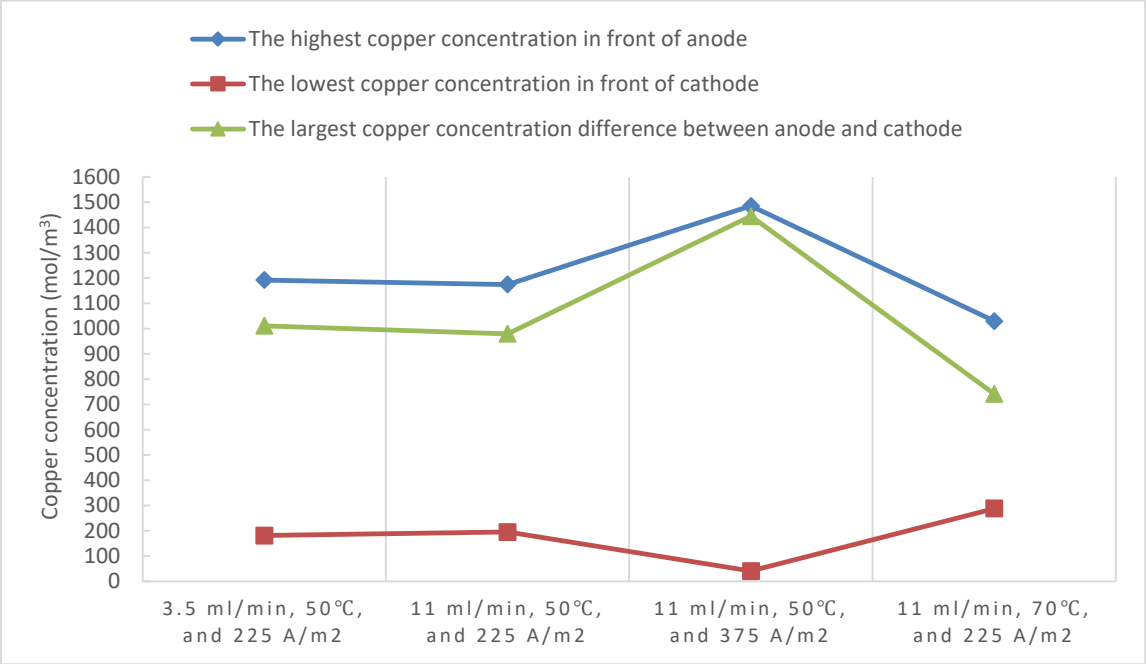

Figure 4.9 Selected copper concentration/concentration difference statistics at steady state under four sets of boundary conditions, in the copper electrorefining cell defined in section 4.2.2

representative fluid density results at steady state and the associated quantified fluid density profile between the left and right edges of the cathode at the top and bottom of the slice for the boundary condition of 11 ml/min, 50 ºC, and 225 A/m^2. Figure 4.11 shows the selected electrolyte density/density gradient statistics among different boundary conditions.

Notice that there are gaps between the cathode and the cell walls on the left, right, and bottom parts of the slices. Note that there are two rectangles with black borders, with the smaller one representing the anode and the larger one representing the cathode. Furthermore, there are major density gradients between the anode and the cathode (not shown in the graphs), which are obvious and can be deduced from the concentration profiles in the cell. It is the density gradients between the electrodes that drive the loop-shaped convection (Figure 4.12). The density profiles above show that there are density gradients along the z direction in front of the cathode. It is important to point out that the density gradients in front of the fringes of the cathode are larger than those in front of the middle part of the cathode under all four sets of boundary conditions. The same case applies for the anode (not shown in the graphs), except the density gradients are in the opposite directions. This means that the looping flow between the electrodes driven by density gradients is very likely to be faster through the two sides than through the middle part of the electrodes.

The density distributions are slightly different among four different sets of boundary conditions. As discussed before, higher inlet flow rate will intensify convection between the electrodes and therefore help abate the concentration differences, resulting in smaller density gradients. This is why the electrolyte density gradients under conditions of 11 ml/min, 50 ºC, and 225 A/m^2 are smaller than those under conditions of 3.5 ml/min, 50

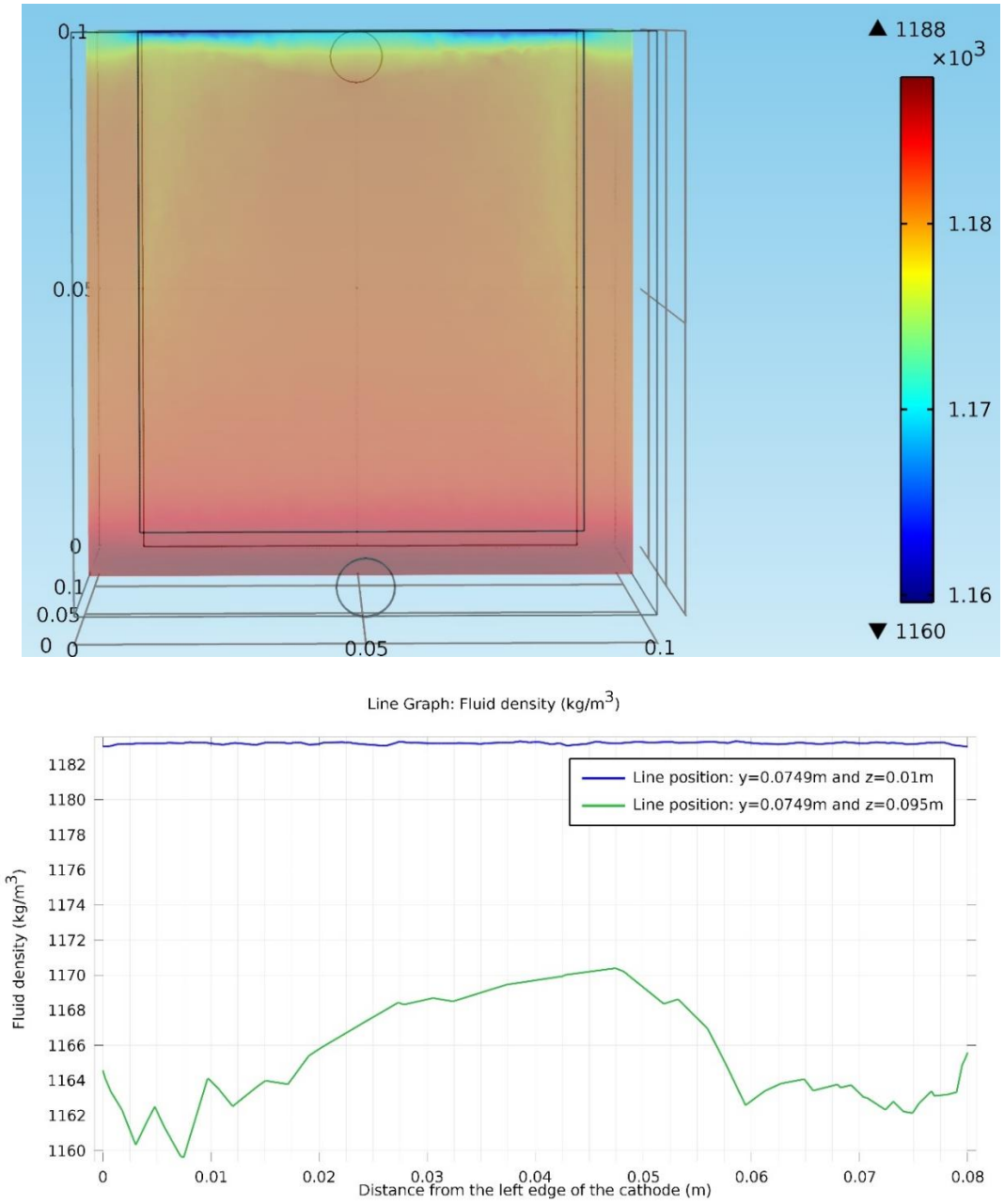

Figure 4.10 Fluid density distribution on a slice 100 microns away from the front surface of the cathode at steady state under conditions of 11 ml/min, 50 ºC, and 225 A/m^2, in the copper electrorefining cell defined in section 4.2.2 (the color expresses the magnitude of localized electrolyte density) and the associated quantified fluid density profile between the left and right edges of the cathode at the top and bottom of the slice

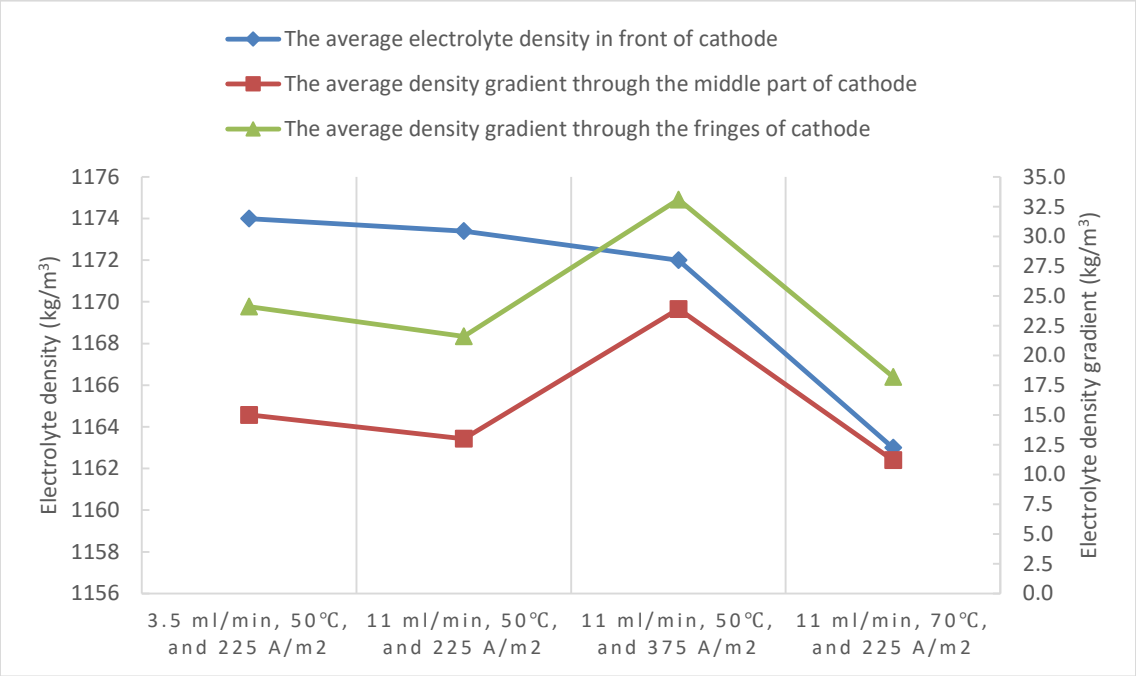

Figure 4.11 Selected electrolyte density/density gradient statistics at steady state under four sets of boundary conditions, in the copper electrorefining cell defined in section 4.2.2 (the average electrolyte densities in front of cathode are plotted using the left Y-axis and the average density gradients through the middle part and the fringes of the cathode are plotted using the right Y-axis).

ºC, and 225 A/m^2.

When the current density is increased from 225 A/m^2 to 375 A/m^2 as shown in Figure 4.11, it is obvious that density gradients in front of the cathode should increase due to the intensified accumulation of cupric ions in the diffusion layer in front of the anode and the depletion of cupric ions in front of the cathode.

When the temperature is increased from 50 ºC to 70 ºC as shown in Figure 4.11, the electrolyte densities decrease as the temperature goes up. Moreover, the diffusivity coefficient for each ion, especially the cupric ion, is significantly increased, according to eq. (4.21). Consequently, the diffusion rate is much higher, and it results in removing more accumulated cupric ions in front of the anode and replenishing more cupric ions to the diffusion layer in front of the cathode, which makes the density distribution of the depletion region more uniform. As a result, the density gradients are smaller at higher temperature as shown in Figure 4.11.

The fluid velocity field in the cell is driven by both the inlet inflow and the density gradients between the electrodes. Figure 4.12 shows a representative plot of fluid velocity field at steady state in the entire cell and the associated z component of fluid velocity profile between the electrodes for the boundary condition of 11 ml/min, 50 ºC, and 225 A/m^2. Figure 4.13 presents the selected fluid flow velocity magnitude statistics among different boundary condition sets.

As shown in Figure 4.12, the fluid comes from the inlet, goes into the cell with a set velocity, and then encounters the anode. Part of the fluid goes up along the left side of the anode and forms loops in the left part of the cell. Another part of the fluid flows through the gaps between the side edges of the electrodes and the cell walls, and enters into

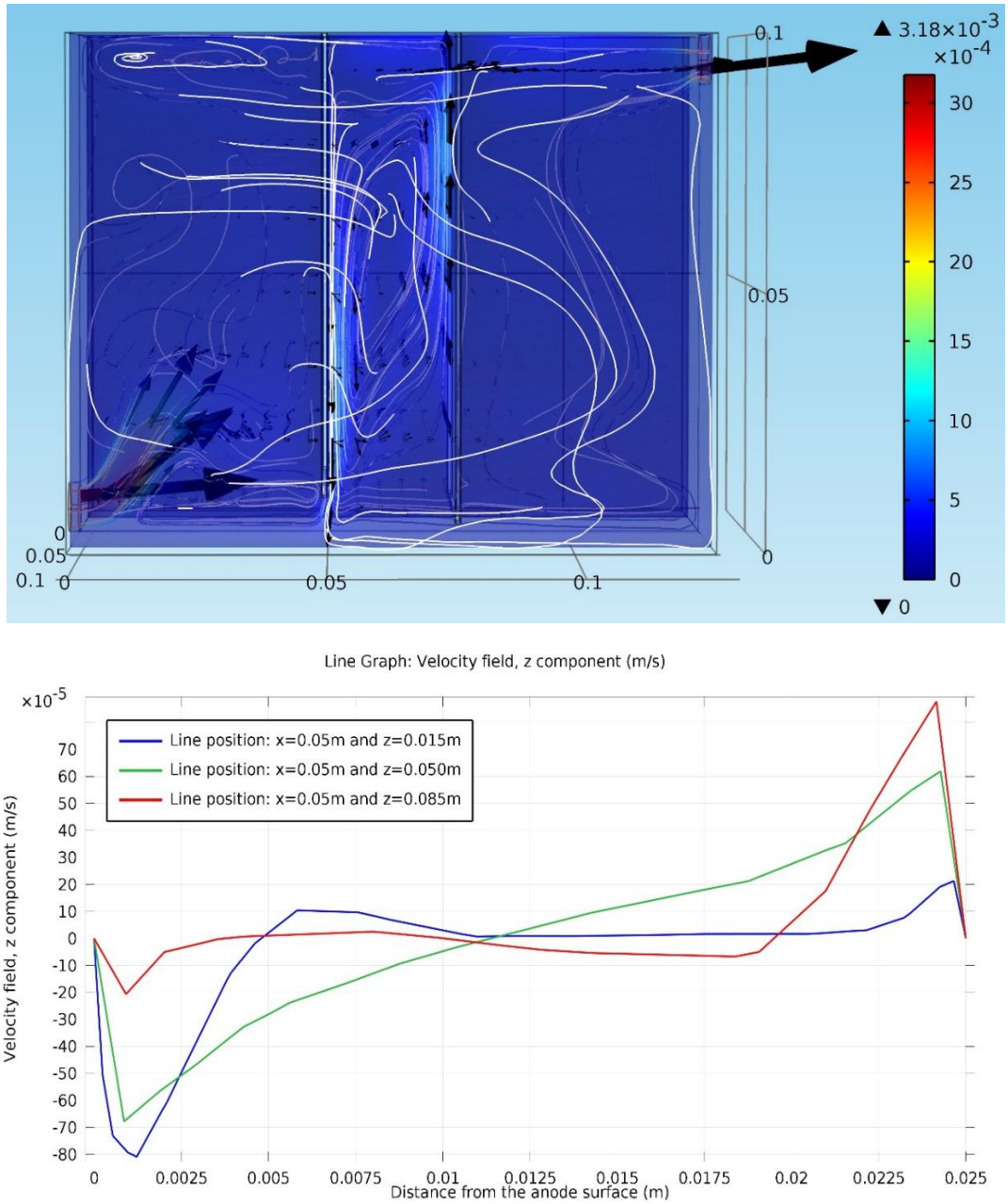

Figure 4.12 Fluid flow velocity field at steady state under conditions of 11 ml/min, 50 ºC, and 225 A/m^2, in the copper electrorefining cell defined in section 4.2.2 (the color expresses the magnitude of fluid velocity, the black arrows represent velocity vectors, and the white lines are streamlines) and the associated z component of fluid velocity profile between the anode (the left side) and the cathode (the right side)

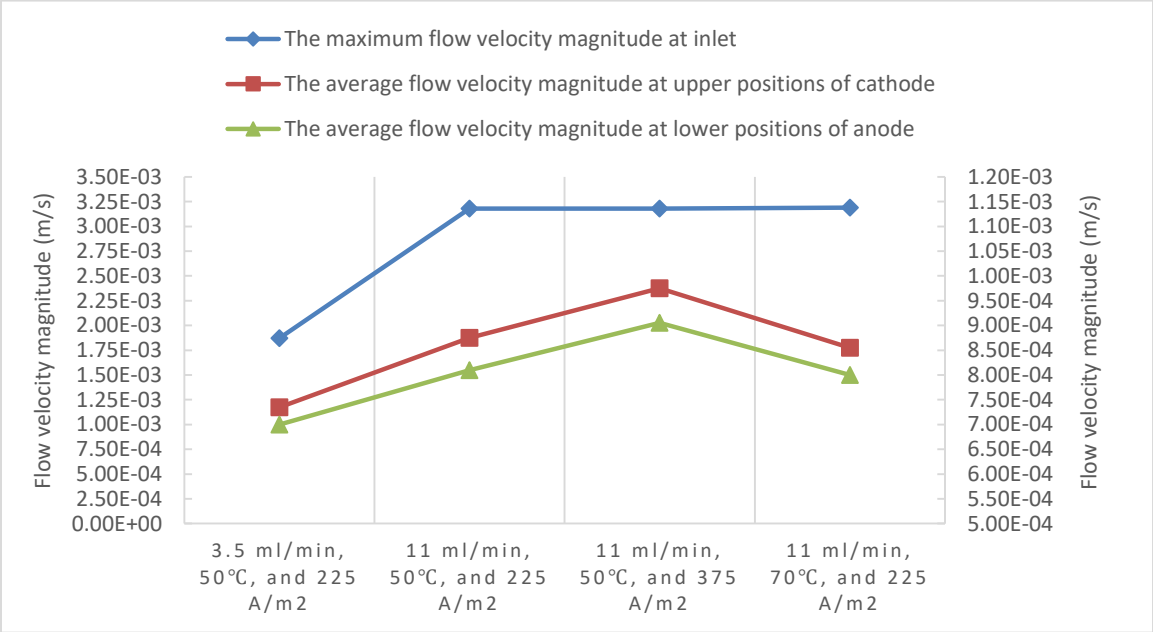

Figure 4.13 Selected flow velocity magnitude statistics at steady state under four sets of boundary conditions, in the copper electrorefining cell defined in section 4.2.2 (the inlet maximum flow velocity magnitudes are plotted using the left Y-axis and the average flow velocity magnitudes at upper positions of cathode and lower positions of anode are plotted using the right Y-axis).

the right part of the cell. The rest of the fluid enters the domain between the electrodes from the bottom and side gaps between the edges of the anode and the cell walls. The electrolyte in between the electrodes flows along loop-shaped paths influenced by both the density gradients and the inlet inflow. Then some of it exits the loops at the bottom and enters the right part of the cell. Finally, the fluid flows out of the cell through the outlet by pressure. This is the general fluid velocity pattern observed in all boundary condition sets. However, as conditions vary, the fluid flow velocity field changes accordingly.

Several observations can be made from the Figures 4.12 – 4.13. Firstly, the electrolyte comes with larger velocities through the inlet, when the inlet flow rate is increased from 3.5 ml/min to 11 ml/min. Secondly, velocity magnitudes of the flow field between the electrodes (the looping flow) are affected by both the density gradients between the plates and the inlet flow rate. At the low flow rate condition (3.5 ml/min), the flow velocities are comparatively small. While at the high flow rate condition (11 ml/min), the fluid flow in the cell is intensified and the flow between the electrodes is more influenced by the incoming flow from the bottom and side gaps. According to Figure 4.13, this results in flow with larger velocities between the electrodes, though the density gradients decrease a little. Furthermore, at higher current density condition (375 A/m^2), since the density gradients between the electrodes are larger, the flow field generated has larger velocities. Finally, when the temperature is increased from 50 ºC to 70 ºC, the flow velocities will increase due to lower fluid viscosity, but the density gradient, which turns out to be the dominant factor, becomes smaller, due to significantly increased diffusivity of cupric ion. Therefore, the velocities of the flow field are decreased.

Since the flow velocity field near the cathode is not shown in detail in Figure 4.12,

which is presented mainly to show general flow pattern in the cell, a slice of velocity field 100 microns away from the front surface of the cathode, which determines the motion of impurity particles near the cathode front surface, is shown for the boundary condition set of 11 ml/min, 50 ºC, and 225 A/m^2 as a representative (Figure 4.14), as a complement to Figure 4.12. Figure 4.15 presents the variation of the average z component velocity magnitude in front of cathode among four boundary condition sets.

Similarly to the fluid density distribution figures, in Figure 4.14, there are gaps between the cathode and the cell walls on the left, right, and bottom parts of the slices, where the z components of fluid velocities are relatively small.

It is apparent that most fluid velocity vectors are almost vertical, which means they are nearly along the z direction and have almost no x and y components. Another significant finding is that the z components of fluid velocities are almost all in the positive direction and their magnitudes are larger in front of the fringes of the cathode than in front of the middle part of the cathode. This should result from the density gradients difference between the two areas. Furthermore, the z components of fluid velocities become larger gradually along the positive z direction, resulting from the density gradients along that direction.

As shown in Figure 4.15, the z components of fluid velocities are generally the smallest under conditions of 3.5 ml/min, 50 ºC, and 225 A/m^2, and are higher when the inlet flow rate is increased to 11 ml/min, due to the intensification of the flow. When the current density is raised from 225 A/m^2 to 375 A/m^2, they are increased, due to the larger density gradients. When the temperature is increased from 50 ºC to 70 ºC, they are decreased, because of the smaller density gradients due to significantly increased

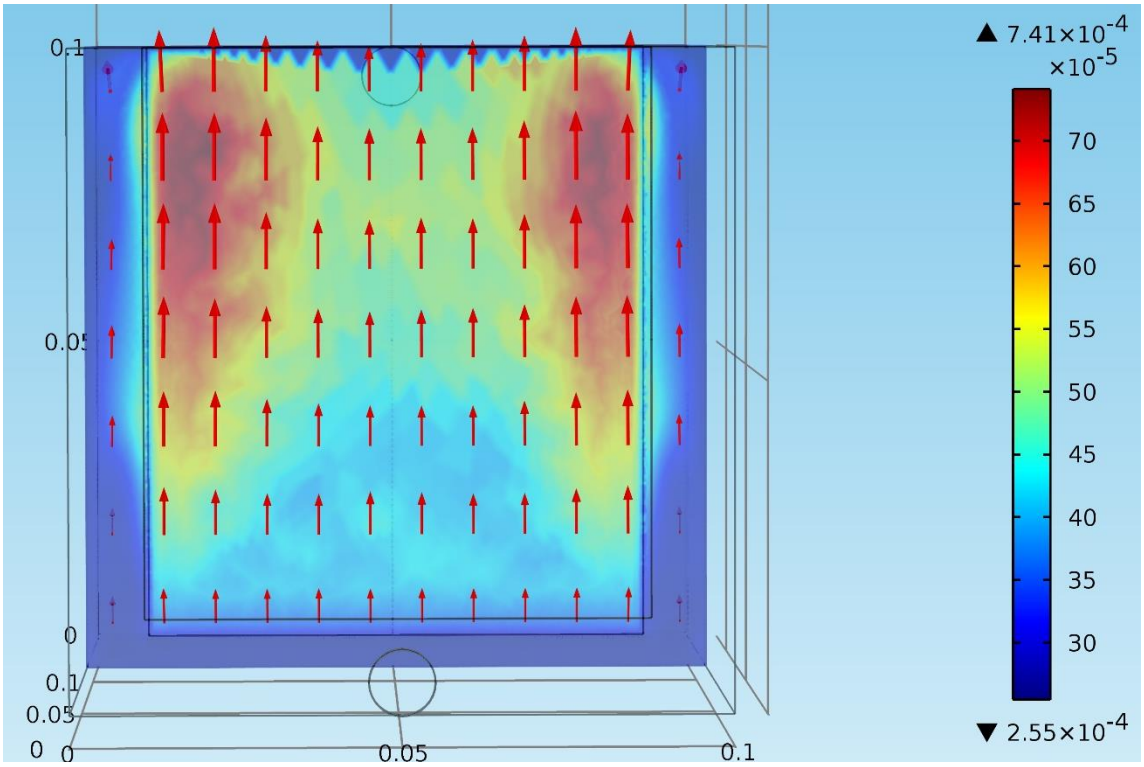

Figure 4.14 The fluid velocity field on a slice 100 microns away from the front surface of the cathode at steady state under conditions of 11 ml/min, 50 ºC, and 225 A/m^2, in the copper electrorefining cell defined in section 4.2.2 (the arrows represent velocity vectors and the color expresses the magnitude of the z component of fluid velocity).

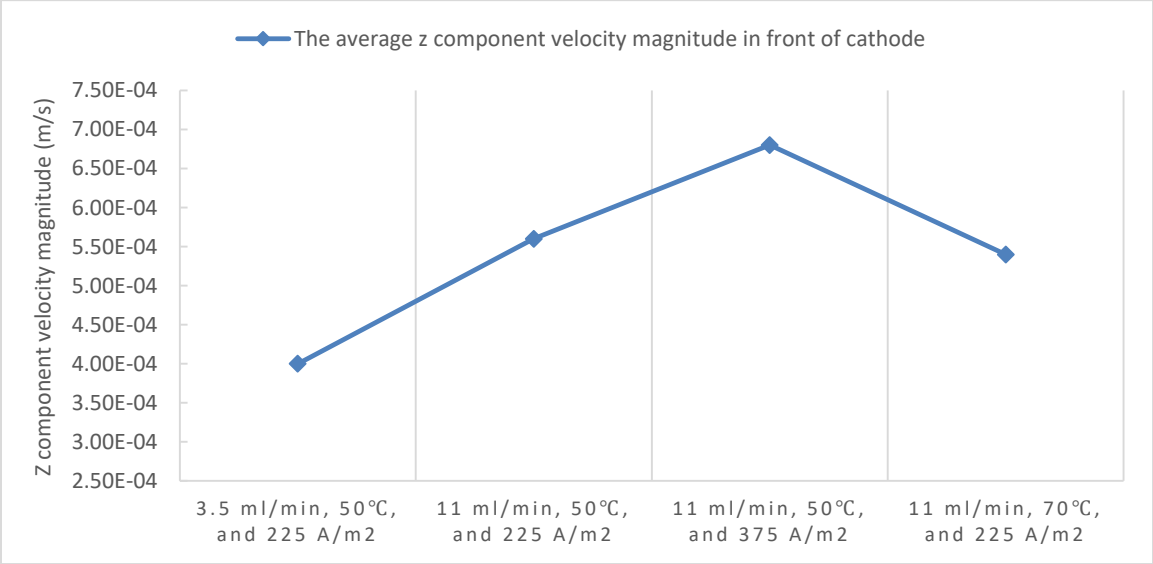

Figure 4.15 The average z component velocity magnitude in front of cathode at steady state under four sets of boundary conditions, in the copper electrorefining cell defined in section 4.2.2

diffusivity of cupric ion, despite lower viscosities.

4.4 Tracer Particle Movement Simulation Results and Discussion

The motion of impurity particles in front of the cathode needs to be discussed. In order to understand this, how the particles are transported to the cathode needs to be understood. Figure 4.16 shows the general motion of the particles in the cell from four moments in the electrorefining simulation process. Notice that the particles were injected from the inlet every 500 seconds. As a result, Figure 4.16(a) shows only the position distribution of the first group of particles injected at t = 0 s; Figure 4.16(b) shows the position distributions of two groups of particles (one injected at t = 0 s and the other one injected at t = 500 s); Figure 4.16(c) shows three superimposed groups of particles, injected at t = 0 s, t = 500 s, and t = 1000 s, respectively; and four superimposed groups of impurity particles injected at t = 0 s, t = 500 s, t = 1000 s, and t = 1500 s, respectively, are shown in Figure 4.16(d). Due to the relatively large time interval between injection bursts, each group of particles can be distinguished clearly in the plots. Note that the motions of each group of particles in the cell are almost identical and the position distribution of one group of particles virtually represents the position distribution of the previous group of particles at the time point 500 seconds ago. Thus, the position distributions of four groups of particles in Figure 4.16(d) can be considered as the particle trajectories of the first group of particles injected at t = 0 s.

The motion of these particles is determined by Newton’s second law and is driven by both drag force based on Stokes’ law and the gravity force. Therefore, the electrolyte flow velocity field exerts great effect on their motion. As a result, after the particles enter the cell from the inlet, some of the particles move along similar loops in the left part of the

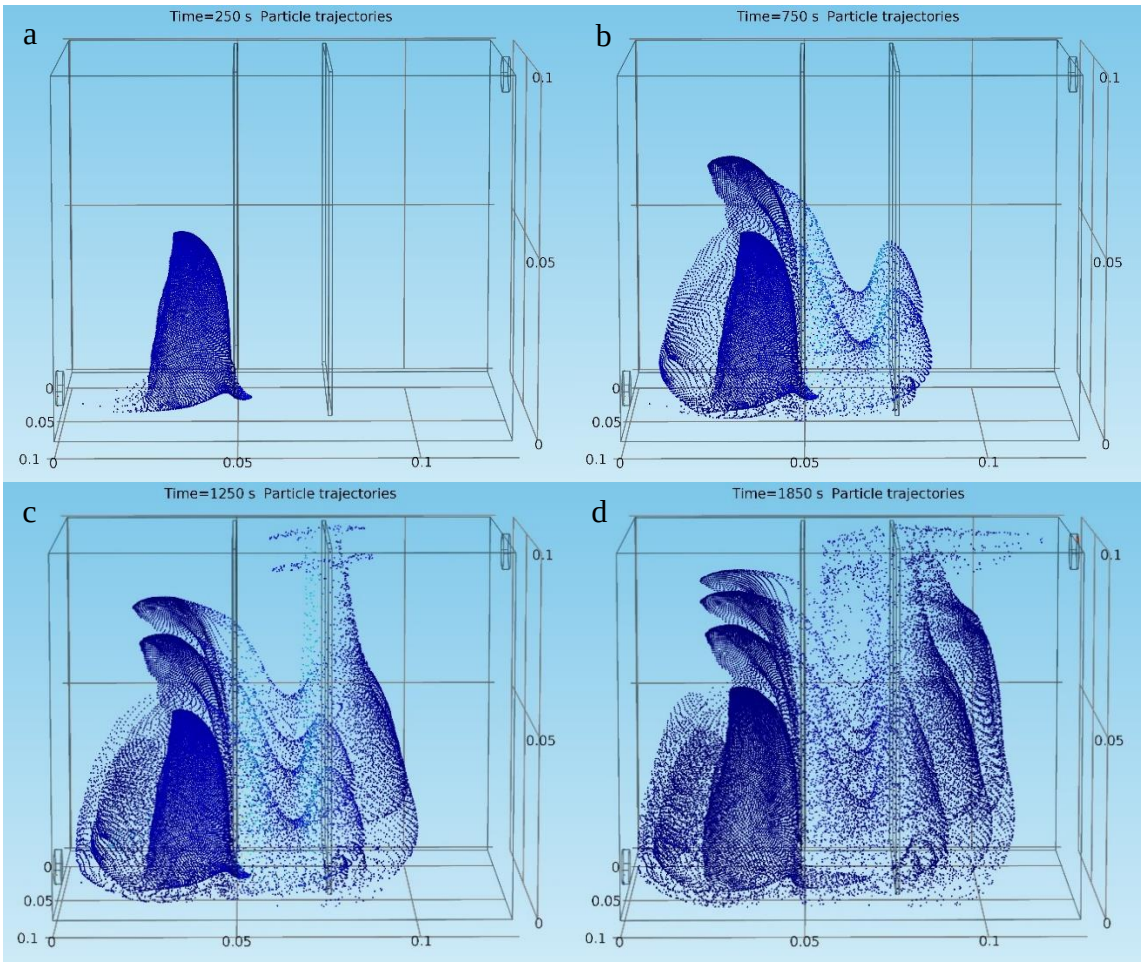

Figure 4.16 Instantaneous particle (uniform size of 14.5 μm) position distributions at (a) t = 250 s, (b) t = 750 s, (c) t = 1250 s, and (d) t = 1850 s, under conditions of 11 ml/min, 50 ^{o}C, and 225 A/m^2, in the copper electrorefining cell defined in section 4.2.2

cell as the fluid flow. Some of them flow into the domain between the electrodes and approach the cathode through the gaps between the side edges of the anode and the cell walls, while another part of them flows over the domain and enter into the right part of the cell through the gaps between the side edges of the cathode and the cell walls. The rest of the particles go into this middle domain and come close to the cathode through the gap between the bottom edge of the anode and the cell bottom wall. As some of these particles approach the cathode, some of them will settle down and others of them will go up along the cathode surface and suspend in the electrolyte. Particles suspended in the middle domain would move along loops between the electrodes. Some of these particles exit the loops at the bottom of the domain and enter into the right part of the cell, eventually leaving the cell through the outlet. Whether a particle in a position close to the cathode will suspend or settle down depends on the superposition of the settling velocity of the particle and the z component of the localized flow velocity. Since the concentration of the particles is extremely low compared to other species, we can assume that the motion of each particle is not influenced by other particles. Thus, for dilute suspensions and laminar flow, Stokes' law predicts the settling velocity of small spheres in fluid, which was discussed in Chapter 3, and Table 3.3 shows the settling velocity results at high and low temperatures.

The z components of fluid velocities in positions close to the cathode for four sets of boundary conditions were computed through the model and are shown in Figures 4.14 – 4.15. Then the net z direction velocities of the impurity particles at steady state on a slice 100 microns away from the front surface of the cathode can be computed, which are shown in Figure 4.17 for the boundary condition of 11 ml/min, 50 ºC, and 225 A/m^2 as a representative. Particles with positive net z direction velocities tend to suspend in the

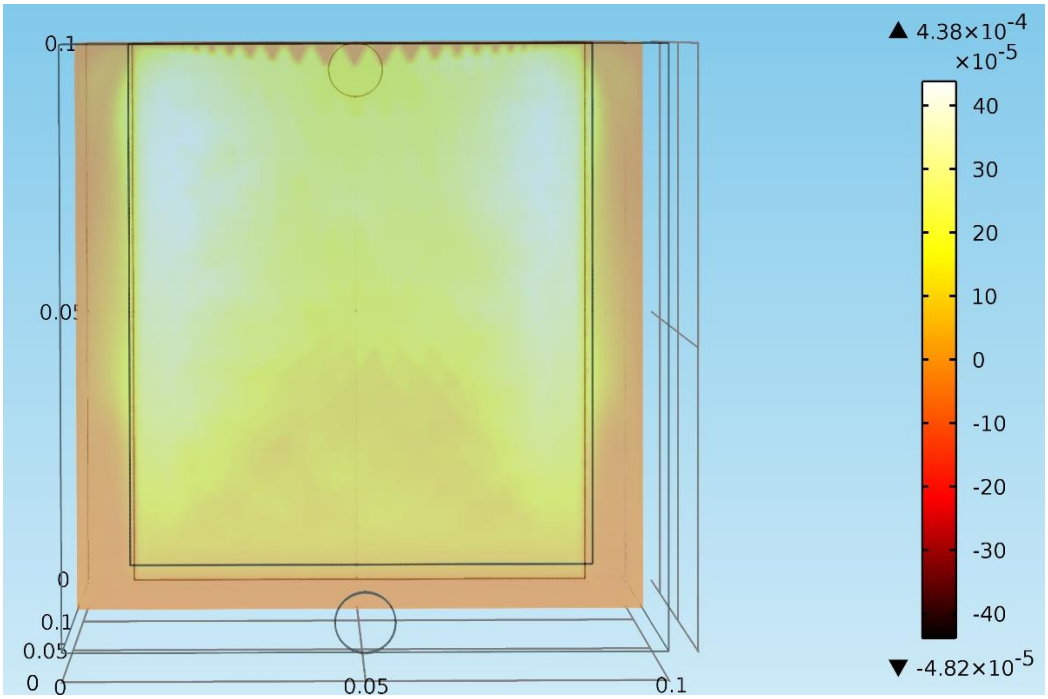

Figure 4.17 The net z direction velocities of impurity particles at steady state on a slice 100 microns away from the front surface of the cathode under conditions of 11 ml/min, 50 ºC, and 225 A/m^2, in the copper electrorefining cell defined in section 4.2.2

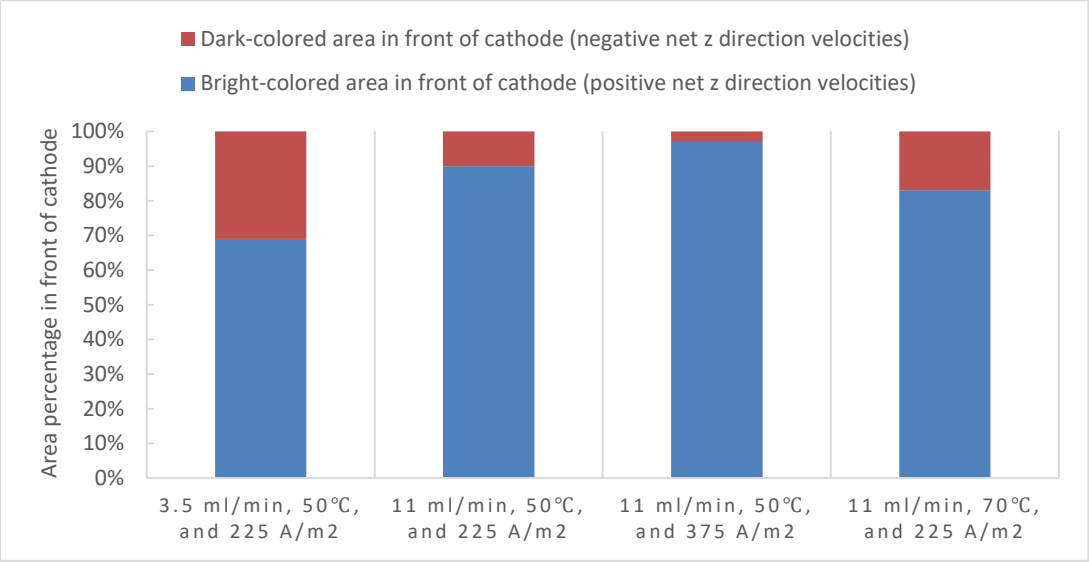

Figure 4.18 Percentages of dark-colored and bright-colored areas in front of cathode at steady state under four sets of boundary conditions, in the copper electrorefining cell defined in section 4.2.2

electrolytic solution, while particles with negative net z direction velocities have the tendency to settle down to the bottom of the cell.

Similarly to previous figures, there are gaps between the cathode and the cell walls on the left, right, and bottom parts of the slices, where the net z direction velocities of impurity particles are not pertinent to the electrode surface contamination.

Because of the symmetric color range setting in the figures, it is clear that a dark-colored area representing negative net z direction velocities is in front of the lower middle area of the cathode. While in front of the fringes of the cathode, there is a bright-colored area representing positive net z direction velocities. The brighter the color, the larger the net z direction velocities of impurity particles; the darker the color, the smaller the net z direction velocities. Figure 4.18 presents the percentages of bright-colored and dark-colored areas under each set of boundary conditions. When the inlet flow rate is raised from 3.5 ml/min to 11 ml/min, the dark-colored area shrinks and the bright-colored area expands from the fringes to the middle. Also, when the current density is increased from 225 A/m^2 to 375 A/m^2, the net z direction velocities on the slice increase. When the temperature is raised from 50 ºC to 70 ºC, the dark-colored area expands from the lower middle area to the fringes and the net z direction velocities on the slice decrease.

Generally, larger particles with higher settling velocities tend to settle to the bottom of the cell and are less likely to be co-deposited, while smaller particles with lower settling velocities can remain in suspension, providing them with more opportunities to be incorporated into the cathodic deposit. In this simulation, although the particle size is fixed, temperature has significant effect on the settling velocities of the particles and thus affects the net z direction velocities of the particles. Besides, inlet flow rate, current density, and

temperature together influence the fluid velocity field in front of the cathode, and therefore play key roles in determining the net z direction velocities of the particles.

When impurity particles get close to the cathode, those with positive net z direction velocities have the tendency to go up and remain in suspension, while those with negative net z direction velocities tend to fall down and settle to the bottom of the cell. Consequently, at the condition of 3.5 ml/min, 50 ºC, and 225 A/m^2, the number of particles suspended would be the smallest and should be correlated with the highest cathode purity. At the condition of 11 ml/min, 50 ºC, and 375 A/m^2, the number of particles remaining in suspension would be the largest and should be correlated with the most contaminated cathode, followed by the condition of 11 ml/min, 50 ºC, and 225 A/m^2, and then the condition of 11 ml/min, 70 ºC, and 225 A/m^2.

At last, the impurity particle distribution maps on a slice with the identical area as the cathode, 100 microns away from the front surface of the cathode at t =18000 s, are shown for four sets of boundary conditions in Figure 4.19. The number of impurity particles was counted from the simulation results by COMSOL for the four corner positions and the center position, which are shown in Table 4.3.

The calculated impurity densities are in accordance with the trends observed in the results of the net z direction velocities of impurity particles at steady state shown in Figures 4.17 – 4.18. The total number of particles on the map is the smallest at the condition of 3.5 ml/min, 50 ºC, and 225 A/m^2, and is the largest at the condition of 11 ml/min, 50 ºC, and 375 A/m^2. The total number of particles at the condition of 11 ml/min, 50 ºC, and 225 A/m^2 is the second largest, corresponding to the second largest bright-colored area shown in Figure 4.18. Similarly, since the bright-colored area under

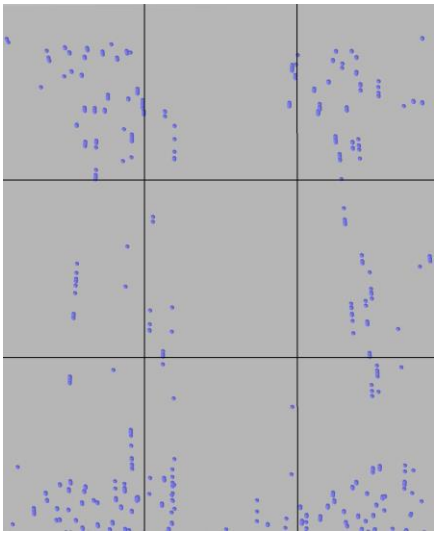

(a) 3.5 ml/min, 50° C, 225 A/m^2

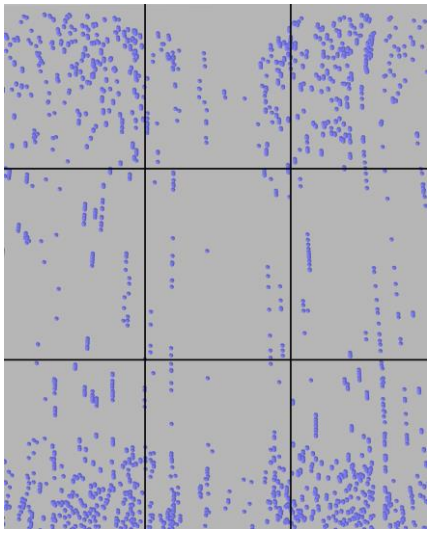

(b) 11ml/min, 50° C, 225 A/m^2

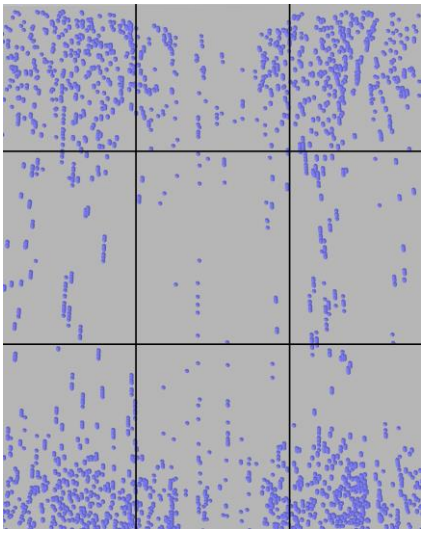

(c) 11 ml/min, 50° C, 375 A/m^2

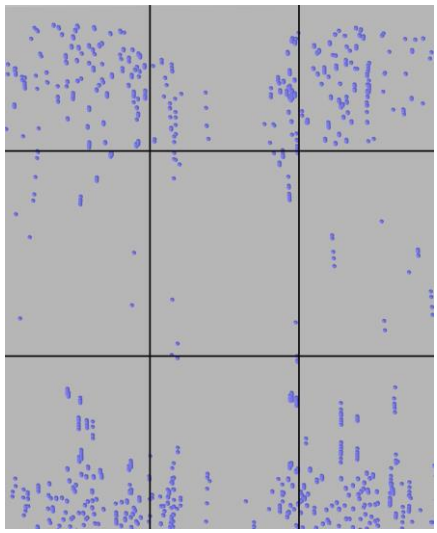

(d) 11 ml/min, 70° C, 225 A/m^2

Figure 4.19 Impurity particle distribution maps on a slice 100 microns away from the front surface of the cathode at t = 18000 s, divided into 9 sections

Table 4.3 Impurity particle counts at certain sections for each set of conditions

Section	Left top corner	Right top corner	Center	Left bottom corner	Right bottom corner
3.5 ml/min, 50 ºC, 225 A/m^2	39	31	9	43	50
11ml/min, 50 ºC, 225 A/m^2	273	278	48	291	302
11 ml/min, 50 ºC, 375 A/m^2	446	423	51	486	494
11 ml/min, 70 ºC, 225 A/m^2	156	145	21	160	166

conditions of 11 ml/min, 70 ºC, and 225 A/m^2 is the third largest, the total number of impurity particles under this set of conditions is also the third largest. Another reason why there are more particles under the condition of high inlet flow rate than under the condition of low inlet flow rate is that larger inlet flow can transport more particles to the bottom of the domain between the electrodes and therefore increase the number of suspended particles there. These particles can then be picked up by the recirculation between the plates.

It is noteworthy that the number of particles at the center section is much smaller than that at corner sections. This is partly because of the smaller net z direction velocities of particles at the center section and larger net z direction velocities at corners, according to Figure 4.17. More importantly, the number of impurity particles on a position also depends on whether or not there is a high velocity pathway to that particular position. In an approximate way, from Figure 4.14 and Figure 4.17, it can be deduced that there are high velocity upward pathways to corner positions and low velocity upward pathways to center positions. The relatively smaller number of particles in the edge-middle sections results from higher particle velocities and therefore shorter particle residence time in these two sections. In fact, the particle distribution maps are essentially cross-sections from the particle trajectories. At some positions in the maps, there are particles in lines, which show the effects of upward flow that drives particles moving upward in lines.

Figure 4.20 shows high/low velocity pathways in a more accurate way by directly showing particles' z components of velocities and the z direction positions (distance from bottom of the cell). More particles move into the interelectrode domain through the gaps between the side edges of the anode and the cell walls than through the gap between the bottom edge of the anode and the cell bottom wall as seen in the graphs.

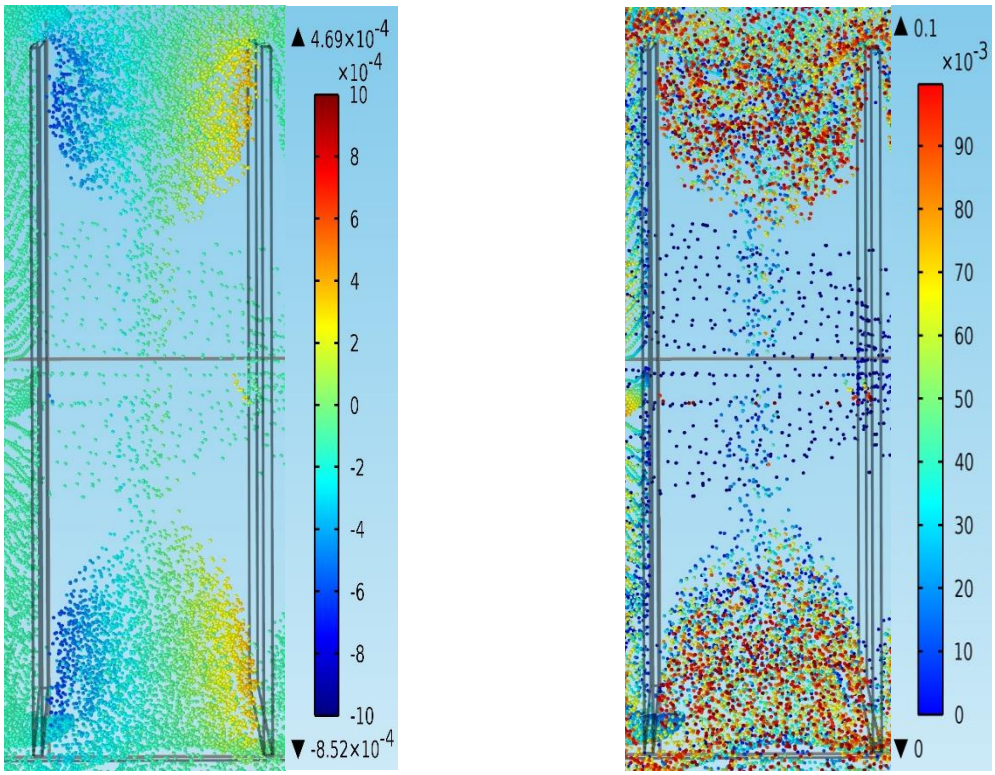

(a) The z components of particles velocities (m/s) (b) The z direction positions of particles (m)

Figure 4.20 Velocities and positions of impurity particles between the anode (left cuboid) and the cathode (right cuboid), from a bird's-eye top view, at t=3000 s, under conditions of 11 ml/min, 50 ºC, and 225 A/m2, in the copper electrorefining cell defined in section 4.2.2 (the color expresses the magnitude of the z component of particle velocity for the left graph and expresses the magnitude of the z direction position of particle for the right graph).

Note that this set of figures shows the particle distribution in the interelectrode domain at an early stage (t=3000 s) when particles do not have enough time to flow into the middle part of the domain. As shown in the graphs, there are more particles moving along the loops in the two side parts of the domain between the electrodes than in the middle part of the domain. Most of the impurity particles moving in the middle part of the domain have settled to the bottom of the cell, and only a small portion of these particles still flow along the loops between the electrodes. As seen in Figure 4.20(a), in the two side parts of the domain, most particles are moving upward (yellow and orange color) along the cathode, then flowing horizontally (green color) from the cathode to the anode, then moving downward (blue color) along the anode, finally flowing horizontally (green color) back to the cathode. Nevertheless, for particles in the middle part of the domain, most of them are green/yellow, indicating that they do not move in loops. From Figure 4.20(b), it is apparent that most of the particles in the middle part of the domain are resting on the bottom of the cell (dark blue color), with only a small portion of them still flowing between the electrodes above the bottom cell wall. This shows that most particles in the middle part settle to the bottom and only a few of them remain in suspension. On the other hand, for particles in the two side parts of the domain, most of them are suspended above the bottom of the cell and only a small portion of them settle to the bottom. This demonstrates that there are fewer opportunities for particles to deposit on the cathode in the middle part of the domain than in the side parts of the domain at early stages and explains partly why there are more particles distributed at corner sections than at the center section in Figure 4.19. This also demonstrates smaller net z direction velocities of particles in front of the middle part of the cathode and lower velocity upward pathways through the middle part of the cathode.

However, this only analyzes the situation at early stages and the particle distribution in the interelectrode domain at later stages (such as 9000 s, 15000s, 18000 s) also needs to be examined to see if there are still fewer opportunities for particles to deposit at the center than at the corners of the cathode.

As seen in Figure 4.21, more impurity particles flow to the middle part of the domain at later stages. It is important to notice that there are two small vacancies between the particles and the front side surfaces of the electrodes, which indicates that particles at the middle part of the domain flow in loops with a larger distance from the electrodes than particles at the side parts of the domain. The closer to the middle line of the domain, the larger the distance from the electrodes and the fewer opportunities for particles to deposit on the cathode. As a result, it is still difficult for particles to deposit at the center part of the cathode. Similarly, this phenomenon is due to the smaller net z direction velocities of particles in front of the middle part than in front of the edge parts of the cathode and lower velocity upward pathways through the middle part than through the edge parts of the cathode. Consequently, particles in the middle part of the interelectrode domain tend to flow in loops with certain distances away from the cathode so that larger net z direction velocities of particles and higher velocity upward pathways exist. Thus at later stages there are still fewer opportunities for particles to deposit at the center part than at the edge parts of the cathode and this also explains why there are more particles distributed at corner sections than at the center section in Figure 4.19.

When the impurity particles move into the range of 0.0001 m or shorter distance from the cathode, they are more likely to be transported and attached to the cathode surface and become co-deposited with copper as impurities in the final product. No matter what

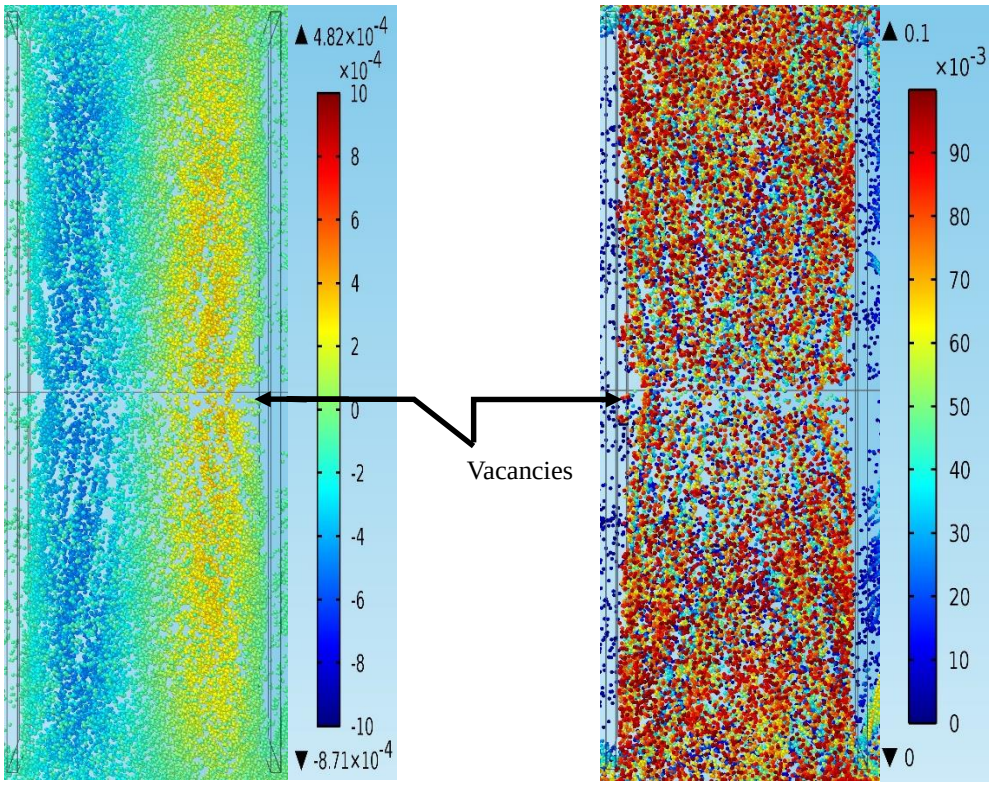

(a) The z components of particles velocities (m/s) (b) The z direction positions of particles (m)

Figure 4.21 Velocities and positions of impurity particles between the anode (left cuboid) and the cathode (right cuboid), from a bird's-eye top view, at t=18000 s, under conditions of 11 ml/min, 50 ºC, and 225 A/m^2, in the copper electrorefining cell defined in section 4.2.2 (the color expresses the magnitude of the z component of particle velocity for the left graph and expresses the magnitude of the z direction position of particle for the right graph)

plays the key role in moving the particles to the cathode, their distribution on the cathode should be very close to that on the slice 100 microns away from the front surface of the cathode, due to this limited distance. Therefore, a basic idea of how impurity particles will be distributed on the cathode, as well as the impurity concentration distribution on the cathode, could be acquired from the impurity particle distribution maps in Figure 4.19.

In order to experimentally validate the simulation results from COMSOL, copper electrorefining experiments were performed twice under each of the four sets of conditions in the simulations.[24] Titanium dioxide particles were added to the electrorefining cell from the inlet at a rate of 500 mg/l TiO_2, to act as impurity particles. The particles have a density of 4200 kg/m^3, with their sizes mostly distributed at 14.5μm, as shown in Figure 4.22. All other parameters of the copper electrorefining experiments were the same as the simulation (Table 4.1). After five hours (18000 s) of electrorefining tests, cathodes were harvested and the surface concentration of titanium dioxide impurity was analyzed at the corners and center of each cathode for comparison with the modeling. Laser-Induced Breakdown Spectroscopy (LIBS) was utilized to analyze the surface impurity concentration.[25, 26] The experimental results, corresponding with the results of the simulation, are shown in Table 4.4.

To validate the simulation results, the impurity particle distribution maps on the slice 100 microns away from the front surface of the cathode were compared and correlated with experimental impurity data as shown in Figure 4.23, based on the data in Table 4.4.

It can be seen that most points are close to the fitting line and thus the simulation results correlate with the experimental results well. Since the simulation results show a very good correlation, the impurity particle distribution maps on the slice in front of the

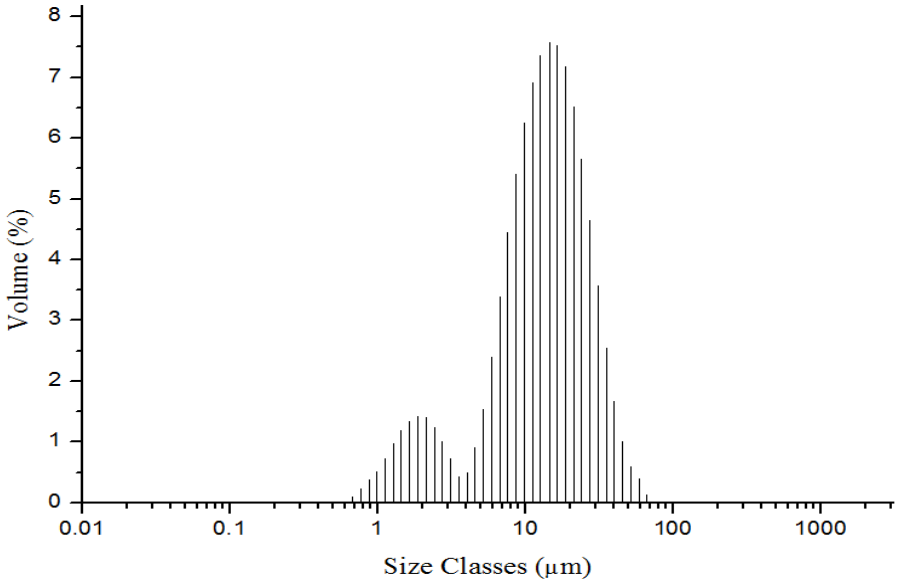

Figure 4.22 Particle size distribution (after 1 minute sonication) of TiO_2 particles used in the copper electrorefining experimental tests (1 minute sonication of the particles was applied because the particles were sonicated before they were added to the electrorefining cell from the inlet)

Table 4.4 Experimental and simulation results for each set of boundary conditions

Condition		Up corners average	Center	Down corners average
3.5 ml/min, 50 ºC, 225 A/m^2	Simulation (counts)	35	9	46.5
	Experiment (wt.%)	1.39%	0.39%	1.71%
11ml/min, 50 ºC, 225 A/m^2	Simulation (counts)	275.5	48	296.5
	Experiment (wt.%)	7.72%	3.73%	8.00%
11 ml/min, 50 ºC, 375 A/m^2	Simulation (counts)	434.5	51	490
	Experiment (wt.%)	13.33%	6.16%	17.85%
11 ml/min, 70 ºC, 225 A/m^2	Simulation (counts)	150.5	21	163
	Experiment (wt.%)	5.69%	1.43%	6.33%

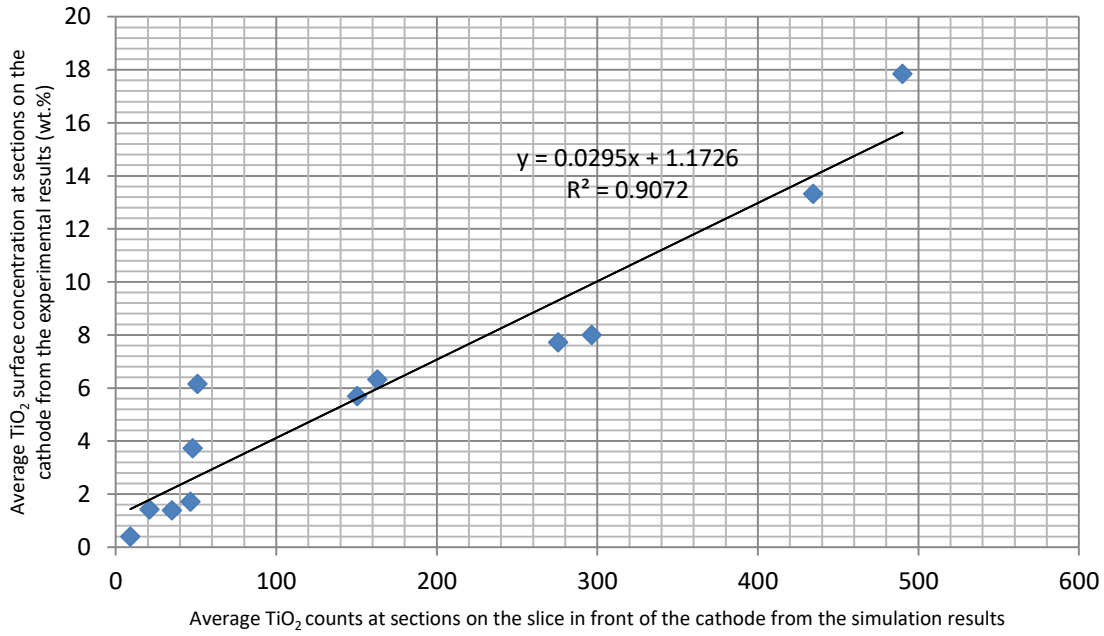

Figure 4.23 Correlation between the simulation results (impurity particle counts) and the experimental results (surface impurity concentration)

cathode can be used to predict the impurity concentration distribution on the cathode in future copper electrorefining experiments with different process parameters by simply changing the boundary conditions in the model. Errors in the simulation may result from incomplete description of the experimental conditions, errors in determining the process parameters in the simulation, and errors in the approximation of the cathode to the slice in front of it, etc.

4.5 Conclusions

According to the COMSOL simulation results, the copper concentration distribution, the electrolyte density distribution, the fluid velocity field, the impurity particle trajectories, and the impurity particle distribution were influenced significantly by boundary conditions of inlet flow rate, temperature and current density. The impurity particle distribution maps on the slice 100 microns away from the front surface of the cathode are validated to a good extent by the experimental data of the titanium dioxide impurity concentration on sections of the cathode. As a result, the simulation results of the particle distribution maps could be utilized to predict the impurity concentration distribution on the cathode obtained in copper electrorefining cell.

The z components of fluid velocities and the settling velocities of impurity particles, which are influenced by inlet flow rate, temperature, and current density, are believed to be the main factors that determine whether or not the particles settle or remain in suspension. Particles with a positive net z direction velocity (upward in the z direction) will suspend in the electrolyte, providing them with more opportunities to be incorporated into the cathodic deposit. Conversely, particles with a negative net z direction velocity (downward in the z direction) will settle and be removed from suspension more rapidly,

and hence be less likely to be co-deposited. In addition, the number of impurity particles at a position is also dependent on whether or not there is a high velocity pathway to that particular position. These have been proven by the correlation of the simulation results of the net z direction velocities of particles, impurity particle distribution maps, and particle trajectories between the electrodes.

From the validated simulation results, process parameters in copper electrorefining can be optimized accordingly. Firstly, the inlet flow rate should be decreased as much as possible, although the minimum flow rate will be limited by the replenishment of additives such as thiourea and glue. If the flow rate is too low, the residence time of electrolyte becomes too long, leading to inadequate replenishment of additives. However, this may be solved by increasing the concentration of additives in the inflow electrolyte. Secondly, the cell temperature should be increased to higher values, though this will be limited by the tankhouse facility ability and high temperatures may raise other problems. Thirdly, the current density should be set as low as possible, though this is limited by the requirement of production. Lastly, cathode blanks should be made with a larger width to height ratio to decrease the effects of more contaminated fringes on the overall purity of copper cathode.

The effects of inlet flow rate, temperature, and current density on the impurity particles behavior in the electrolyte and their distribution on the slice, can be concluded as follows:

1. The inlet flow rate has the most influential effect on the particles behavior and their distribution. It has a positive correlation with the number of particles on the slice. Therefore the inlet flow rate should be set as low as possible, with higher additive

concentrations in the inflow electrolyte.

2. The current density exerts a positive effect on the impurity particle counts on the slice 100 microns away from the front surface of the cathode. Thus it should be decreased to as low as possible with acceptable production rate.
3. There exists a negative correlation between the temperature and the number of particles on the slice, so the temperature should be raised to higher values.
4. The number of impurity particles at corner sections is apparently much larger than that at the center section, regardless of the boundary conditions. Therefore cathode blanks should be made with a larger width to height ratio.

4.6 References

1. M. L. Free: *Hydrometallurgy: Fundamentals and Applications*, John Wiley & Sons, Inc., Hoboken, NJ, 2013.
2. W. G. Davenport, M. King, M. Schlesinger, and A. K. Biswas: *Extractive Metallurgy of Copper*, fourth ed., Pergamon Press, Elmsford, NY, 2002.
3. J. B. C. Kershaw: *Electro-Metallurgy*, Biblio Bazaar LLC, Charleston, SC, 2010.
4. S. Abe, B. W. Burrows, and V. A. Ettel: *Can. Metall. Q.*, 1980, vol. 19, pp. 289-96.
5. X. Ling, Z. H. Gu, and T. Z. Fahidy: *J. Appl. Electrochem.*, 1994, vol. 24, pp. 1109-15.
6. J. Sedzimir and W. Gumowska: *Hydrometallurgy*, 1990, vol. 24, pp. 203-17.
7. G. N. Srinivasan, P. Adaikkalam, P. Radhakrishnamurty, R. Srinivasan, P. Ramachandran, and K. Naganathan: *J. Electrochem. Soc. India*, 1982, vol. 31, pp. 60-63.
8. D. Ziegler and J. Evans: *J. Electrochem. Soc.*, 1986, vol. 133, pp. 559-66.
9. M. J. Leahy and M. P. Schwarz: *16th Australasian Fluid Mechanics Conference*, Gold Coast, Australia, 2007.
10. M. J. Leahy and M. P. Schwarz: *Metall. Mater. Trans. B*, 2011, vol. 42, pp. 875-90.

11. Z. H. Gu, J. Chen, and T. Z. Fahidy: *Hydrometallurgy*, 1995, vol. 37, pp. 149-67.

12. J. A. Sawicki, J. E. Dutrizac, J. Friedl, F. E. Wagner, and T. T. Chen: *Metall. Trans. B*, 1993, vol. 24B, pp. 457-62.

13. T. T. Chen and J. E. Dutrizac: *Can. Metall. Q.*, 1993, vol. 32, pp. 267-79.

14. M. Robinson, Master's Thesis, University of Utah, 2014.

15. M. Tabatabaian: *COMSOL® for Engineers*, Mercury Learning and Information, Dulles, VA, 2014.

16. R. W. Pryor: *Multiphysics Modeling Using COMSOL®: A First Principles Approach*, Jones and Bartlett Publishers LLC, Sudbury, MA, 2011.

17. J. Newman and K. E. Thomas-Alyea: *Electrochemical Systems*, third ed., John Wiley & Sons, Inc., Hoboken, NJ, 2004.

18. *Comsol Multiphysics User's Guide*, version 4.3a, COMSOL, 2012.

19. E. Mattsson and J. O'M. Bockris: *Trans. Faraday Soc.*, 1959, vol. 55, pp. 1586-601.

20. J. D. Anderson, Jr.: *Computational Fluid Dynamics: The Basics with Applications*, McGraw-Hill, Inc., New York City, NY, 1995.

21. M. S. Moats, J. B. Hiskey, and D. W. Collins: *Hydrometallurgy*, 2000, vol. 56, pp. 255-68.

22. D. C. Price and W. G. Davenport: *Metall. Trans. B*, 1980, vol. 11B, pp. 159-63.

23. M. Rhodes: *Introduction to Particle Technology*, second ed., John Wiley & Sons Ltd., West Sussex, England, 2008.

24. W. Zeng, J. Werner, and M. L. Free: *Hydrometallurgy*, 2015, vol. 156, pp. 232-38.

25. D. A. Cremers and L. J. Radziemski: *Handbook of Laser-Induced Breakdown Spectroscopy*, John Wiley & Sons Ltd., West Sussex, England, 2006.

26. N. Reinhard: *Laser-Induced Breakdown Spectroscopy: Fundamentals and Applications*, Springer, Berlin, Germany, 2012.

CHAPTER 5

STUDIES OF SLIME SINTERING/COALESCENCE AND ITS EFFECTS ON ANODE SLIME ADHESION AND CATHODE PURITY

Four series of copper electrorefining tests were performed using four different types of anodes, which have different inclusion types. Test results show that the high impurity anodes and the scrap cycle anodes have more inclusions associated with the Pb-Bi-S compounds that show evidence of sintering at 50 ℃, whereas the low impurity anodes and the strip cycle anodes have more inclusions related with the Pb-Bi-S-As compounds that demonstrate evidence of sintering above 65 ℃. Inclusion (slime) particles sinter and adhere to the anode surface, which happens at lower temperatures for the high impurity anodes. Correspondingly, there are different slime distributions for each type of anode. The anode slimes layers in front of anode surfaces for different types of anodes were observed and analyzed by SEM/EDS. Results show significant effects of particle sintering near anode surfaces, which was also demonstrated by slime size distributions at different cell temperatures. Experimental results demonstrate that slime particle sintering and coalescence can improve anode slime adhesion and reduce the amount of suspended slimes, which are a major source of copper cathode contamination. Arsenic content in copper anode and cell temperature are major factors affecting slime sintering and coalescence.

5.1 Introduction

In the process of copper electrorefining, the secondary phases within copper anodes consist of various impurities, which will be liberated at the surface of the anode as the copper matrix dissolves. Some solid solution impurities are solubilized into the electrolyte, but many impurities found in refractory inclusions do not dissolve. As the metal around insoluble inclusions is removed, the inclusions become individual particles. These inclusion-based particles, which are known as slime particles, can form a porous layer that adheres to the anode or they can be released into the electrolyte.

Anode slime particles can fall from the anode surface if the slime adhesion to the surface is not strong enough. Falling slime particles can lead to serious contamination problems on the cathode and thereby lower the quality of the final copper product. It should be noted that large slime particles will settle down to the bottom of the cell if their settling velocities are larger than the upward fluid velocity. On the other hand, small slimes typically tend to suspend in the electrolytic solution due to their comparatively small settling velocities. As a result, these small slimes, which are circulated in the electrochemical cell and transported to the cathode with the fluid flow, can be a major source of cathodic contamination.[1, 2]

Many studies have been performed on the mineralogy and microstructures of inclusions in copper anodes.[3-12] Furthermore, the phases and structures of anode slimes have also been studied by many researchers.[3, 6-8, 13-16] Dissolved impurities from copper anodes could form floating slimes.[17] Some research has been done to study the adhesion of anode slimes.[18-20]

In order to further study the mechanisms of anode slime adhesion and identify

factors affecting the purity of copper cathode, a series of copper electrorefining tests were performed using different types of anodes, and comprehensive analyses of pretest anode samples, harvested anode samples, harvested cathode samples, and samples of different types of slimes were carried out.

5.2 Experimental Procedures

Two types of anodes with different levels of impurities, provided by Kennecott Utah Copper, were used to perform a series of experimental electrorefining tests. One type of anode, having high impurity levels, especially for arsenic, and another type of anode, having low levels of impurities, were selected. These anodes were cut into cubes 2.5 cm in height and 2.5 cm in width. In order to simulate the strip cycle and scrap cycle, the cubes were further cut into three sections based on depth from the air cooling side of the anode, as shown in Figure 5.1. The top surface section, the middle section, and the bottom section were used as strip cycle anode, scrap cycle anode, and residual anode, respectively. The top section and the middle section have a depth of about 8 mm, based on the anode depth dissolved in a cycle of 11 days. As a result, four types of anodes were utilized in this study: high impurity strip cycle anodes, high impurity scrap cycle anodes, low impurity strip cycle anodes, and low impurity scrap cycle anodes. Samples of the four types of anodes were collected, polished, and analyzed by using a scanning electron microscope (SEM) and energy-dispersive X-ray spectroscopy (EDS) to examine their inclusion types. The composition of these four types of anodes were also analyzed by DC Arc and are summarized in Table 5.1. It can be observed that high impurity anodes have higher levels of almost all impurity elements than low impurity anodes. Strip cycle anodes have lower levels of nearly all impurity elements than scrap cycle anodes. It is also noteworthy that

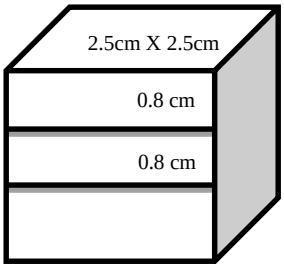

Figure 5.1 Schematic drawing of cutting an anode into three sections

Table 5.1 Compositions of the four types of anodes used in copper electrorefining tests

Type of Anode	As (%)	Pb (%)	Bi (%)	Sb (%)	Se (%)	Ni (%)	Te (%)	Sn (%)	O(%)	S(%)
Low Impurity Strip Cycle Anode	0.143	0.175	0.037	<.0022	0.060	0.038	0.008	0.0007	0.270 ~ 0.320	0.007 ~ 0.010
Low Impurity Scrap Cycle Anode	0.155	0.177	0.038	<.0022	0.063	0.038	0.008	0.0007		
High Impurity Strip Cycle Anode	0.363	0.197	0.079	0.014	0.082	0.023	0.009	0.0007	0.160 ~ 0.220	0.011 ~ 0.014
High Impurity Scrap Cycle Anode	0.385	0.211	0.089	0.014	0.080	0.021	0.009	0.0007		

high impurity anodes and scrap cycle anodes have higher impurity levels mostly in terms of arsenic.

Each anode was soldered with electrical wire on the back side surface and then mounted in cylinder cups using epoxy resins. The front surfaces of the anodes were polished using 400 grit, 600 grit, 800 grit, and 1200 grit polishing papers successively. The resulting mounted anodes were fixed into a designed anode holder (Figure 5.2). Cathodes were made by cutting stainless steel sheet about 1 mm in thickness into proper size (2.5 cm in width). The back of the cathode was covered by polypropylene sheets and the front of the cathode was partially covered to leave an area with a height of 2.6 cm and a width of 2.5 cm. The partially covered cathode was fixed into a designed cathode supporter, as shown in Figure 5.3.

A beaker with total volume of 300 mL was utilized as the copper electrorefining test cell, while the anode holder and the cathode supporter have slots that fit with the beaker (2.5 cm gap between the anode and the cathode). A pumping system including pipes and two peristaltic pumps was used to continuously circulate the electrolyte in the test cell at a specified rate, as well as to feed the cell with glue (0.0081 g/L/day), thiourea (0.0143 g/L/day), and replenishment water. The total amount of electrolyte prepared for each test was about 230 mL, with about 200 mL in the test cell. The electrolytic solution contained 45 g/L Cu (II) as Cu_2SO_4, 180 g/L H_2SO_4, 2 g/L Fe (II) as $FeSO_4$, 30 mg/L Cl^- as HCl, and 100 mg/L Co (II) as $CoSO_4$. The flow rate (pumping rate) was calculated based on a 3-hour residence time and was about 1.11 mL/min. An isothermal bath and heater were utilized to maintain the cell temperature (electrolyte temperature) at the targeted value. The current was provided by a power supply with an applied current density of 250 A/m^2. The entire

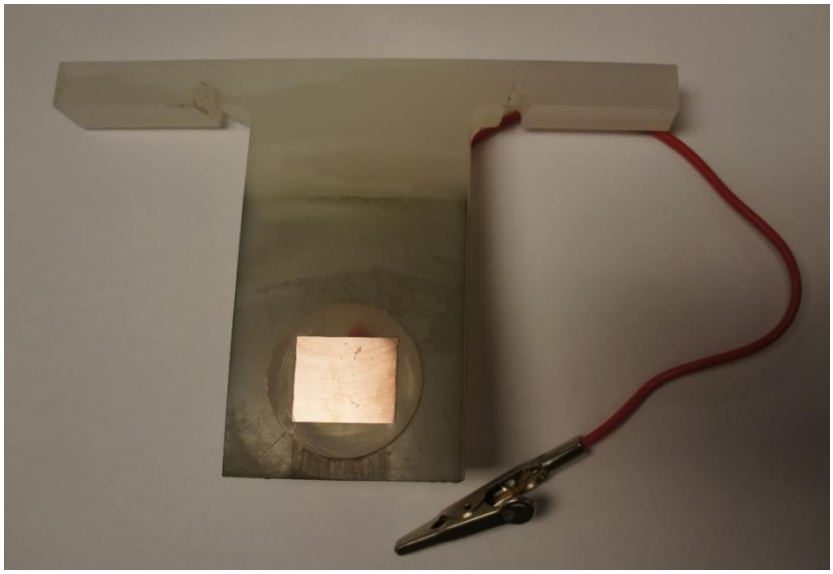

Figure 5.2 Mounted copper anode fixed in a designed anode holder

Figure 5.3 Stainless steel cathode sheet with its back side fully covered and its front side partially covered, fixed in a designed cathode supporter

experimental setup is shown in Figures 5.4 and 5.5.

Each test was performed for two days and eight tests at different cell temperatures from 25 ℃ to 85 ℃ were performed for each type of anode. For the high impurity anodes (both strip and scrap cycles), the cell temperatures were 25, 35, 45, 55, 60, 65, 75, and 85 ℃; for the low impurity anodes (both strip and scrap cycles), the cell temperatures were 25, 35, 45, 55, 65, 70, 75, and 85 ℃. The total number of tests completed was 32 for the four types of anodes used.

After two days of testing, the anode and the cathode were carefully unloaded from the cell, then taken off from the anode holder and the cathode supporter respectively, and finally rinsed by deionized water (Figures 5.6 and 5.7). The harvested cathodes were collected for further compositional analysis to examine impurities concentrations. The resulting anodes were dried naturally and then the slimes adhered to each anode were partially removed. The slimes were collected and weighed, and the exposed area (cleaned of slimes) was measured (Figure 5.8). The remaining slimes on the anode were mounted by epoxy resins, then cross-sectioned, and polished for further SEM and EDS analyses to observe the anode slimes layer structure and its elemental distribution. The slimes suspended in the electrolyte and settled on the bottom of the cell after each test were collected separately from those removed from the exposed part of the anode (Figure 5.9). These slimes were then separated from the electrolyte by a centrifuge, dried in air, weighed, and stored for further size distribution analysis as well as SEM and EDS analyses to observe their structures and elemental distributions. The weight per unit of anode surface area (mg/cm^2) of adhered slimes, suspended slimes, and settled slimes was calculated, compiled, and further analyzed with other analyses results such as slime size distributions

Figure 5.4 Electrochemical cell setup in an isothermal bath

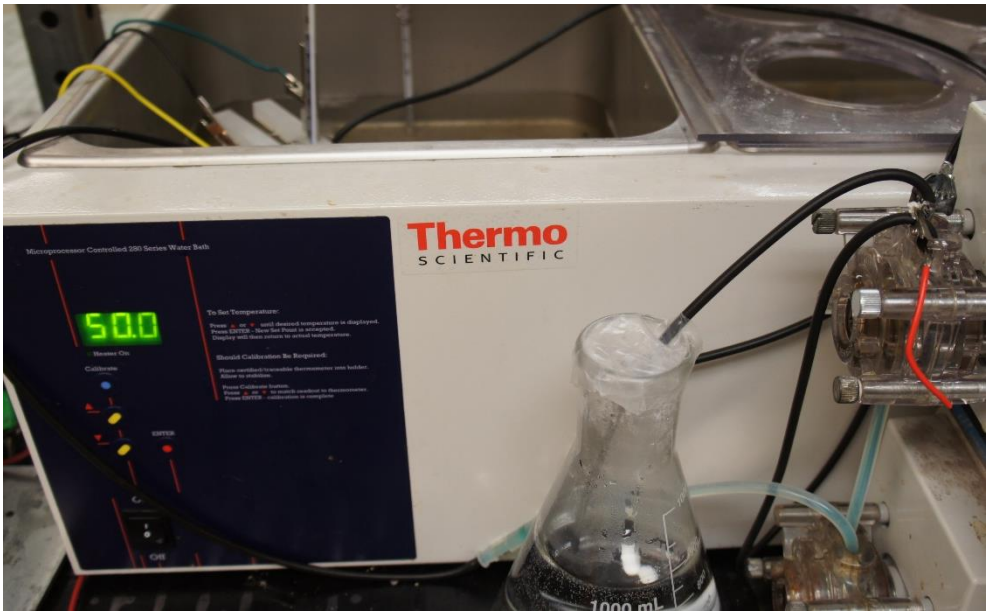

Figure 5.5 Overall experimental setup including the cell, the isothermal bath, and the pumping system

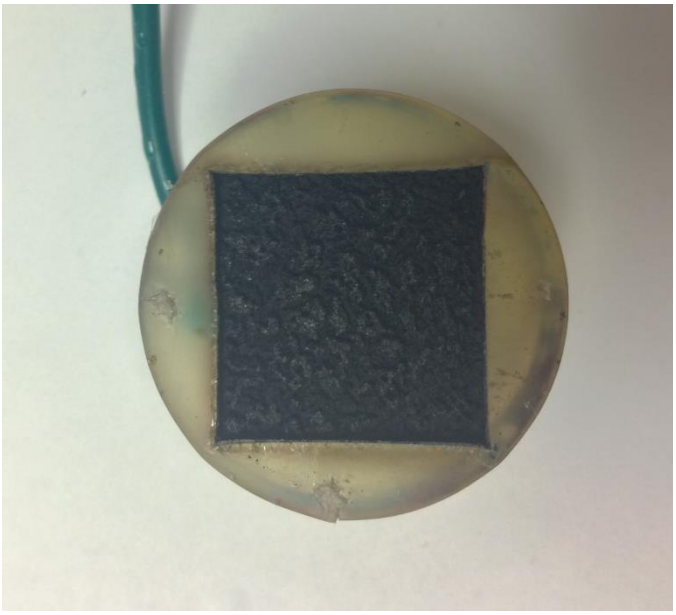

Figure 5.6 Harvested and rinsed copper anode with anode slimes layer on it

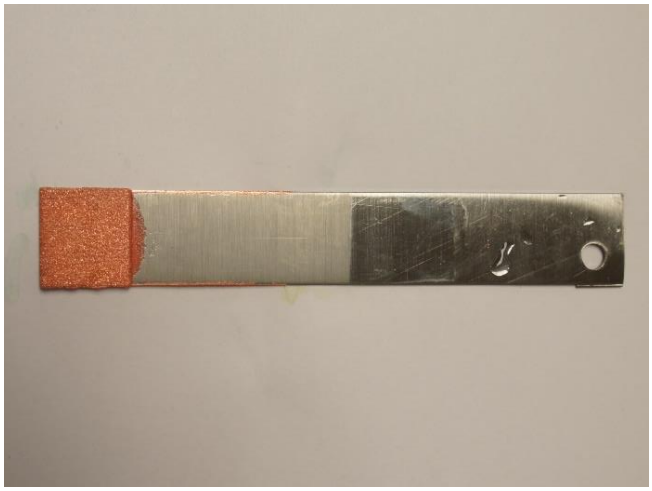

Figure 5.7 Harvested and rinsed cathode sheet with copper deposited on the lower section

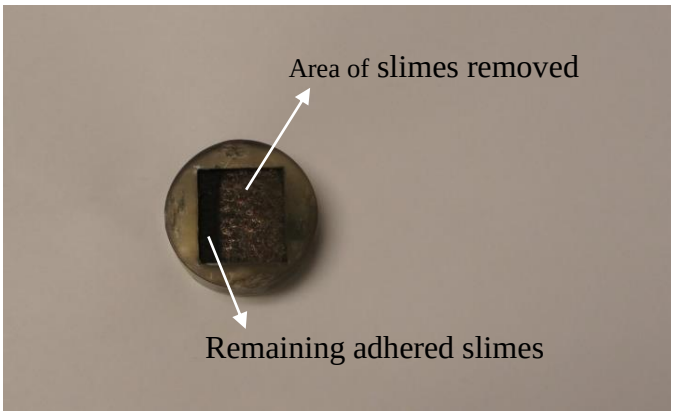

Figure 5.8 Copper anode with part of anode slimes removed from its surface

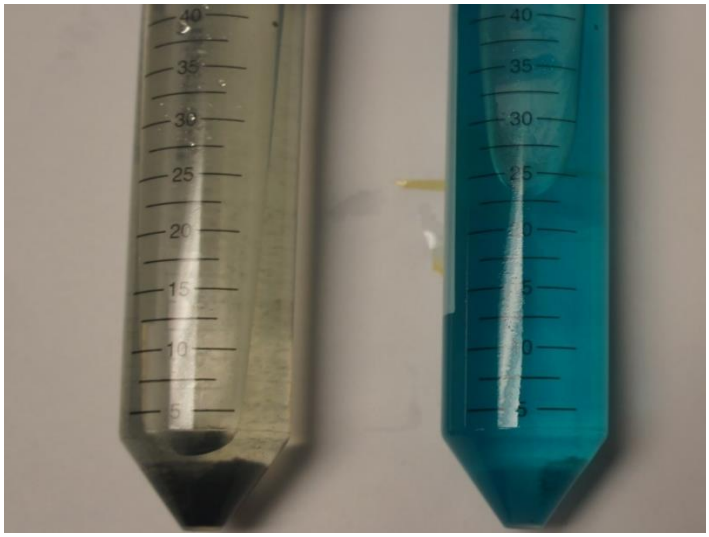

Figure 5.9 Collected settled slimes immersed in deionized water (left tube) and collected suspended slimes in electrolyte (right tube)

and cathode impurity levels.

5.3 Experimental Results

The weight of slime particles that adhered to the surface of the anode after electrorefining was measured for each anode tested, which is a direct indicator of anode slime adhesion. It is significant to point out that the surface area varies a little among different anodes and only part of the slimes on about two thirds of the area of the anode surface were removed and weighed. Thus, the area of slime removal was measured and the weight of adhered slimes per unit of anode surface area was calculated, instead of the absolute weight of adhered slimes. The results of adhered slimes weight per unit of anode surface area at different cell temperatures are shown below in Figures 5.10 and 5.11 for the series of the high impurity anodes and the series of the low impurity anodes, respectively.

From Figures 5.10 and 5.11, it can be observed that slime adhesion varies significantly with temperatures. It is interesting that anodes with a bare surface (no adhered slimes) were obtained from the tests at 25 ℃ regardless of the type of anode that was used. As the temperature increases, the amount of slimes adhered to the anode increased, until it reached a peak with the maximum amount of adhered slimes. After this peak adhesion temperature (the temperature under which the maximum weight of slimes adhered to the anode could be acquired), the weight of adhered slimes per unit of anode surface area decreases with further increase in the temperature. It is also noteworthy that the peak adhesion temperature changes with different types of anodes tested. The peak adhesion temperatures are 55 ℃, 60 ℃, 65 ℃, and 70 ℃ for the high impurity scrap cycle anode, the high impurity strip cycle anode, the low impurity scrap cycle anode, and the low impurity strip cycle anode, respectively. The low impurity strip cycle anodes have the

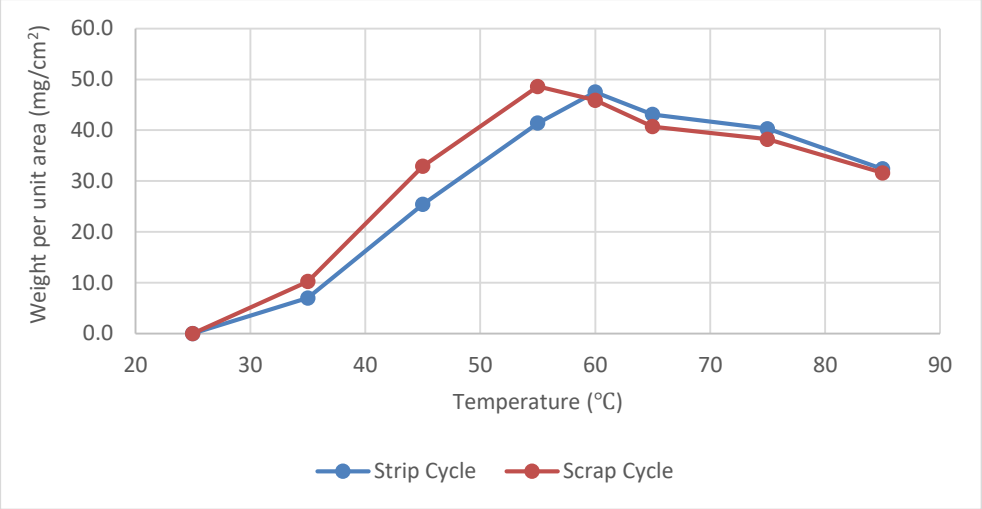

Figure 5.10 Adhered slimes weight per unit of anode surface area at different temperatures for the high impurity anodes

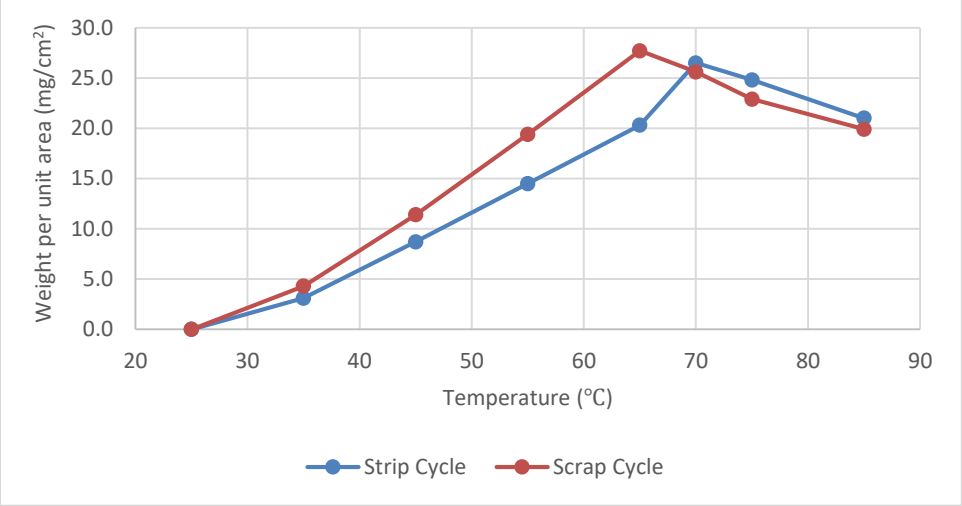

Figure 5.11 Adhered slimes weight per unit of anode surface area at different temperatures for the low impurity anodes

highest peak adhesion temperature, while the high impurity scrap cycle anodes have the lowest. Generally, the low impurity anodes reach the maximum amount of adhered slimes at higher temperatures than the high impurity anodes, and the strip cycle anodes have higher peak adhesion temperatures than the scrap cycle anodes in the same series. Lastly, the series of the high impurity anodes have larger amounts of slimes adhered to the anode than the series of the low impurity anodes, and the scrap cycle anodes generally have more adhered slimes than the strip cycle anodes in the same series. This is consistent with the original impurity levels in the four types of anodes.

The amounts of slimes suspended and settled on the bottom of the cell were also weighed after each 2-day test, and then converted to the weight of slimes per unit of anode surface area by dividing it by the surface area of the anode. The weight per unit area of slimes adhered to the anode, suspended in the electrolyte, and settled on the bottom of the cell at different cell temperatures are summarized in Figures 5.12 – 5.15, for the high impurity strip cycle anodes, the high impurity scrap cycle anodes, the low impurity strip cycle anodes, and the low impurity scrap cycle anodes, respectively.

Several observations can be made from Figures 5.12 – 5.15. Firstly, the total weight per unit of surface area of slimes adhered to the anode, suspended in the electrolyte, and settled on the bottom of the cell together remain approximately constant for different cell temperatures for any type of anode tested. This is due to the similar amount of insoluble inclusions existing in the same type of anodes. Secondly, the weight per unit area of suspended slimes decreases as the temperature increases up to the peak adhesion temperature and it decreases gradually above the peak adhesion temperature. Thirdly, the weight of settled slimes per unit area decreases at low temperatures (below the peak

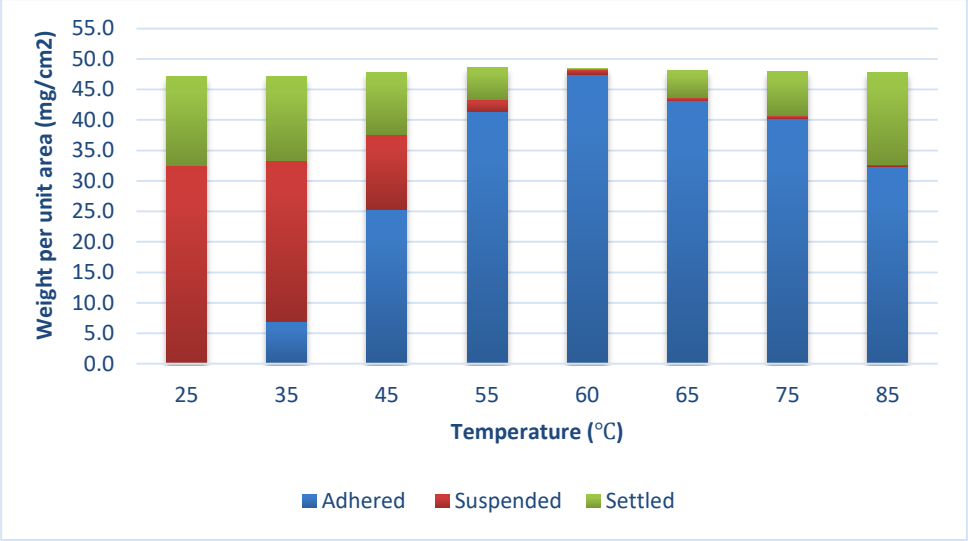

Figure 5.12 Slime distributions at different temperatures for the high impurity strip cycle anodes

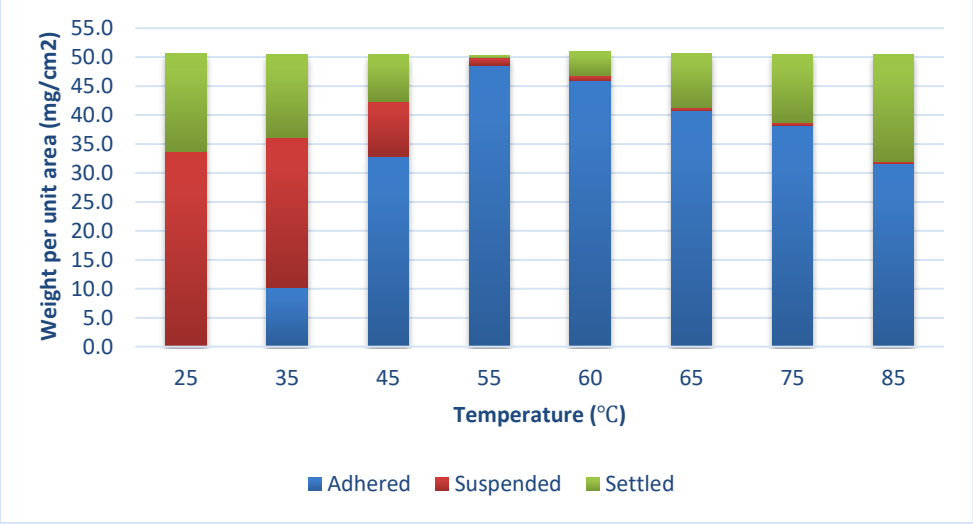

Figure 5.13 Slime distributions at different temperatures for the high impurity scrap cycle anodes

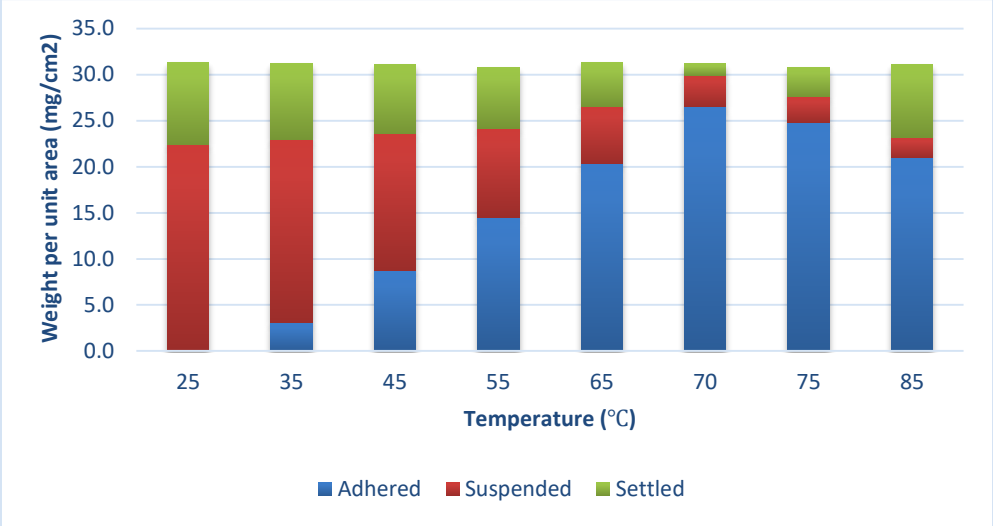

Figure 5.14 Slime distributions at different temperatures for the low impurity strip cycle anodes

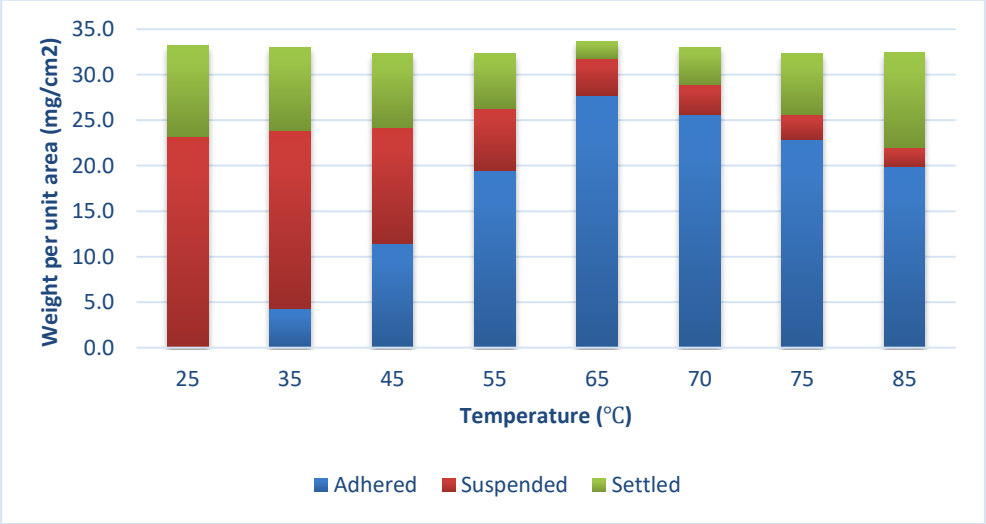

Figure 5.15 Slime distributions at different temperatures for the low impurity scrap cycle anodes

adhesion temperature). After the peak adhesion temperature, the weight of settled slimes is gradually recovered as the temperature continues to increase and at the highest temperature of 85 ℃, it is generally even a little larger than the settled slimes weight at 25 ℃ (explained in section 5.4), for all types of anodes, except the low impurity strip cycle anodes whose peak adhesion temperature is the largest and is close to the highest temperature. Fourthly, at low temperatures, the weight of suspended slimes decreases faster for the high impurity anodes than for the low impurity anodes. At temperatures above the peak adhesion temperature, there are larger amounts of suspended slimes remaining for the low impurity anodes than for the high impurity anodes. Fifthly, at low temperatures, the weight of settled slimes also decreases faster for the high impurity anodes and at the peak adhesion temperature, larger amounts of settled slimes are present for the low impurity anodes than for the high impurity anodes.

The harvested copper cathode after each test was compositionally analyzed by DC Arc for impurity levels. Because most impurities levels in the cathode are too low to analyze, only the bismuth levels in copper cathode, with different cell temperatures and different types of anodes, were analyzed and the results are shown in Tables 5.2 and 5.3. Additionally, other impurities such as lead and sulfur are associated with bismuth, not only in anode inclusions, but also in slimes and inclusions in cathodes. This will be further discussed in the discussion section.

From Tables 5.2 and 5.3, significant findings are summarized as below. Firstly, the bismuth level decreases monotonically with increasing temperature for all types of anodes, but it is more difficult to track and it decreases more slowly after the peak adhesion temperature, especially for the high impurity anodes. Secondly, the copper cathode

Table 5.2 Bismuth levels in copper cathode associated with the high impurity anodes

Cell temperature (℃)	Strip Cycle	Scrap Cycle
25	1.890	2.130
35	1.380	1.050
45	0.340	0.180
55	0.100	< 0.100
60	< 0.100	< 0.100
65	< 0.100	< 0.100
75	< 0.100	< 0.100
85	< 0.100	< 0.100

All units are in ppm

Table 5.3 Bismuth levels in copper cathode associated with the low impurity anodes

Cell temperature (℃)	Strip Cycle	Scrap Cycle
25	0.620	0.660
35	0.580	0.610
45	0.450	0.410
55	0.320	0.170
65	0.170	0.160
70	0.140	0.150
75	0.120	0.120
85	0.100	0.110

All units are in ppm

produced from the high impurity anodes has higher bismuth levels at the low temperature range, but has even lower bismuth levels at temperatures above the peak adhesion temperatures than those produced from the low impurity anodes. This information is valuable and will be further discussed. Thirdly, the cathode bismuth level is correlated with the weight per unit area of suspended slimes, which will also be further discussed.

5.4 Discussion

From the results of adhered slimes weight per unit of surface area at different cell temperatures, an interesting phenomenon can be observed that the temperature exerts a remarkable effect on the amount of slimes remaining on the anode surface or simply the anode slime adhesion, which has significant effect on the cathode purity by affecting the amount of slimes suspended in the electrolyte. The slime adhesion to the anode generally increases at the low temperature range and it begins to decrease above the peak adhesion temperature, which means there exists a maximum amount of adhered slimes that can be achieved. It is even more interesting that no slimes adhered to the anode surface at 25 ℃, regardless of the type of anode that was used. In addition, temperature also exerts a strong effect on the weights of suspended and settled slimes per unit of anode surface area. The weight of suspended slimes generally decreases as the temperature increases, while the weight of settled slimes decreases as the temperature increases until the peak adhesion temperature and then increases back as the temperature continues to increase. Note that the suspended slimes are generally smaller in particle size than the settled slimes and are much more likely to affect cathode purity, as will be discussed subsequently.

The hypothesis for these phenomena is that slime particles consisting of low melting point compounds are easier to sinter or coalesce together to form larger particles

and adhere to the anode surface during the process of copper electrorefining. On the other hand, slime particles involving high melting temperature compounds are harder to sinter together and adhere to the surface of the anode during copper electrorefining. Furthermore, it is the outer surface of particles rather than particle cores that play the most significant role in particle sintering and coalescence. Therefore the melting and sintering temperatures of the compounds that constitute the outer surface of particles determine whether or not particles can sinter and coalesce at certain temperatures. In addition, lead, bismuth, and sulfur, which are common anode impurities, have low melting temperatures, and compounds made up of these elements generally have low melting and sintering temperatures. Arsenic, on the other hand, has a much higher melting temperature (817 ℃) and compounds involving it commonly have high melting and sintering temperatures. Note that slime particles are originally inclusion particles in the anode and are liberated from the anode when the copper dissolves. Also, note that the sintering temperature in this study is referred to as the temperature at which appreciable sintering and coalescence occurs.

5.4.1 Characterization of Anode Inclusion Particles

In order to investigate the different types of inclusion particles in the anodes, samples were cut from the high and low impurity anodes, then polished and analyzed by SEM and EDS to acquire the surface morphology and elemental distributions on anode cross-sections. The results show that different types of anodes have different types of inclusions.

Figure 5.16 shows the SEM electron microscope image and EDS elemental distribution maps on the cross-section of one of the high impurity anodes and Figure 5.17 is another set of EDS maps of the cross-section of one of the high impurity anodes. There

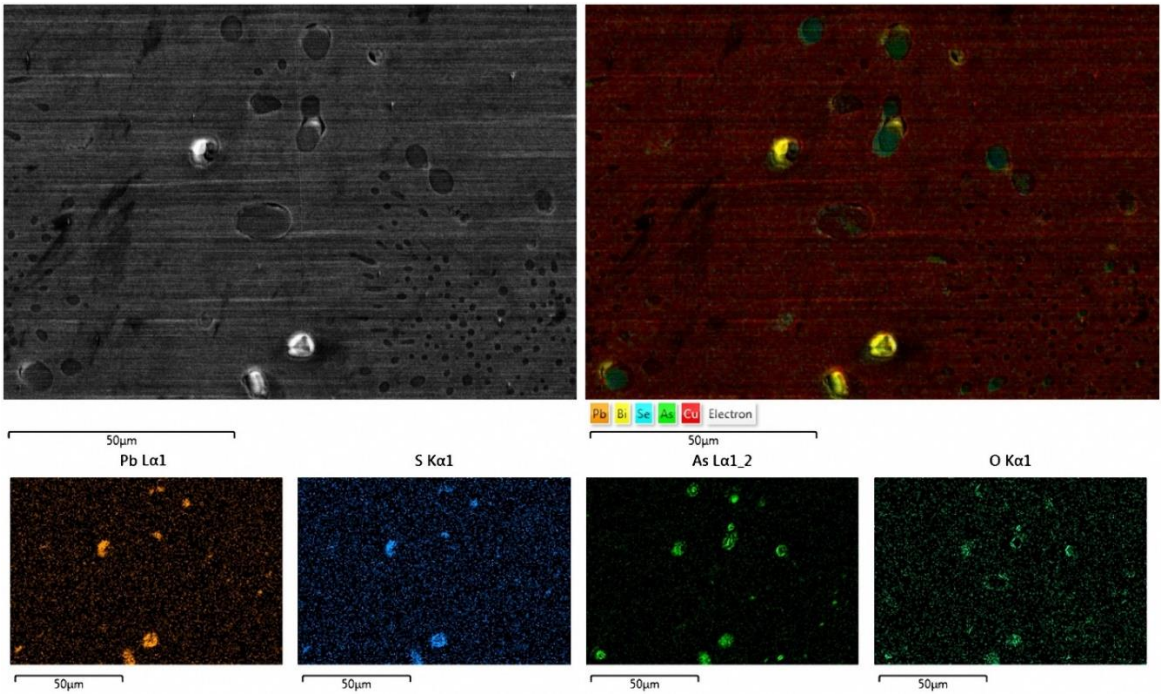

Figure 5.16 SEM electron microscope image and EDS elemental distribution maps of the high impurity anode cross-section

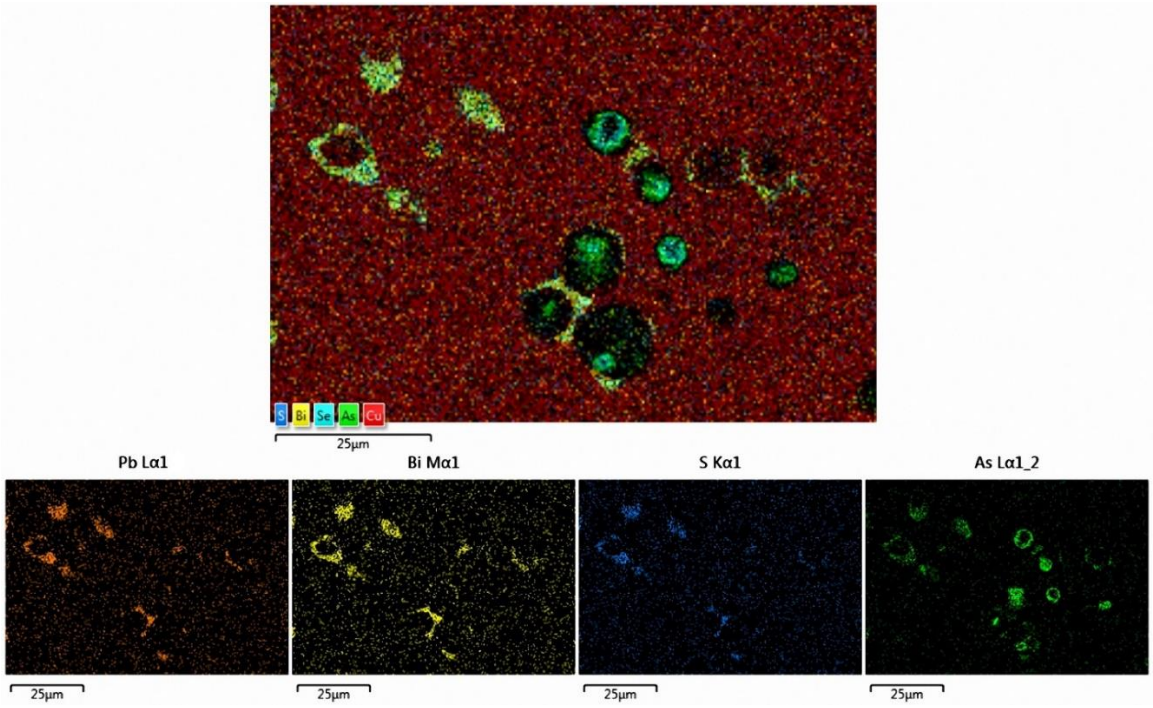

Figure 5.17 Additional set of EDS elemental distribution maps of the high impurity anode cross-section

are two types of elemental distribution maps shown: one is a layered elemental distribution map involving several elements and the other is an individual element distribution map for certain important elements. Several observations can be made from the EDS results of the high impurity anodes. Firstly, lead, bismuth, and sulfur coexist at certain areas and they tend to form the Pb-Bi-S compounds as the outer surface or shell of inclusion particles. Secondly, arsenic has a different distribution than lead, bismuth, and sulfur, and most arsenic is distributed at the center of inclusion particles with other elements such as oxygen and selenium. Thus, arsenic generally plays the role of forming the core of inclusion particles as As-O compounds (sometimes as As-Se compounds). Because the arsenic content is high in this type of anode (Table 5.1), it tends to form phases dominated by arsenic such as the As-O/As-Se compounds rather than phases dominated by other elements such as the Pb-Bi-S-As compounds during solidification, as demonstrated in Figures 5.16 and 5.17. Thirdly, some inclusions have an As-O core with Pb-Bi-S shell, while some just have an As-O core. Fourthly, lead, bismuth, sulfur, and arsenic can also coexist to form isolated Pb-Bi-S-As compound inclusions at some places where arsenic content is low, as shown in Figure 5.17. These phenomena can be explained by the fact that different compounds/solid solutions have different melting points. The As-O compounds would have relatively higher melting points than the Pb-Bi-S compounds, so the As-O structures would be solidified first after the solidification of copper matrix in copper grain boundaries, during the process of copper smelting. Then the Pb-Bi-S compounds would be solidified later around the formed As-O cores. However, the amount of lead and bismuth might not be sufficient to form shells around every As-O core (lead and bismuth contents are considerably less than that of arsenic in the high impurity anode as shown in Table 5.1), so

some uncovered As-O cores exist in the high impurity anode as shown in Figures 5.16 and 5.17. Additionally, at some places where arsenic content is low, lead, bismuth, sulfur, and arsenic could be solidified together along the copper grain boundaries to form isolated Pb-Bi-S-As compound particles as shown in Figure 5.17.

Figure 5.18 shows the SEM and EDS results of the cross-section of one of the low impurity anodes and several observations can also be made. Firstly, lead, bismuth, sulfur, and arsenic have very similar distributions in this type of anode, and they tend to form the Pb-Bi-S-As compounds as the shells of inclusion particles or as isolated inclusion particles. Since arsenic has a low concentration in the low impurity anode (even lower than lead as shown in Table 5.1), it generally exists within phases dominated by lead and bismuth such as the Pb-Bi-S-As compounds, instead of in phases dominated by arsenic such as the As-O/As-Se compounds as demonstrated in Figure 5.18. Secondly, oxygen has a different distribution than Pb, Bi, S, and As. Most oxygen is located at the core of inclusion particles with copper, potentially forming cuprous oxide. So oxygen plays the role of forming cores of inclusion particles with copper as copper oxide (sometimes selenium also exists as Cu-Se compounds (likely to be Cu_2Se), and it forms selenide spheroids with Cu_2O). Thirdly, some inclusion particles are just uncoated copper oxide cores, but other inclusions have a copper oxide core surrounded by a Pb-Bi-S-As shell, as shown in Figure 5.18. These phenomena can be explained similarly as for the high impurity anodes. The copper oxide, likely to be cuprous oxide, would have higher melting points than the Pb-Bi-S-As compounds, so the copper oxide would be solidified before the solidification of the Pb-Bi-S-As compounds during anode solidification. As result, the copper oxide structures are formed firstly at the grain boundaries of the copper matrix as cores, and the Pb-Bi-S-As

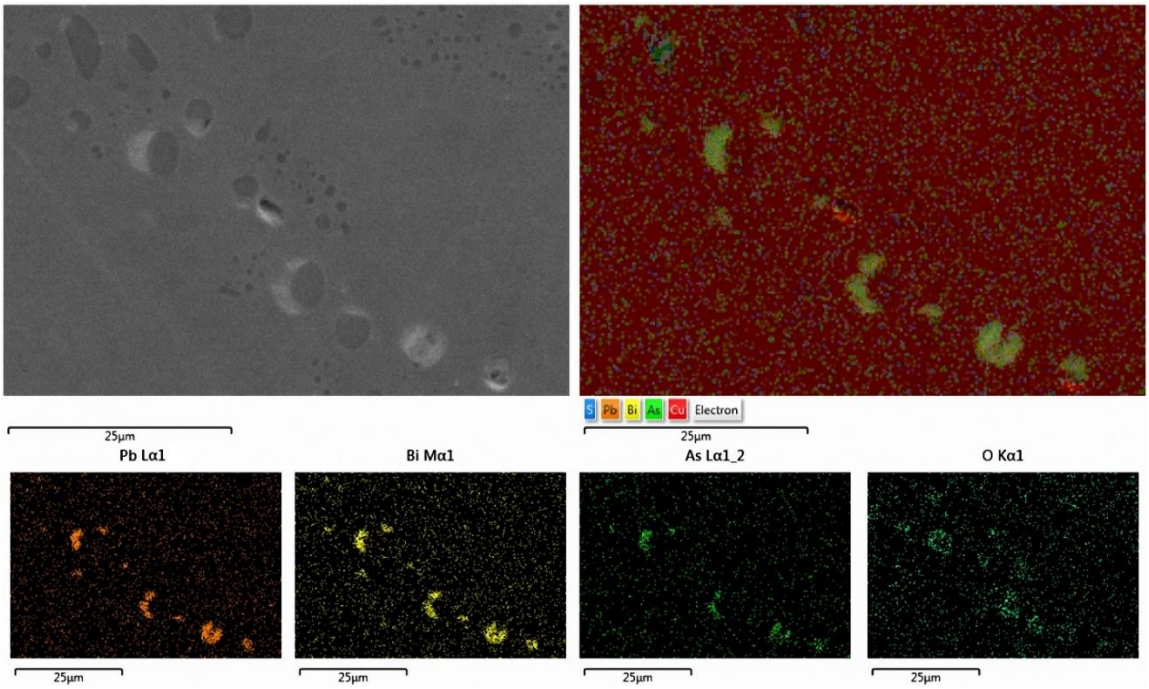

Figure 5.18 SEM electron microscope image and EDS elemental distribution maps of the low impurity anode cross-section

compounds are formed later around these cores at the grain boundaries as shells. The uncovered copper oxide cores in Figure 5.18 result from the fact that the contents of lead, bismuth, sulfur, and arsenic in the low impurity anode are much lower than that of copper and oxygen. Therefore, there is insufficient Pb, Bi, S, and As to form shells around all copper oxide cores.

Nevertheless, it is noteworthy that the low impurity anodes also contain typical types of inclusions found in the high impurity anodes including As-O cores with Pb-Bi-S shells and As-O cores without shells. Conversely, the high impurity anodes also have some inclusion particles that belong to the typical inclusion types of the low impurity anodes. The percentage of each type of inclusion was calculated for the high impurity anodes and the low impurity anodes in order to analyze the inclusion distribution in terms of inclusion types. Table 5.4 shows the results. Note that Pb-Bi-S/Pb-Bi-S-As shells with missing core inclusion particles (potentially due to polishing procedures that may have removed some cores) in the anodes were considered as As-O/Cu-O cores with Pb-Bi-S/Pb-Bi-S-As shell inclusions.

From the results shown in Table 5.4, it is obvious that most of the inclusions in the high impurity anode belong to the first type of inclusion characterized by the Pb-Bi-S compounds: As-O cores with Pb-Bi-S shells. Nevertheless, the low impurity anode has an entirely different inclusion type distribution, with most inclusions characterized by the Pb-Bi-S-As compounds: Cu-O cores with Pb-Bi-S-As shells and isolated Pb-Bi-S-As compound particles. Consequently, these two types of anodes should have very different behavior when exposed to the electrolyte in the copper electrorefining process. The insoluble inclusion particles would become slime particles when liberated from the anode.

Table 5.4 Inclusion type distribution in the high and low impurity anodes

Inclusion Type	High Impurity	Low Impurity
As-O core with Pb-Bi-S shell	52%	1%
As-O core without shell	21%	2%
Pb-Bi-S-As compound isolated particle	16%	22%
Cu-O core with Pb-Bi-S-As shell	5%	45%
Cu-O core without shell	6%	31%

The inclusion types in the anodes are not discussed in terms of the strip cycle and scrap cycle anodes, because the inclusion type distributions for the strip cycle anodes and the scrap cycle anodes are very similar, in both the high impurity and low impurity anodes. The only difference between them is that the strip cycle anodes have slightly larger percentages of inclusion types of Cu-O cores with Pb-Bi-S-As shells and Cu-O cores without shells than the scrap cycle anodes, according to SEM and EDS analyses.

It is significant to identify the melting temperatures of the Pb-Bi-S compounds and the Pb-Bi-S-As compounds as they form particle shells or isolated particles. Figure 5.19 shows some binary phase diagrams involving lead, bismuth, sulfur, and arsenic, which are the major impurity elements in the anodes used in this study.

From these phase diagrams, it is apparent that the binary system of Pb and Bi has solidus lines at low temperature levels and has a eutectic temperature of only 125 ℃, whereas binary systems involving arsenic have solidus lines that are raised to higher temperature levels by arsenic and they have relatively high eutectic temperatures. The ternary phase diagrams involving these four elements are currently unavailable, but some inferences can still be made based on the binary phase diagrams. Since sulfur has a melting point of only 113 ℃, the solidus line and the eutectic temperature of the Pb-Bi-S ternary system would be further lowered by sulfur. It is very likely that the melting temperatures of Pb-Bi-S compounds with compositions near the eutectoid are below 150 ℃. For the quaternary system of Pb-Bi-S-As, the addition of arsenic may further decrease the melting points, by a small amount and only for alloys having a very small amount of arsenic (less than a few degrees Celsius decrease and less than 1 wt.% arsenic content according to properties of binary diagrams involving arsenic). So Pb-Bi-S-As compounds with a very

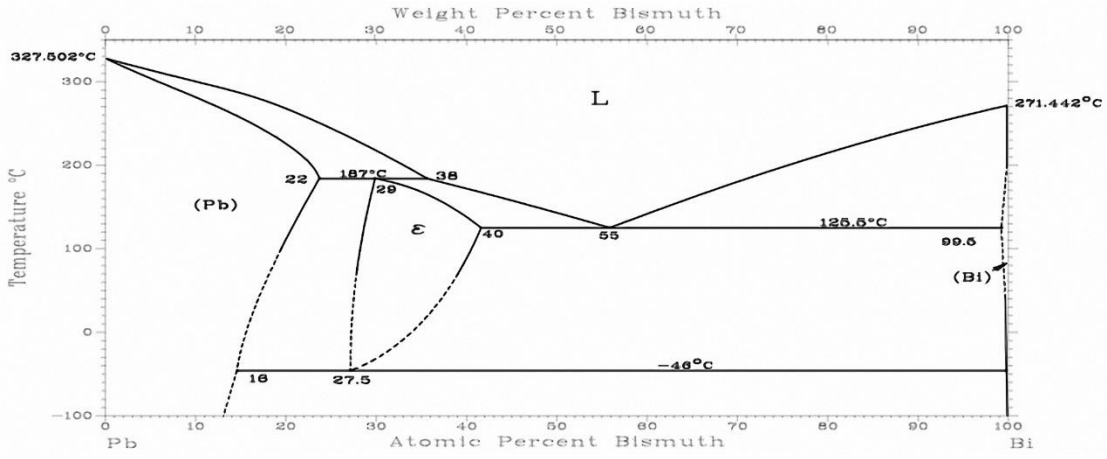

(a) Pb-Bi binary phase diagram

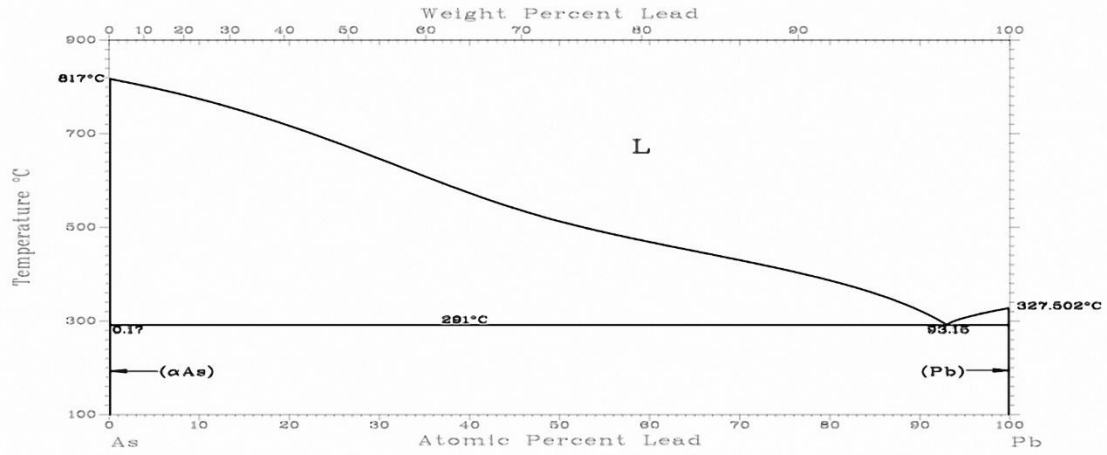

(b) As-Pb binary phase diagram

Figure 5.19 Binary phase diagrams from the database of ASM International

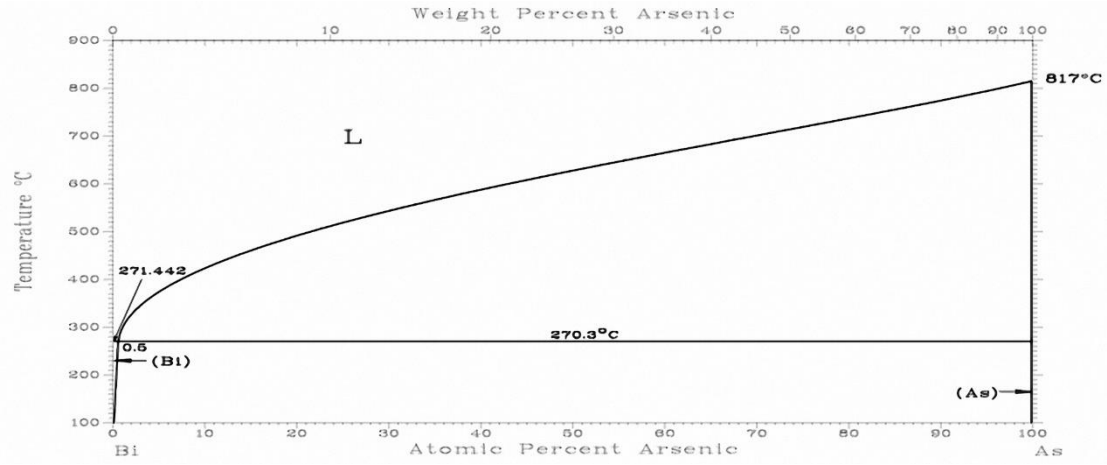

(c) Bi-As binary phase diagram

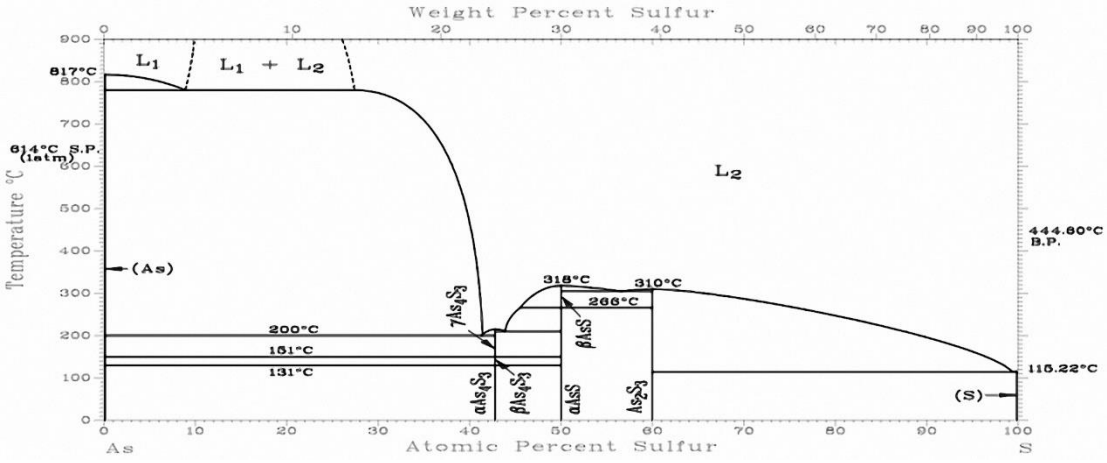

(d) As-S binary phase diagram

Figure 5.19 Continued

small amount of arsenic would likely have melting temperatures lower than 200 ℃. But most compounds in the quaternary system of Pb-Bi-S-As with a moderate amount of As would have melting temperatures raised by arsenic that has a melting point of 817 ℃. The higher the arsenic content, the higher the melting temperature. Therefore, the Pb-Bi-S-As compounds would very likely have melting points higher than 200 ℃, higher than those of the Pb-Bi-S compounds.

For convenience, in this chapter, Pb-Bi-S-As compounds with a very small amount of arsenic will be classified as Pb-Bi-S compounds, in terms of the melting temperature and sintering temperature. Only Pb-Bi-S-As compounds with a significant amount of arsenic will be treated as Pb-Bi-S-As compounds. Furthermore, the occurrence of sintering requires temperatures near melting points. Generally, sintering is negligible at low temperatures near room temperature, but it becomes significant when the temperature is elevated. Typically sintering occurs above 70% of the melting temperature (in degrees Kelvin) of the material to be sintered.[21, 22] Therefore, Pb-Bi-S compounds with appropriate compositions can have sintering temperatures lower than 60 ℃ whereas Pb-Bi-S-As compounds would have sintering temperatures above 60 ℃.

5.4.2 Characterization of Slime Particles

In order to verify the above inferences, additional tests of the slimes generated from the electrorefining tests were performed. The slime particles generated from the tests at 25 ℃ were taken and placed in mounting cups. Then the mounting cups with slimes were heated in an oven to different temperatures from 30 ℃ to 100 ℃. After two days of heating, the mounting cups were removed from the oven, and epoxy resins were added to

mount the heated slimes. The mounted slimes were polished and observed under SEM and EDS. It turned out that these slimes did not sinter and coalesce together until the heating temperature reached 50 ℃. Evidence for unsintered particles after heating at 40 ℃ for two days is shown in Figure 5.20. Nevertheless, the slime particles did sinter and coalesce to different extents, after heating at temperatures above 50 ℃ for two days. The SEM images of sintered slime particles after heating at 50 ℃ and 100 ℃ are shown in Figures 5.21 and 5.22.

The SEM images of Figures 5.20 – 5.22 have some charging issues resulting from the poor conductivity of epoxy, but the slimes particles are still clear and distinguishable for observation and evaluation. Figure 5.20 shows mounted slime particles after 2-day oven heating at 40℃, and it can be observed that almost all particles remained separated from each other with no evident sintering and coalescence of slime particles. Figure 5.21 shows that part of these slime particles sintered and coalesced together to form larger slime particles after 2-day heating at 50 ℃. Figure 5.22 shows that most of the slimes coalesced together and formed larger particles, with some small unsintered slimes left after 2-day heating at 100 ℃. Therefore, it is demonstrated that slime particles can sinter together to become larger particles when the temperature is high enough.

Figures 5.23 – 5.25 show the results of EDS analysis of slimes heated at 50 ℃, 60 ℃, and 65 ℃ for two days. The impurity elements' distribution on the epoxy resins could be due to the polishing of slimes before analysis or the background noise. The results show that shells of the different slime particles generated from the electrorefining tests are made of different types of compounds and these shells play a significant role in particle

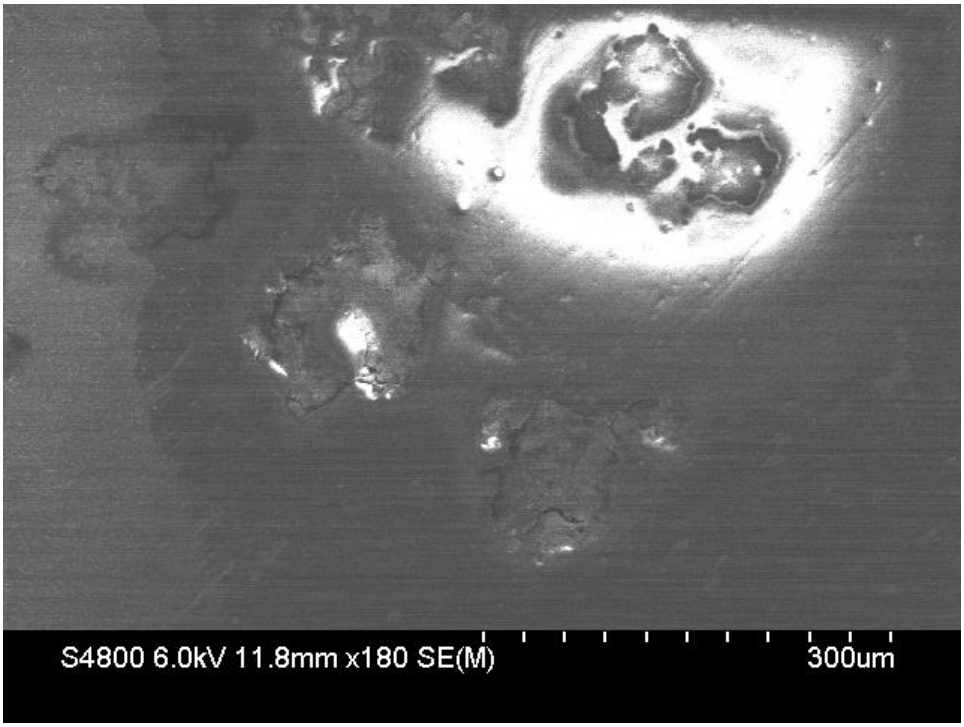

Figure 5.20 SEM electron microscope image of heated slimes mounted in epoxy resins after 2-day oven heating at 40℃

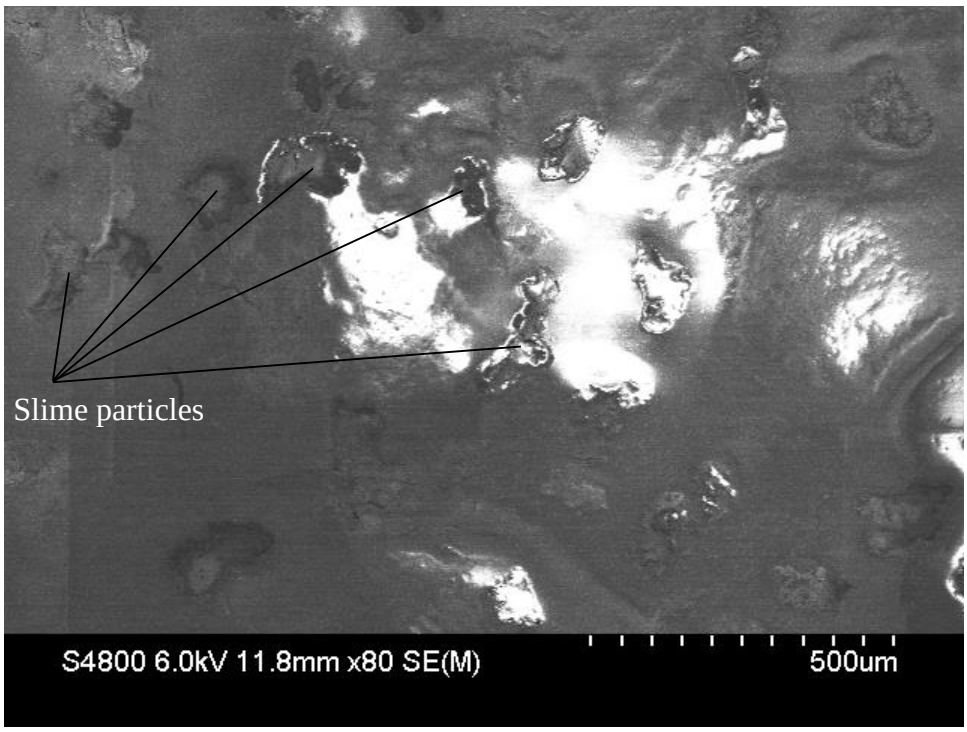

Figure 5.21 SEM electron microscope image of heated slimes mounted in epoxy resins after 2-day oven heating at 50℃

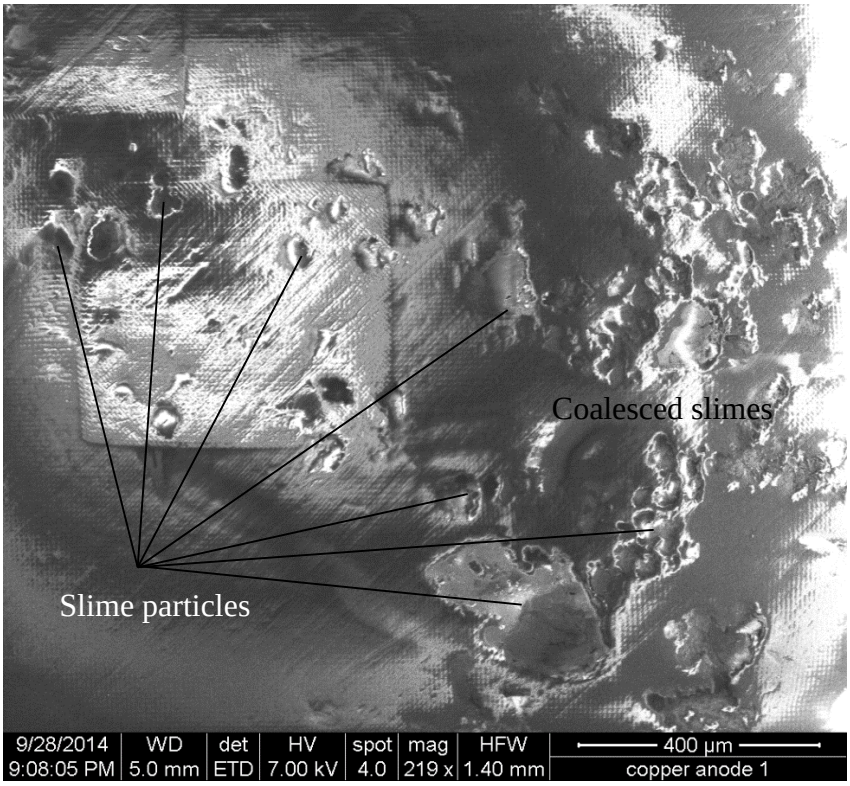

Figure 5.22 SEM electron microscope image of heated slimes mounted in epoxy resins after 2-day oven heating at 100℃

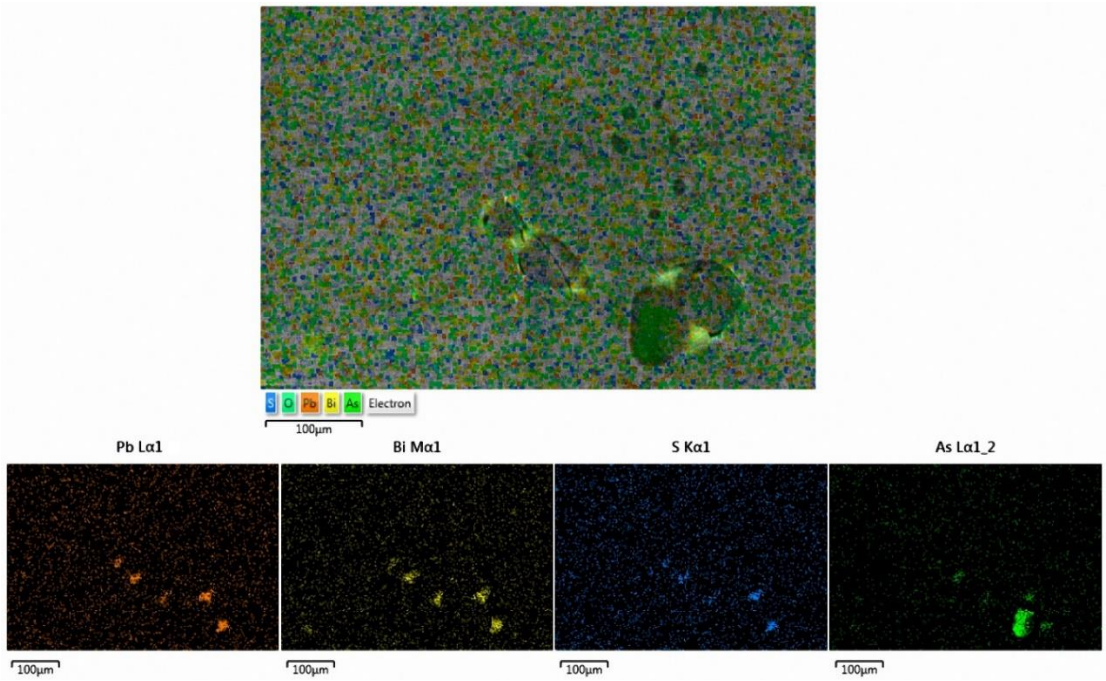

Figure 5.23 EDS elemental distribution maps of the polished slimes in epoxy after heating at 50 ℃ for two days

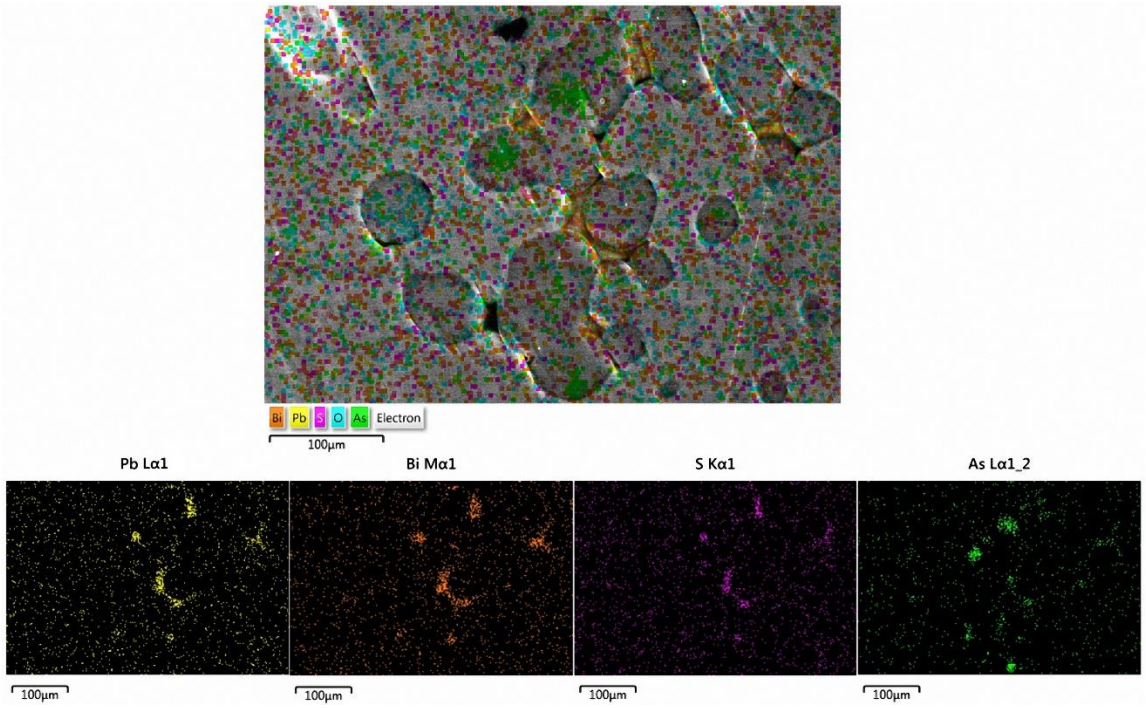

Figure 5.24 EDS elemental distribution maps of the polished slimes in epoxy after heating at 60 ℃ for two days

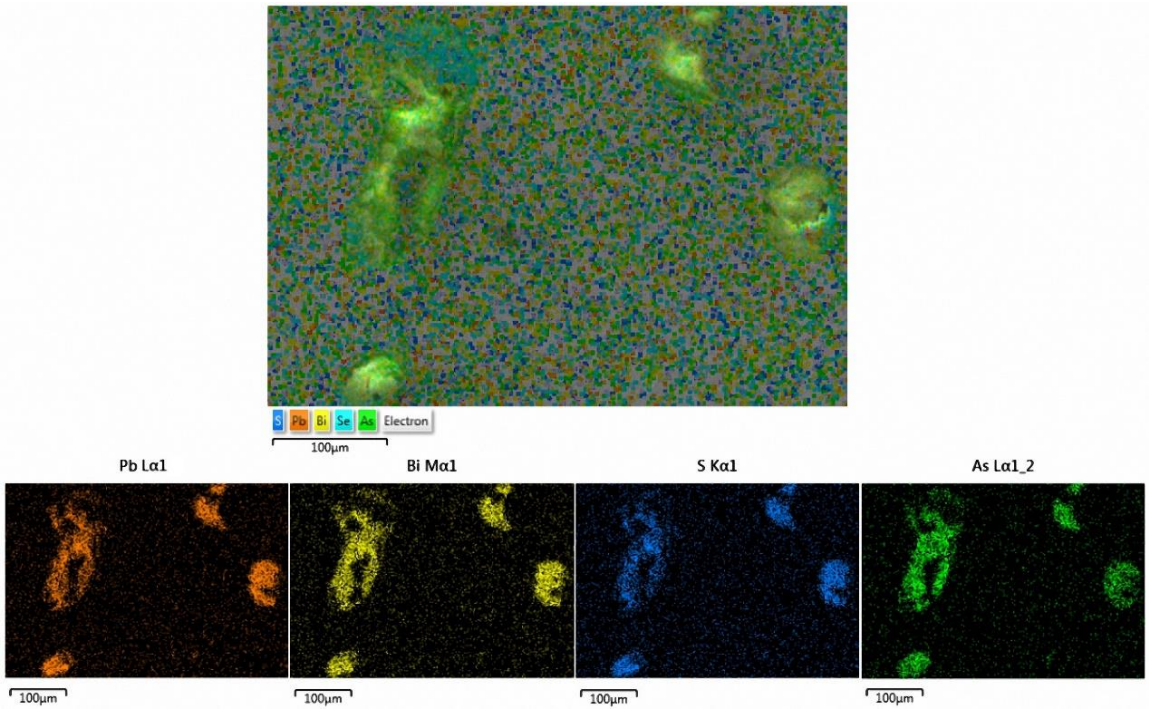

Figure 5.25 EDS elemental distribution maps of the polished slimes in epoxy after heating at 65 ℃ for two days

sintering and coalescence as it is the sintering temperature of the shell rather than that of the core that mostly determines if particles can sinter together or not. Arsenic is the key in determining the type of shell a slime particle has. Some slimes have arsenic distributed at the center core and these slimes have shells made up of mostly Pb, Bi and S (as seen in large coalesced slime particles in Figures 5.23 and 5.24), while some other slimes have arsenic distributed in shells instead of at the core and these slimes have shells involving Pb, Bi, S, as well as As (as seen in large coalesced slime particles in Figure 5.25 and small non-coalesced slimes in Figure 5.23). These are the two major types of shells in the slime particles generated from the tests: one is the type of shell made of the Pb-Bi-S compounds and the other is the type of shell made of the Pb-Bi-S-As compounds.

These two different compounds have different sintering temperatures. The sintering and coalescence of slime particles with different types of compound shells started to happen at different temperatures. Slime particles with shells made of the Pb-Bi-S compounds started to sinter and coalesce at a temperature of 50 ℃ as shown in Figure 5.23, while slime particles with shells made of the Pb-Bi-S-As compounds did not start to sinter and coalesce until heated to 65 ℃ as shown in Figure 5.25. It was found that most slime particles with Pb-Bi-S compound shells were sintered together at the heating temperature of 60 ℃, as shown in Figure 5.24. However, for the slime particles with Pb-Bi-S-As compound shells, there were a few small unsintered slimes remaining after heating at 100 ℃ for two days. This is as expected. Generally, the higher the arsenic content in the Pb-Bi-S-As compound, the higher its sintering temperature will be.

Consequently, further testing of slime particles generated from the electrorefining tests demonstrates the previous hypothesis and inferences. It turned out that the Pb-Bi-S

compounds in the slimes generated from the electrorefining tests have low sintering temperatures of between 50 ℃ and 60 ℃ whereas the Pb-Bi-S-As compounds in the slimes generated from the tests have sintering temperatures higher than 65 ℃, and the higher the arsenic content, the higher the sintering temperature. It is noteworthy that a poor thermal and electrical conductivity cuprous oxide layer attached to the anode surface can result in resistive heating and elevated temperatures in the region in front of the layer during electrorefining, which will be discussed later. Therefore, the sintering and coalescence of slimes in front of the anode surface can happen at even lower cell (electrolyte) temperatures if a resistive surface film is present.

As seen in Table 5.4, most inclusion particles existing in the high impurity anode are associated with the Pb-Bi-S compounds of generally low melting and sintering temperatures (50 ℃ – 60 ℃), which can help inclusion particles that become slime particles to sinter together and adhere to the anode surface in copper electrorefining. For slimes that are uncoated As-O or As-Se cores, they are not likely to sinter together and are more likely to be released from the anode surface and remain suspended in the electrolyte due to small sizes. On the other hand, the low impurity anode has most of its slimes related with the Pb-Bi-S-As compounds, which generally has higher sintering temperatures (> 65 ℃) than the Pb-Bi-S compounds. As a result, these slimes require higher temperatures to sinter together and adhere to the anode surface. Among these slimes, only the slime particles with relatively low arsenic content in the Pb-Bi-S-As compounds can sinter under the cell temperature conditions of less than 85 ℃. Slimes having only Cu-O cores (likely to be Cu_2O) or Cu-Se cores (potentially as Cu_2Se) are very difficult to sinter with other particles and stick to the anode surface.

Different types of anodes are different in slime distributions as shown in Figures 5.12 – 5.15, because they have different inclusion (slime) type distributions as discussed previously. As temperature increases, more and more slime particles in both the high and low impurity anodes can sinter together and adhere to the anode surface. The slime particles can be large or small in presintering initial sizes depending on the original inclusion particle sizes, which will be discussed later. Both large and small inclusion (slime) particles could sinter and adhere to the anode surface as temperature increases, resulting in decreasing weight of both suspended and settled slimes. At the peak adhesion temperature, the slimes mostly adhere to the anode, leaving a small fraction of slimes in suspension or as settled slimes. In fact, the peak adhesion temperature is reached when the slime particles are mostly sintered and coalesced to the extent to which sintering junctions cannot support any more. It is natural for coalesced large particle clusters to become unstable and fall from the anode slimes layer structure to become large slime particles. As a result, the weight of adhered slimes per unit of anode surface area decreases and the weight of settled slimes (large slimes) increases after the peak adhesion temperature.

The fact that high impurity anodes have lower peak adhesion temperatures is because most of their slimes are associated with the low sintering temperature Pb-Bi-S compounds as shells and thus can be mostly sintered and coalesced to the anode surface at lower temperatures. On the other hand, the low impurity anodes have most of their slimes associated with the Pb-Bi-S-As compounds, for which even the slimes with relatively low arsenic content shells have slightly higher sintering temperatures (65 ℃ – 85 ℃) compared to those of most slimes in the high impurity anodes (50 ℃ – 60 ℃). Therefore, the low impurity anodes have higher peak adhesion temperatures, as shown in Figures 5.12

– 5.15. The fact that the strip cycle anodes have slightly higher peak adhesion temperatures than the scrap cycle anodes could be due to the fact that slightly larger percentages of Cu-O core with Pb-Bi-S-As shell inclusions (slimes) and Cu-O core without shell inclusions (slimes) exist in the strip cycle anodes. Please note that cuprous oxide layers attached to anode surfaces can elevate local temperatures and make appreciable slime sintering and coalescence happen at cell temperatures below the sintering temperatures of slime particles as will be discussed further in a subsequent section.

Other phenomena in Figures 5.12 – 5.15 can also be explained. The phenomenon that below the peak adhesion temperatures, the weights of both suspended and settled slimes per unit area decrease faster for the high impurity anodes than for the low impurity anodes is attributed to the fact that most slimes of the high impurity anodes are associated with the Pb-Bi-S compounds that are easier to sinter together and stick to the anode surface, whereas most slimes of the low impurity anodes involve the Pb-Bi-S-As compounds that are harder to sinter and coalesce together. As a result, there are larger amounts of suspended slimes remaining at temperatures higher than the peak adhesion temperatures and larger amounts of settled slimes present at the peak adhesion temperatures for the low impurity anodes than for the high impurity anodes. The fact that the weights of settled slimes from the 85 ℃ tests are even higher than those from the 25 ℃ tests is attributed to the conversion of suspended slimes (small slimes) to coalesced slimes adhered at the anode surface, and finally to settled slimes (large slimes) in solution during electrorefining.

5.4.3 Characterization of Anode Slimes Layer

To demonstrate that slimes associated with the Pb-Bi-S compounds or some of the Pb-Bi-S-As compounds having relatively low arsenic content can sinter together and

adhere to the anode surface, the polished anode slimes layer structure adhered to the surface of the anode was observed and analyzed by SEM and EDS for different types of anodes. Figure 5.26 presents the surface morphology and elemental distributions on the cross-section of a harvested high impurity anode after the 2-day electrorefining test at 55 ℃.

Figure 5.26 shows how typical inclusions existing in the high impurity anodes behaved when they were liberated, exposed to the electrolyte, and became anode slimes in the anode slimes layer structure in front of the anode surface during copper electrorefining. The charging issue in the electron microscope image is because of the nonconductive mounting epoxy existing in the space surrounding anode slimes. The remaining copper anode is shown on the right side of the images and the copper distributions on the left and middle parts of the images is due to polishing procedures that transferred some microscopic copper debris from the anode to the slimes. As the elemental distribution maps show, the anode slimes in front of the anode surface (in the left and middle parts of the maps) originate predominately from the As-O core with Pb-Bi-S shell inclusions. It can be observed that the slime particles firmly coalesced together and adhered to the anode surface, due to slime sintering and coalescence.

In Figure 5.27, it is surprising that small slimes originating from the As-O core with Pb-Bi-S shell inclusions could sinter and coalesce so tightly to the surface of the anode. The copper anode is present on the left side of the images with adhered anode slimes present on the middle and right sides of the images. Lead, bismuth, and sulfur have almost the same elemental distributions. Small slimes in Figure 5.27 could sinter and coalesce together even more tightly than large slimes shown in Figure 5.26. These small slimes were tightly adhered to the anode surface with low porosities. Figure 5.28 shows the SEM/EDS

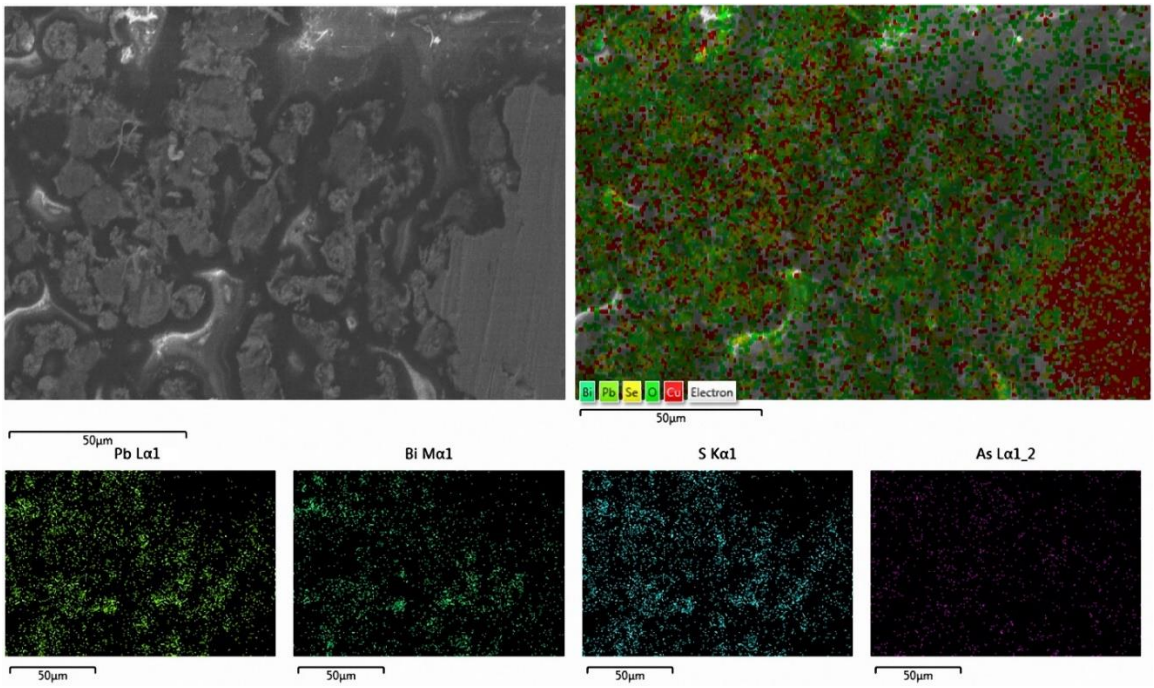

Figure 5.26 SEM electron microscope image and EDS elemental distribution maps of the cross-section of the harvested high impurity strip cycle anode after the 2-day electrorefining test at 55 ℃

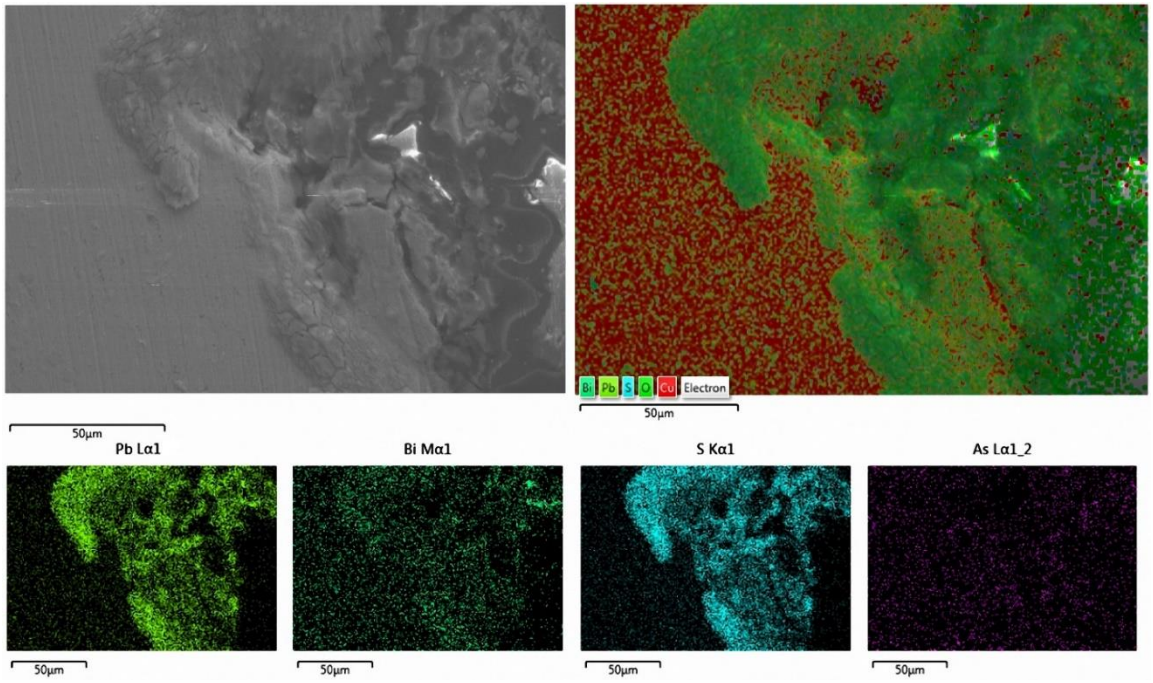

Figure 5.27 SEM electron microscope image and EDS elemental distribution maps of the cross-section of the harvested high impurity scrap cycle anode after the 2-day electrorefining test at 55 ℃

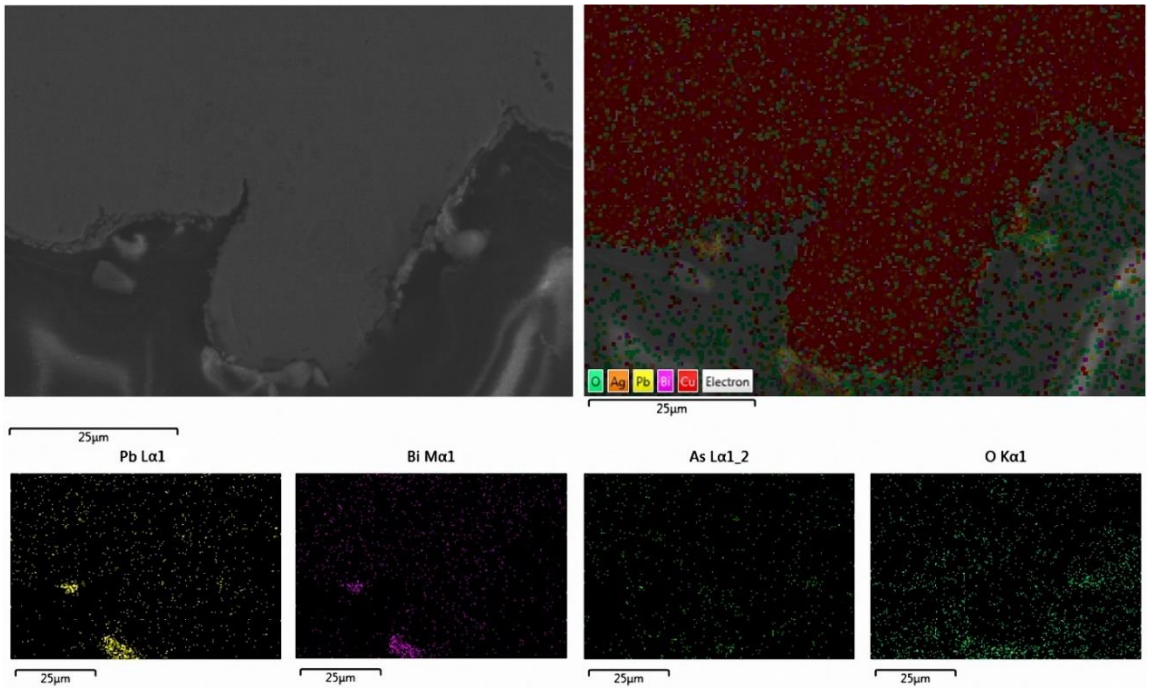

Figure 5.28 SEM electron microscope image and EDS elemental distribution maps of the cross-section of the harvested high impurity scrap cycle anode after the 2-day electrorefining test at 35 ℃

images of the cross-section of a harvested high impurity anode after the electrorefining test at 35 ℃. A small amount of anode slimes is adhered to the anode surface, as only a small scale of slime particle sintering can happen at low cell temperatures. Since the strip cycle anodes and the scrap cycle anodes have very similar inclusion (slime) type distributions, the anode slimes layer structure is not discussed in terms of strip cycle and scrap cycle anodes. In conclusion, the slime particles of the high impurity anodes generally have great capability and tendency to sinter and adhere to the anode surface during the electrorefining process, especially for small slime particles.

Figure 5.29 shows the electron microscope image and elemental distribution maps on the cross-section of a harvested low impurity anode after the electrorefining test at 55 ℃. The remaining copper anode is on the top of the images, with anode slimes on the bottom of the images. The elemental distributions in the anode slimes in the low impurity anode are different from those in the high impurity anodes. Arsenic has a distribution similar to lead, bismuth, and sulfur, which suggests that most of these anode slimes originate from the inclusions associated with the Pb-Bi-S-As compounds. It is noteworthy that there is an oxide layer (most likely cuprous oxide) attached to the anode surface and it may be formed as a result of copper oxidation and can be an indication of anode passivation.[23] The oxide layer was continuous along the anode surface during the test based on SEM images, and a cell voltage increase was noticed after the test was started for some time. The oxide layers were typically found in tests performed at the cell temperature range of 35-60 ℃ for the high impurity anodes and in tests conducted at temperature range of 45-70 ℃ for the low impurity anodes. The oxide layer has much lower thermal and electrical conductivity than the copper matrix and can result in localized resistive heating.

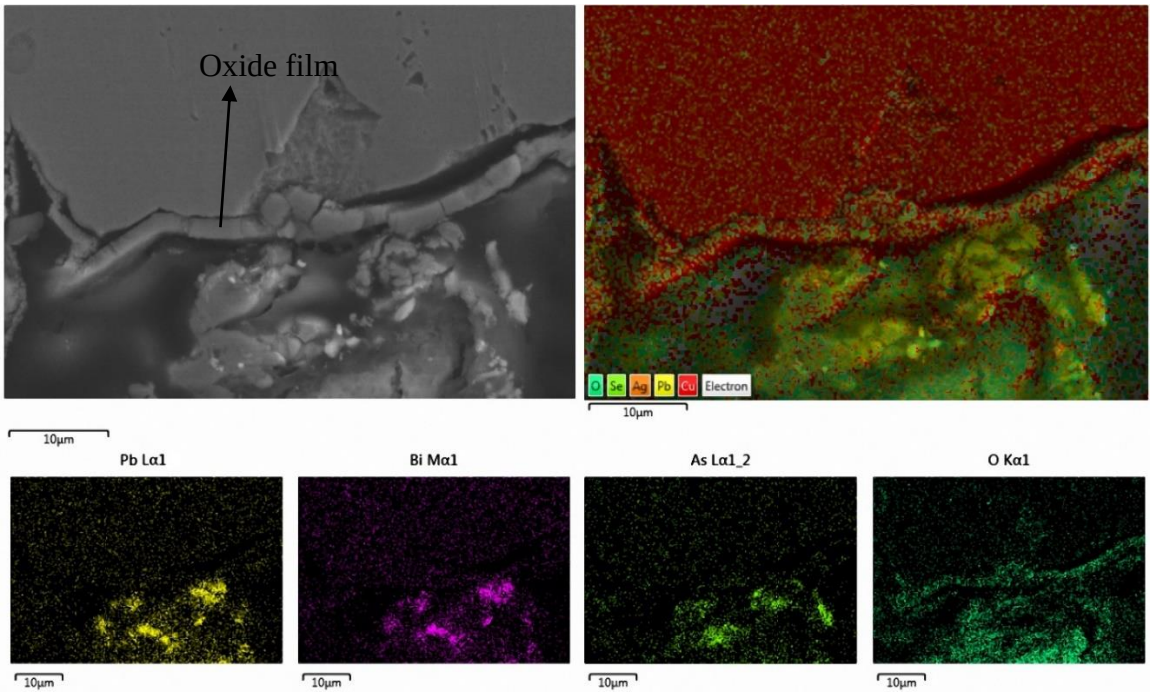

Figure 5.29 SEM electron microscope image and EDS elemental distribution maps of the cross-section of the harvested low impurity strip cycle anode after the 2-day electrorefining test at 55 ℃

As a result, the local temperatures in the region in front of the oxide layer can be elevated and higher than the cell temperature (electrolyte temperature), providing more opportunities for these high sintering temperature slime particles associated with the Pb-Bi-S-As compounds (> 65 ℃) to sinter together and adhere to the anode at lower cell temperatures. As shown in Figure 5.29, many anode slimes coalesced together and adhered to the oxide layer on the anode surface. Figure 5.30 shows the cross-section of a harvested low impurity anode after the electrorefining test at 70 ℃. A large amount of anode slimes are adhered to the anode surface, for slime particles can easily sinter together at high cell temperatures.

The oxide layer on the anode surface also exists in the harvested high impurity anodes to help slimes associated with the Pb-Bi-S compounds of low sintering temperatures (50 ℃ – 60 ℃) to sinter and adhere to the anode at even lower cell temperatures, which is shown in Figure 5.31.

As seen in the graph, the element intensities vary as the line moves across the copper anode, the sintering particle, and the remainder of coalesced anode slimes. In the copper anode, only copper has high peaks without appreciable intensities of other impurity elements. At the position where sintering and coalescence happened, the copper peaks drop rapidly and the intensities of lead, bismuth, and arsenic increase to significant levels. Notice that the top shell of this sintering particle was partially stripped off due to sample polishing and part of the core was exposed and thus could be detected by EDS. This is the reason why the arsenic peaks are distributed at the center of the sintering particle (the position of the arsenic core) and why the peaks of lead and bismuth drop at this position. The remaining peaks of lead and bismuth at this position may be due to the existence of a residual shell

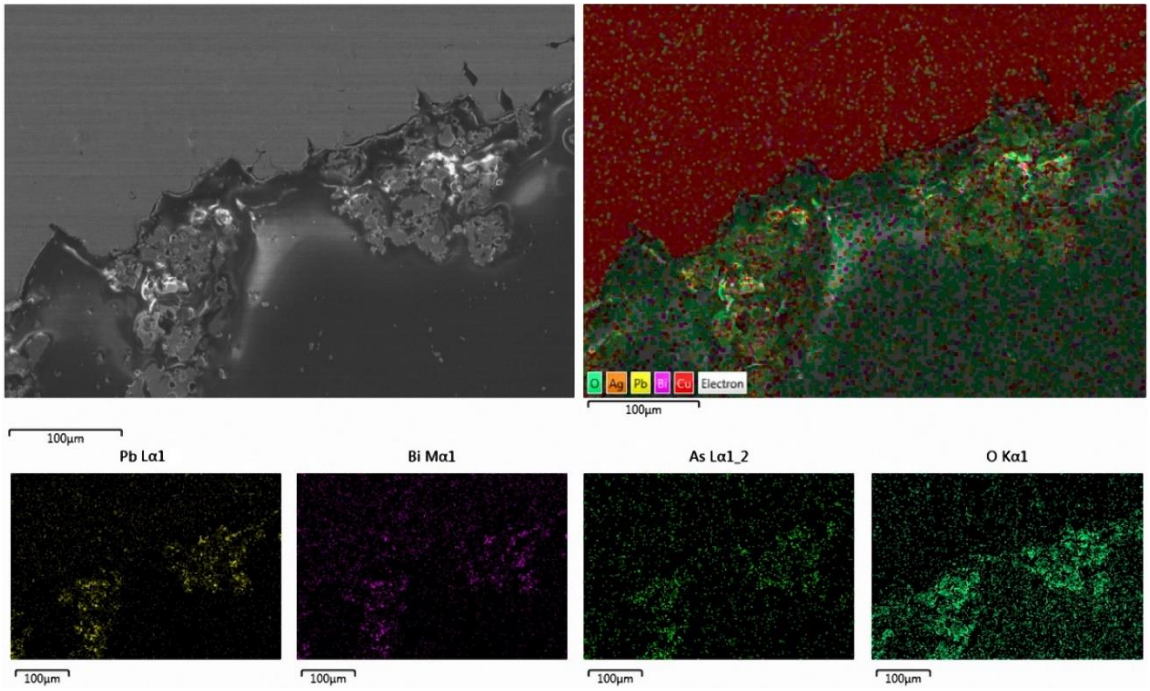

Figure 5.30 SEM electron microscope image and EDS elemental distribution maps of the cross-section of the harvested low impurity strip cycle anode after the 2-day electrorefining test at 70 ℃

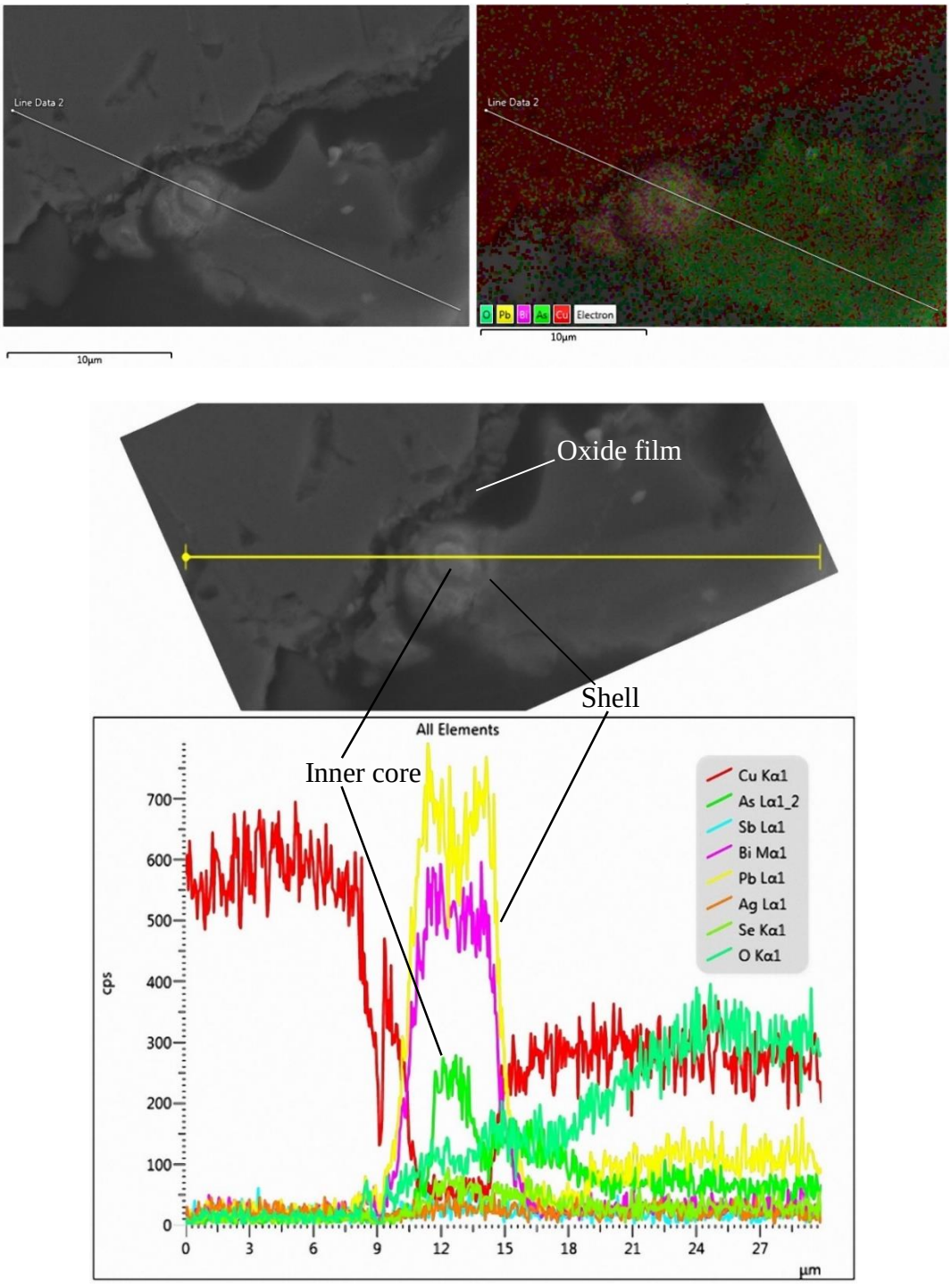

Figure 5.31 EDS elemental line scan results of the anode slimes layer structure in front of the anode surface of the harvested high impurity strip cycle anode after the 2-day electrorefining test at 35 ℃

over the particle core. In the coalesced anode slimes at the right position, the peaks of copper and oxygen increase, demonstrating that copper oxide (potentially cuprous oxide) is the major constituent of slimes at this position. Figure 5.31 shows that the oxide layer on the anode surface can also help slime particles with the low sintering temperature Pb-Bi-S compound shell to sinter and adhere to the anode at even lower cell temperatures (35 ℃). This set of images also demonstrates that slime particle sintering does not require the whole slime particle to be made up of materials of low sintering temperatures and it can happen with only part (the shell) of slime particles made up of low sintering temperature materials.

The sintering and coalescence of anode slimes can help them to adhere to the surface of the anode in the anode slimes layer as shown in Figures 5.26 – 5.31, thus improving slime adhesion to the anode and reducing cathode contamination. Nevertheless, as temperature was further increased above the peak adhesion temperature, the slime adhesion to the anode decreased and the settled slimes on the bottom of the cell increased for all types of anodes tested, as shown in the experimental results section. This phenomenon is attributed to sintering junctions that could not hold coalesced particle clusters of large slime particles in the anode slimes layer adhered to the anode surface. Thus, these particle clusters were dissociated from the layer structure and released to the electrolyte. These released slime clusters were large in size and tended to settle down to the cell bottom. This phenomenon of released slime clusters above the peak adhesion temperature was observed for all types of anodes tested.

5.4.4 Further Analyses of Slime Particles

Due to the effect of particle sintering and coalescence, the sizes of slimes in the anode slimes layer and the slimes liberated from it should become larger as temperature

increases, for more and more slime particles sinter and coalesce together at higher temperatures. In order to verify this, samples of settled slimes on the cell bottom were collected after the tests, as well as the suspended slimes in the solution. These slimes were separated from the electrolyte by a centrifuge and dried in air. Finally the sizes of these slimes were analyzed for particle size distributions. Figure 5.32 shows the settled slime size distribution at cell temperature 35 ℃ for the high impurity anodes as an example. According to the particle size distribution results, the sizes of suspended slimes are mostly smaller than 9-10 microns and the sizes of settled slimes are commonly larger than 9-10 microns. To present particle size changes of suspended and settled slimes, Figure 5.33 shows the relationship between the median diameter D_{50} (the value of the particle diameter at 50% in the cumulative distribution) and the cell temperature for the suspended and settled slimes of the high impurity anodes.

A small increase of the particle sizes of suspended and settled slimes from the original sizes of inclusion particles was observed at 35 ℃, which means a small amount of particle coalescence or aggregation happened at 35 ℃. However, particle sizes of suspended slimes and settled slimes at higher temperatures show significant increases, as shown in Figure 5.33. The higher the temperature, the larger the sizes of suspended and settled slimes, which means that more and more slime particles sintered together as temperature increased. Therefore, it demonstrates that slime particles can sinter and coalesce together in front of the anode during copper electrorefining and the extent of sintering becomes larger with increasing cell temperature. For the low impurity anodes, a similar plot is shown in Figure 5.34, presenting the relationship between the slime particle median diameter and the cell temperature. It is noteworthy that the particle sizes show

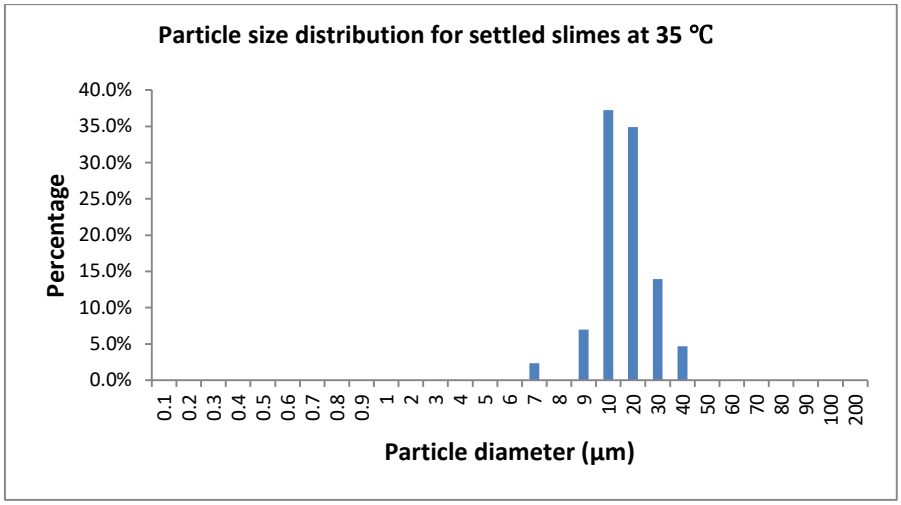

Figure 5.32 Settled slime particle size distribution at cell temperature 35 ℃ for the high impurity scrap cycle anode

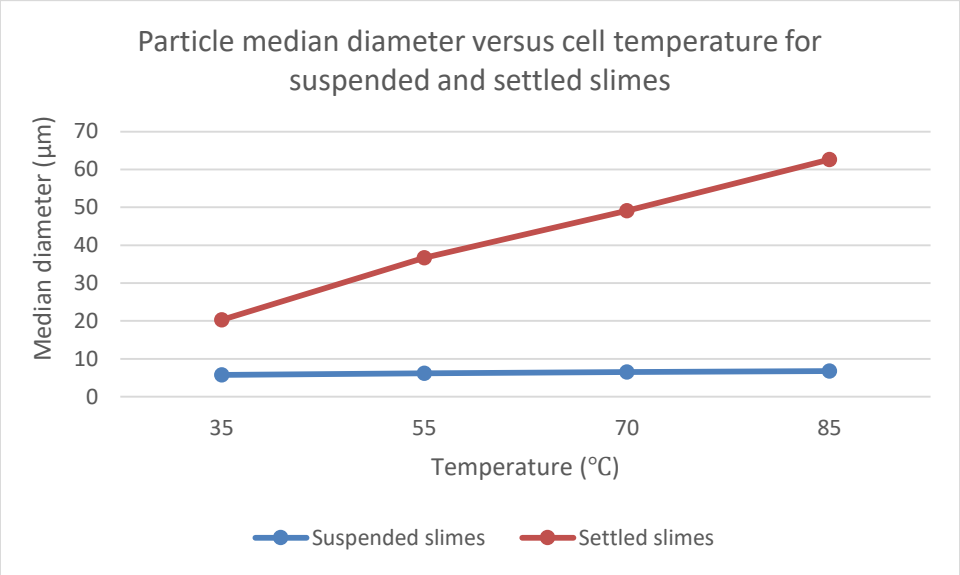

Figure 5.33 Relationship between the slime particle median diameter D_{50} and the cell temperature for the high impurity scrap cycle anode

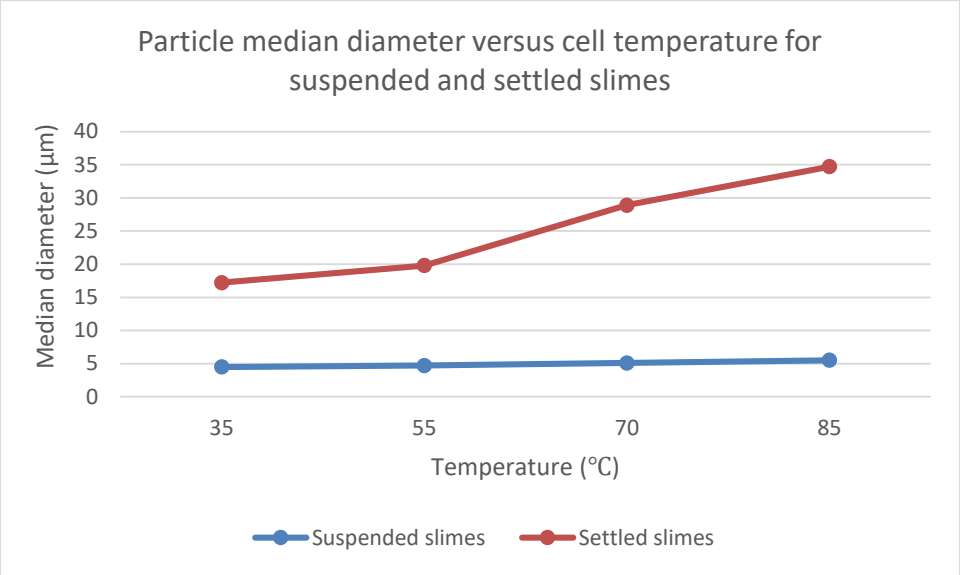

Figure 5.34 Relationship between the slime particle median diameter D_{50} and the cell temperature for the low impurity strip cycle anode

significant increase at higher temperatures, which is consistent with higher sintering temperatures of the slimes in the low impurity anodes.

Samples of collected slimes from the electrolyte after the 2-day electrorefining tests were also analyzed by EDS to examine the shell compositions of large (settled) slimes and small (suspended) slimes. As shown in Figure 5.35, lead, bismuth, and sulfur have very similar distributions while arsenic has an entirely different distribution. Moreover, arsenic is mostly distributed on small slimes, which are on the top of large slimes, while lead, bismuth, and sulfur are distributed with large slimes as well as with small slimes. Notice that only the elements in the shell of slime particles can be detected. The results indicate that small slimes, which are unsintered or less sintered, have shells associated with the Pb-Bi-S-As compounds but large slimes, which are sintered and coalesced slimes, have shells related with the Pb-Bi-S compounds. These results are consistent with previous findings that slime particles with Pb-Bi-S shells are easier to sinter and coalesce as large particles than slime particles with Pb-Bi-S-As shells that tend to remain as small particles.

The sintering and coalescence of anode slimes can increase the amount of settled slimes and decrease the amount of suspended slimes by converting small suspended slimes to large settled slimes, which was demonstrated by the slime distributions at different temperatures presented in Figures 5.12 – 5.15. However, the type of slimes that contributes most to the contamination of copper cathode needs to be discussed. By using the weight data of suspended slimes and settled slimes at different temperatures shown in Figures 5.12 – 5.15 and the data of bismuth levels in copper cathode at different temperatures presented in Tables 5.2 and 5.3, it was found that the weight of suspended slimes is positively correlated with the bismuth level in the cathode while no appreciable correlation between

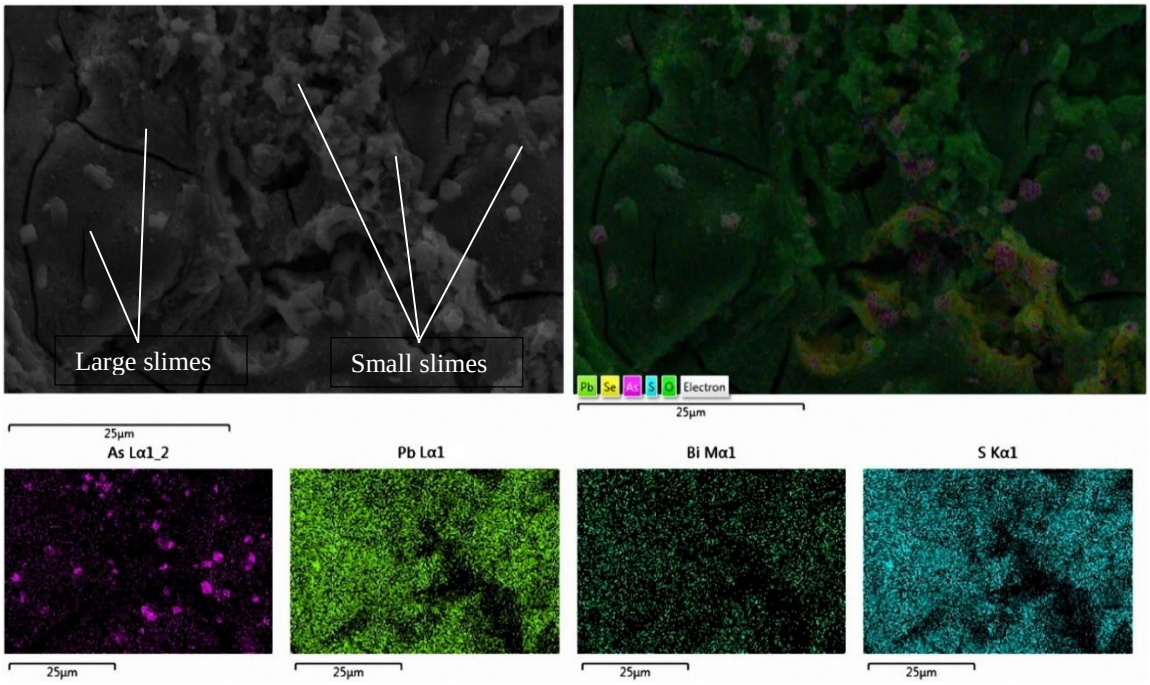

Figure 5.35 SEM electron microscope image and EDS elemental distribution maps of large (settled) slimes and small (suspended) slimes collected from the electrolyte after the 2-day electrorefining tests

the weight of settled slimes and the cathode bismuth level could be found. Hoffman also indicated that bismuth contamination of the copper cathode could be reduced if almost all bismuth exists in the anode slimes layer rather than in the precipitates (small slimes) in the electrolyte.[24] Figure 5.36 shows the modeling of the relationship between the weight of suspended slimes and the bismuth level in copper cathode.

As shown in Figure 5.36, the relationship between the bismuth level in copper cathode and the weight of suspended slimes in electrolyte follows a logarithmic trend. The result shows that the bismuth level in the cathode has a positive correlation with the weight of suspended slimes, which indicates that increasing suspended slimes in the electrolyte increases the contamination in the cathode. Although only bismuth levels in copper cathode were analyzed, other impurity elements such as lead and sulfur may have similar distributions in the cathode, as these elements have very similar distributions in the anode and they form the shell of some anode inclusion particles. Consequently, impurities such as lead and sulfur in the cathode should have similar positive relationships with the weight of suspended slimes in electrolyte. In addition, this positive correlation between the amount of suspended slimes in electrolyte and the impurity levels in copper cathode explains the experimental results. The amounts of suspended slimes at cell temperatures equal or above 45 ℃ are smaller for the high impurity anodes than for the low impurity anodes. As a result, the bismuth levels are lower on copper cathodes harvested in experiments using the high impurity anodes than on those harvested in experiments using the low impurity anodes, when the cell temperature is equal to or higher than 45 ℃.

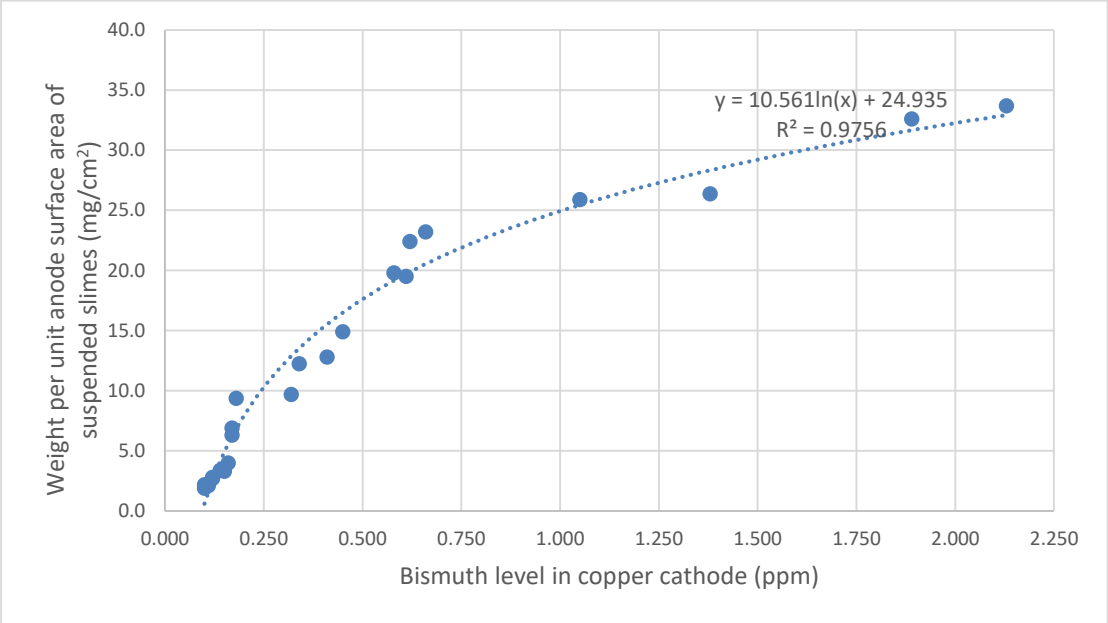

Figure 5.36 Relationship between the weight per unit anode surface area of suspended slimes and the bismuth level in copper cathode

5.4.5 Characterization of Copper Cathode

The positive correlation between the impurity level in the cathode and the amount of suspended slimes in electrolyte indicates that the contamination of copper cathode is mainly due to suspended slimes in electrolyte. In order to further verify this, SEM electron microscope images showing the inclusions in harvested cathodes after the 2-day electrorefining tests at cell temperatures of 35 ℃ and 70 ℃ are presented in Figures 5.37 and 5.38. As seen in the graphs, the inclusions existing in the copper cathodes are small particles, with their sizes increased at higher cell temperature. The particle sizes of the inclusions in the cathodes are within the size range of suspended slimes (below 9 microns), rather than that of the settled slimes, which indicates that these inclusion particles in the cathodes originate from suspended slimes in the electrolyte. In other words, it is the suspended (small) slimes that were co-deposited on the cathode with copper, rather than the settled (large) slimes. Thus, the suspended slimes are indeed responsible for a substantial part of the contamination of copper cathode and the larger the amount of suspended slimes in the electrolyte, the more contamination in the cathode, as discussed. Consequently, not only can the sintering and coalescence of slime particles help increase the cathode purity by improving adhesion of slimes to the anode, it can also reduce cathode contamination by decreasing the amount of suspended slimes in the electrolyte.

5.4.6 The Effects of Temperature and Anode Composition

Temperature is certainly one key to enhance sintering and coalescence of slimes, as higher temperature can let more slime particles reach their sintering temperatures, coalesce with other slimes to form larger slime particles, and better adhere to the anode surface. Another key to strengthen sintering of slime particles is the composition of copper

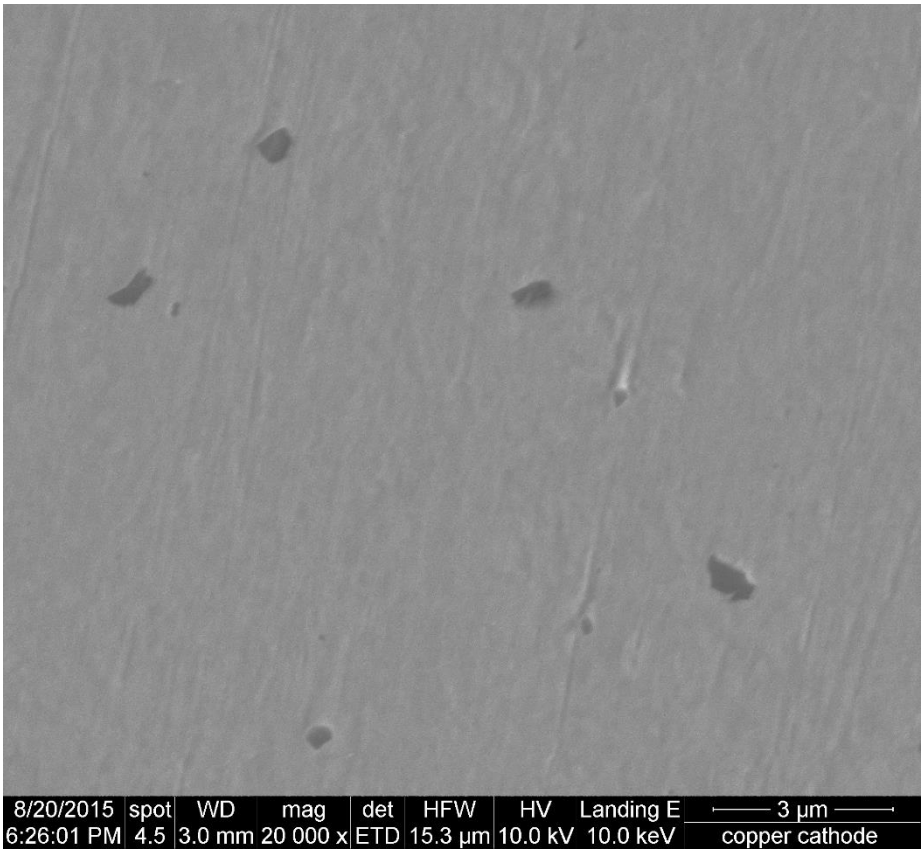

Figure 5.37 SEM electron microscope image of the cross-section of a harvested cathode from the 2-day electrorefining tests at cell temperature 35 ℃

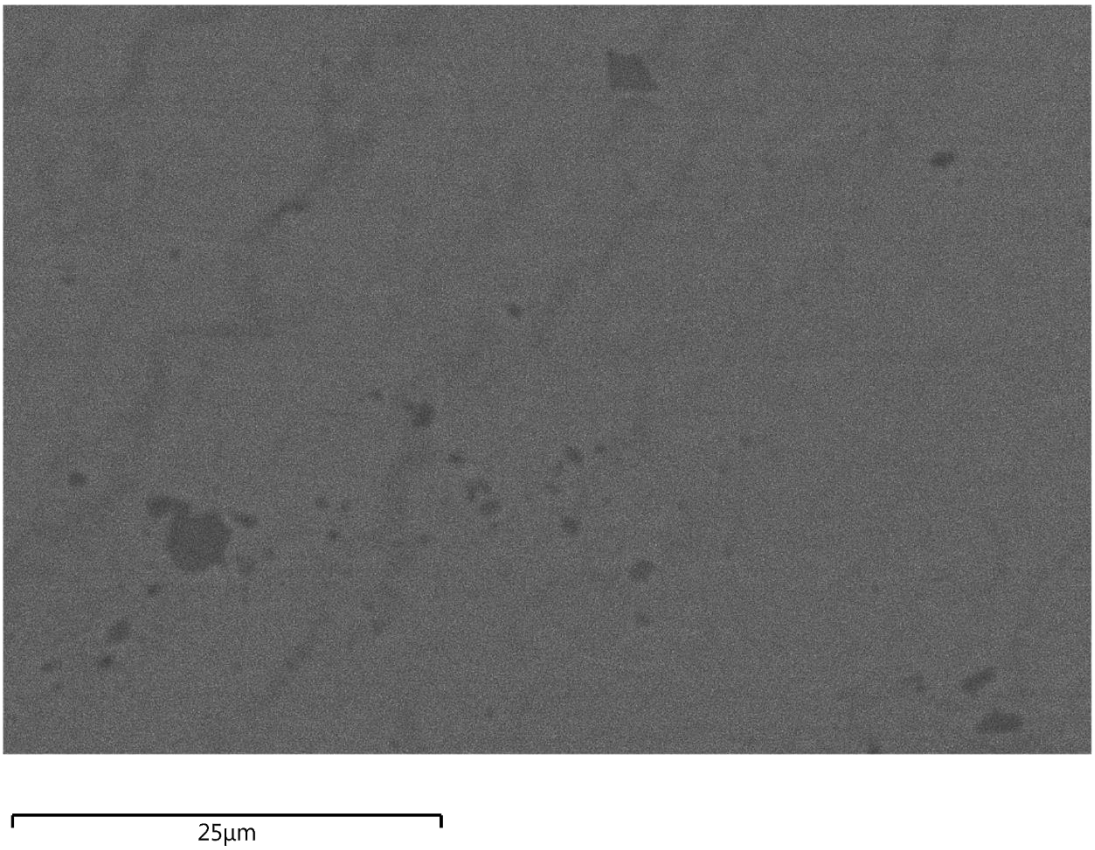

Figure 5.38 SEM electron microscope image of the cross-section of a harvested cathode from the 2-day electrorefining tests at cell temperature 70 ℃

anodes. It can be concluded from the above discussions that the high impurity anodes have better performance in slime particle sintering and coalescence than the low impurity anodes. Also, according to the experimental results of slime distributions and bismuth levels in copper cathode at different cell temperatures, the scrap cycle anodes have better performance than the strip cycle anodes, because the scrap cycle anodes have lower peak adhesion temperatures (indicating that slime sintering happens at lower temperatures) and the copper cathode harvested using the scrap cycle anodes have even lower bismuth levels at higher cell temperatures (≧45 ℃) although the scrap cycle anodes have generally higher impurity levels than the strip cycle anodes. This phenomenon is mainly because arsenic concentrations in the high impurity anodes and the scrap cycle anodes are higher and thus the associated arsenic has a greater tendency to be solidified as arsenic dominant compounds such as the As-O compounds instead of in solid solutions or compounds dominated by other elements such as the Pb-Bi-S-As compounds, as discussed previously. Thus, at high arsenic levels more cores are formed as As-O compound based nuclei on which the shells of lower melting point compounds can precipitate. Therefore, the shell of most inclusion (slime) particles in the high impurity anodes and the scrap cycle anodes is more likely to be made of the Pb-Bi-S compounds of low sintering temperatures (50 ℃ – 60 ℃) instead of the Pb-Bi-S-As compounds of high sintering temperatures (> 65 ℃). As a result, the high impurity anodes and the scrap cycle anodes have smaller percentages of inclusion types of Cu-O core with Pb-Bi-S-As shell and Cu-O core without shell than the low impurity anodes and the strip cycle anodes. Smaller percentages of inclusions (slimes) associated with high sintering temperature compounds lead to lower peak adhesion temperatures, smaller amounts of suspended slimes, and lower impurity levels in the

cathode.

The beneficial role of arsenic in copper electrorefining is evident in the experimental results that the high impurity anodes that have higher content of bismuth and arsenic produced copper cathodes with even lower bismuth levels at higher cell temperatures (≧45 ℃) than the low impurity anodes, as shown in Tables 5.2 and 5.3. Therefore, the composition of anodes used in copper electrorefining should be adjusted such that the arsenic concentration in the anode is increased to a certain level at which the As-O cores can be formed favorably while the Pb-Bi-S-As compounds of high sintering temperatures cannot form during the copper anode smelting process.

5.5 Conclusions

Four series of copper electrorefining tests were performed using four different types of anodes with different impurity contents. The results show that the high impurity anodes and the scrap cycle anodes have better performance than the low impurity anodes and the strip cycle anodes respectively, in terms of the peak adhesion temperature, the amounts of different types of slimes, and the impurity level on the cathode. The inclusion type distributions were analyzed for all types of anodes. The high impurity anodes are characterized by the inclusion types of As-O core with Pb-Bi-S shell and As-O core without shell, while the low impurity anodes are characterized by the inclusion types of Cu-O core with Pb-Bi-S-As shell and Cu-O core without shell. The strip cycle anodes have larger percentages of inclusion types of Cu-O core with Pb-Bi-S-As shell and Cu-O core without shell than the scrap cycle anodes.

Slimes associated with different types of compounds were heated to test the sintering temperature ranges of these compounds. The results demonstrate that the Pb-Bi-

S compounds have sintering temperatures ranging from 50 ℃ to 60 ℃ and the Pb-Bi-S-As compounds have sintering temperatures above 65 ℃. The high impurity anodes have most of their inclusion (slime) particles associated with the Pb-Bi-S compounds while the inclusion particles in the low impurity anodes are mostly associated with the Pb-Bi-S-As compounds. Therefore, inclusion (slime) particles released from the high impurity anodes are easier to sinter together as larger particles and stick to the anode surface than those released from the low impurity anodes. The scrap cycle anodes perform better in slime particle sintering and coalescence than the strip cycle anodes, because of the smaller percentage of inclusions associated with the Pb-Bi-S-As compounds.

Furthermore, the SEM and EDS analyses results of anode slimes layers adhered to anode surfaces are consistent with previous findings and show that anode slimes sintered at lower cell temperatures for the high impurity anodes than for the low impurity anodes. It is believed that the cuprous oxide layer attached to the anode surface can help slime particles to sinter at even lower cell temperatures by elevating local temperatures in front of the anode surface due to localized resistive heating. The particle size distributions of original inclusions in the anode, suspended slimes, and settled slimes confirm the occurrence of slime particle sintering and coalescence. In addition, the EDS elemental distribution maps of small slimes and large slimes are also consistent with previous conclusion that the small slimes have a lot of arsenic in the shell but the large slimes do not.

Another finding is that suspended slimes, rather than settled slimes, were shown to be a major source of the contamination of copper cathode. Therefore, to reduce cathode contamination, slime particle sintering and coalescence in front of the anode surface should

be enhanced to increase the amount of large (settled) slimes and decrease the amount of small (suspended) slimes, as well as to improve anode slime adhesion. However, anode slime adhesion can be reduced with excessive particle sintering that increases the tendency for slime fall with large slimes that settle rapidly without contributing to the cathode contamination.

The cell temperature and the composition of copper anode are the two major factors that determine the extent of slime particle sintering and coalescence. Increasing cell temperature and the content of arsenic in the anode when appropriate lead, bismuth, and sulfur levels are present can result in more slime sintering, leading to better anode slime adhesion, less suspended slimes, and higher cathode purity.

5.6 References

1. W. Zeng, J. Werner, and M. L. Free: *Hydrometallurgy*, 2015, vol. 156, pp. 232-38.
2. W. Zeng, M. L. Free, J. Werner, and S. Wang: *J. Electrochem. Soc.*, 2015, vol. 162, pp. E338-52.
3. T. T. Chen and J. E. Dutrizac: *JOM*, 1990, vol. 42, pp. 39-44.
4. T. T. Chen and J. E. Dutrizac: *Can. Metall. Q.*, 1988, vol. 27, pp. 91-96.
5. T. T. Chen and J. E. Dutrizac: *Can. Metall. Q.*, 1990, vol. 29, pp. 27-37.
6. T. T. Chen and J. E. Dutrizac: *Can. Metall. Q.*, 1989, vol. 28, pp. 127-34.
7. T. T. Chen and J. E. Dutrizac: *Can. Metall. Q.*, 1991, vol. 30, pp. 95-106.
8. T. T. Chen and J. E. Dutrizac: *Metall. Mater. Trans. B*, 2005, vol. 36, pp. 229-40.
9. T. T. Chen and J. E. Dutrizac: *Can. Metall. Q.*, 1991, vol. 30, pp. 173-85.
10. T. T. Chen and J. E. Dutrizac: *Can. Metall. Q.*, 1996, vol. 35, pp. 337-51.
11. O. Forsen and K. Lilius: *The Electrorefining and Winning of Copper: Proceedings of the Symposium in TMS 116th Annual Meeting*, Denver, CO, 1987, pp. 47-69.

12. M. Mitan: *Microstructure and Morphology of Impure Copper Anodes*, University of AZ, 1997.

13. T. T. Chen and J. E. Dutrizac: *Can. Metall. Q.*, 1988, vol. 27, pp. 97-105.

14. J. D. Scott: *Metall. Trans. B*, 1990, vol. 21, pp. 629-35.

15. T. T. Chen and J. E. Dutrizac: *Metall. Trans. B*, 1989, vol. 20, pp. 345-61.

16. X. Cheng and J. B. Hiskey: *Metall. Mater. Trans. B*, 1996, vol. 27, pp. 610-16.

17. J. B. Hiskey: *T.T. Chen Honorary Symposium on Hydrometallurgy, Electrometallurgy and Materials Characterization*, John Wiley & Sons, Inc., Hoboken, NJ, 2012, pp. 101-12.

18. F. Noguchi, N. Iida, T. Nakamura, and Y. Ueda: *Proceedings of the Copper 1991-Cobre 91*, Ottawa, Canada, 1991, vol. 3, pp. 391-404.

19. J. P. Demaerel: *The Electrorefining and Winning of Copper: Proceedings of the Symposium in TMS 116th Annual Meeting*, Denver, CO, 1987, pp. 195-209.

20. D. Hanus: *Pr. Inst. Met. Niezelaz.*, 1987, vol.16, pp. 35-39.

21. P. C. Angelo and R. Subramanian: *Powder Metallurgy: Science, Technology and Applications*, PHI Learning Private Ltd., New Delhi, 2008.

22. G. Cao and Y. Wang: *Nanostructures and Nanomaterials: Synthesis, Properties, and Applications*, World Scientific Publishing Co. Pte. Ltd., Singapore, 2011.

23. M. S. Moats and J. B. Hiskey: *Proceedings of Copper 2010 Conference*, Hamburg, Germany, 2010, vol. 4, pp. 1463-82.

24. J. E. Hoffmann: *JOM*, 2004, vol. 56, pp. 30-33.

CHAPTER 6

EXPERIMENTAL AND SIMULATION STUDIES OF ELECTROLYTE FLOW AND SLIME PARTICLE TRANSPORT IN A PILOT SCALE COPPER ELECTROREFINING CELL

Copper electrorefining tests were conducted in a pilot scale cell made of transparent cell walls, allowing direct observation and microscopic video recording of the electrolyte flow. Fluid flow velocities in the gaps between adjacent anodes and cathodes were measured by analyzing the recorded video using video analysis and modeling software. Modeling and simulation of copper electrorefining in this cell were performed using COMSOL Multiphysics, a finite element method simulation software. The flow velocity field results from modeling agree reasonably well with the measured electrolyte velocities. The transport of slime particle in electrolyte flow was also simulated and the appearance frequencies of slime particles in the domain within 200 microns from cathode surfaces at different positions of cathodes were compared with impurity levels in the copper cathodes harvested from experimental tests. The results show good correlation especially with the total concentration of major impurities. Thus the cathodic contamination can be predicted by the slime particle appearance frequency in front of the cathode.

6.1 Introduction

In copper electrorefining, much of the final cathode metal contamination originates from anode inclusions that involve various impurities including silver, lead, arsenic, antimony, bismuth, selenium, etc. Most of these impurities can be transported to the cathode through two major mechanisms: 1) the impurities in refractory inclusions that become anode slimes in the process can be transported to the cathode by electrolyte flow, and 2) the dissolved impurities as ions can also be transported to the cathode and become electrochemically co-deposited with copper. It is also noteworthy that some dissolved impurities can precipitate in the electrolyte, leading to floating slimes that can also jeopardize cathodic quality.[1] Some researchers found that arsenic can co-precipitate antimony and bismuth through homogeneous precipitation, which helps remove dissolved impurities from the electrolyte.[2-4]

Cathode contamination by slime particles is significant in copper electrorefining. In the bottom of electrorefining cells, settled slimes are collected and processed further to recover valuable elements. Settled slimes generally do not harm the purity of the cathode and contain precious metals such as gold. However, suspended slimes in electrorefining cells are troublesome and can reduce cathode purity. Previous study shows that suspended slimes have positive correlation with impurity levels in cathodes while no appreciable correlation can be found between settled slimes and cathode impurity concentrations.[5] It was found that the suspension of slime particles mostly depends on the interaction between their settling velocities and local upward flow velocities.[6] Settled slimes are generally particles with large diameters that facilitate rapid settling. Suspended slimes, on the other hand, have small diameters and low settling velocities, allowing them to remain suspended

in electrolyte by upward electrolyte flow. The settling velocities of slime particles and local upward flow velocities can be affected[6, 7] by inlet flow rate, temperature, and current density. The composition of anodes and the cell temperature have significant effects on the sizes of slime particles by affecting slime particle sintering and coalescence during copper electrorefining.[5] Increasing cell temperature and anode arsenic concentration with proper lead, bismuth, and sulfur contents can lead to more slime sintering and coalescence, less suspended slimes, and purer cathode copper.[5]

The fluid flow velocity field plays a key role in determining slime particle movement in copper electrorefining cells and is worthy of a comprehensive study. Experimental measurements and simulation studies on fluid flow fields in copper electrorefining have been done by researchers.[6, 8-14] Eklund, et al. measured copper concentration field and flow velocity field by Holographic Laser Interferometry and Laser-Doppler Velocimetry respectively.[8] Their experimental results agreed with their simulation predictions well. Konishi, et al. used holographic interferometry and tracer technique to measure copper concentration profile and velocity profile.[9] Fluid recirculation between the plates (anode and cathode) caused by electrolyte density gradients was found to be significant.[10] Upward flow is typically along the cathode surface and downward flow accompanies the anode surface. The inlet flow also exerts effects on the flow pattern between the electrodes.[6] Leahy, et al. used ANSYS to model natural convection in copper electrorefining and they validated their model for different cases varying in size.[11] Kawai, et al. examined the effects of electrolyte circulation ways on the flow pattern between the plates.[12] Recently, modelling of the electrolyte flow in industrial scale electrorefining cells has been done and was utilized to optimize cell performance.[13, 14] Furthermore, Ling, et al.

found that anode slime behavior is significantly affected by the flow circulation pattern and the rate and direction of the movements of fine slime particles can be changed by the circulation rate and direction.[15]

In this study, the fluid velocity field in a pilot scale copper electrorefining cell was studied by both experimental measurements and CFD simulations. Also, the slime particle transport in the electrolyte flow was simulated. Experimental copper electrorefining tests were performed in this pilot scale cell (48 inches height, 10.875 inches depth, and 7 inches width). The cell wall is made of transparent material allowing direct observation of electrolyte flow from outside of the cell. Videos of fluid flow patterns were recorded during the experiments. The video files were analyzed for flow velocities by a video analysis software named Tracker.

Modeling and simulation of the copper electrorefining process in this cell were performed by using COMSOL Multiphysics. The simulation results of the fluid velocity field in the cell were validated by the experimentally measured flow velocities from recorded videos. The simulations allow additional predictions of fluid flow fields in the electrorefining cell under different conditions (e.g., current density, temperature, inflow rate).

Based on the experimental and simulation results, features of the flow velocity field in the cell are discussed. The connection between the flow field and particle transport is also discussed. The simulation results of the slime particle appearance frequency in the domain within 200 microns from cathode surface were compared with experimental cathodic impurity concentrations.

6.2 Experimental Description

A specially designed pilot scale electrorefining cell (by Dr. Shijie Wang, Principal Advisor) located in the tankhouse of Kennecott Utah Copper LLC refinery was utilized for the experimental copper electrorefining tests. A photo of the cell on site is shown in Figure 6.1 and a design drawing of the cell is shown in Figure 6.2. As shown in the graphs, the cell is about 50 inches in height, 12 inches in depth, and 8.5 inches in width (the electrolyte domain is 48 inches in height, 10.875 inches in depth, and 7 inches in width). The cell walls are made of transparent, acid-resistant polymer materials. An inlet and associated valve are located at a position 6 inches from the bottom of the cell and an outlet weir and tube are located at the top of the cell. All pipes connected with the inlet and the outlet are similar in composition to those used for commercial cells. Five electrodes are placed in the cell in the sequence of "cathode-anode-cathode-anode-cathode," forming four gaps as shown in Figure 6.1. Each anode is 35.5 inches in height (32.25 inches immersed in electrolyte), 1.5 inches in depth, and 4.2 inches in width. Each cathode blank is 36.625 inches in height (33.375 inches under electrolyte level), 0.3 inches in depth, and 4.75 inches in width. Thus, cathode blanks are 1.125 inches longer than anodes in height. The distance between the centers of the two anodes is 4 inches and the width of the gaps between each adjacent anode and cathode is about 1 inch.

A rectifier was utilized to supply constant current to the anodes, through the electrolyte, and to the cathodes. All anodes sit on a conductive metal plate located on one side of the top of the cell, connected to the positive pole of the rectifier; all cathodes sit on another conductive metal plate located on the other side of the top of the cell, connected to the negative pole of the rectifier. The electrolyte used in the tests comes from the circulation

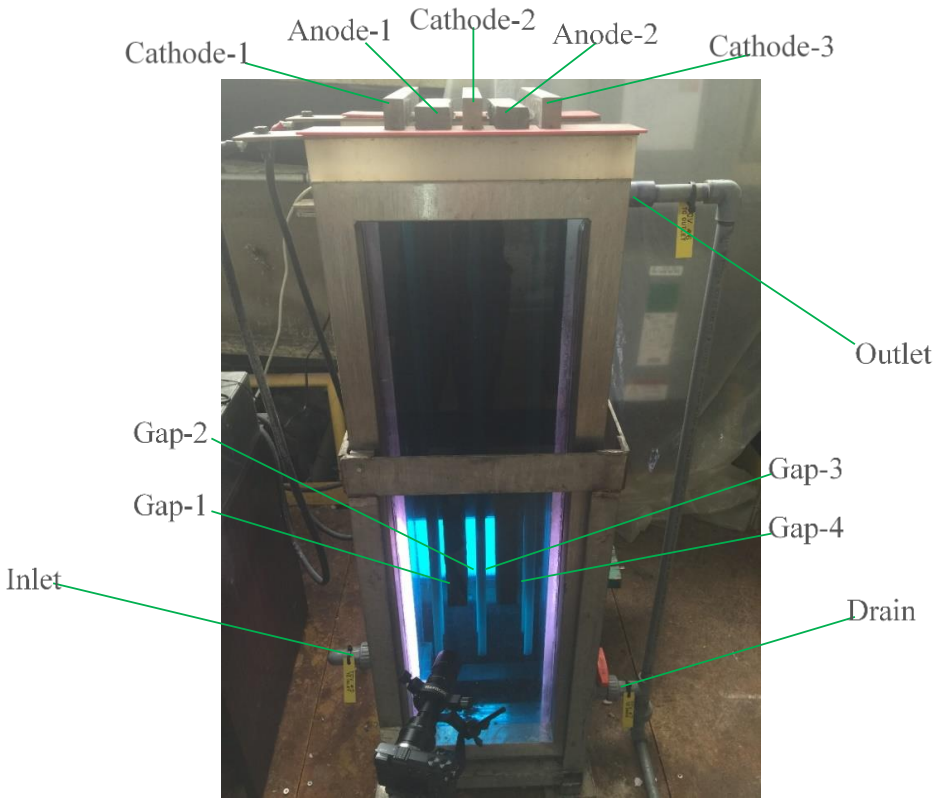

Figure 6.1 The experimental setup of the pilot scale copper electrorefining cell

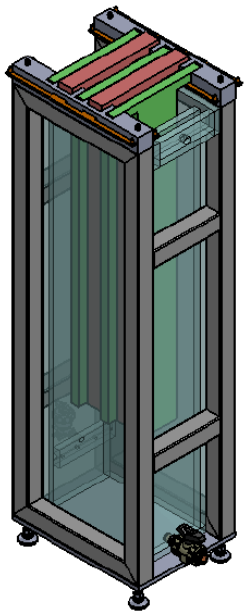

Figure 6.2 The design drawing of the pilot scale copper electrorefining cell

system of the tankhouse and has the same species concentrations and additive concentrations as the electrolyte in commercial cells. The cell is filled up and constantly fed with the electrolyte at the specified flow rate, after the anodes and cathodes are inserted and aligned. Then the rectifier is powered on to start the test. During the test, heat insulating foam was used and attached to the cell walls to reduce heat loss within the cell. The electrolyte temperature is about 60 ℃ throughout the test. After the tests, copper sheets are stripped off the cathode blanks for further analysis to determine impurity concentrations. The general experimental conditions are summarized in Table 6.1.

Video recording of the fluid flow pattern in the cell was performed in the test to measure flow velocities. A Sony NEX-7 camera and two selective lenses were utilized: one macroscopic lens to record flow pattern in low magnification; one microscopic lens to observe flow pattern in high magnification (20X). The flow velocity fields at different positions (different heights from the bottom of electrodes) in the four gaps between adjacent electrodes were recorded for 30 seconds at each position.

The recorded videos were then analyzed by Tracker, a video analysis and modeling tool. The software can present videos frame by frame and track the motion of a cluster of pixels (e.g., part of a wave of fluid flow) throughout frames from a selected time range. Before flow velocity measurement, a coordinate system was established and the calibration of length in the system was performed by giving the length of a previously measured reference (e.g., the widths of gaps between adjacent electrodes). Then the instantaneous position of the tracked cluster of pixels was tracked for each frame. The displacements of the cluster of pixels between every two adjacent time points (frames) could then be measured by the software. The instantaneous velocities and even the accelerations could

Table 6.1 Main parameters used in electrorefining experiments

Parameter	Value
Temperature	335 [K]
(Average) Current density on cathode	240 [A/m^2]
Inlet flow rate	5 [ml/s]
Initial concentration of dissolved Cu	45 [g/l]
Concentration of H_2SO_4	180 [g/l]

be acquired from the displacement data in the selected time range, and the average velocity of the cluster of pixels was calculated by the software. Errors in the average velocity and the x-direction position are considered in further analysis. The velocity data, especially the vertical velocities at all measured positions, were compiled to compare with simulation velocity results.

6.3 Model Description

6.3.1 Geometry

The geometry of the model is presented in Figure 6.3 with a three-dimensional coordinate system. The size of the electrorefining cell in the model is 48×10.875×7 inches, which is the same as the pilot scale experimental cell. The two anodes (shown as A-1 and A-2 in Figure 6.3(a)) are 32.25×1.5×4.2 inches in size, and the three cathodes (shown as C-1, C-2 and C-3 in Figure 6.3(a)) are 33.375×0.3×4.75 inches in size. The distance between each adjacent anode and cathode is 1 inch. Four anode-cathode gaps are formed under this setup (shown as gap-1 to gap-4 in Figure 6.3(a)). The four inflow pipes are 0.125 inches in radius and the axes of the inflow pipes are in the y direction, with their coordinates of x = 1.1, 2.7, 4.3, 5.6 inches, respectively, and z = 6 inches. The outflow duct is 7×0.15×0.05 inches in size. Notice that only half of the cell is shown and was simulated, due to the symmetry of the cell. All faces of the anodes and the back/front faces of the cathodes were selected as active electrode faces ($\mathrm{Cu(s)} \leftrightarrow \mathrm{Cu^{2+}_{(aq)}} + 2\mathrm{e^-}$), except the back face of cathode-1 and cathode-3, which were not adjacent to anodes. The left ends of the inflow pipes were selected as the inlet faces and the right end of the outflow duct was selected as the outlet face.

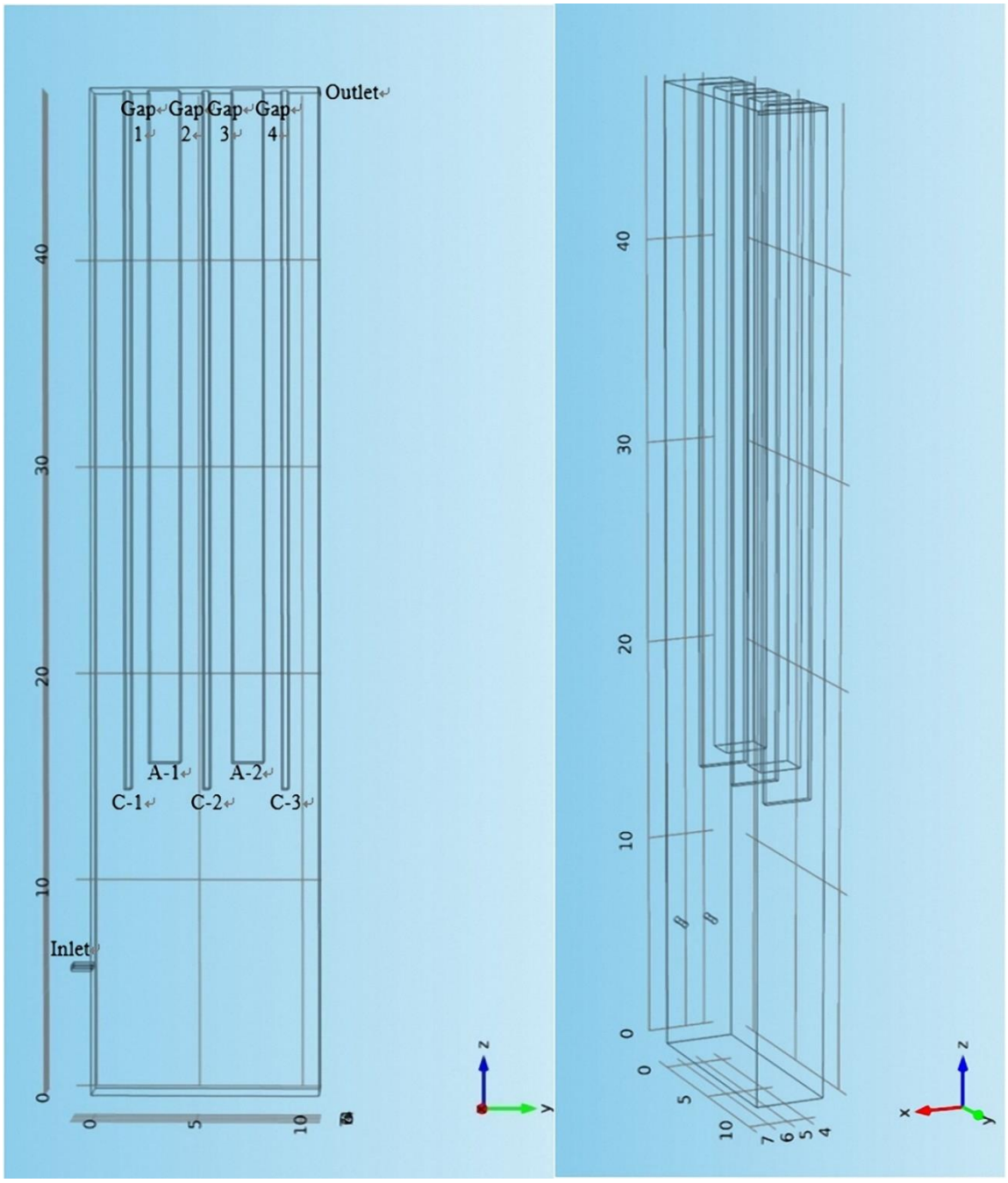

(a) Front view (b) Side view

Figure 6.3 The geometry of the pilot scale electrorefining cell in the model (all dimensions in inches)

6.3.2 Mesh

The model in this study discretizes the electrorefining cell into tetrahedral mesh elements as shown in Figure 6.4. The maximum element size in the domain is 0.301 inches and the minimum element size is 0.0325 inches, as shown in Figure 6.4. Finer element layers are along all surface boundaries. These layers of finer elements are integrated into the existing tetrahedral mesh elements in the 3D model. There are two boundary layers over each boundary, and the thicknesses of the first and second layers are 0.03 inches and 0.046 inches respectively. Along surface boundaries of the anode and cathode, there are four even finer layers of elements, with the first layer thickness of 0.006 inches and a boundary layer stretching factor of 1.53 (the thickness increases by 53% from one layer to the next).

These surface boundaries in the model are discretized into triangular boundary elements, which have a maximum element size of 0.187 inches and a minimum element size of 0.0122 inches. The geometry edges and vertices are discretized into edge elements and vertex elements. Through the development of the model, the current meshes are the result of several mesh refinements especially for the boundary layer mesh.

6.3.3 Governing Equations and Boundary Conditions

The electrochemistry model and fluid flow model used in Chapter 4 are applied in this pilot scale electrorefining cell. Thus, the governing equations and the boundary condition equations will not be repeated in this section. Major parameters used in this model are specified in Table 6.2. Note that a linear temperature gradient along the z-direction was applied in the cell to simulate the electrolyte temperature drop of about two degrees Celsius from the inlet to the outlet in the pilot scale cell:

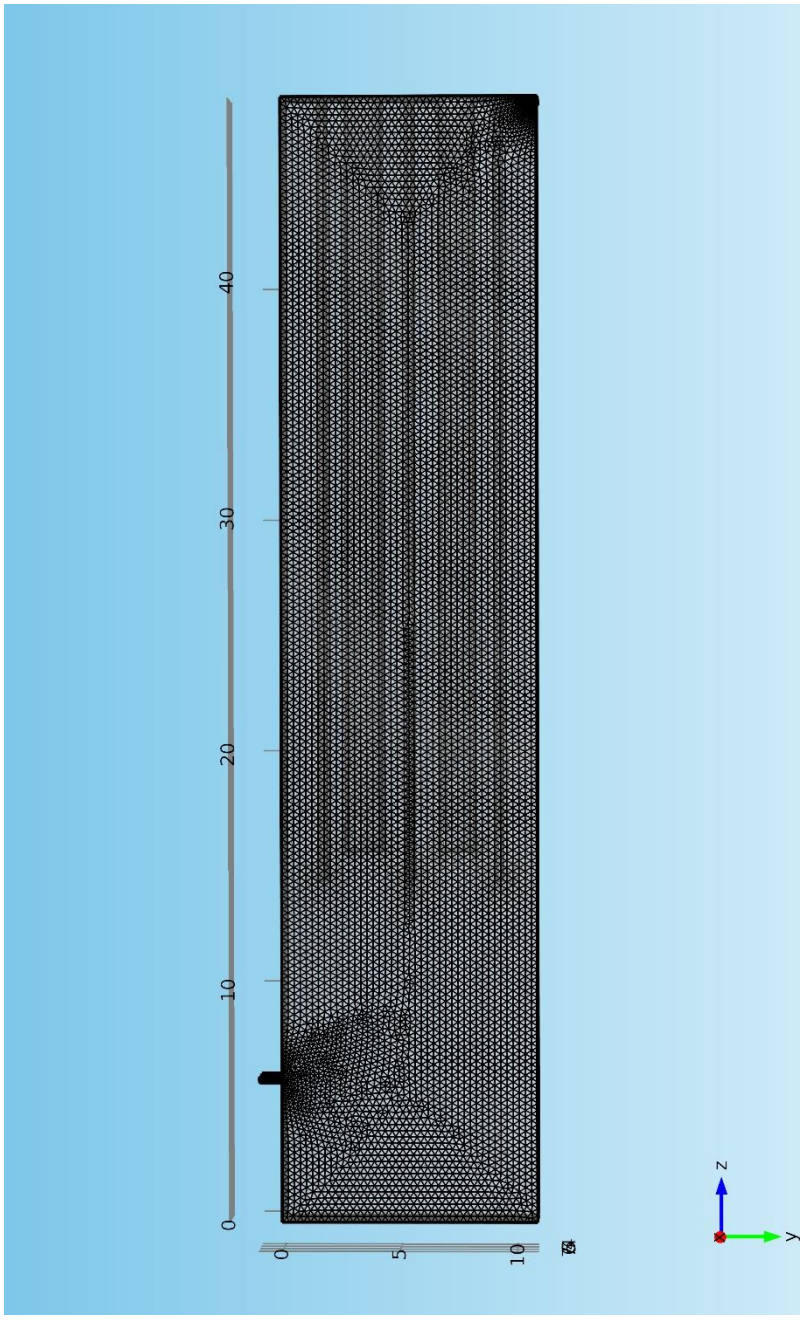

Figure 6.4 The meshes in the electrorefining cell defined in the geometry section (all dimensions in inches)

Table 6.2 Major parameters used in the model

Parameter	Value	Parameter	Value
Temperature	335 [K]	Anode symmetry factor	1.5
(Average) Current density	240 [A/m^2]	Cathode symmetry factor	0.5
Inlet flow rate	5 [ml/s]	Exchange current density	0.2 [A/m^2]
Slime particle diameter	2E-6 [m]	Initial concentration of Cu^{2+}	45 [g/l]
Slime particle density	8000 [kg/m^3]	Concentration of H_2SO_4	180 [g/l]

$$T[℃] = T_0 - \frac{|z-6|}{21} \tag{6.1}$$

where T_0 is the initial temperature of the inflow electrolyte, and z is the z-direction position of the electrolyte.

The front anode surfaces were set as the inlet faces of slime particles. Four thousand particles were uniformly released at t = 0 s from the inlet faces. The particle parameters are specified in Table 6.2.

6.4 Results and Discussion

The steady state solution of cupric ion concentration, fluid density, and fluid velocity field in the cell are shown in three-dimensional graphs. Figure 6.5 shows the cupric ion concentration profile in the cell. It is clear that the copper concentration is higher in front of all anode surfaces and is lower in front of all cathode surfaces. This is due to copper dissolution from the anodes. The dissolved copper diffuses to the electrolyte flowing along the anodes, is transported to the cathodes by convection, then diffuses to the cathode boundary layers, and finally deposits on the cathodes. Furthermore, the cupric ion concentration is higher at lower positions and lower at upper positions in the gaps, as shown in Figure 6.5. This phenomenon is due to the accumulation of cupric ions in the electrolyte as it flows downward in front of the anodes as well as due to the gradual depletion of dissolved copper as the electrolyte flows upward in front of the cathodes. Notice that the copper concentration profile shown in Figure 6.5 is on a cross-section at x = 4.3 inches, which is approximately the focal plane of the camera when recording videos.

The electrolyte density profile in the cell is similar to the copper concentration profile, because fluid density is influenced strongly by copper concentration. Thus, in these

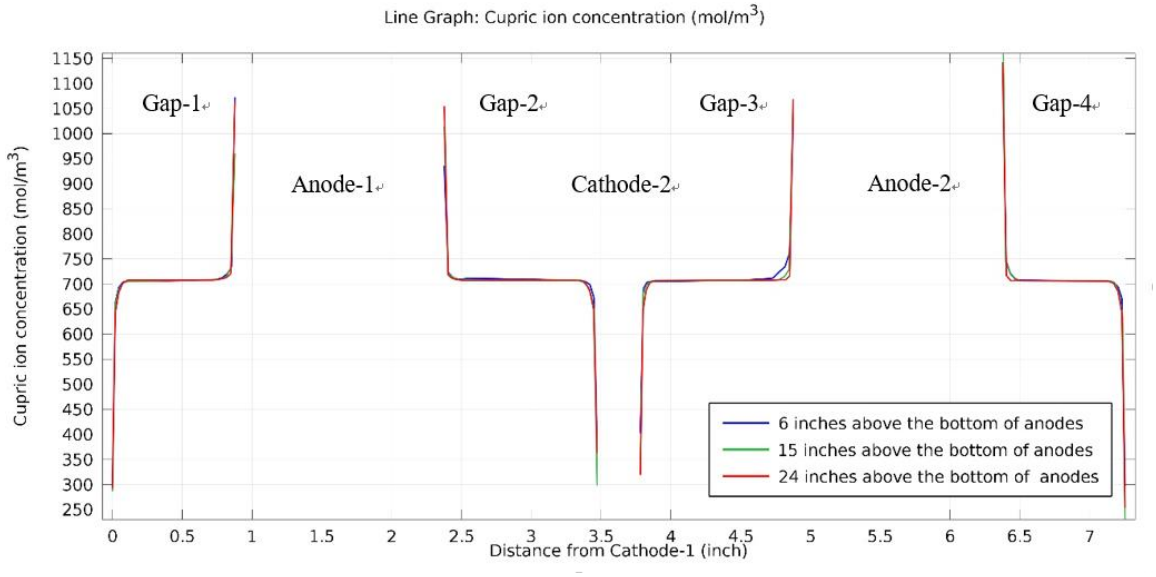

Figure 6.5 Cupric ion concentration profile at three different heights across the four gaps at the cross-section of x = 4.3 inches in the electrorefining cell defined in the geometry section

tests at a fixed acid concentration level, the electrolyte has higher density near the anodes and lower density near the cathodes, which drives the looping flow pattern between adjacent electrodes.

Figure 6.6 shows the flow velocity field in the cell in a three-dimensional graph. The inflow turns upward after coming out from the inlet, because of the large height to width/depth ratio of the cell geometry, as well as the temperature gradient. Natural convection is developed in all gaps between each adjacent anode and cathode. Downward flow can be seen along every anode face and upward flow exists in front of cathode faces that have cathodic reactions. The downward and upward flows constitute the looping flow pattern within every anode-cathode gap. The flow from the inlet encounters and interacts with the looping flow at the bottom of the electrodes, especially for gap-1 and gap-2.

The flow velocity field between adjacent electrodes has a significant effect on the behavior of slimes falling from anodes and therefore affects the quality of cathodes. To better present it, Figure 6.7 shows the fluid velocity field in the four gaps by vector arrow and color-magnitude respectively. Most flow velocity vectors are nearly along the z-axis, with almost no x and y component. The z-direction flow velocity is very significant in electrorefining cells, as it plays a large role in determining slime movement in the process. The downward flow along the anodes generally reaches the largest velocity magnitude at low positions and the upward flow in front of the cathodes typically has its largest velocity magnitude at high positions. Notice that the velocity field shown in Figure 6.7 is also on the cross-section at x = 4.3 inches, the approximate focal plane of the video recording camera.

The fluid flow velocities were measured at different heights for the four gaps by

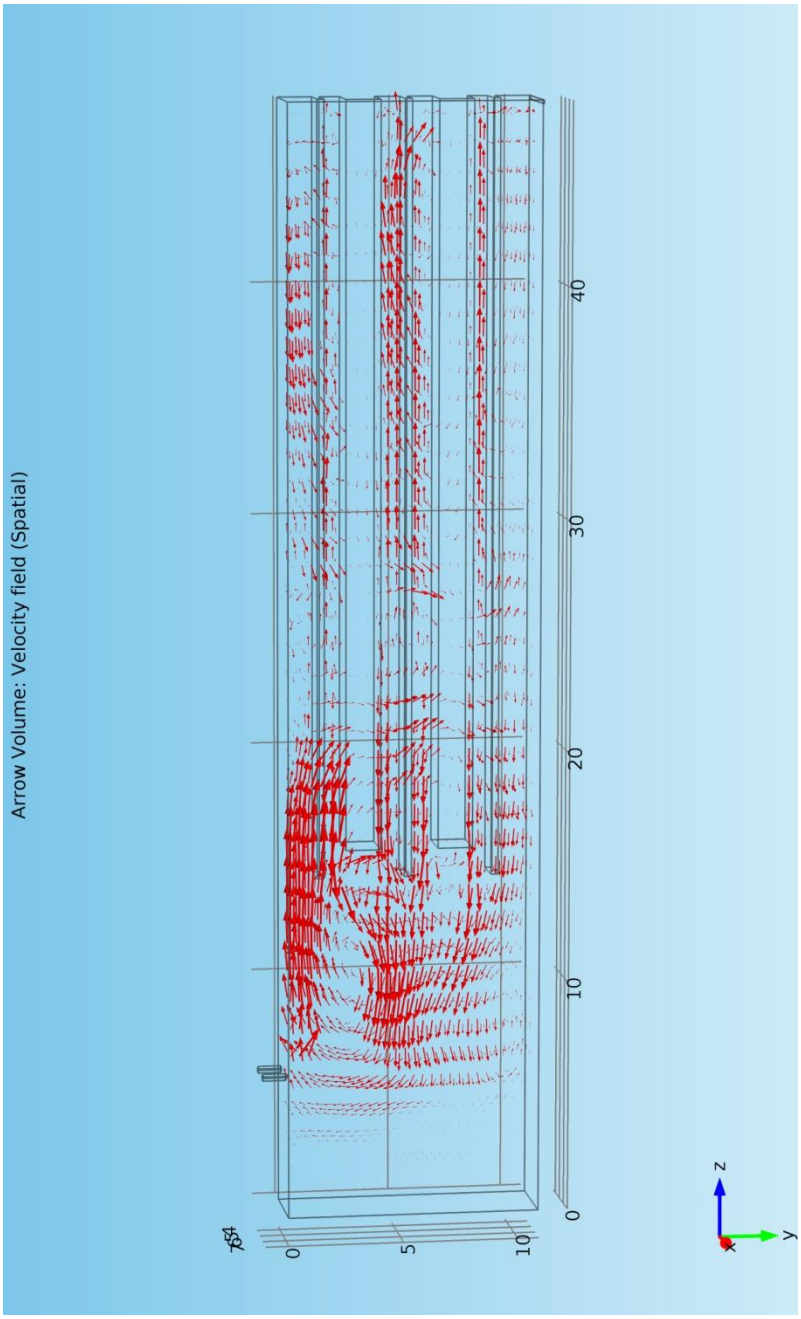

Figure 6.6 Fluid flow velocity field represented by vector arrows in the electrorefining cell defined in the geometry section (all dimensions in inches)

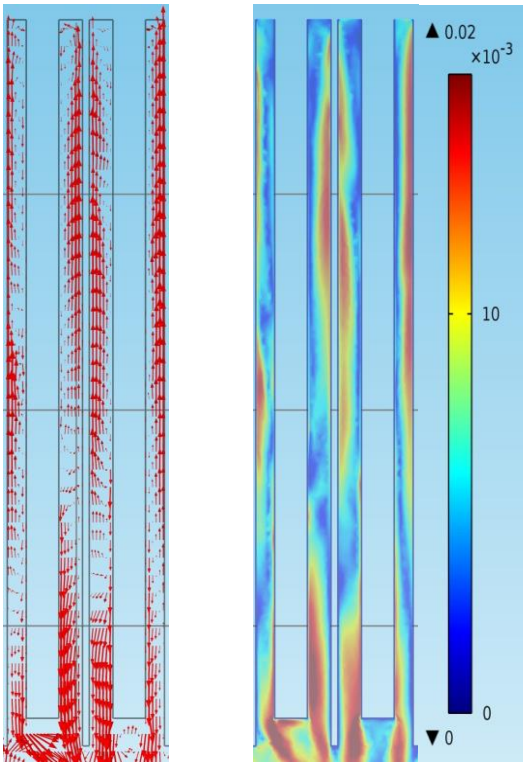

(a) Vector arrows (b) Color magnitude (m/s)

Figure 6.7 Fluid flow velocity field across the four gaps at the cross-section of x = 4.3 inches in the electrorefining cell defined in the geometry section

analyzing the recorded videos of electrolyte flow, as mentioned in section 6.2. Therefore, the z-direction flow velocity results from the simulation at the same positions in the four gaps are compared with the experimentally measured results. Figure 6.8 shows the four positions where flow velocities were measured and compared.

At the position near the top of the cell (z = 46 inches), Figure 6.9 presents the corresponding simulation and measured results of z-direction flow velocities. It can be seen that the measured z-direction flow velocities match the simulation results well. The measured velocities show more deviation from the simulation results near the anodes, where larger negative z-direction velocities were measured. From both experimental and simulation results, upward flow dominates most of the flow velocity field at the upper position near the top of the cell, as the upward flow has accelerated and expanded from the bottom of the cathodes due to the electrolyte density gradient and the downward flow along the anodes has barely started. It is noteworthy that part of the upward flow turns around and contributes to the downward flow when it reaches the top.

Then at a lower height position (z = 36 inches), the measured and simulation results of z-direction flow velocities are shown in Figure 6.10. The measured data match the simulation results well overall. Nevertheless, the measured velocities indicate higher downward velocity along the anodes and less dominance of upward velocity in the middle region than the simulation data. Both experimental and simulation results show that at gap-2 and gap-3, the upward velocities near the cathodes at this height are even larger than those at z = 46 inches. This may be due to that the flow velocity field in the gaps is also affected by the surrounding flow field. In other words, the flow field within the gaps is the result of overall boundary conditions and geometries, not just the fluid

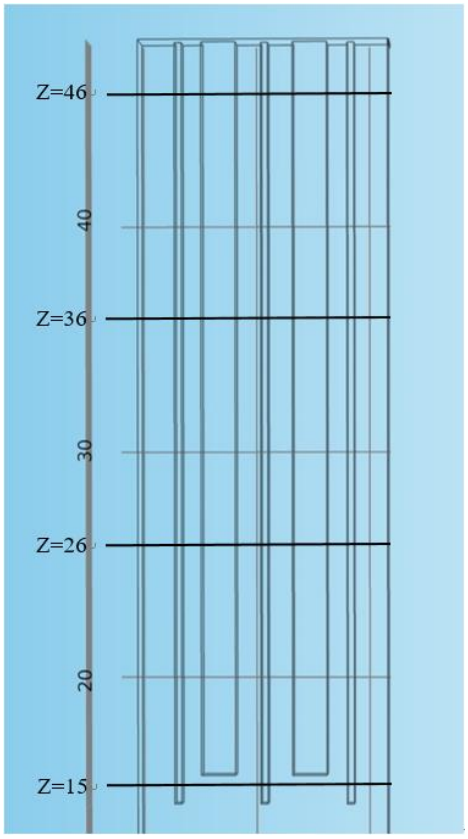

Figure 6.8 Four positions at different heights in the cell defined in the geometry section where fluid flow velocities were measured and compared (all dimensions in inches)

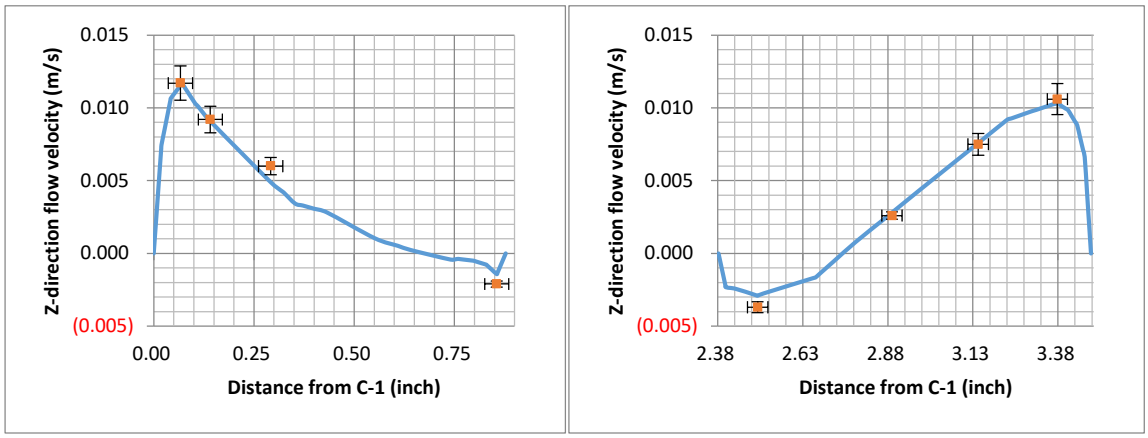

(a) Gap-1 (b) Gap-2

(c) Gap-3 (d) Gap-4

Figure 6.9 Z-direction fluid flow velocities across the four gaps at the cross line of x = 4.3 inches and z = 46 inches in the electrorefining cell defined in the geometry section. Blue lines show simulation results and orange points represent measured velocities. An error bar of plus/minus 10% of measured velocity values and an error bar of plus/minus 0.03 inches at measured positions are applied.

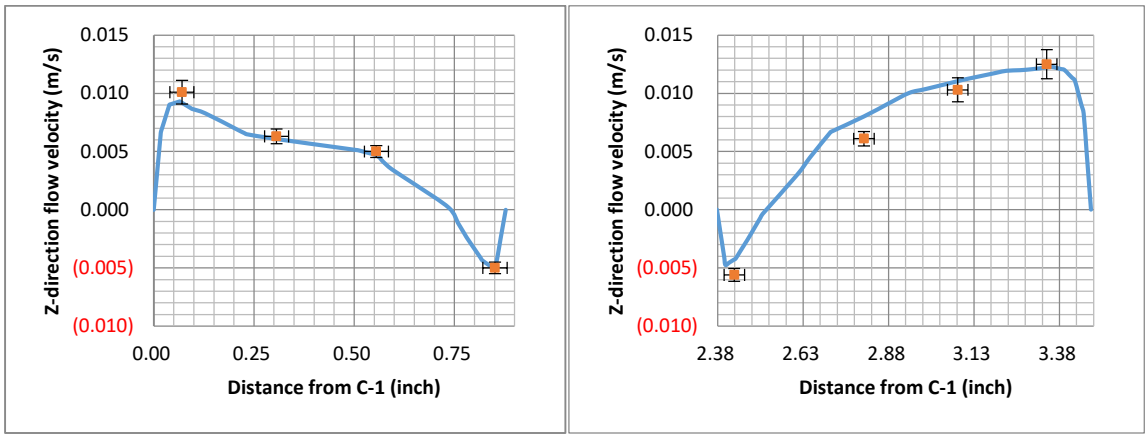

(a) Gap-1 (b) Gap-2

(c) Gap-3 (d) Gap-4

Figure 6.10 Z-direction fluid flow velocities across the four gaps at the cross line of x = 4.3 inches and z = 36 inches in the electrorefining cell defined in the geometry section. Blue lines show simulation results and red points represent measured velocities. An error bar of plus/minus 10% of measured velocity values and an error bar of plus/minus 0.03 inches at measured positions are applied.

density gradient along electrodes. It can also be observed from both measured and simulation data that the downward flow along the anodes increases at this lower height position.

At an even lower height position (z = 26 inches), Figure 6.11 presents the experimental and simulation data of z-direction flow velocities. The measured velocities still show good matching with the simulation data. For the gap-4, the measured data show lower upward velocity near the cathode and higher downward velocity near the anodes than the simulation data. It is apparent from both experimental and simulation results that the upward velocity along the cathodes drops significantly at this position while the downward velocity along the anodes continues to increase after further acceleration due to the electrolyte density gradient. The highest magnitude of downward flow is even larger than that of upward flow and the influence area of downward flow expands at this height, as shown in Figure 6.11.

Lastly, the measured and simulation results of z-direction flow velocities at the position of z = 15 inches are shown in Figure 6.12, which shows reasonably good matching. The downward velocity has increased significantly and reaches a moderate magnitude (over 1.6 cm/s under gap 3). On the other hand, the upward velocity barely exists at this low height position. In other words, the downward flow dominates at the bottom of the electrodes. The flow velocity field in this area shows some interaction between the flow from inlet and the flow from the gaps. The downward flow is slightly counterbalanced by the upward flow from the inlet, especially under gap-1. A small magnitude upward flow can be found near Cathode-1, due to the effect of the upward flow from the inlet. The measured velocity has larger magnitude for this upward flow than the computed magnitude.

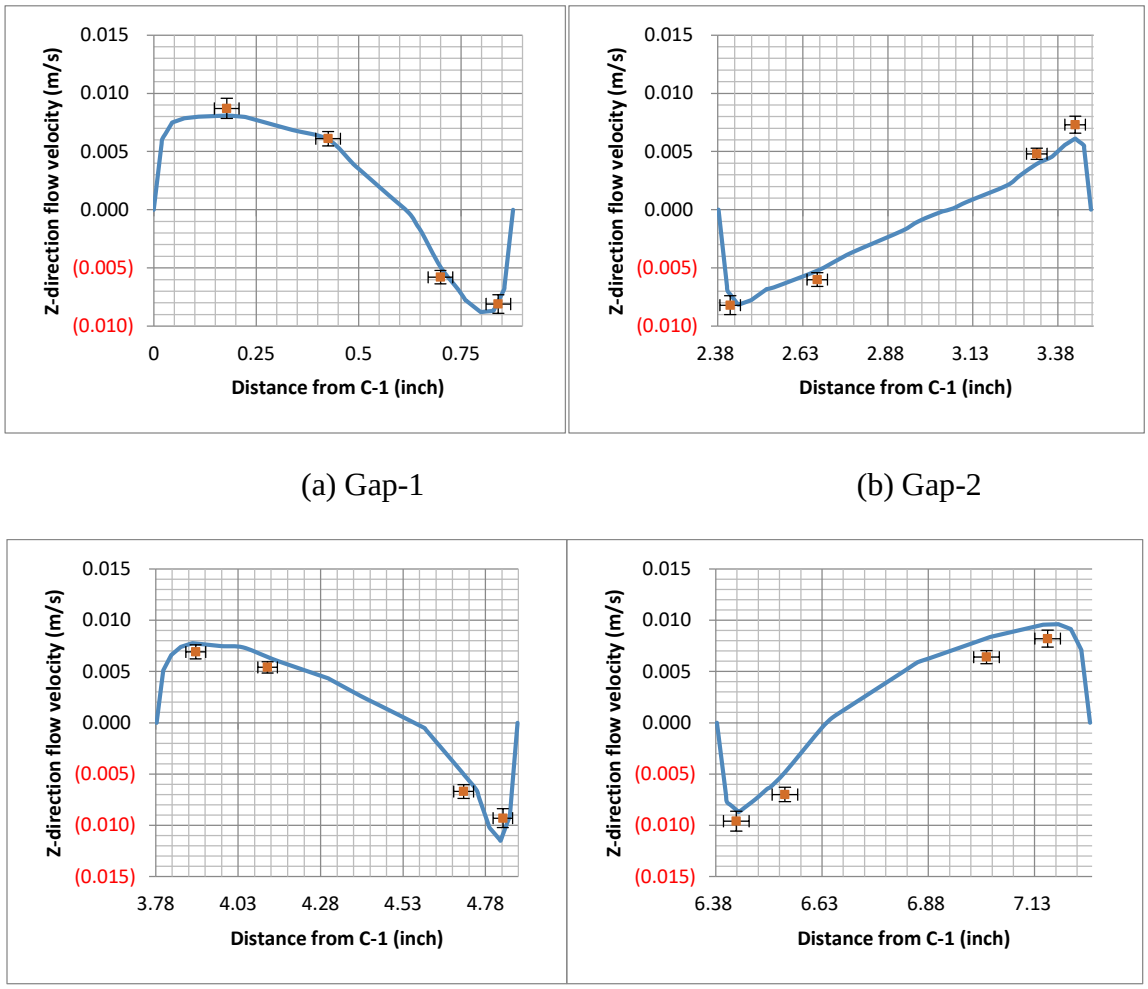

(a) Gap-1 (b) Gap-2

(c) Gap-3 (d) Gap-4

Figure 6.11 Z-direction fluid flow velocities across the four gaps at the cross line of x = 4.3 inches and z = 26 inches in the electrorefining cell defined in the geometry section. Blue lines show simulation results and orange points represent measured velocities. An error bar of plus/minus 10% of measured velocity values and an error bar of plus/minus 0.03 inches at measured positions are applied.

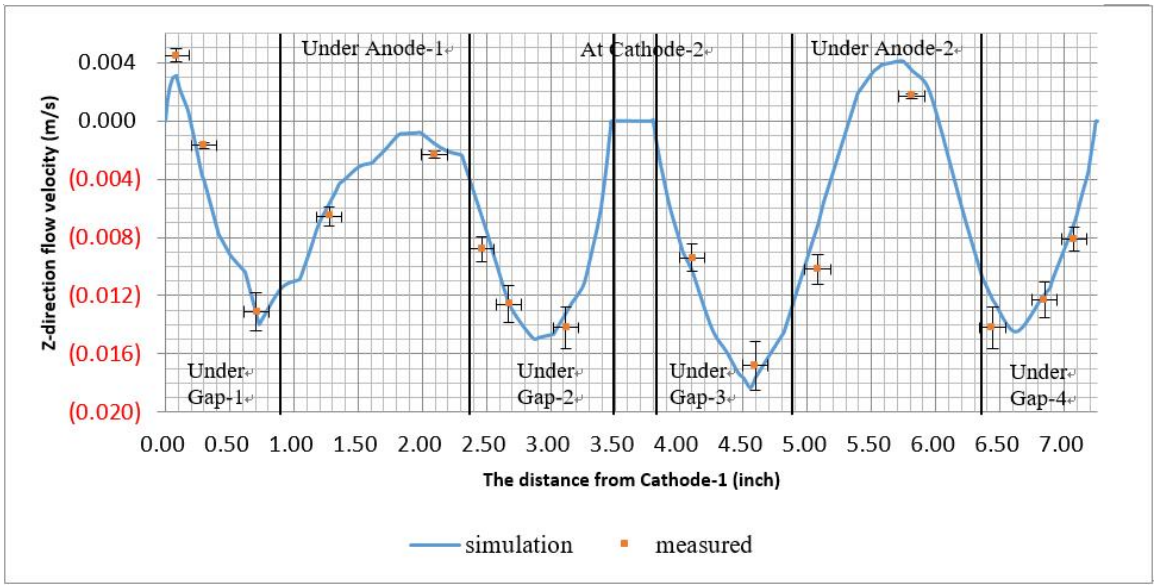

Figure 6.12 Z-direction fluid flow velocities across the four gaps at the cross line of x = 4.3 inches and z = 16 inches in the electrorefining cell defined in the geometry section. An error bar of plus/minus 10% of measured velocity values and an error bar of plus/minus 0.1 inches at measured positions are applied.

Besides, a small magnitude downward flow exists under the bottom of Anode-1, which indicates that part of the downward flow from gap 1 flows to the places under Anode-1 due to the upward flow from the inlet. The downward flow from gap 2 is also affected and slightly moved to the right. In addition, upward flows with small magnitudes due to the turning-around of the downward flow from gap-3 and gap-4 exist under the bottom of Anode-2, though the experimentally measured data are approximately two thirds of the simulation value as shown in Figure 6.12.

When anode slimes are released from the anodes, they can be carried by the electrolyte flow and move in the cell, especially in the domains between electrodes. The purity of cathodes depends on the quantity of slimes that are transported to the region very near the cathodes (e.g., within 200 microns from the cathode surface), because slimes within this region are more likely to attach to the cathode and co-deposit with copper. No matter what force drives slimes in this region to the cathode surface, the impurity levels at different positions on the cathodes should be related to the number of slime particles transported to the regions in front of these positions.

Figure 6.13 shows the slime particles positions at different time points after they are released from the anodes. From the figures, the general movements of released slime particles can be tracked as a function of time. Slime particles that are released from lower positions of anodes tend to be carried by the downward flow along the anodes and enter the lower portion of the cell. On the other hand, slime particles released from upper positions of anodes are less affected by the downward flow, which is less dominant at upper positions in the gaps, and settle much more slowly. These particles can be picked up by the upward flow along the cathodes or continue drop to lower positions.

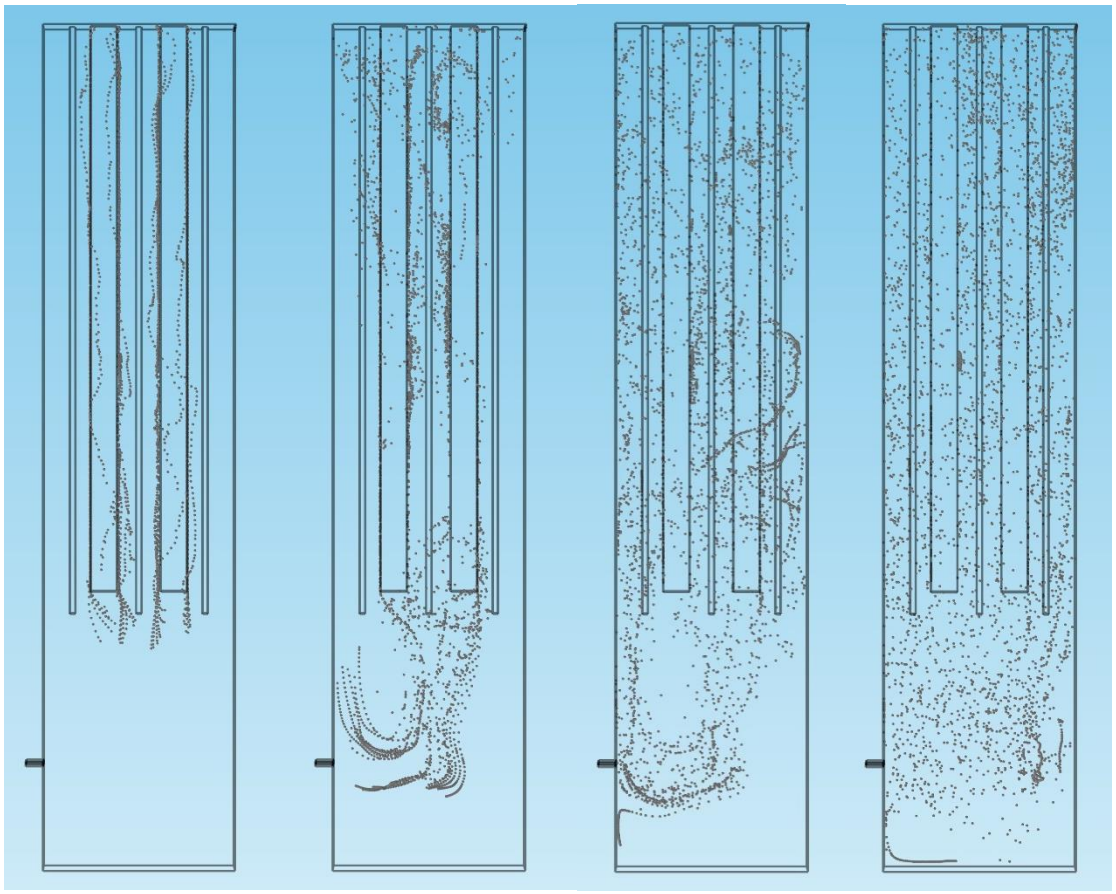

(a) t = 10 s (b) t = 70 s (c) t = 250 s (d) t = 550 s

Figure 6.13 Positions of slime particles released from the front anode surfaces at four time points (particles are released at t = 0 s)

The looping flow within the gaps can turn particles in the upward flow back to the downward flow at the cell top, which will transport them to lower positions. Slime particles that have entered the lower portion of the cell can be transported back to the gaps through the recirculation flow loop near the inlets, but some of them are out of the recirculation flow and gradually drop to the cell bottom following some minor flow patterns there. The transport of slime particles via the recirculation flow was also observed in the experimental cell.

This simulation of slime particle transport tracks the movements of one group of released slime particles with a diameter of 2 microns (as shown in Table 6.2), which is in the typical range of suspended slimes in copper electrorefining. Therefore, this simulation studies the behavior of small slimes in the cell after their release from anodes. Since suspended (small) slimes are mostly responsible for cathodic contamination,[5, 16] it is significant to understand their transport in the electrolyte, which is strongly influenced by the upward and downward flows along the electrodes.

In order to compare the effects of small slimes on different positions of cathodes, which are equally divided into upper, middle, and lower portions, the frequency of appearance of slime particles in the domain within 200 microns from cathode surface through 900 seconds from the release were analyzed for the three portions on each cathode. The higher the appearance frequency of slime particles, the more contamination the corresponding cathode tends to have. Table 6.3 shows the results.

From the results, it is apparent that the appearance frequency of slime particles generally becomes higher and higher from the upper position to the lower position for all cathodes. Also, the right two cathodes have slightly higher appearance frequencies than the

Table 6.3 Appearance frequency of slime particles in the domain within 200 microns from cathode surface at different positions of cathodes

Position	Frequency	Position	Frequency	Position	Frequency	Position	Frequency
C-1-upper	279	C-2-L-upper	262	C-2-R-upper	341	C-3-upper	260
C-1-middle	274	C-2-L-middle	326	C-2-R-middle	420	C-3-middle	370
C-1-lower	337	C-2-L-lower	446	C-2-R-lower	526	C-3-lower	533

C-1-upper represents Cathode-1-Upper_position;

C-2-L-upper represents Cathode-2-Left_side-Upper_position

left two cathodes. The results in the table were compared with experimental results of impurities concentrations at these positions. Figures 6.14 – 6.16 show the correlations between the appearance frequencies of slime particles and the concentrations of certain impurities on cathodes.

As shown in the graphs, the simulation results of the slime particle appearance frequency in the domain within 200 microns from cathode surface correlate quite well (R^2 = 0.80) with the experimental results of silver concentration on the cathode. This may indicate that most silver contamination in the cathodes in this cell originates from slime particles, though silver is typically electrodeposited into electrorefined copper. The simulation results correlate fair (R^2 = 0.58) with arsenic concentration on the cathode and well (R^2 = 0.71) with the total concentration of major impurities on the cathode including lead, arsenic, bismuth, antimony, and selenium. In general, the results of the slime particle appearance frequency from the simulation have good correlation with experimental results. Thus the appearance frequency of slime particles could be used to predict cathodic contamination in copper electrorefining. The errors may result from the fact that these impurities originate from different types of slime particles that have different sizes and densities. After all, the property, structure, and behavior of slime particles in copper electrorefining are complex and need more study in experiments and simulation to have a better understanding of them.

6.5 Conclusions

Copper electrorefining experimental tests were performed in a pilot scale cell along with corresponding simulations. From the recorded microscopic videos, the electrolyte flow velocities in the gaps between adjacent electrodes were measured. From

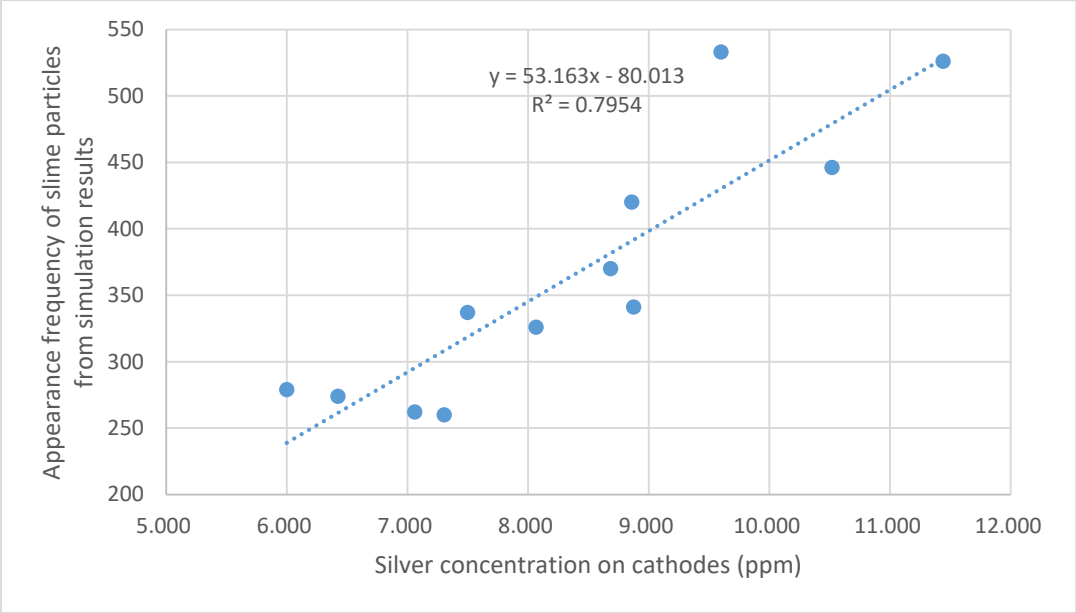

Figure 6.14 Correlation between the appearance frequency of slime particles from the simulation and the silver concentration on the cathodes harvested from the experiments

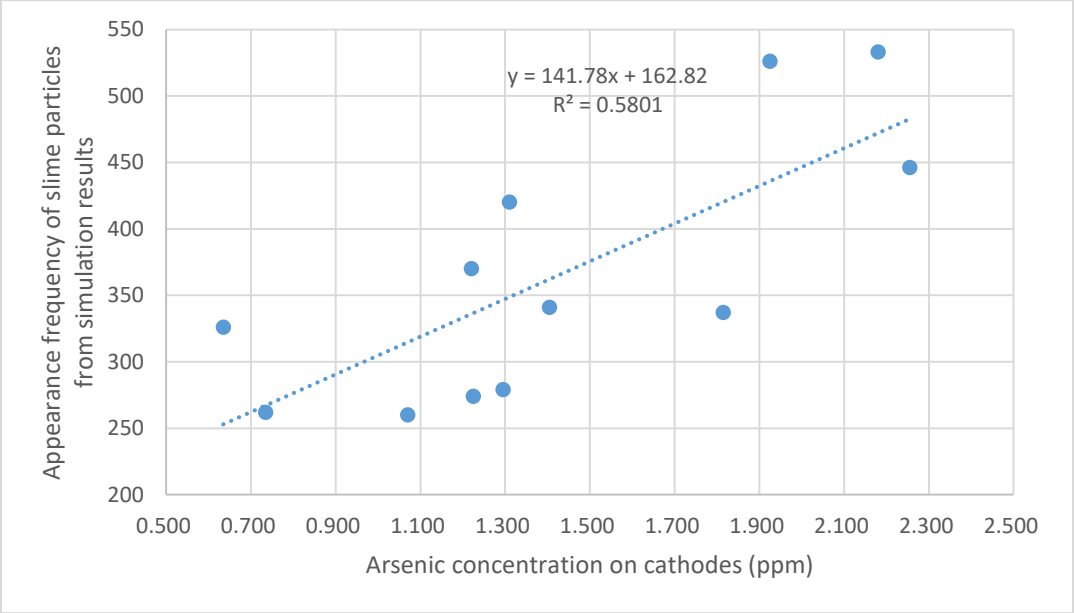

Figure 6.15 Correlation between the appearance frequency of slime particles from the simulation and the arsenic concentration on the cathodes harvested from the experiments

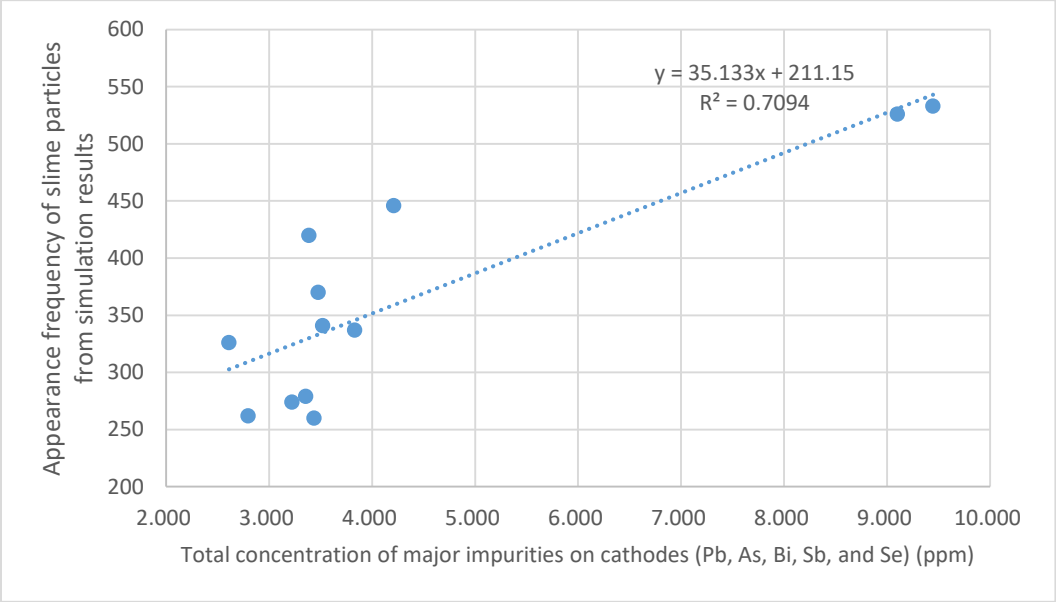

Figure 6.16 Correlation between the appearance frequency of slime particles from the simulation and the total concentration of major impurities on the cathodes harvested from the experiments

the simulation, copper concentration profile, electrolyte density profile, and flow velocity field were obtained. The results of the flow velocity field simulation data were compared with the experimentally measured electrolyte velocities and they match well with reasonable errors.

From both experimental and simulation results, the magnitude of upward flow along cathode surface increases from the bottom to the top of the cathodes while the downward flow along the anodes accelerates from the top to the bottom of the anodes. As a result, the fluid flow at upper positions of the gaps between adjacent electrodes are dominated by upward flow with the maximum magnitudes varying from 1.0 cm/s to 1.5 cm/s among different gaps. On the other hand, downward flow takes control of the fluid flow at lower positions of the gaps, with the maximum magnitudes varying from 1.4 cm/s to 1.9 cm/s. The upward flow coming from the inlet has a significant effect on the electrolyte velocity profile at the bottom of the electrodes, resulting in downward flow from the left two gaps that moves to the right and minor upward flow at some positions. A recirculation flow loop near the inlets was observed during experiments and in simulation results. This flow loop can transport slime particles in the lower portion of the cell back to the gaps.

The transport of slime particles in the electrolyte flow was also simulated, from which the movements of slime particles released from the anodes can be tracked as a function of time. Since the cathode purity is much more affected by the slime particles in the region very near its surface than by those away from its surface, the appearance frequency of slime particles in the domain within 200 microns from cathode surface was analyzed at different positions for each cathode. The results indicate that more particles

appear in front of the lower positions of cathodes.

The results of the appearance frequency of slime particles near the cathode were compared with impurity levels in the copper cathodes harvested from the experimental tests, and they show a good correlation with the total concentrations of major impurities. Thus, cathodic contamination in copper electrorefining can be predicted by the slime particle appearance frequency in front of the cathodes.

6.6 References

1. E. N. Petkova: *Hydrometallurgy*, 1997, vol. 46, pp. 277-86.
2. X. Wang, Q. Chen, Z. Yin, M. Wang, B. Xiao, and F. Zhang: *Hydrometallurgy*, 2011, vol. 105, pp. 355-58.
3. X. W. Wang, Q. Y. Chen, Z. L. Yin, M. Y. Wang, and F. Tang: *Hydrometallurgy*, 2011, vol. 108, pp. 199-204.
4. F. X. Xiao, Y. J. Zheng, Y. Wang, W. Xu, C. H. Li, and H. S. Jian: *Trans. Nonferrous Met. Soc. China*, 2007, vol. 17, pp. 1069-74.
5. W. Zeng, M. L. Free, and S. Wang: *J. Electrochem. Soc.*, 2016, vol. 163, pp. E14-31.
6. W. Zeng, M. L. Free, J. Werner, and S. Wang: *J. Electrochem. Soc.*, 2015, vol. 162, pp. E338-52.
7. W. Zeng, J. Werner, and M. L. Free: *Hydrometallurgy*, 2015, vol. 156, pp. 232-38.
8. A. Eklund, D. Simonsson, F. Alavyoon, R. Karlsson, and F. Bark: *Inst. Chem. Eng. Symp. Ser.*, 1989, vol. 112, pp. 47-58.
9. Y. Konishi, Y. Tanaka, Y. Kondo, and Y. Fukunaka: *Electrochim. Acta*, 2001, vol. 46, pp. 681-90.
10. D. Ziegler and J. W. Evans: *J. Electrochem. Soc.*, 1986, vol. 133, pp. 559-66.
11. M. J. Leahy and M. P. Schwarz: *16th Australasian Fluid Mechanics Conference*, Gold Coast, Australia, 2007.
12. S. Kawai and T. Miyazawa: *Miner. Eng.*, 2014, vol. 63, pp. 81-90.

13. A. Kemminger and A. Ludwig: *Proceedings of European Metallurgical Conference 2013*, Weimar, Germany, 2013, vol. 2, pp. 795-806.

14. H. Hemmati, A. Mohebbi, A. Soltani, and S. Daneshpajouh: *Hydrometallurgy*, 2013, vol. 139, pp. 54-63.

15. X. Ling, Z. H. Gu, and T. Z. Fahidy: *Can. J. Chem. Eng.*, 1994, vol. 72, pp. 683-94.

16. J. E. Hoffmann: *JOM*, 2004, vol. 56, pp. 30-33.

CHAPTER 7

EXPERIMENTAL STUDIES OF THE EFFECTS OF ANODE COMPOSITION AND PROCESS PARAMETERS ON ANODE SLIME ADHESION AND CATHODE PURITY IN A PILOT SCALE CELL

Copper electrorefining tests were conducted in a pilot scale cell under commercial tankhouse environment to study the effects of anode compositions, current density, cathode blank width, and flow rate on anode slime behavior and cathode copper purity. Three different types of anodes (high, mid, and low impurity levels) were used in the tests and were analyzed under SEM/EDS. The harvested copper cathodes were weighed and analyzed for impurities concentrations by DC Arc. The adhered slimes and released slimes were collected, weighed, and analyzed for compositions by ICP. It was shown that the lead to arsenic ratio in the anodes affects the sintering and coalescence of slime particles. High current density can improve anode slime adhesion and cathode purity by intensifying slime particles' coalescence and dissolving part of the particles. Wide cathode blanks can raise the anodic current densities significantly in a test cell where the fraction of cathode to anode area is greater than 1 (1.17 in this cell) and result in massive release of large slime particle aggregates, which are not likely to contaminate the cathode copper. Low flow rate can cause anode passivation and increase local temperatures in front

of the anode, which leads to very intense sintering and coalescence of slime particles. The results and analyses of the tests present potential solutions for industrial copper electrorefining process.

7.1 Introduction

In Chapter 5, the sintering and coalescence of slime particles and its effects on anode slime adhesion and cathode purity were studied. Significant findings can be summarized: the sizes of slime particles can be increased by sintering/coalescence; anode slime adhesion increases from room temperature to a peak adhesion temperature (the peak adhesion temperatures are around 333.15 K (60 ℃) for most anodes) and then decreases as cell temperature goes up further, due to the effects of slime particle sintering/coalescence; slime particles tend to fall off the anode after the peak adhesion temperature because of their larger and larger sizes (these slime particles are generally larger than 9-10 microns); slime particles with Pb-Bi-S shells have lower sintering temperatures and are easier to coalesce together and/or adhere to the anode than those with Pb-Bi-S-As shells; anodes having more slime particles with Pb-Bi-S shells demonstrate lower peak adhesion temperatures than anodes having more slime particles with Pb-Bi-S-As shells; better anode slime adhesion and/or larger slime particle sizes lead to cathode copper with higher purity.

Copper users prefer low bismuth levels, as bismuth is an undesirable element in copper cathode. It is likely that the existing 0.5 ppm Bi targeted limit for LME grade A copper will be lowered in the future. Therefore, there is a need to lower bismuth levels in cathodes to ensure high productivity of high quality copper. It is generally observed that high slime adhesion reduces cathode impurities by making the anode slime particles less likely to be transported and deposited in the cathode. Thus the understanding of slime

adhesion and transport in copper electrorefining is critical to refineries. Nevertheless, systematic studies of anode composition and process parameters on the adhesion, mobility, and transport of anode slimes can be rarely found in the past research and are worthy of further study. Therefore, a series of copper electrorefining tests have been performed in a pilot scale electrorefining cell, using anodes with different compositions under different experimental conditions. By using anodes cut from commercial cell standard anodes, circulating electrolyte from tankhouse pipeline system, and performing the tests in the tankhouse environment, these experimental copper electrorefining tests were designed to be as close to real industrial processes as possible. The resulting cathodes, slime particles, and anodes were analyzed, with the fluid flow field in the cell studied by experimental measurement and simulation in Chapter 6.

Lead to arsenic ratio in anodes is proposed in this chapter to be incorporated in refinery practice to control slime adhesion and transport. It can help refineries to control cathode contamination by providing a view of the process from a different angle. Currently, most copper refineries use As/(Bi+Sb) ratio and/or As/Sb ratio (dissolved As, Bi, and Sb in electrolyte) for contamination control as these have been widely studied in the past decades.[1-5] While the impurities concentrations in electrolyte are adjusted according to the As/(Bi+Sb) and/or As/Sb ratio, the impurities levels in the anodes can also be adjusted according to the Pb/As ratio. Their combination can provide better control of the entire copper electrorefining process and further reduce impurity levels in the cathode including bismuth.

From the results of the impurities levels of harvested cathodes and the compositions and weights of adhered slimes and released slimes, the effects of process

parameters and anode compositions on the behavior of slime particles and the purity of cathode copper can be analyzed. From SEM/EDS analysis of inclusions in different anodes, as well as slime particles and cathode copper, the underlying mechanisms are discussed.

7.2 Experimental

The experiments were performed in the tankhouse of Rio Tinto Kennecott Refinery. A pilot scale electrorefining cell built with transparent and acid resistive Lexan and supported by steel tube frames sits on the tankhouse floor, as shown in Figure 7.1. The dimensions of the cell have been described in Chapter 6. The electrolyte used for the tests comes directly from the tankhouse circulation system and has impurities concentrations shown in Table 7.1. The drain valve is closed during the tests and open after each test to collect slimes in the cell. There are two anodes (shown as A-1 and A-2 in Figure 7.1) and three cathode blanks (shown as C-1, C-2, and C-3, respectively, in Figure 7.1) symmetrically placed in the cell.

Three different types of anodes were used in the experiments (as shown in Table 7.2) and were analyzed for compositions by DC Arc. The results are shown in Table 7.3. Figure 7.2 shows the photo of one anode as an example. There are two types of cathode blanks utilized in the tests: the normal cathode blanks and the wide cathode blanks. Each normal cathode blank is 3.5 inches in width, 0.3 inches in depth, and 36.625 inches in height (33.375 inches immersed in electrolyte); and each wide cathode blank is 4.75 inches in width, with the same depth and height dimensions as the normal one. The ratio of cathode to anode area is 0.86 for normal cathode blanks and 1.17 for wide cathode blanks. The total current applied is determined by the applied current density (240 A/m^2 baseline current density) and the total cathodic area. Note that the back sides of Cathode-1 and Cathode-3

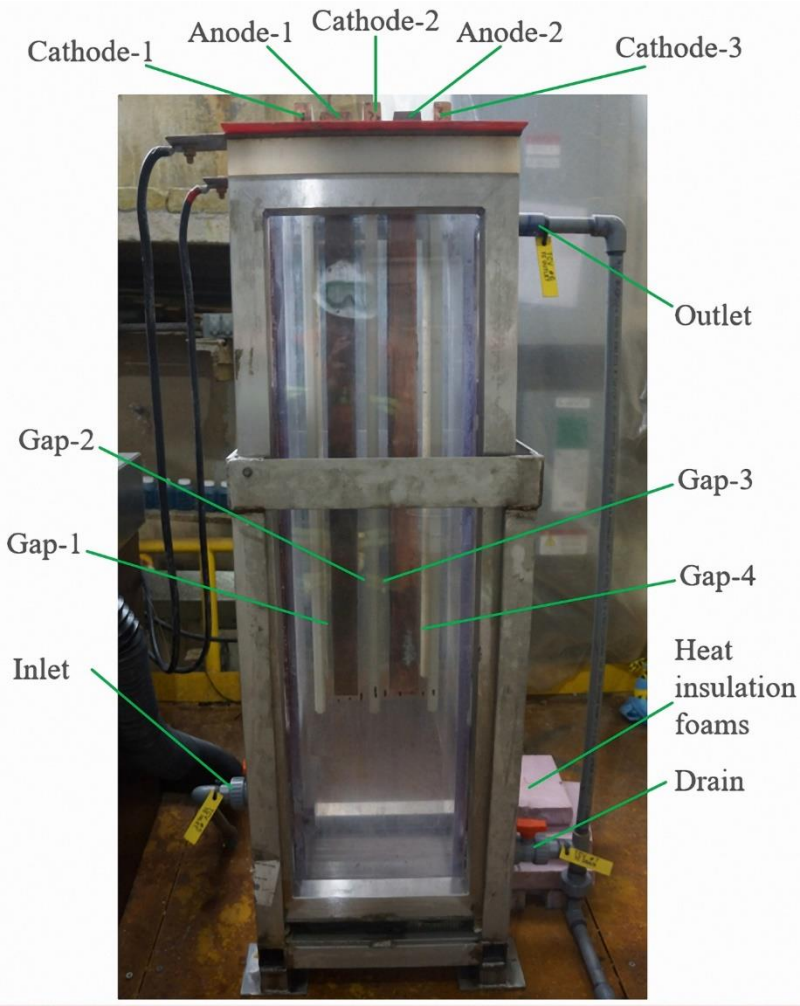

Figure 7.1 The pilot scale copper electrorefining cell used in the experiments with its major components labeled

Figure 7.2 The specially cut copper anode used in the copper electrorefining experiments

Table 7.1 The content of the electrolyte from the tankhouse circulation system

Electrolyte constitute	Cu	H_2SO_4	Bi	Fe	Ni	Pb	Sb	Se
Concentration (g/L)	44.82	168.37	0.04	0.15	2.80	0.01	0.10	<0.001

Table 7.2 Experimental conditions applied for each copper electrorefining test

Condition	Test-1	Test-2	Test-3	Test-4	Test-5	Test-6	Test-7
Anode	Type-1	Type-2	Type-3	Type-1	Type-1	Type-2	Type-2
Cathode	Normal	Normal	Normal	Normal	Wide	Wide	Wide
Flow rate (ml/s)	5	5	5	5	5	2.5	5
Current density (A/m^2)	240	240	240	300	240	240	240
Temperature (K)	334	334	334	334	334	334	330

Table 7.3 The compositions of the anodes used in the experiments

Anode type	Pb	As	Bi	Se	Sb	Ni	Fe	Te	Sn
1	0.198	0.19	0.049	0.067	<.0023	0.044	<.0020	0.008	0.001
2	0.505	0.26	0.068	0.051	0.012	0.031	<.0018	0.012	0.001
3	0.195	0.113	0.036	0.051	0.008	0.021	<0.0019	0.006	0.001

All units in ppm

are coated with electric insulation paint, in order to have better current density distribution in the cell. The baseline flow rate is about 5 ml/s and is determined by the inflow velocity (0.0488 m/s, same as Kennecott commercial cells) and the total inlet area. The baseline electrolyte temperature is about 334 K (61 ℃). The side walls of the cell are covered by heat insulation foams as to maintain constant cell temperature. Each test had two cycles of 11 days. The experimental conditions applied in each test are summarized in Table 7.2.

7.3 Results

Mostly in terms of lead, arsenic, and bismuth, the type-1 anode has mid-level impurities contents; the type-2 anode has high impurities levels especially for lead; and the type-3 anode has low contents of impurities.

Four strips of deposited copper were harvested from each test: one from cathode-1, two from cathode-2, and one from cathode-3. A photo of a copper strip on a cathode blank is shown in Figure 7.3. These copper strips were weighed and analyzed by DC Arc to determine impurity levels. The current efficiency for each test and the current density on each cathode can be estimated based on the weights of cathode copper. The results for each test are shown in Tables 7.4 and 7.5. Note that Cathode-2-W and Cathode-2-E represent the copper strips on the west and east sides of Cathode-2 respectively.

From the results shown in Table 7.4, the current densities on the cathodes vary in a reasonable range around the average value in the tests. This is because the contact resistance of the connection between the sitting arm of the cathode blank and the metal plate connected to the negative pole is slightly different among three cathode blanks. Note that minor current is distributed on the coated side of Cathode-1 and Cathode-3 due to some penetration through the paint. The current density on each cathode is calculated based on

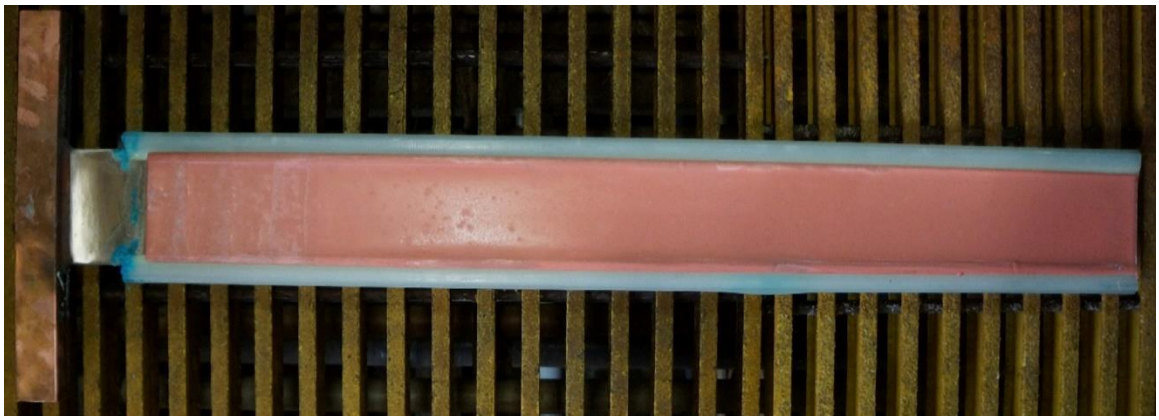

Figure 7.3 The unstripped cathode copper on a cathode blank after the copper electrorefining experiment

Table 7.4 Weights, current densities, and current efficiencies for the cathodes harvested in each copper electrorefining test

	Test-1		Test-2		Test-3		Test-4	
	Weight	Current_D	Weight	Current_D	Weight	Current_D	Weight	Current_D
C-1	5.20	246.26	6.11	253.03	4.67	215.18	5.29	309.98
C-2	9.58	226.64	11.44	236.90	9.76	225.10	10.85	318.21
C-3	4.26	201.47	4.99	206.52	5.80	267.40	4.34	254.20
C.E.	98.87%		98.13%		97.28%		98.97%	

	Test-5		Test-6		Test-7	
	Weight	Current_D	Weight	Current_D	Weight	Current_D
C-1	7.13	204.24	6.32	222.70	7.69	272.16
C-2	16.71	239.42	13.00	229.09	11.38	201.32
C-3	9.59	274.74	7.65	269.64	7.79	275.53
C.E.	99.49%		98.59%		98.55%	

Weight in the unit of Kg and current density in the unit of A/m^2;

C-1 represents Cathode-1; C.E. is current efficiency

Table 7.5 Impurities concentrations in the cathode copper harvested from each electrorefining test

Impurity		Bi	Pb	As	Se	Sb	Ni	Fe	Sn	Te
Test 1	C-1	0.17	< 0.500	< 1.000	< 0.500	< 1.00	< 1.0	4.3	< 0.500	< 0.500
	C-2-W	0.13	< 0.500	< 1.000	< 0.500	< 1.00	< 1.0	< 3.0	< 0.500	< 0.500
	C-2-E	< 0.100	< 0.500	1.13	< 0.500	< 1.00	< 1.0	< 3.0	< 0.500	< 0.500
	C-3	0.12	< 0.500	< 1.000	< 0.500	< 1.00	< 1.0	< 3.0	< 0.500	< 0.500
Test 2	C-1	< 0.100	< 0.500	< 1.000	< 0.500	< 1.00	< 1.0	< 3.0	< 0.500	< 0.500
	C-2-W	< 0.100	0.81	1.15	0.5	< 1.00	1.1	< 3.0	< 0.500	< 0.500
	C-2-E	< 0.100	< 0.500	< 1.000	< 0.500	< 1.00	1.1	< 3.0	< 0.500	< 0.500
	C-3	< 0.100	< 0.500	1.01	< 0.500	< 1.00	1.2	< 3.0	< 0.500	< 0.500
Test 3	C-1	< 0.100	< 0.500	< 1.000	< 0.500	< 1.00	< 1.0	< 3.0	< 0.500	< 0.500
	C-2-W	< 0.100	< 0.500	< 1.000	< 0.500	< 1.00	< 1.0	< 3.0	< 0.500	< 0.500
	C-2-E	< 0.100	< 0.500	< 1.000	< 0.500	< 1.00	< 1.0	< 3.0	< 0.500	< 0.500
	C-3	1.28	5.08	1.11	1.43	< 1.00	1.1	3.6	< 0.500	0.54
Test 4	C-1	< 0.100	< 0.500	1.03	< 0.500	< 1.00	1.2	< 3.0	< 0.500	< 0.500
	C-2-W	< 0.100	< 0.500	1.24	< 0.500	< 1.00	1.1	< 3.0	< 0.500	< 0.500
	C-2-E	< 0.100	< 0.500	1.19	< 0.500	< 1.00	1.1	< 3.0	< 0.500	< 0.500
	C-3	< 0.100	< 0.500	1.32	< 0.500	< 1.00	1.2	< 3.0	< 0.500	< 0.500
Test 5	C-1	< 0.100	< 0.500	1.06	0.5	< 1.00	2.1	< 3.0	< 0.500	< 0.500
	C-2-W	< 0.100	< 0.500	1.2	< 0.500	< 1.00	1.9	< 3.0	< 0.500	< 0.500
	C-2-E	< 0.100	< 0.500	1	< 0.500	< 1.00	1.7	< 3.0	< 0.500	< 0.500
	C-3	< 0.100	< 0.500	1.17	< 0.500	< 1.00	1.7	< 3.0	< 0.500	< 0.500
Test 6	C-1	0.1	0.8	< 1.000	< 0.500	< 1.00	< 1.0	< 3.0	< 0.500	< 0.500
	C-2-W	< 0.100	0.79	< 1.000	< 0.500	< 1.00	< 1.0	< 3.0	< 0.500	< 0.500
	C-2-E	0.11	0.98	< 1.000	< 0.500	< 1.00	< 1.0	< 3.0	< 0.500	< 0.500
	C-3	0.1	0.84	< 1.000	< 0.500	< 1.00	< 1.0	< 3.0	< 0.500	< 0.500
Test 7	C-1	< 0.100	0.89	1.12	< 0.500	< 1.00	< 1.0	< 3.0	< 0.500	< 0.500
	C-2-W	< 0.100	1.47	< 1.000	< 0.500	< 1.00	< 1.0	< 3.0	< 0.500	< 0.500
	C-2-E	0.15	0.98	1.05	0.59	< 1.00	< 1.0	< 3.0	< 0.500	< 0.500
	C-3	< 0.100	0.76	< 1.000	< 0.500	< 1.00	< 1.0	< 3.0	< 0.500	< 0.500

All units in ppm; C-1 represents Cathode-1;

C-2-W represents Cathode-2-West_side

the following equation according to Faraday's Law:

$$Current\_D = \frac{nFW}{\beta MAt} \tag{7.1}$$

where *n* is the number of electrons transferred, *F* is Faraday constant, *W* is the actual weight of the cathode copper, β is the estimated current efficiency, *M* is the molecular weight for copper, *A* is the cathodic area, and *t* is the total time.[6]

The current efficiency for each test is estimated through the equation below and is above 97% for all tests.

$$Current\_Efficiency = \frac{Actual\_Weight}{Theoretical\_Weight} = \frac{W}{\frac{ItM}{nF}} = \frac{nFW}{ItM} \tag{7.2}$$

where *W* is the actual weight of the harvested copper, *I* is the total current applied, and *t* is the total time of the test.[6]

Table 7.5 shows the concentrations of major impurities in the harvested cathode copper. The significant impurities are bismuth, lead, sulfur, selenium, and arsenic, which will be mainly discussed in this chapter. The most challenging impurity is bismuth, with the aim of the tests to reduce bismuth content in cathode copper. Bismuth is one of most detrimental impurity elements in copper, as it significantly reduces the ductility of copper and affects the production of copper rod and wire. The target bismuth level in the cathode copper is below 0.2 ppm.

As shown in Table 7.2, Test-1 acts as the control experiment, with normal levels of test conditions and the type-1 anodes with mid-level impurities concentrations. Test-2 uses the type-2 anodes with high-level impurities concentrations especially for lead, and the corresponding results show less bismuth levels in the harvested copper in comparison with Test-1. Test-3 uses the type-3 low impurity level anodes and the resulting cathode

copper also has low impurities contents except Cathode-3, which was a little tilted toward Anode-2 in the test and might therefore may have collected and entrapped more slime particles. Test-4 examines the effect of current density on the results as it was conducted at 300 A/m^2. The results show that high current density has the effect of reducing bismuth levels in cathode copper, as compared with Test-1. From Test-5, the wide cathode blanks were utilized for the experiments and the impurities contents in the harvested copper from the wide blanks were well controlled. However, some impurity concentration differences between the edge and the center of the cathode copper were observed, which will be discussed in section 4.3. Test-6 was designed to run at low flow rate (2.5 ml/min) using the type-2 anodes and the wide cathode blanks, and the bismuth levels in the resulting cathode copper are similar to Test-2. The effects of low flow rate on impurities levels in the harvested copper are further discussed in section 4.4. Test-7 was performed under low cell temperature using the type-2 anodes and the wide cathode blanks. Nevertheless, the cell temperature could not be effectively reduced substantially and 330 K (57 ℃) is the lowest temperature that could be reached because of the system design. From the results shown in Table 7.5, the type-2 anodes performed well under slightly lower cell temperature as compared with Test-2, and low bismuth level cathode copper was produced.

The adhered slimes on the harvested anodes and the released slimes in the cell including settled and suspended slimes were collected after each test. A photo of the remaining anode with adhered slimes is shown in Figure 7.4. The weights of cell slimes and adhered slimes were measured for each test, which are shown in Table 7.6.

It can be observed that the adhered slime weight ratio is about 0.18 in the control test and it increases to 0.5 in Test-2 using the type-2 anodes. A similar weight ratio of

Figure 7.4 The residual anode with adhered anode slimes after the copper electrorefining experiment

Table 7.6 Weights and weight ratios of cell slimes and adhered slimes for each test

Test number	Test-1	Test-2	Test-3	Test-4	Test-5	Test-6	Test-7
Cell slime weight (g)	392	356	222	32	183	882	816
Cell slime weight ratio	82.18%	49.58%	48.16%	25.81%	98.92%	99.77%	97.84%
Adhered slime weight (g)	85	362	239	92	2	2	18
Adhered slime weight ratio	17.82%	50.42%	51.84%	74.19%	1.08%	0.23%	2.16%
Total slime weight (g)	477	718	461	124	185	884	834

adhered slimes is observed in Test-3 using the type-3 anodes. In Test-4, which was conducted under high current density using the type-1 anodes, the total weight of slimes decreases significantly and the adhered slimes occupy almost three fourths of all slimes in weight. In Test-5 where the wide cathode blanks were utilized, the weight of total slimes is also reduced, with most of the slimes as cell slimes (settled and suspended slimes in the cell). In Test-6, which was performed under low flow rate using the type-2 anodes, the total slime weight is not lowered and almost all slimes exist in the form of cell slimes. The resulting anodes have interesting surface morphologies, which are shown in Figure 7.5. Note that the significant drops of the total weight of slimes in Test-4 and Test-5 could be partially due to the loss of slime particles through the drain pipe. A similar phenomenon happened in Test-7, which was conducted under low cell temperature using the type-2 anodes, with a slightly higher weight ratio of adhered slimes. Consequently, the type-2 high impurity level anodes and the type-3 low impurity level anodes present better anode slime adhesion than the type-1 anodes with mid-level impurities contents; high current density condition lowers the total weight of slimes and improves adhesion of anode slimes; the wide cathode blanks with normal cathodic current density result in lowered total weight of slimes and very poor anode slime adhesion, probably due to the much higher current density on the anodes; the low flow rate test and the low cell temperature test also show poor slime adhesion on the anode with quite large amounts of cell slimes, which could be the results of the interaction between high impurities contents in the anodes and high current density on the anodes due to the use of wide cathode blanks (1.17 of the ratio of cathode to anode area). These will be further discussed in section 7.4. Test-7 will not be further discussed, because the temperature drop was not significant enough to

Figure 7.5 The residual anode with distinct surface morphologies after copper electrorefining Test-6

observe or arrive at a conclusion on the effects of cell temperature on slime adhesion and transport in the pilot scale electrorefining cell, although our individual small scale tests with excellent temperature control showed temperature is a very important parameter as discussed in section 5.4.

7.4 Discussion

7.4.1 The Effect of Anode Compositions

The effects of impurities contents in the anode on slime behavior and cathode purity can be discussed from the results of Test-2, Test-3, and the control test. In order to analyze the inclusion particle types in each type of anodes, the cross-sections cut from the type-1, type-2, and type-3 anodes were polished and observed under SEM/EDS. The results are shown in Figures 7.6 – 7.8, which include an SEM image, an EDS overlapping map involving several elements, and four individual elemental distribution maps for significant elements.

From Figures 7.6 – 7.8, the inclusion particle types in these three types of anodes are similar. Firstly, lead, bismuth, sulfur, and arsenic have similar distributions in the anodes and are mostly distributed at the outer coating around inclusion particles, while oxygen has different distribution than other elements and is mostly distributed at the core of inclusion particles with copper. Therefore, oxygen plays the role of forming copper oxide cores (mostly likely to be cuprous oxide according to previous studies),[7] and lead, bismuth, sulfur, and arsenic generally constitute the outer shell of inclusions. Sometimes, cuprous selenide can also form the core as demonstrated in previous research.[7, 8] Secondly, there are some cuprous oxide cores without coatings distributed in the anodes, due to insufficient amounts of lead, bismuth, sulfur, and arsenic.[8] Thirdly, Pb-Bi-S-As compound

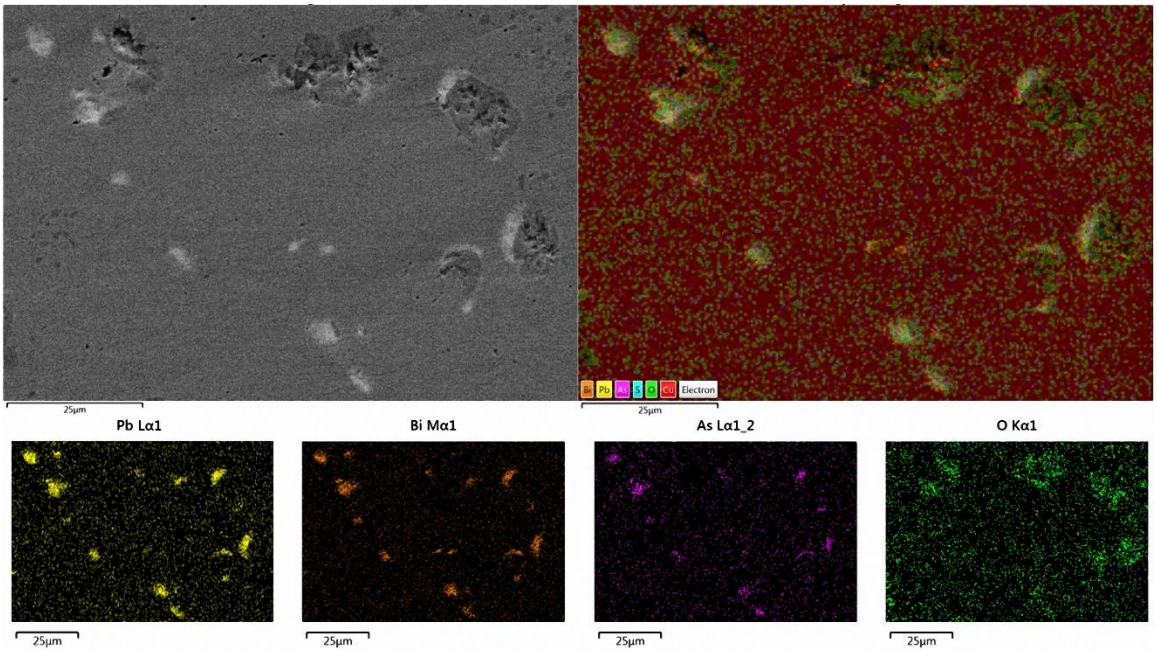

Figure 7.6 SEM/EDS images of the cross-section of the type-1 anodes used in the tests

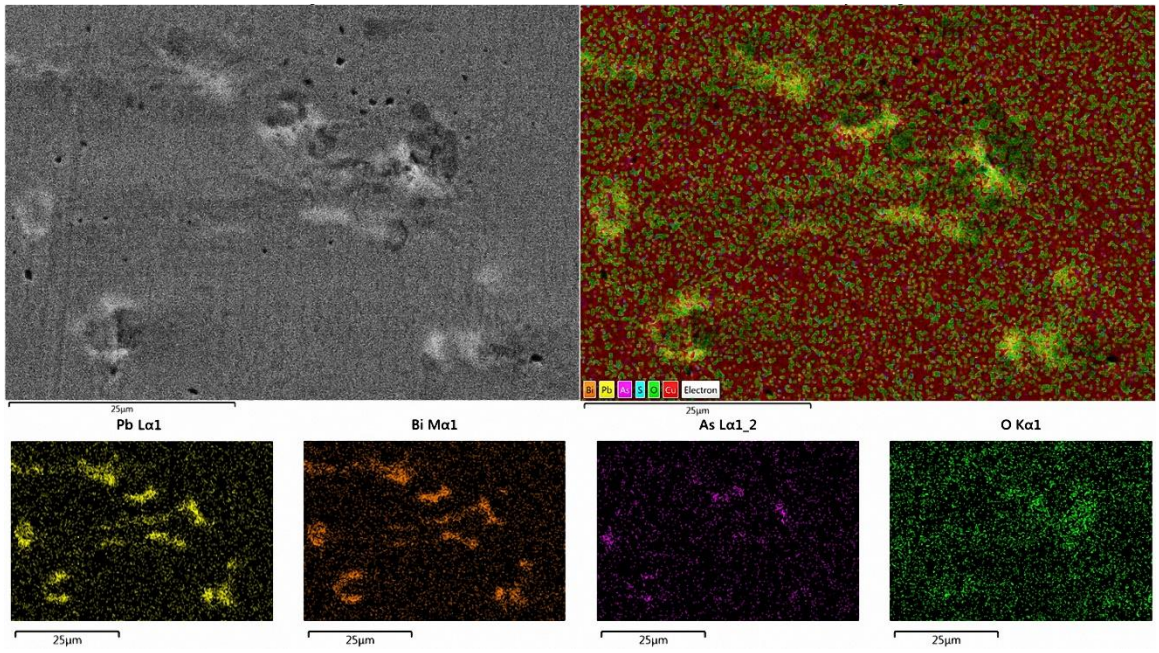

Figure 7.7 SEM/EDS images of the cross-section of the type-2 anodes used in the tests

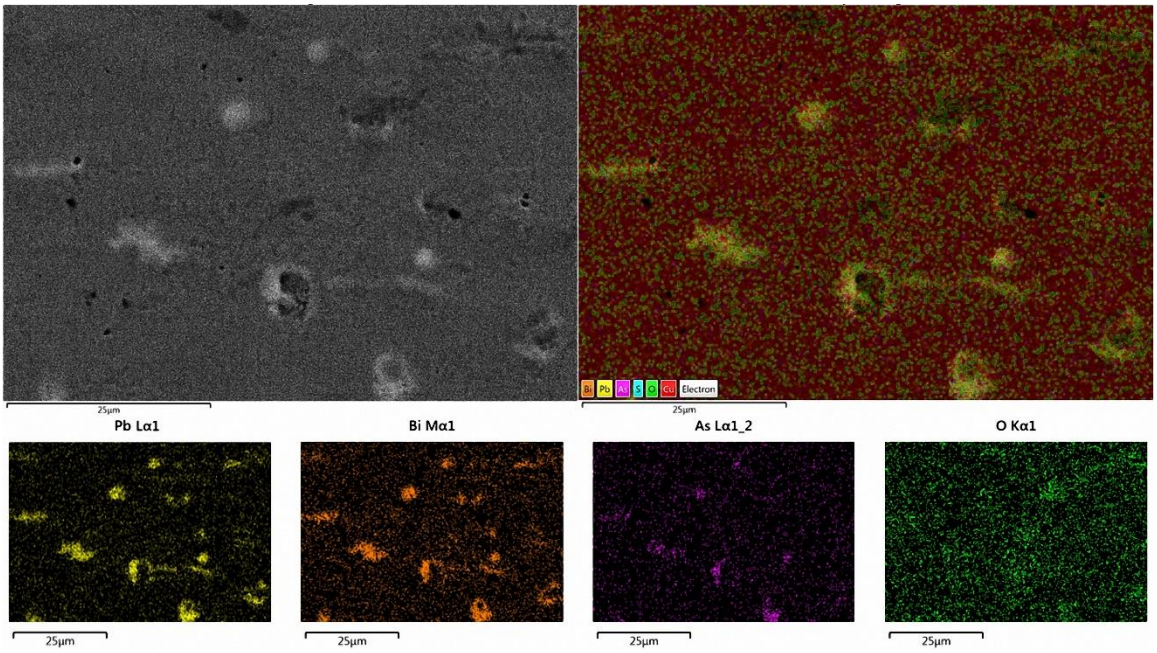

Figure 7.8 SEM/EDS images of the cross-section of the type-3 anodes used in the tests

isolated particles exist in the anodes. Consequently, most inclusion particles in the three different types of anodes have Cu-O cores with Pb-Bi-S-As shells and the remaining inclusions are uncoated Cu-O cores and Pb-Bi-S-As compound isolated particles. The mechanism of forming Cu-O core with Pb-Bi-S-As shell inclusion particles is that:[8] copper oxide generally has a melting temperature around 1273.15 K (1000 ℃) and would be solidified first in the grain boundary region; the Pb-Bi-S-As compounds have lower melting temperatures and would solidify around the preformed Cu-O cores.

However, the three types of anodes have some differences in terms of inclusion particles, according to Figures 7.6 – 7.8. Firstly, cuprous oxide cores are better surrounded by Pb-Bi-S-As shells in the type-2 and type-3 anodes. Secondly, arsenic distribution in Pb-Bi-S-As compounds is almost as dense as the distributions of lead and bismuth in the type-1 anodes, but is sparser in the type-2 and type-3 anodes. These phenomena should be due to the high Pb/As ratio (about 2) in the type-2 and type-3 anodes and the low Pb/As ratio (about 1) in the type-1 anodes. According to Chapter 5, inclusion particles with Pb-Bi-S shells have lower sintering temperatures and are easier to adhere to the anode surface and coalesce as larger particles, than inclusion particles with Pb-Bi-S-As shells. This is mostly because the addition of high melting temperature arsenic would increase the sintering temperatures of the shells. Although As-O core with Pb-Bi-S shell inclusion particles are not formed in the three types of anodes, the relative content of arsenic in Pb-Bi-S-As shells of existing inclusion particles should affect their sintering and coalescence temperatures. In order to examine arsenic distribution in Pb-Bi-S-As shells of the inclusions in the three different types of anodes, EDS area scans on inclusion particle shells were performed. Typical arsenic distribution in the shell of inclusions in the type-1 anodes is shown in Figure

7.9. The type-2 and type-3 anodes have similar arsenic distribution in the shell of their inclusion particles, which is shown in Figure 7.10.

It can be seen that the relative arsenic content in comparison with lead and bismuth in the shell of inclusion particles is much higher in the type-1 anodes than in the type-2/type-3 anodes. This is very likely due to the lower Pb/As ratio in the type-1 anodes compared with the type-2 and type-3 anodes. Since the sintering and coalescence of slime (inclusion) particles are mostly affected by their shells, the slime particles from the type-2 and type-3 anodes can coalesce together and adhere to the anode more easily than those from the type-1 anodes, because of lower sintering temperatures due to lower arsenic content in the shell and more coatings (shell) on the core (as shown in Figures 7.6 – 7.8). Consequently, Test-2 and Test-3 have better anode slime adhesion (as shown in Table 7.6) and lower bismuth levels in the harvested cathode copper (as shown in Table 7.5) except Cathode-3 in Test-3. This cathode was slightly tilted toward Anode-2 during the test due to uneven sitting surface and could have more slime particles deposited. The effects of the relative arsenic content in the shells of slime particles can be further discussed with the ICP results of the compositions of the slimes collected from the tests, which are shown in Table 7.7.

As shown in Table 7.7, the adhered anode slimes have a higher Pb/As ratio than the cell slimes (settled and suspended slimes in the cell) in both tests, which indicates that slime particles with a higher lead to arsenic ratio in their shells (cores are mostly Cu_2O) can sinter together and adhere to the anode more easily than those with a lower lead to arsenic ratio in the shells.

In sum, anodes with a lead to arsenic ratio larger than 1.5 perform better in copper

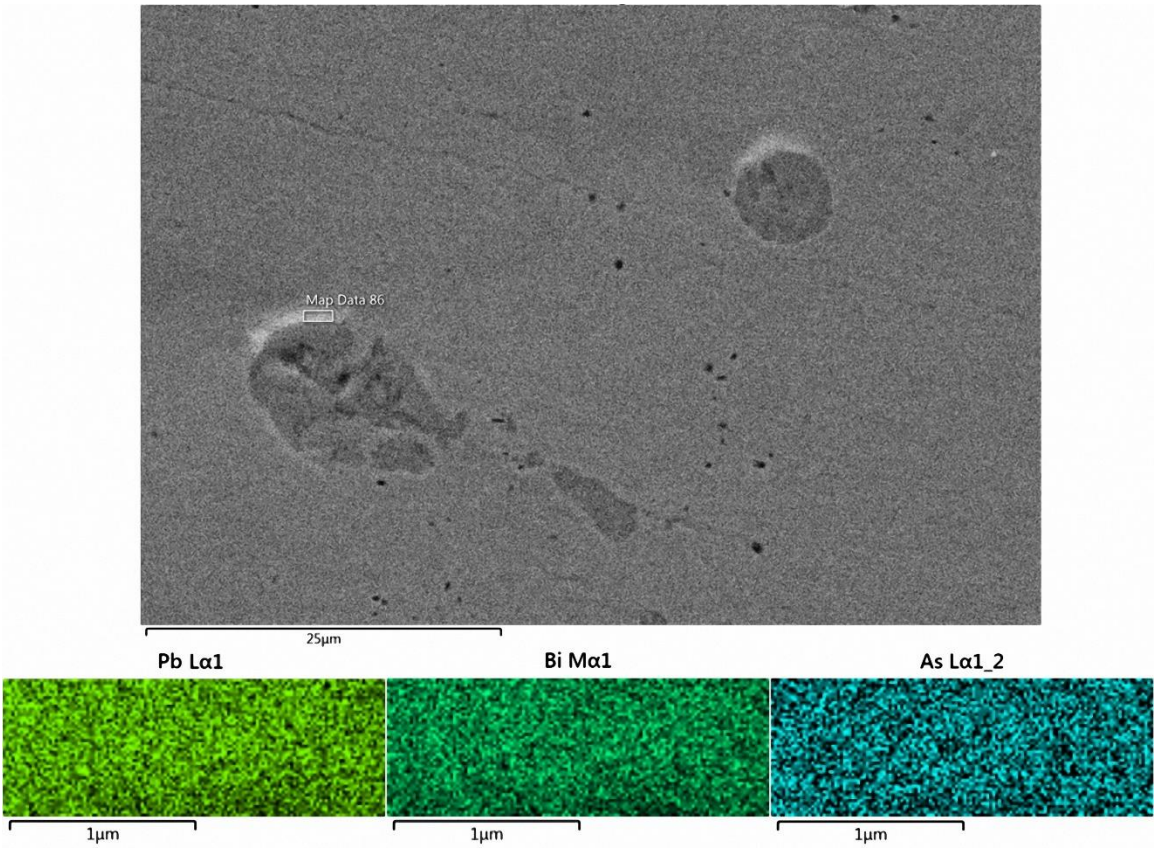

Figure 7.9 EDS area scan on the shell of a typical inclusion particle in the type-1 anodes

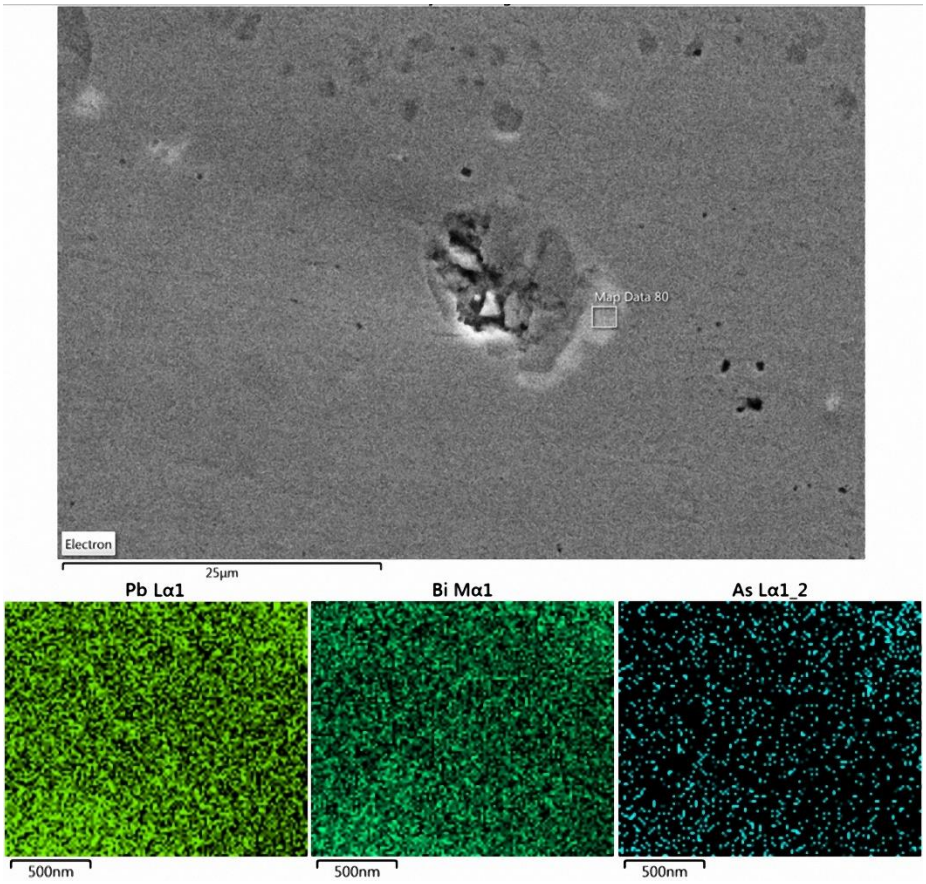

Figure 7.10 EDS area scan on the shell of a typical inclusion particle in the type-2/type-3 anodes

Table 7.7 Compositions of different types of slimes collected from Test-1 and Test-2

Test Number	Slime Type	Pb	As	Bi	Cu	Se	Te	Sb	Sn	Pb/As
Test-1	Adhered Slime	23.5	4.94	4.43	25.8	7.64	0.959	0.3	0.033	4.8
	Cell Slime	15.11	3.94	3.01	19.6	4.43	0.602	0.316	0.05	3.8
Test-2	Adhered Slime	34	2.95	3.64	15	2.65	0.934	0.423	0.068	11.5
	Cell Slime	21.7	2.08	2.28	8.65	2.03	0.48	0.289	0.031	10.4

All units in wt.%

electrorefining by having a larger amount of adhered slimes and producing cathode copper with lower bismuth levels than anodes with almost equal amounts of lead and arsenic. Anodes with a lead to arsenic ratio smaller than one are not studied in these tests, but according to Chapter 5, anodes with a lead to arsenic ratio smaller than 0.6 produced high purity cathode copper by forming inclusion particles with As-O cores and Pb-Bi-S shells.

7.4.2 The Effect of High Current Density

From the results of Test-4 using the type-1 anodes under an average cathodic current density of 300 A/m^2, the effects of high current density on the behavior of slime particles and the production of cathode copper can be discussed by comparison with the control test. The most significant findings in Test-4 include: 1) the anode slime adhesion is exceptionally good (74.19% adhered slimes, compared with 17.82% in the control test); 2) the total weight of slimes collected in Test-4 are reduced by 74% from that in the control test; 3) the bismuth levels in the cathode copper are reduced to lower than 0.1 ppm, which is better than the copper produced in the control test. Apparently, the anode slimes have significantly different behavior in this test and therefore the compositions of different types of slimes collected in the test need to be analyzed in order to find the reasons for these phenomena. The results are shown in Table 7.8.

It is very interesting that the copper concentration in the adhered slimes is less than 0.0004 wt.%, which means almost no copper is left in the attached slimes after this high current density copper electrorefining test. Note that under high current density, the heat generated on the anodes by contact resistance is larger than that under normal conditions and the local temperatures at the anode surface would be higher than those in Test-1. The temperatures of the electrolyte in the interelectrode gap in Test-4 and the

Table 7.8 Compositions of different types of slimes collected from Test-4 and Test-1

Test Number	Slime Type	Pb	As	Bi	Cu	Se	Te	Sb	Sn	Pb/As
Test-4	Adhered Slime	23.59	4.08	5.85	<0.0004	7.38	1.17	0.386	0.045	5.8
	Cell Slime	18.35	4.02	4.79	22.3	4.95	0.81	0.344	0.042	4.6
Test-1	Adhered Slime	23.5	4.94	4.43	25.8	7.64	0.959	0.3	0.033	4.8
	Cell Slime	15.11	3.94	3.01	19.6	4.43	0.602	0.316	0.05	3.8

All units in wt.%

control test were measured using an infrared thermometer. The electrolyte temperature in the gap increased about 3 K from around 335 K (62 ℃) in the control test to about 338 K (65 ℃) in Test-4. Additionally, the number of slime particles released from the copper matrix per unit time is larger than in Test-1. As a result, more sintering and coalescence of slime particles can take place in front of the anode surface, leading to better adhesion of slimes on the anode. When the larger current passes through the stronger adhered anode slimes on the remaining copper anode, the cuprous oxide core and even part of the shell of slime particles can be dissolved by this current. The dissolution of part of the slime particles results in lighter weight of the anode slimes layer. Therefore, even under the same adhesion strength, more slime particles can be kept in the layer. Slime particles that have a smaller lead to arsenic ratio would fall off the anodes as discussed in section 4.1, and the cuprous oxide cores would be kept in the slimes. These explain the different compositions of the two types of slimes from Test-4. Besides, the collected cell slimes and adhered slimes were observed under SEM/EDS, which are shown in Figures 7.11 – 7.12. Note that structures of slime particles might be affected in the process of collection. Some charging issues are reflected on the images of Figure 7.12, due to the poor electrical conductivity of slime particles.

From Figure 7.11, it can be observed that the cell slimes collected in Test-4 show the existence of a large amount of elemental copper, which indicates that most cuprous oxide cores remain in the released slimes from the anode. From Figure 7.12, the adhered slimes on the anode do not have much copper left but have significant amounts of lead, bismuth, arsenic. Many shell-like structures agglomerated together and can be seen in the SEM image of the adhered slimes, which means that most cuprous oxide cores have been

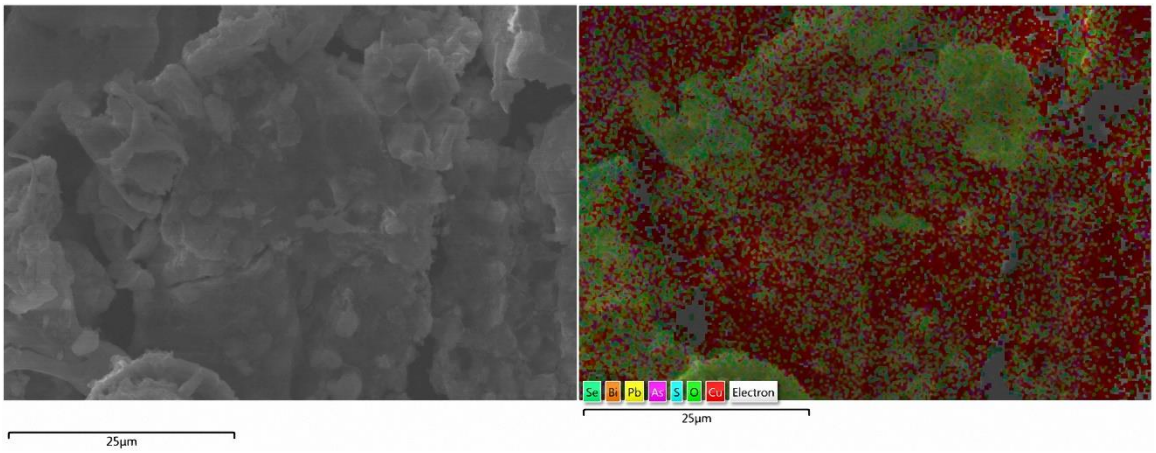

Figure 7.11 SEM image and EDS layered map of elemental distributions for cell slimes collected in Test-4

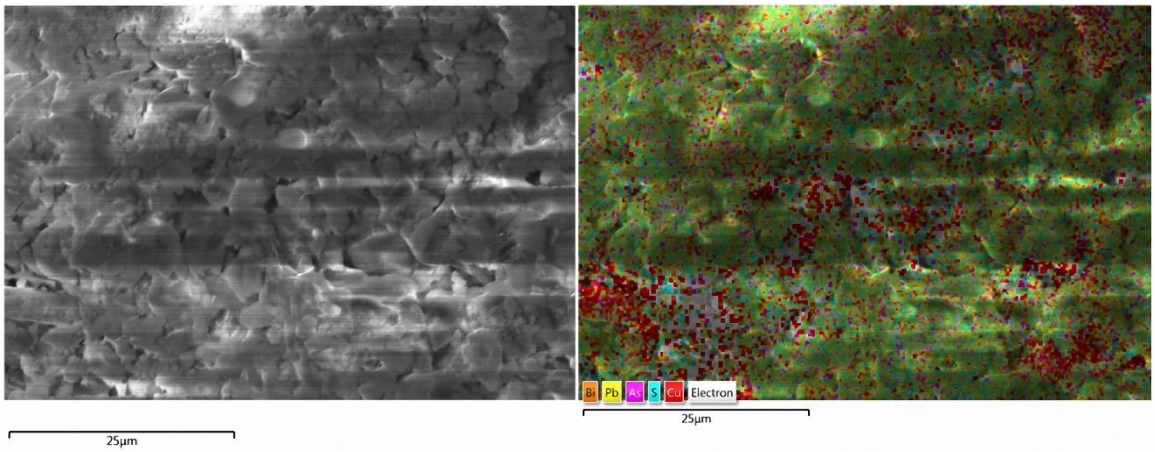

Figure 7.12 SEM image and EDS layered map of elemental distributions for adhered slimes stripped from the residual anodes in Test-4

consumed by the large current passing through the anode slimes layer. Another SEM image of the adhered slimes from Test-4 is shown in Figure 7.13 and it can be seen that these slime particles have almost only shells left with most of their cuprous oxide cores consumed. The dissolution of cuprous oxide cores and even part of shells is a significant cause of the weight loss of slime particles collected in Test-4.

The better control of bismuth levels in the harvested copper in Test-4 mostly results from the largely improved anode slime adhesion with less slimes released to the electrolyte. In addition, higher current densities on the anodes can create larger electrolyte density gradients along the anodes, which can result in downward electrolyte flows with larger magnitudes.[9] Then the released slimes are more likely to settle to the cell bottom rather than stay in the electrolyte flow and become entrapped in the cathode copper.

Consequently, the high current density condition can be a solution for copper electrorefining using anodes with a lead to arsenic ratio of approximately one. High current density can lead to more sintering and coalescence of slime particles and lighter weight of anode slimes, which gives better anode slime adhesion. Also, it generates faster downward electrolyte flows along the anodes, which help settle the released slimes to the bottom of the cell.

7.4.3 The Effect of Wide Cathode Blanks

From the results of Test-5, the wide cathode blanks generally have two major effects in the process. Firstly, since the wide blanks are approximately 1.36 times as large as the normal blanks in width and deposition area, the anodic current density under the condition of 240 A/m^2 cathodic current density on the wide blanks is even higher than that under the condition of 300 A/m^2 cathodic current density on the normal blanks. The total

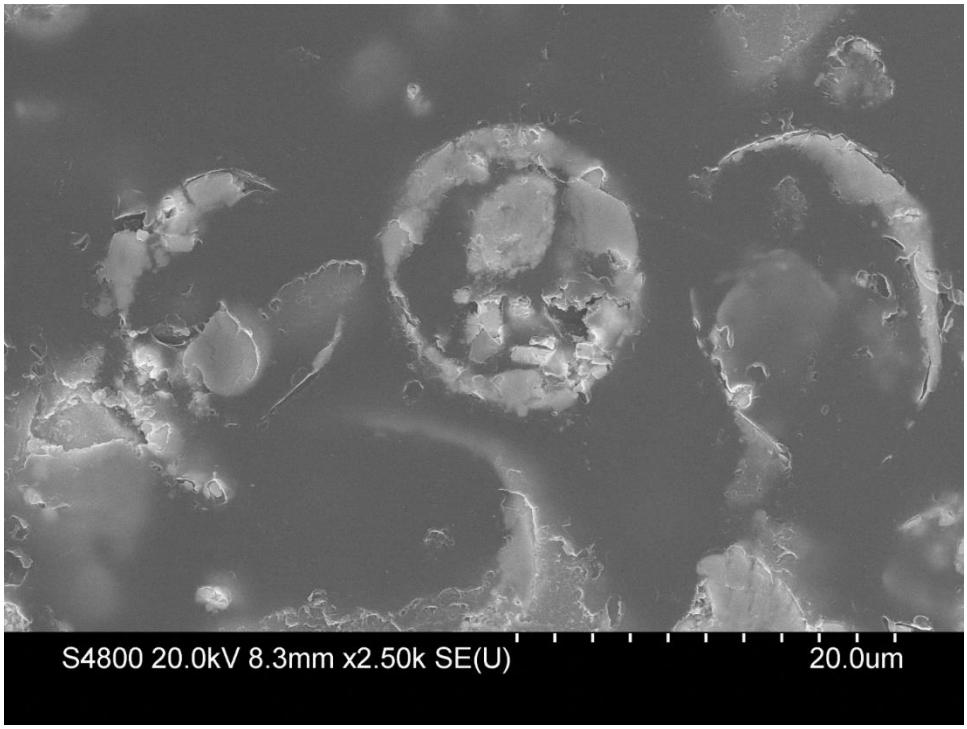

Figure 7.13 SEM image of the adhered slimes stripped from the residual anodes in Test-4

current on the anodes is 98 A in Test-5 (281 A/m^2 anodic current density) and 81 A in Test-4 (232 A/m^2 anodic current density), with the same anode dimensions throughout all the tests. Secondly, wider cathode blanks provide more opportunities to entrap slime particles moving in the gap between each adjacent anode and cathode. Therefore, there could be some impurity concentration differences between the edges and the center of cathode copper, which will be discussed in this section.

The compositions of the two types of slimes collected in Test-5 were also analyzed by ICP and the results are shown in Table 7.9.

Notice that the weight of adhered slimes in Test-5 is only 2 grams and most slimes are cell slimes (settle and suspended slimes) that are 183 grams. Under the condition of even higher anodic current density, the copper in the slime particles in Test-5 were not consumed as dramatically as Test-4. Also, the anode slime adhesion is very poor in Test-5, as the weight percentage of adhered slimes is only 1.08%. These indicate that the adhered slimes failed to remain attached on the anode surface for the cuprous oxide cores to be completely dissolved. Rather, they fell off the anode after partial dissolution of cores, with about 14% of copper left. The dissolution of the shells of slime particles may become more intense under this high anodic current density. The reason behind this phenomenon could be that the sintering and coalescence of slime particles in front of the anode becomes so intensive under such high anodic current density that the adhesion force cannot hold the resulting large slime particle aggregates anymore. Besides, the number of anode slimes released from the copper matrix per unit time is even larger than in Test-4 and thus the sizes of anode slime aggregates can increase very quickly with the fast release of slime particles. Consequently, most anode slimes would fall off the anode due to their large sizes before

the complete dissolution of cuprous oxide cores. The fact that the impurities levels in the harvested copper were well controlled in Test-5 may demonstrate that the sizes of most cell (released) slimes in Test-5 are sufficiently large to settle down with less opportunities to affect the purity of cathode copper. After all, suspended slimes are the major source of cathode contamination rather than settled slimes.[8]

To examine the edge effect of wide cathode blanks, the edges of the harvested copper from cathode-1 and cathode-2-W were cut off and analyzed separately for impurities concentrations, in order to compare with those in the center. The results are shown in Table 7.10. Note that the width of the cut edges is equivalent to the width difference between the normal blank and the wide blank. Thus, it determined whether the extra areas on the wide blanks are more contaminated or not. Also notice that these edge and center samples were cut at the same height on the cathode.

In Table 7.10, C-1-L, C-1-C, and C-1-R represent the left edge, the center, and the right edge of Cathode-1 respectively. The same naming method applies for Cathode-2-W. It can be observed from the results that the edges of the harvested copper contain more impurities than the centers of the cathode copper. For example, the left edge of Cathode-1 has excessive bismuth, arsenic, and lead, and thus could not be further processed if produced in real plants. In contrast, the centers of Cathode-1 and Cathode-2-W have low levels of impurities and are acceptable for further processing. Therefore, from a purity perspective only, the results indicate that cathode blanks that are wider than the anode (4.75 inches (0.12 m) versus 4.2 inches (0.11 m)) can entrap more slime particles due to the edge effect. Thus, it is better to have the cathode to anode width ratio less than one in order to have purer cathode copper. However, the current distribution and production rate would be

Table 7.9 Compositions of different types of slimes collected from Test-5 and Test-1

Test Number	Slime Type	Pb	As	Bi	Cu	Se	Te	Sb	Sn	Pb/As
Test-5	Adhered Slime	24.39	1.16	2.44	10.5	6.92	0.8	0.151	0.053	21.0
	Cell Slime	30.28	3.11	3.22	13.6	4.35	0.759	0.295	0.054	9.7
Test-1	Adhered Slime	23.5	4.94	4.43	25.8	7.64	0.959	0.3	0.033	4.8
	Cell Slime	15.11	3.94	3.01	19.6	4.43	0.602	0.316	0.05	3.8

All units in wt.%

Table 7.10 Impurities concentrations in the edges and centers of the harvested copper from Cathode-1 and Cathode-2-W in Test-5

Impurity		Bi	As	Pb	Se	Sb	Ni	Fe	Sn	Te
Test 5	C-1-L	0.8	4.16	5.53	< 0.500	< 1.00	2.2	3.3	< 0.500	0.54
	C-1-C	0.12	1.68	0.73	< 0.500	< 1.00	< 1.0	3.6	< 0.500	< 0.500
	C-1-R	0.13	3.89	0.76	< 0.500	< 1.00	1.3	3.7	< 0.500	< 0.500
	C-2-W-L	0.38	2.76	2.15	< 0.500	< 1.00	1.8	5.9	< 0.500	< 0.500
	C-2-W-C	0.1	< 1.000	0.5	< 0.500	< 1.00	< 1.0	3.2	< 0.500	< 0.500
	C-2-W-R	0.11	2.18	< 0.500	< 0.500	< 1.00	1.4	< 3.0	< 0.500	< 0.500

All units in ppm; C-1-L represents Cathode-1-Left_edge;

C-2-W-L represents Cathode-2-West_side-Left_edge

affected if the cathode blank is narrower than the anode. A better method is to cut off the edges of subquality cathodes whose impurity levels are beyond the limits, in order to make the rest of the cathodes meet the purity requirements.

In total, the wide cathode blanks intensify the sintering and coalescence of slime particles in front of the anode by raising the anodic current densities. When the sizes of the large slime aggregates increase to a point where they cannot be supported by the adhesion force anymore, the slime aggregates fall off the anode and settle to the cell bottom. Therefore, the cathode copper in Test-5 was not influenced significantly by the released slimes though the anode slime adhesion was poor under such conditions. Furthermore, edge effects of the wide cathode blanks were found by analyzing the impurities contents in the edges and the centers of the harvested copper. The results show that the edges have higher impurities levels than the centers.

7.4.4 The Effect of Low Flow Rate

Test-6 was performed under the flow rate of 2.5 ml/s, which is half of the normal value. The anodes used are the type-2 anodes, which have slime particles with lower sintering temperatures than those from the type-1 anodes as discussed in section 4.1. The wide cathode blanks were utilized in the test. Note that the electrolyte temperature in the four electrode gaps dropped about 4 K from the normal value of 334 K (61 ℃) due to less heat convection from the inlet flow and the temperature was 334 K (61 ℃) in regions near the inlet. Passivation was observed on the surfaces of the anodes especially Anode-2 during Test-6 and the voltage changes as the passivation begins as shown in Figure 7.14. Distinct surface morphologies were observed on the anodes after passivation, as shown in Figure 7.5.

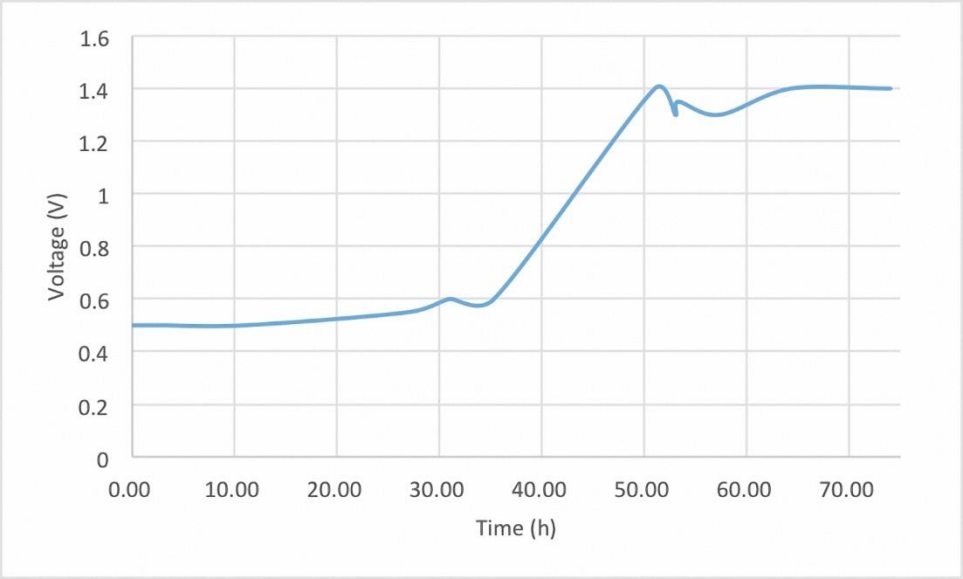

Figure 7.14 Cell voltage versus time at the beginning of passivation during Test-6

The occurrence of passivation is usually accompanied by the formation of copper oxide layers attached to the anode and poor heat and electrical conductivities of the layers can elevate local temperatures in front of the anode.[8] Thus the local temperatures could be increased though the cell temperature dropped. Furthermore, the type-2 anodes have slime particles that are easier to sinter together (high Pb/As ratio) and coalesce as larger particles than the type-1 anodes under similar temperatures. As a result, with the same anodic current density, slime particles in front of the anode in Test-6 can have more intensive sintering and coalescence than Test-5, which can lead to very early release of larger slime particle aggregates from the anode before the consumption of cuprous oxide cores. The compositions of the slimes collected in Test-6 confirm the early release of cell slimes before the cores can dissolve under the high anodic current density. The results are shown in Table 7.11.

The results of Test-2 are shown in Table 7.11 instead of the control test, because the type-2 anodes were used in both Test-6 and Test-2. Note that the adhered slimes are only 2 grams in this test and the remaining adhered slimes were dissolved significantly by the high current according to Table 7.11. Copper in the cell slimes were almost not consumed, which means that most slimes did form large slime aggregates and fall off the anode surface very early due to the very intense sintering and coalescence of the slime particles. The inlet electrolyte flow had smaller velocities in Test-6 due to the low flow rate and thus generated less agitation at the bottom of electrodes. Consequently, the released large slimes could settle down more easily and had less effects on cathode copper, which is consistent with the low levels of bismuth in the harvested copper from Test-6.

Therefore, low flow rate exerts effects on anode slime behavior in front of the

Table 7.11 Compositions of different types of slimes collected from Test-6 and Test-2

Test Number	Slime Type	Pb	As	Bi	Cu	Se	Te	Sb	Sn	Pb/As
Test-6	Adhered Slime	13.36	0.691	0.722	7.58	1.34	0.288	0.098	0.032	19.3
	Cell Slime	17.4	2.32	1.26	15.3	2.62	0.576	0.161	0.026	7.5
Test-2	Adhered Slime	34	2.95	3.64	15	2.65	0.934	0.423	0.068	11.5
	Cell Slime	21.7	2.08	2.28	8.65	2.03	0.48	0.289	0.031	10.4

All units in wt.%

anode. Although it results in temperature drop in the bulk solution, low flow rate increases local temperatures in front of the anode by causing anode passivation and forming oxide layers. With the type-2 anodes and wide cathode blanks under such conditions, slimes can coalesce as large particles and fall off quite early due to very intense slime particle sintering and coalescence, without significant dissolution of cuprous oxide cores. Low flow rate can also reduce the agitation below the electrodes and thus help these large slime particles settle even faster.

7.5 Conclusions

A series of copper electrorefining tests were performed in a pilot scale cell to examine the effects of anode compositions, current density, cathode blank width, temperature, and flow rate on the anode slime behavior and cathode copper purity. Although the effect of temperature could not be determined due to limited temperature changes that can be reached in the cell, other factors demonstrated significant effects on slime adhesion and cathode purity. Since the experiments were conducted using the same electrolyte as the commercial cells in a large electrorefining cell under tankhouse environment, the results and analyses are valuable for directing the industrial copper electrorefining process. Table 7.12 suggests a set of optimal operating conditions for copper electrorefining based on the results of this study.

First of all, the anode compositions, especially the contents of lead and arsenic, affect the anode slime behavior. Anodes that have a lead to arsenic ratio larger than 1.5 demonstrated better anode slime adhesion and lower impurity levels in cathode copper than the anodes that have similar amounts of lead and arsenic. This is mostly because the relative arsenic content in the shell of inclusion particles can affect their sintering temperatures.

Table 7.12 Optimal anode composition and operating conditions for copper electrorefining based on the results of this study

Parameters	Pb/As ratio	Cathode current density	Flow rate/velocity/residence time		Cathode size
Optimal value/range	>1.5 or <0.6	300 A/m^2 with normal blank	5 ml/s	0.04 m/s	Normal blank for high quality
		240 A/m^2 with wide blank	3.3 hours residence time		Wide blank for high productivity

Inclusion particles in the anodes with the lead to arsenic ratio larger than 1.5 have less arsenic content in the shell and thus have lower sintering temperatures. Therefore, these particles are easier to coalesce together and adhere to the anode, with reduced opportunities to fall off and/or reach the cathode. According to Chapter 5, anodes that have a lead to arsenic ratio smaller than 0.6 also performed better than the anodes with this ratio close to 1.

Secondly, high current density can intensify the sintering and coalescence of slime particles. Besides, it can heavily dissolve the cuprous oxide core in slime particles, leading to lighter weight of anode slimes layer. Thus the anode slime adhesion is improved under high current density, with larger percentages of adhered slimes on the anode. It can help reducing impurities levels in copper electrorefining using anodes with the lead to arsenic ratio close to one.

Thirdly, wide cathode blanks with the same cathodic current density can significantly intensify slime particles' sintering and coalescence in front of the anode by largely increasing the anodic current density. Under such conditions, the slime particle aggregates would grow to a point where the adhesion force cannot support their weight anymore. As a result, the slime particle aggregates fall off the anode and settle down due to their too large sizes. Therefore, the produced cathode copper has low impurity levels, though the amount of cell (released) slimes is considerably larger under these conditions. In addition, the edges of cathode copper were shown to be more contaminated than the center.

Lastly, low flow rate generally causes less agitation under the electrodes, lower bulk electrolyte temperature and anode passivation that can raise local temperatures in front

of the oxide layers attached to the anode. When anodes with the lead to arsenic ratio larger than 1.5 and wide cathode blanks were used under such conditions, the sintering and coalescence of slime particles in front of the anode would be very significant and the slime particles would fall off the anode quite early without significant dissolution of cores.

7.6 References

1. S. Wang, D. Kim, and M. Moats: *Proceedings of Copper 2013 Conference*, Santiago, Chile, 2013, vol. 5, pp. 577-94.

2. M. Moats, S. Wang, and D. Kim: *T.T. Chen Honorary Symposium on Hydrometallurgy, Electrometallurgy and Materials Characterization,* John Wiley & Sons, Inc., Hoboken, NJ, 2012, pp. 3-21.

3. C. A. Moller and B. Friedrich: *Proceedings of Copper 2010 Conference*, Hamburg, Germany, 2010, vol. 4, pp. 1495-510.

4. J. E. Hoffmann: *JOM*, 2004, vol. 56, pp. 30-33.

5. S. Wang: *JOM*, 2004, vol. 56, pp. 34-37.

6. Michael L. Free: *Hydrometallurgy: Fundamentals and Applications*, John Wiley & Sons, Inc., Hoboken, NJ, 2013, pp. 218-28.

7. T. T. Chen and J. E. Dutrizac: *JOM*, 1990, vol. 42, pp. 39-44.

8. W. Zeng, M. L. Free, and S. Wang: *J. Electrochem. Soc.*, 2016, vol. 163, pp. E14-31.

9. W. Zeng, M. L. Free, J. Werner, and S. Wang: *J. Electrochem. Soc.*, 2015, vol. 162, pp. E338-52.

CHAPTER 8

CONCLUSIONS AND FUTURE RESEARCH

In this dissertation, a comprehensive and thorough research on copper electrorefining including process optimization by statistical methods, mathematical modeling of electrochemical processes, simulations of species transport, fluid flow field, and slime particle transport, characterizations of anode inclusions/slimes, mechanisms of anode slime adhesion and coalescence, and the effects of process parameters on anode slime behavior and cathode purity, have been done by using both lab-scale and pilot-scale electrolytic cells.

First of all, the effects of main process parameters on impurity particle transport in copper electrorefining were evaluated by statistical analysis: 1) the inlet flow rate, temperature, and current density were found to have either positive or negative effects on impurity particles' behavior and their distributions on the cathode; 2) the two-way interactions between process parameters especially the interaction between the inlet flow rate and temperature play significant roles in the process; 3) it was found that corner positions of a cathode tend to have more contaminations than the center position.

Secondly, mathematical modeling of copper electrorefining in a lab-scale cell was performed to simulate electrochemical process, fluid flow, and particle transport, which were demonstrated to be significantly influenced by the boundary conditions of inlet flow rate, temperature, and current density. Similar effects of these main process parameters on

impurity particle behavior were found from the simulation results as from the experimental results (summarized in the previous paragraph). The simulation results are well correlated with the experimental results in terms of impurity particle distributions on the cathode. Thus, the model could be utilized to predict impurity concentration distributions on cathodes harvested in copper electrorefining cells. The interaction between the settling velocities of impurity particles and the z component of local fluid velocities, which are influenced by inlet flow rate, temperature, and current density, is demonstrated to be the main factor that determines whether or not the particles settle or remain in suspension.

Thirdly, anode slime adhesion and transport were found to be significantly affected by slime particle sintering and coalescence. The cell temperature and the composition of copper anode are the two major factors that determine the extent of slime particle sintering and coalescence. Increasing cell temperature and the content of arsenic in the anode when appropriate lead, bismuth, and sulfur levels are present can result in more slime sintering, leading to better anode slime adhesion, less suspended slimes, and higher cathode purity.

Fourthly, simulations of copper electrorefining in a pilot scale cell were performed and validated by experimentally measured electrolyte flow velocities in the gaps between adjacent electrodes. From both experimental and simulation results, the fluid flow at upper positions of the gaps are dominated by upward flow with the maximum magnitudes varying from 1.0 cm/s to 1.5 cm/s among different gaps. On the other hand, downward flow takes control of the fluid flow at lower positions of the gaps, with the maximum magnitudes varying from 1.4 cm/s to 1.9 cm/s. The transport of slime particles in the electrolyte flow was also simulated. The results of the appearance frequency of slime particles near cathode

were compared with impurity levels in the copper cathodes harvested from the experimental tests, and they show a good correlation with the total concentrations of major impurities.

Fifthly, the effects of anode compositions, current density, cathode blank width, temperature, and flow rate on the anode slime behavior and cathode copper purity were examined by performing copper electrorefining in the pilot scale cell. The results show that: anode compositions, especially the contents of lead and arsenic, affect the anode slime behavior; high current density can intensify the sintering and coalescence of slime particles and heavily dissolve the cuprous oxide core in slime particles, leading to improved anode slime adhesion; wide cathode blanks with the same cathodic current density can significantly intensify slime particles' sintering and coalescence in front of the anode, resulting in very large slime particle aggregates that would fall off the anode; low flow rate generally causes less agitation under the electrodes, lower bulk electrolyte temperature and anode passivation that can raise local temperatures in front of the oxide layers attached to the anode.

In the future, design and application of innovative copper electrolytic cells are worth studying. Species transfer, electrolyte flow, and slime particle transport can be significantly improved with the application of innovative electrolytic cells. Mathematical modeling and experimental tests can be performed to test innovative electrolytic cells.

APPENDIX

LIST OF PUBLICATIONS RELATED TO THIS THESIS

1. W. Zeng, J. Werner, and M. L. Free: *Hydrometallurgy*, 2015, vol. 156, pp. 232-38.
2. W. Zeng, M. L. Free, J. Werner, and S. Wang: *J. Electrochem. Soc.*, 2015, vol. 162, pp. E338-52.
3. W. Zeng, M. L. Free, and S. Wang: *J. Electrochem. Soc.*, 2016, vol. 163, pp. E14-31.
4. W. Zeng, S. Wang, and M. L. Free: *J. Electrochem. Soc.*, 2016, vol. 163, pp. E111-22.
5. W. Zeng, S. Wang, and M. L. Free: *Metall. Mater. Trans. B*, 2016, vol. 47, pp. 3178-91.